

Geodätisch-geophysikalische Arbeiten in der Schweiz

(Fortsetzung der Publikationsreihe
«Astronomisch-geodätische Arbeiten in der Schweiz»)

herausgegeben von der

Schweizerischen Geodätischen Kommission
(Organ der Akademie der Naturwissenschaften Schweiz)

**Zweiundachtzigster Band
Volume 82**

**Analysis of long-term GPS observations
in Greece (1993-2009) and geodynamic
implications for the Eastern
Mediterranean**

Michael D. Müller

2011

Adresse der Schweizerischen Geodätischen Kommission:

Institut für Geodäsie und Photogrammetrie
Eidg. Technische Hochschule Zürich
ETH Zürich
8093 Zürich
Switzerland

Internet: <http://www.sgc.ethz.ch>

ISBN 978-3-908440-28-4

Redaktion des 82. Bandes:
Dr. M. Müller, Dr. B. Bürki
Druck: Print-Atelier ADAG, Zürich

VORWORT

Der vorliegende Bericht enthält satellitengeodätische Untersuchungen von geodynamischen Prozessen zwischen der Nubischen und Eurasischen Lithosphärenplatte. Den Mittelpunkt bildet die Frage, wie das kinematische Feld in der Übergangszone zwischen diesen beiden Platten aussieht und in welchem Zusammenhang das Deformationsfeld mit dem Erdbebenpotenzial im Ägäischen Raum steht. Zudem wurden Modellrechnungen mit Finiten Elementen ausgeführt, um das Deformationsfeld mit dem Spannungsfeld in Verbindung zu setzen. Grundlage bildet ein permanentes GPS-Messnetz, das sich vom Ionischen Meer über das griechische Festland bis zur Ägäis erstreckt.

Im Anschluss an die Datenanalyse werden Zeitreihen für die Erdkrustenbewegungen, sowie Geschwindigkeits- und Deformationsfelder berechnet. Das Geschwindigkeitsfeld wurde mit Hilfe einer kinematischen Blockmodellierung systematisch analysiert. Nordwest- und Zentralgriechenland rotieren relativ zu Eurasien im Uhrzeigersinn und erreichen Geschwindigkeiten bis zu 35 mm/a nach Südwesten. Die Trennzone gegenüber Eurasien liess sich genau lokalisieren. Sie verläuft zwischen den Ionischen Inseln Levkada und Kephalaria (Kephalaria Transform Fault). Stationen in der Süd-Ägäis zeigen, dass die Extension entlang des Hellenischen Bogens nur in diskreten Abschnitten stattfindet. Dies dürfte für die Beurteilung des Erdbeben- und Tsunami-Risikos von grossem Interesse sein. Wichtig ist zudem der Nordägäische Graben, für den Herr Müller ein Verschiebungsmodell erarbeitet hat, das den Graben als Fortsetzung der Nord-anatolischen Verwerfung ausweist.

Das geodätische Deformationsfeld zeigt gute Übereinstimmung mit den Haupt-Deformationsrichtungen, wie sie aus Herdflächenlösungen von Erdbeben erhalten wurden. Die GPS-Messungen ermöglichten es zudem, co-seismische Verschiebungen zu quantifizieren. Am Schluss wendet Michael Müller die Methode der Finiten Elemente an, zum einen auf die Subduktionszone der Nubischen Platte in der Südägäis, zum anderen auf die Transformstörungen in der Nordägäis. Wichtiges Ergebnis ist, dass die GPS Daten eine weitgehende Entkopplung der Nubischen von der Ägäischen Platte nahelegen.

Herr Müller hat die GPS Daten ausserordentlich sorgfältig ausgewertet und erfolgreich in ein realistisches geodynamisches Modell eingebunden. Ohne seinen grossen Einsatz bei Feldmessungen wie auch in der Auswertung hätte das Projekt nicht so erfolgreich durchgeführt werden können. Eine Reihe von Publikationen unterstreicht die Aktualität seiner Arbeiten. Die gefundenen Resultate stellen einen wichtigen Fortschritt für das Verständnis der Deformationsvorgänge im östlichen Mittelmeer dar. Das grosse internationale Interesse an den Naturgefahren im östlichen Mittelmeerraum unterstreicht die Bedeutung der Forschungsarbeit. Die Schweizerische Geodätische Kommission (SGK) dankt Herrn Müller für den wertvollen Beitrag. Der Schweizerische Nationalfonds (SNF) und die Deutsche Forschungsgemeinschaft (DFG) haben dieses Projekt finanziell unterstützt, wofür die SGK ihren grossen Dank ausspricht. Der Schweizerischen Akademie für Naturwissenschaften danken wir für die Übernahme der Druckkosten.

Prof. Dr. H.-G. Kahle
Institut für Geodäsie und Photogrammetrie
ETH Zürich

Prof. Dr. A. Geiger
ETH Zürich
Präsident der SGK

PREFACE

Le rapport qui suit concerne des recherches en géodésie satellitaire appliquées à l'étude de phénomènes géodynamiques entre les plaques lithosphériques Eurasienne et Nubienne. L'accent est porté sur la détermination du champ cinématique entre ces deux plaques ainsi que sur les relations qu'il pourrait y avoir entre le champ de déformation et les risques sismiques potentiels dans la région hellénique. Des modélisations par éléments finis ont été réalisées afin de mieux comprendre le couplage entre les champs de déformation et de contrainte. L'étude s'est basée sur un réseau de stations GPS permanentes distribuées entre la mer Ionienne et la mer Egée en passant par la terre ferme grecque.

A la suite des analyses de données, les séries temporelles des vitesses de déplacement de la croûte terrestre ainsi que le champ de déformation ont été calculés. Le champ de vitesse a été analysé de façon systématique à l'aide de modèles par blocs. Il est démontré que les parties Nord-ouest et centrale de la Grèce subissent une rotation horaire et atteignent des vitesses jusqu'à 35 mm/a en direction du Sud-ouest. La séparation avec l'Eurasie est parfaitement identifiée. Elle peut-être localisée entre les îles ioniennes Levkada et Kephallonia (Kephallonia Transform Fault). Les stations dans le Sud de la mer Egée montrent que l'extension de l'arc hellénique est confinée uniquement à certaines sections bien distinctes. Ce constat est de toute première importance en vue de l'estimation des risques de séismes et de tsunamis dans la région. En outre, le modèle de déplacement détaillé réalisé par Monsieur Müller semble corroborer l'hypothèse selon laquelle la fosse du Nord de la mer Egée est une continuation de la faille transformante Nord-Anatolienne.

Le champ de déformation géodésique représenté par les axes principaux des tenseurs de déformation correspond fidèlement aux déformations simulées à partir des mécanismes aux foyers des principaux séismes. Les mesures GPS permettent donc de quantifier les déplacements co-sismiques. Dans la partie finale du rapport, le modèle par éléments finis est appliqué à la zone de subduction Nubienne dans le Sud de la mer Egée ainsi qu'à la faille transformante principale dans le Nord de la mer Egée. Il en résulte un constat important : les données GPS semblent démontrer un découplage significatif entre les plaques Nubienne et Egée.

Monsieur Müller a traité les données GPS de façon exceptionnellement approfondie et minutieuse et les a introduites avec succès dans un modèle géodynamique réaliste. Sans son grand engagement lors des campagnes de mesures ainsi que pendant le traitement des données, le projet n'aurait pas pu être mené à bien avec autant de succès. Une liste de publications souligne l'actualité de son travail. Les résultats obtenus constituent des avancées importantes en ce qui concerne la compréhension des processus de déformation de la partie orientale de la Méditerranée. L'intérêt international croissant pour les risques naturels dans la Méditerranée renforce l'importance de ce travail de recherche. La commission géodésique suisse (SGC) tient à remercier Monsieur Müller pour son travail de haute valeur. Le fonds national suisse pour la recherche et la Deutsche Forschungsgemeinschaft (DFG) ont soutenu financièrement ce projet et la SGC tient pour cela à les en remercier. Nous remercions l'Académie suisse des sciences naturelles pour avoir pris à sa charge les frais d'impression du présent fascicule.

Prof. Dr. H.-G. Kahle
Institut de Géodésie et Photogrammétrie
ETH Zürich

Prof. Dr. A. Geiger
ETH Zürich
Président de la CGS

PREFACE

Satellite geodetic research work has been carried out to study geodynamic processes in the transition zone between the Nubian and Eurasian lithospheric plates. A focal point was to quantify the kinematic field and to address the question on how the deformation field relates to the seismic potential encountered in the Hellenic domain. In addition, calculations have been performed by applying the finite element model with the aim to better understand the relationship between the deformation and the stress field. The study was based on a permanent GPS network which extends from the Ionian sea across the Hellenic mainland to the Aegean sea.

Following a careful data analysis time series of 3D crustal movements have been established, and velocity as well as deformation fields were calculated. The kinematic field was systematically analyzed by block modeling. Northwest- and central Greece are rotating clockwise relative to Eurasia reaching rates of up to 35 mm/yr oriented to the southwest. The course of the transition zone towards Eurasia was exactly identified. It can be followed along a fault system located between the Ionian islands of Levkada and Kephallonia (Kephallonia Transform Fault). Stations in the south Aegean area clearly show that extension along the Hellenic arc is confined to discrete sections. This result is of significant interest to assess the potential of seismic and tsunami risk. In this respect also the North Aegean trough is of importance. Michael Müller has established a detailed displacement model which corroborates the assumption that the trough forms the continuation of the North Anatolian transform fault.

The geodetic deformation field represented by the strain tensor fits well with the principal axes of stress obtained from fault plane solutions of major earthquakes. The GPS measurements also enable to quantify co-seismic displacements. In the final part of the report the finite element model is applied to the subduction zone of the Nubian plate in the southern Aegean as well as to major transform faults in the north Aegean. The GPS data allows the conclusion that the Nubian plate is greatly decoupled from the Aegean plate.

The GPS data were extremely carefully analyzed by Michael Müller and successfully implemented in a realistic geodynamic model. He has pursued this project with painstaking endeavour. This does not only include software development and data processing but also field work. The project would not have been possible without his persistent commitment in all aspects of the activities. Several papers already published by Michael Müller underscore the importance of the work accomplished and show the international interest in the spatio-temporal resolution of recent crustal movements he has obtained. The results form an important step forward towards a better understanding of the tectonic processes going on in the eastern Mediterranean. The Institute of Geodesy and Photogrammetry of the ETH Zürich and the Swiss Geodetic Commission (SGC) of the Swiss Academy of Natural Sciences would like to thank Michael Müller for his highly valuable contribution. We are grateful to the Swiss National Science Foundation and the Deutsche Forschungsgemeinschaft (DFG) for co-funding the research project and to the Swiss Academy of Sciences for financing the printing costs.

Prof. Dr. H.-G. Kahle
Institute of Geodesy and Photogrammetry
ETH Zürich

Prof. Dr. A. Geiger
ETH Zurich
President of SGC

Abstract

The Global Positioning System (GPS) is used to determine rates of crustal motion in the Hellenic plate boundary zone since the late eighties. The zone comprises Greece and its adjacent regions. It is characterized by the interaction of the Eurasian, Anatolian and Nubian plates moving relative to each other. Tectonic processes associated with this motion cause the highest seismic activity of Europe. Nine earthquakes with magnitude six or higher occurred within this region in the period 2006 to 2011. International efforts are being made to achieve a better understanding of the origin and characteristics of ongoing seismotectonic processes. The ETH Zurich has taken active part in these efforts. Results achieved so far provide valuable boundary conditions for geodynamic modeling. In close collaboration with other institutes an extensive GPS network has been established and periodically remeasured. The network consists of campaign-type and continuous GPS sites. The corresponding data record has been significantly extended in the course of this project. A 16 year record of GPS data (1993–2009) is available now for Greece.

In its first part the report deals with the evaluation of the data record. The strategy of GPS analysis was enhanced compared to preceding projects by applying recent GPS processing models and improving postprocessing procedures. The concept of including data of numerous IGS and EUREF sites located in Europe, North Africa and the Middle East was continued. This allowed for a precise alignment of the GPS network to a global reference frame (ITRF2005), the reduction of processing induced systematic signals and the determination of a pole of rotation for the Eurasian plate.

An improved kinematic field was derived which was analyzed in terms of slowly deforming regions by using a block model. The modeling provides several insights. For instance, northwestern Greece rotates clockwise (cw) and the region south of the North Aegean trough (NAT) rotates counterclockwise (ccw) relative to Eurasia. Both areas form blocks with small internal deformation. Moreover, they describe the western termination of the North Aegean trough. A large part of ongoing deformation is located in confined regions.

The GPS derived deformation field provides information about ongoing tectonic processes. These include N-S extension between Northern Greece and the Gulf of Corinth and dextral shear strain in the North Aegean sea as well as along the Kefalonia fault zone in the Ionian sea. New results concerning ongoing deformation processes were achieved in the Southeast Aegean sea and in Northern Greece. Pronounced N-S extension (100 nstrain/yr) was determined across the Mygdonian graben. NNW-SSE extension amounting to 150 nstrain/yr was found between the islands of Kalymnos and Tilos in the SE Aegean sea.

The NAT and the Kefalonia fault zone are among the most pronounced transform faults in the Hellenic plate boundary zone. Rates of closely located GPS sites were used for the estimation of the slip rates and locking depths of the structures. Four profiles across the NAT show a decrease of slip rates from the Ganos fault (23 mm/yr) towards the southwestern edge of the Sporades basin (<5 mm/yr). The geodetic results provide further evidence that the NAT forms the westward continuation of the North Anatolian fault zone commencing at the Saros basin. The decrease of slip rates west of the Chalkidiki peninsula is related to a different orientation of the NAT and to NNE-SSW extension in the Sporades basin.

Finite element models were used to relate GPS rates to basic geodynamic models. The first model

focused at the analysis of the subduction rate near the central Hellenic trench. The results point to a largely uncoupled interface between the Nubian and Aegean plates. The second model quantifies the slip rates along the three major NE-SW to ENE-WSW trending transform faults in the North Aegean sea. Rates amounting to 21 mm/yr were derived for the NAT, 10 mm/yr for the Skyros-Edremit fault and 4 mm/yr for the Psara-Lesvos fault. Moreover, the model reveals additional deformation zones such as NNE-SSW extension in the Sporades basin.

The derived GPS rates and the conducted analyses improve the current understanding of seismotectonic processes in Greece. The investigations also highlight remaining problems and bring forward new ideas which will ultimately be valuable for further analysis and assessment of natural hazard in Greece.

Zusammenfassung

Seit den achtziger Jahren wird das Globale Positionierungssystem (GPS) genutzt, um rezente Krustenbewegungen in der Hellenischen Plattenrandzone zu bestimmen. Diese Zone umfasst Griechenland sowie deren angrenzende Gebiete. Sie ist geprägt von der Interaktion zwischen den sich relativ zueinander bewegenden eurasischen, anatolischen und nubischen Lithosphärenplatten. Die tektonischen Prozesse bewirken in Griechenland die höchste Seismizität in Europa. Zwischen 2006 und 2011 ereigneten sich in dieser Region neun Erdbeben mit einer Magnitude von sechs oder höher. Um die Ursachen und Auswirkungen der aktuellen seismotektonischen Aktivitäten besser zu verstehen, werden verstärkt internationale Anstrengungen unternommen, an denen sich auch die ETH Zürich intensiv beteiligt. Bisher erzielte Resultate liefern wertvolle Randbedingungen für geodynamische Modellierungen. In Zusammenarbeit mit anderen Institutionen wurde im Verlauf von mehreren Projekten ein umfangreiches GPS Netz aufgebaut und gemessen, das sowohl aus Kampagnenstationen als auch aus kontinuierlich-betriebenen Stationen besteht. Der Datensatz wurde im Rahmen dieses Projektes wesentlich erweitert. Für Griechenland steht nun eine Langzeit-Datenreihe von 16 Jahren (1993–2009) zur Verfügung.

Im ersten Teil des Berichtes wird die Auswertung dieses Datensatzes behandelt. Die Auswertestrategie wurde weiterentwickelt, indem neue GPS Prozessierungsmodelle angewandt und Nachbearbeitungsprozeduren verbessert wurden. Das Konzept, zusätzlich zu den griechischen Stationen Daten einer Vielzahl von IGS und EUREF Stationen in Europa, Nordafrika und dem Nahen Osten in die Prozessierung einzubinden, wurde weitergeführt. Dies ermöglichte die präzise Einbindung des GPS Netzes in einen globalen Referenzrahmen (ITRF2005), die Reduktion von prozessierungsbedingten systematischen Störsignalen sowie die Bestimmung eines konsistenten Rotationspols für Eurasien.

Als Ergebnis steht ein verbessertes kinematisches Feld zur Verfügung, das mit einem Blockmodell untersucht wurde, um langsam deformierende Gebiete zu identifizieren. Nordwestgriechenland beispielsweise, das relativ zu Eurasien kohärent rechtsdrehend rotiert, sowie eine linksdrehend rotierende Region südlich des Nordägäischen Grabens konnten als Blöcke mit geringer interner Deformation detektiert werden. Die beiden Blöcke bilden das westliche Ende des Nordägäischen Grabens. Die Blockmodellierung zeigt zudem auf, dass ein grosser Teil der Deformation in räumlich begrenzten Gebieten lokalisiert ist. Die Berechnung des Deformationsfeldes basierend auf der neu erzielten GPS Geschwindigkeitslösung gibt Hinweise auf aktuelle tektonische Prozesse. Hierzu gehören N-S Extension zwischen Nordgriechenland und dem Golf von Korinth sowie dextrale Scherdeformation in der Nordägäis und entlang der Kefalonia Transformverwerfung im Ionischen Meer. Neue Kenntnisse aktueller Deformationsprozesse wurden in Nordgriechenland und in der Südostägäis erzielt: Akzentuierte N-S Extension von 100 nstrain/yr über den Mygdonischen Graben sowie NNW-SSE Extension von bis zu 150 nstrain/yr zwischen Kalymnos und Tilos in der SE Ägäis.

Der Nordägäische Graben (NAG) und die Kefalonia Verwerfung gehören mit zu den ausgeprägtesten Transformverwerfungen in der Hellenischen Plattenrandzone. GPS-basierte Geschwindigkeiten in der Nähe dieser Strukturen wurden genutzt, um die Verschiebungsgeschwindigkeit und Koppelungstiefe der Verwerfungen zu bestimmen. Vier Profile über den NAG zeigen eine Abnahme der Geschwindigkeit von der Ganos Verwerfung (23 mm/yr) zum südwestlichen Ende des Sporaden Beckens hin (<5 mm/yr). Die Resultate zeigen auf, dass der NAG entlang des Saros Grabens eine Fortsetzung der Nordanatolischen Verwerfung darstellt. Die Reduktion der Verschiebungsge-

schwindigkeit westlich der Chalkidiki Halbinsel steht im Zusammenhang mit der Änderung der Orientierung der Verwerfung sowie mit der NNE-SSW Extension im Sporaden Becken.

Um die Bewegungsraten zu einfachen geodynamischen Modellen in Bezug zu setzen, wurde die Methode der Finiten Elemente angewandt. Im ersten Modell wurde die Subduktionsrate entlang des zentralen Hellenischen Grabens analysiert. Die Ergebnisse deuten auf eine weitgehend ungekoppelte Plattengrenze hin. Das zweite Modell quantifiziert die Verschiebungsgeschwindigkeiten der drei NE-SW bis ENE-WSW orientierten Haupttransformverwerfungen in der Nordägäis. Die erzielten Raten betragen 21 mm/yr für den Nordägäischen Graben, 10 mm/yr für die Skyros-Edremit Verwerfung sowie 4 mm/yr für die Psara-Lesvos Verwerfung. Zudem zeigt das Modell aktuelle Deformationszonen im Sporaden Becken auf, wo NNE-SSW Extension von bis zu 100 nstrain/yr berechnet wurde.

Die erzielten GPS Geschwindigkeiten sowie die durchgeführten Analysen verbessern das Verständnis für die seismotektonischen Prozesse in Griechenland. Zudem zeigen die Untersuchungen neue Fragestellungen und Ansätze auf, die für die Erforschung und Beurteilung der dortigen Naturgefahren hilfreich sein können.

Contents

1	Introduction	1
1.1	State of research	1
1.2	Goals	1
2	Geologic setting	3
2.1	Evolution of the central and eastern Mediterranean	3
2.2	Tectonic framework of Greece	4
3	GPS data evaluation	7
3.1	Description of relevant GPS networks	7
3.1.1	Campaign-type GPS network in Greece and southern Bulgaria	7
3.1.2	Continuous GPS networks in Greece	8
3.1.3	IGS and EUREF sites	8
3.2	Strategy of GPS data processing	9
3.3	Definition of the geodetic datum	11
3.4	Velocity estimation of CGPS sites	12
3.4.1	Introduction	12
3.4.2	Discontinuities in position time series	13
3.4.3	Removing outliers	13
3.4.4	Exclusion periods	14
3.4.5	Estimation of velocities and offsets	14
3.4.6	Reduction of apparent scale changes of the processed GPS network	15
3.4.7	Scaling of formal errors of velocities	22
3.5	Velocity estimation of campaign-type GPS sites	23
3.6	Factors affecting the velocity estimates	24
3.6.1	Tracking performance of GPS sites	24
3.6.2	Used orbits and earth orientation parameters	24
3.6.3	Campaign-type data of the years 1993 and 1994	26
3.7	Concluding remarks	30
4	Kinematic field in Greece (1993–2009)	31
4.1	Introduction	31
4.2	Euler vector and estimation of a pole of rotation for Eurasia (ITRF2005)	31
4.3	Kinematic block model for Greece	32
4.4	Kinematic field and modeling in the North Aegean domain	37
4.4.1	Kinematic field	37
4.4.2	Slip rates and locking depths along the North Aegean trough	39
4.5	Kinematics along the Hellenic trench system	45
4.5.1	Ionian islands, Western Greece and NW Peloponnesos	45
4.5.2	Southern Peloponnesos and South Aegean sea	48
4.6	Vertical motion in Greece	51
4.7	Concluding remarks	53
5	Strain rates derived by using the method of collocation	55
5.1	Least-squares collocation	55

5.2	Velocity and strain rate fields calculation implemented in the program 'strain'	55
5.3	Strain rates and differential rotations in Greece	56
5.4	Concluding remarks	63
6	Seismic signals in GPS time series	65
6.1	Introduction	65
6.2	Estimation of earthquake displacements	65
6.3	Analytical surface dislocation model	65
6.4	Earthquakes in the Aegean domain	68
6.4.1	1999 Ms 5.9 Athens earthquake	68
6.4.2	2001 Mw 6.4 Skyros earthquake	71
6.4.3	2008 Mw 6.4 Rhodes earthquake	72
6.5	Earthquakes in the Ionian sea	72
6.5.1	1997 Mw 6.6 Strofades earthquake	72
6.5.2	2003 Mw 6.2 Lefkada earthquake	73
6.5.3	2006 Zakynthos earthquake series	73
6.5.4	2008 Mw 6.4 NW Peloponnesos earthquake	75
6.5.5	Comparison of seismicity and interseismic strain rates	77
6.6	Concluding remarks	80
7	Finite element models	81
7.1	Finite element method	81
7.1.1	Basic theory	81
7.1.2	Displacement-based finite element analysis	82
7.2	Physical properties of a model lithosphere	84
7.2.1	Introductory notes	84
7.2.2	Elasticity	84
7.2.3	Brittle failure	85
7.2.4	Ductile deformation	87
7.2.5	Temperature in the continental lithosphere	87
7.3	Interaction between the overriding and the subducting plate at the central Hellenic trench	88
7.3.1	Geodetic constraints	88
7.3.2	Developed finite element model	89
7.4	3D finite element model of the North Aegean sea	96
7.4.1	Introduction	96
7.4.2	Model set up	96
7.4.3	Results	97
7.5	Concluding remarks	104
8	Conclusions	105
	Bibliography	108
A	Additional notes on GPS data processing	123
A.1	Positions and velocities used for aligning the GPS network to ITRF2005	123
A.2	Discontinuities and exclusion periods introduced in GPS time series	125
A.3	Time series of parameters related to the GPS processing runs	128
A.4	Sites selected for the algorithm reducing apparent scale changes	131
B	Additional notes on the derived velocity field for the period 1993–2009	133
B.1	Pole of rotation for the Eurasian plate	133
B.2	Nubian plate motion relative to Eurasia	135
B.3	Comparison of rates of closely located continuous and campaign-type GPS sites	136

B.4	Periodic motion of sites PAXI and APAX	136
B.5	Conspicuous signals in the time series of site SKIN	136
B.6	Notes on the use of the data from Straub et al. [1997] and McClusky et al. [2000] .	138
C	GPS velocity results	141
C.1	Introduction	141
C.2	Rates of continuous GPS sites	141
C.3	Rates of campaign-type GPS sites	144
D	Time series of continuous GPS sites in Greece	147
E	Residual time series of campaign-type GPS sites in Greece	157
F	Additional notes on the applied dislocation models	175
F.1	Statistics of the locking depth models	175
F.2	Description of the dislocation model for the calculation of strain accumulation at a subduction zone	178
G	Additional notes on finite element modeling	179
G.1	Strain tensors used in this thesis	179
G.2	Supplementary notes on the FE model of the central Hellenic trench (chapter 7.3)	181
G.2.1	Geometry of the FE model	181
G.2.2	Energy fractions in the FE model	181
G.3	Supplementary notes on the FE model of the North Aegean domain (chapter 7.4) .	185
G.3.1	Statistics of the model residuals	185
G.3.2	Errors in calculated strain rates due to the used projection method	186

Abbreviations

AEF	Agios Efstratios fault
CCW	Counterclockwise
CGPS	Continuous GPS
CODE	Center for Orbit Determination in Europe
CW	Clockwise
DOY	Day of year
EGPS	Campaign-type GPS
ETH	Swiss Federal Institute of Technology
EUREF	Regional Reference Frame Sub-Commission for Europe
FEM	Finite element model
FPS	Fault plane solution
GGL	Geodesy and Geodynamics Lab
GNSS	Global Navigation Satellite System
GPS	Global Positioning System
HTS	Hellenic trench system
IGP	Institute of Geodesy and Photogrammetry
IGS	International GNSS service
ITRF	International terrestrial reference frame
KFZ	Kefalonia fault zone
kyr	Thousand years
MIT	Massachusetts Institute of Technology
MJD	Modified Julian date
Myr	Million years
NAF	North Anatolian fault
NAT	North Aegean trough
NOA	National Observatory of Athens
NTUA	National Technical University of Athens
PCV	Phase center variation
PLF	Psara-Lesvos fault
PPB	Parts per billion
RINEX	Receiver independent exchange format
RMS	Root mean square
SEF	Skyros-Edremit fault
UNAVCO	University Navstar Consortium
WHT	West Hellenic trench
WRMS	Weighted root mean square

1 Introduction

1.1 State of research

Techniques of satellite geodesy have significantly improved in terms of accuracy over the last decade. They have become a valuable instrument for observing crustal motion on the earth's surface accurate to a few millimeters per year. Especially the Global Positioning System (GPS) has found widespread usage in the field of geodynamics. The broad applications of GPS in engineering and sciences have led to a steady increase in the number of permanent GPS sites worldwide. Simultaneously, the GPS user group aims to enhance modeling techniques and the quality of derived products. Efforts made in this field have contributed to a steady improvement of achievable GPS results.

In the Eastern Mediterranean GPS measurements have been performed for more than 20 years in view of the precise determination of crustal motion. The first projects carried out in the Hellenic plate boundary zone aimed to reveal the main patterns of the velocity field (e.g., *Gilbert et al.* 1994; *Oral et al.* 1995; *Mueller* 1996; *Straub and Kahle* 1995; *Straub et al.* 1997). In later studies the accuracy and robustness of the results were enhanced, new insights in the kinematic and strain rate fields were found, and signatures of time dependent processes such as earthquake displacements were observed and quantified (e.g., *Reilinger et al.* 1997; *Clarke et al.* 1998; *Peter et al.* 1998; *Briole et al.* 2000; *Peter* 2000; *Kahle et al.* 2000; *McClusky et al.* 2000; *Avallone et al.* 2004; *Reilinger et al.* 2006; *Hollenstein* 2006; *Burchfiel et al.* 2006; *Kotzev et al.* 2006; *Hollenstein et al.* 2008a,b). The geodetic results achieved so far can be considered as a first important step towards a better understanding of the tectonic evolution, geophysical structure and present-day dynamics in the Hellenic plate boundary region. However, most of the observed deformation processes are not yet fully understood. More comprehensive geodetic measurements will provide additional constraints and contribute to a deeper understanding of ongoing tectonic processes.

First models describing the kinematics of the Eastern Mediterranean were proposed in the 1970s by studying seismicity and structural geology [*McKenzie*, 1972, 1978; *Le Pichon and Angelier*, 1979]. These studies have been continued revealing more details of ongoing geophysical processes and the tectonic evolution (e.g., *Jackson and McKenzie* 1988; *Gautier et al.* 1999; *Kreemer et al.* 2004). Various geophysical branches are involved in geodynamic research thereby forming it to an interdisciplinary topic. The comparison of geodetic estimates with results from other research disciplines have provided interesting insights. For instance, *Jenny et al.* [2004] compared geodetic strain rates with the average seismic strain release and found considerable deficits in seismically-released strain along the West Hellenic trench. An overview over the tectonic framework of the Eastern Mediterranean is presented in chapter 2. More specific findings from research disciplines such as e.g. seismology or structural geology are discussed specifically with respect to modeling approaches and obtained results.

1.2 Goals

The Geodesy and Geodynamics Lab (GGL) of the Institute of Geodesy and Photogrammetry (IGP) of ETH Zurich compiled an 11 year record of campaign-type and continuous GPS data which was

processed in previous studies [Hollenstein, 2006; Hollenstein et al., 2008a]. The compilation of the data record covering the Hellenic plate boundary zone was done in close collaboration with other institutions. This data record has been considerably extended by additional five years of continuous and campaign-type GPS data. Taking advantage of the long time span of available GPS data this thesis is focused on following three main topics.

1. Computation of accurate GPS results

A 16 year record of GPS data for the years 1993 to 2009 is available. Developments in GPS techniques (e.g., satellite constellation, GPS measuring equipment), improvements in GPS processing models and numerous reference frame releases are leading to inhomogeneities in the processing of such a long data record. In addition, the data sets obtained by the two principal GPS measuring modi (continuous GPS and campaign-type GPS) have different characteristics. The derivation of a consistent and accurate velocity solution requires the evaluation and implementation of numerous processing strategies and their assessment with respect to high accuracy demands. GPS data analysis using the Bernese GPS software, the compilation and improvement of time series, the calculation of precise rates and the combination of rates of continuous and campaign-type GPS are examples of this task. The compilation of homogeneous time series is the basis for the retrieval and investigation of time-dependent signals, such as e.g. pre-, co- or postseismic signals. A careful separation of geophysical signals and processing related artifacts is required to assess the amount of preseismic motions.

2. Analysis and modeling of the kinematic field

The densification of the CGPS network and further repetitions of measurements at non-permanent sites will allow to improve knowledge of the kinematic field especially in the North Aegean and in the Southeast Aegean sea. Longer CGPS time series and remeasured campaign-type sites probably provide more accurate and reliable rates also in other regions of Greece. An improvement in accuracy of vertical rates is expected with reference to longer time series of CGPS sites. The analysis of the kinematic field will elucidate features not known before in that detail and provide constraints for ongoing tectonic processes. Various modeling approaches, such as block modeling and strain rate calculation based on the method of collocation, are employed. These efforts will provide a first-order structuring of the kinematic field and reveal the style and rates of present-day deformations. The results are discussed in terms of tectonic structures and seismicity. Moreover, they provide a base for further analyses.

3. Tectonic implications

Geoscientific interpretations shall be derived starting from the kinematic field. The main task is the description of ongoing deformation processes in terms of style and rate. Modeling approaches (e.g., dislocation models, finite element analysis) are taken into consideration relating geodetically observed crustal motion with geophysical parameters. The values and limitations of the methods will be investigated with respect to the derived geodetic information. Investigations are also directed towards modeling techniques which explicitly include vertical rates. The degree of constraint provided by the vertical rates has to be investigated because this information is still sparse. Another focus of interest is the provision of additional evidence for the correlation between deformation and seismicity. Several earthquakes occurred in close distance to GPS sites in the period 1995 to 2009. Displacements associated with these earthquakes shall be estimated and discussed with respect to their fault plane solutions.

The three main topics are addressed in chapters 3 to 7. The topics are not entirely independent since the tectonic analyses and interpretations are primarily based on the GPS data and its evaluation strategy. The chapters are structured corresponding to the applied methods. Consequently, tectonic features of regions such as the North Aegean sea are discussed in several chapters. The most important findings are summarized in chapter 8.

2 Geologic setting

2.1 Evolution of the central and eastern Mediterranean

The Mediterranean region is located in the contact zone between the Eurasian and the Nubian plates (Fig. 2.1). The higher spreading rate in the south Atlantic compared to the north Atlantic causes a counterclockwise rotation of Nubia leading to a northwestward directed collision with Eurasia [Mueller, 1984; Mueller and Kahle, 1993]. The convergence of these plates resulted in the subduction of the Nubian plate under the Eurasian plate in late Cretaceous (~80 Myr ago) [Faccenna *et al.*, 2001]. In Oligocene (~30 Myr ago) the stress regime changed and caused the opening of extensional basins [Cherchi and Montadert, 1982; Lister *et al.*, 1984] simultaneously from west to east (Alboran sea, Liguro-Provençal Basin, Tyrrhenian sea, Aegean sea) [Jolivet and Faccenna, 2000]. Slab detachment [Wortel and Spakman, 1992] or a decrease of the northward motion of the Nubian plate caused by Nubia/Arabia-Eurasia collision [Jolivet and Faccenna, 2000] may have provoked the initiation of the retreat of the Nubian slab. Extension largely decreased in the central and western Mediterranean sea by now [Faccenna *et al.*, 2004]. Fast seismic velocity anomalies are observed from North Africa to the Calabria-Apennines, twisting beneath the Alps, the Carpathians-Dinarides-Hellenides to the Bitlis-Zagros zone. Most of them are not connected to the surface. This indicates a fragmented subduction zone which was almost continuous once. Deep to intermediate seismicity in the Mediterranean is restricted to the Hellenic and Calabria Wadati-Benioff zones and locally beneath the Alboran region (Faccenna and Becker [2010] and references therein).

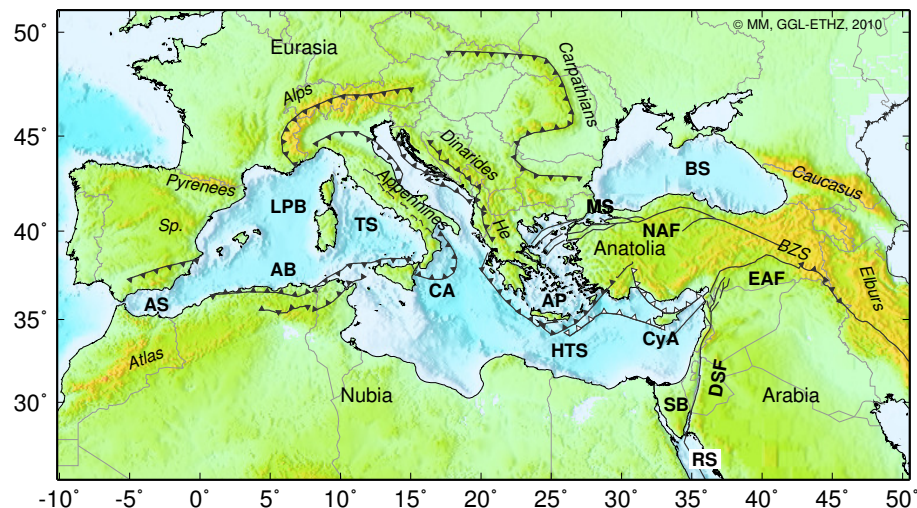


Figure 2.1: Tectonic framework of the Mediterranean sea and adjacent regions. AB: Algerian basin, AP: Aegean plate, AS: Alboran sea, BS: Black sea, BZS: Bitlis-Zagros suture, CA: Calabrian arc, CyA: Cyprus arc, DSF: Dead Sea fault, EAF: East Anatolian fault, He: Hellenides, HTS: Hellenic trench system, LPB: Liguro-Provençal Basin, MS: Marmara sea, NAF: North Anatolian fault, RS: Red Sea, SB: Sinai block, Sp: Spain, TS: Tyrrhenian sea.

The evolution to the present-day tectonics in the Eastern Mediterranean, the region of interest

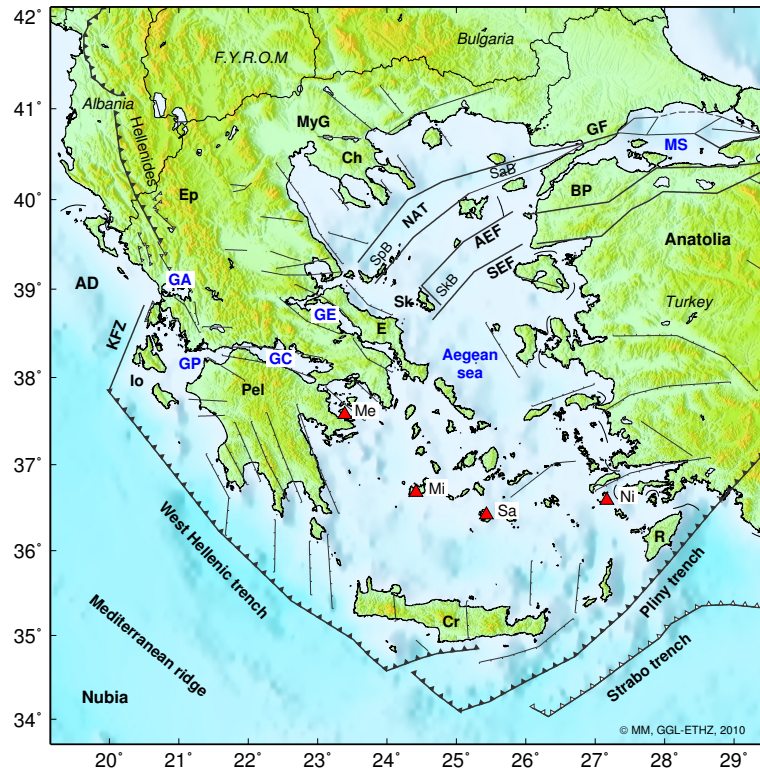


Figure 2.2: Tectonic framework of Greece. AD: Apulian domain, AEF: Agios Efstratios fault, BP: Biga peninsula, Ch: Chalkidiki peninsula, Cr: Crete, E: Evia, Ep: Epirus, F.Y.R.O.M.: Former Yugoslav Republic of Macedonia, GA: Gulf of Arta, GC: Gulf of Corinth, GE: Gulf of Evia, GF: Ganos fault, GP: Gulf of Patras, Io: Ionian islands, KfZ: Kefalonia fault zone, MS: Marmara sea, MyG: Mygdonian graben, NAT: North Aegean trough, Pel: Peloponnesos, R: Rhodes, SaB: Saros basin, Sk: Skyros, SkB: Skyros basin, SEF: Skyros-Edremit fault, SpB: Sporades basin. The South Aegean volcanic arc is depicted as red triangles (Me: Methana, Mi: Milos, Sa: Santorini, Ni: Nisyros).

of this thesis, is complex and widely debated. In addition to the interaction between the Nubian and Eurasian plates the Arabian and Anatolian plates are involved in these processes. Arabian and Nubian relative plate motion is located in the Red Sea and along the Dead Sea fault whereas a separate Sinai block possibly lies in between [Wdowinski *et al.*, 2004; Mahmoud *et al.*, 2005]. Extension of the Aegean lithosphere previously thickened during alpine collision started in Lower Miocene (~ 21 Myr ago) or earlier [Gautier *et al.*, 1999]. The Aegean extension is closely related to the retreat of the Nubian slab along the Hellenic trench system [Le Pichon and Angelier, 1979]. The indentation of Arabia into Eurasia commenced about 16 Myr ago and likely effected the onset of westward motion of Anatolia and the westward propagation of the North Anatolian fault (NAF). The NAF formed approximately 11 Myr ago [Sengör *et al.*, 2005] and reached the Aegean domain about 5 Myr ago [Armijo *et al.*, 1999]. The initiation of the Corinth rift is dated 1 Myr ago and is considered to be connected with the westward propagation of the southern branch of the NAF [Armijo *et al.*, 1996].

2.2 Tectonic framework of Greece

The present-day tectonic framework of Greece comprises a diversity of active structures. This section provides a concise overview. Geographic names and tectonic features are shown in Figure 2.2.

The Hellenic trench system (HTS) acts as plate boundary between the subducting Nubian plate (moving with ~ 5 mm/yr north-northwestward relative to Eurasia) and the overriding Aegean microplate (moving with a rate of ~ 30 mm/yr southwestward relative to Eurasia). While convergence dominates along the West Hellenic trench, there is significant shear deformation along the Strabo and Pliny trenches. The subducting slab penetrates the Aegean upper mantle at depths larger than 600 km [Spakman *et al.*, 1988]. The slope of the Nubian slab varies along the Hellenic trench system. It is shallower beneath the Peloponnesos and steeper in the eastern part [Sodoudi *et al.*, 2006]. The depth of earthquake hypocenters mark the downgoing Nubian slab from the Hellenic trench towards the Aegean (Fig. 2.3 (a)). The Mediterranean ridge located south of the Hellenic trench system is a large accretionary complex that results from Nubia-Eurasia-Aegean plates convergence [Masclé and Chaumillon, 1998].

The grade of coupling between the Nubian slab and the overriding Aegean plate and the rate of slab retreat are not precisely known. Jackson and McKenzie [1988], Jenny *et al.* [2004], Reilinger *et al.* [2010] found, for instance, significant aseismic convergence. Ganas and Parsons [2009] argue for a highly coupled plate boundary. Archaeological and geological investigations revealed uplift of the Hellenic arc islands from Rhodes to southern Peloponnesos during the Holocene (e.g., Lambeck [1995]). Besides coseismic effects (e.g., Stiros 2001; Shaw *et al.* 2008), also gravitational forces may have contributed to this uplift [Snopek *et al.*, 2007]. The South Aegean volcanic arc is located parallel to the Hellenic trench. These volcanoes are quaternary structures, especially active in the Late Pleistocene-Holocene (0.12 Myr ago to present) [Tibaldi *et al.*, 2008].

Active north-south extension is observed in central and northern Greece. It is closely related to the retreat of the Hellenic trench. The extensional regime extends into southern Bulgaria and F.Y.R.O.M. [Burchfiel *et al.*, 2006, 2008; Kotzev *et al.*, 2006]. Many normal faults are observed in the Greek mainland [e.g., Caputo and Pavlides 1993; Goldsworthy *et al.* 2002]. The dominant structure in this context is the Corinth rift which opened at a rate of 1 cm/yr for the last ~ 1 Myr [Armijo *et al.*, 1996]. Variations in crustal thickness in the Hellenic plate boundary zone were observed. Maximum values are encountered in northwestern Greece (~ 40 km). The crust is thinnest in the South Aegean sea (~ 20 km) [Tirel *et al.*, 2004; Sodoudi *et al.*, 2006]. This is attributed to ongoing extensional processes. The rollback of the Nubian slab along the Hellenic trench induced rotation of wide areas of Greece. Western Greece rotated clockwise by about 50° since Middle-Miocene (~ 15 Myr ago) [Kissel and Laj, 1988; Van Hinsbergen *et al.*, 2005].

The North Aegean trough (NAT) forming the western continuation of the North Anatolian fault (NAF) and the Kefalonia fault zone (KFZ) are the predominant dextral strike-slip faults in Greece. The KFZ marks the northwestern termination of the Hellenic trench system. It separates the slowly north-northwestward moving northern Ionian islands and the rapidly southwestward drifting central Ionian islands. Dextral strike-slip motion is also indicated by fault plane solutions obtained in the area between the Ionian islands and western Peloponnesos [Kiritzi and Louvari, 2003]. Ongoing collision between the Apulian domain and Greece/Albania is encountered north of the KFZ in Epirus.

The NAF splits into several branches west of 31°E and intersects Western Turkey and the North Aegean sea with three major strands. Right lateral strike slip motion is observed along these features. The northernmost strand, the North Aegean trough (NAT), is seismically active and accommodates most of Eurasian-Aegean relative motion [Straub *et al.*, 1997]. Faults striking perpendicular to the NAT are also encountered in the North Aegean region. These structures are related to normal or left-lateral faulting [e.g., Koukouvelas and Aydin 2002; Papanikolaou *et al.* 2006; Ganas *et al.* 2005]. Several basins were formed in the North Aegean sea which are related to normal faulting (e.g., Saros basin, Skyros basin, Sporades basin). The predominant strike-slip motion of the North Aegean sea is transferred to normal faulting towards Evia and the Greek mainland [Kiritzi, 2002]. Central Anatolia exhibits block-like motion while western Anatolia is mainly characterized by N-S extension [McClusky *et al.*, 2000].

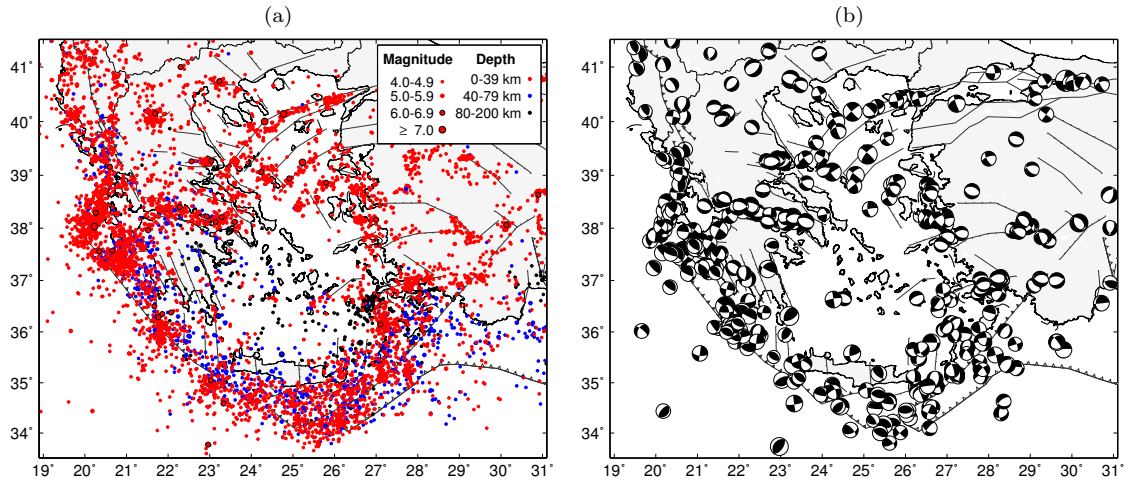


Figure 2.3: (a) Seismicity pattern ($M \geq 4$) in Greece and adjacent regions for the period 1973–2009 [NEIC catalog, 2009]. Seismicity concentrates along active structures such as the Hellenic trench system, the Kefalonia fault zone, the Gulf of Corinth and the North Aegean trough. (b) Fault plane solutions of earthquakes for the period 1976–2010 [CMT catalog, 2011]. The earthquake mechanisms indicate the particular deformation styles such as extension across the Gulf of Corinth or right-lateral strike-slip in the North Aegean sea.

The Hellenic plate boundary zone forms the seismically most active region in Europe. Style and pattern of reported earthquakes indicate present-day deformation. Figure 2.3 (a) depicts the seismicity ($M \geq 4$) for the period 1973–2009 [NEIC catalog, 2009]. Seismicity is clustered along fault structures such as the Gulf of Corinth, the KFZ, the NAT and the HTS. Remarkably low seismicity is reported in the South Aegean sea. The recurrence interval of large earthquakes on certain faults is expected to reach several hundreds or thousands of years (e.g., Ambraseys and Finkel 1987; Armijo et al. 1991; Caputo et al. 2010) and, thus, is longer than the time-span of available earthquake catalogs. Figure 2.3 (b) depicts fault plane solutions of earthquakes for the period 1976–2010 [CMT catalog, 2011]. For instance, the earthquake mechanisms indicate the extensional regime extending from northern to central Greece, distinct extension across the Gulf of Corinth, and strike-slip motion in the North Aegean sea.

Numerous geological and geophysical processes are evolving in the Eastern Mediterranean. These processes are active during various time scales from millions of years to a few seconds. The GPS technique which is the base of this thesis has been applied in the Eastern Mediterranean for about 20 years. GPS derived results cover only a snapshot of the geodynamic evolution. The detection of short term signals is limited either. It depends on the frequency of position estimation. In this thesis daily coordinates were derived at best. GPS derived rates of crustal motion are important constraints for the investigation and the understanding of geophysical processes. The comparison of geodetic results with results from other disciplines like seismology or structural geology is required to improve the understanding of present-day tectonics.

3 GPS data evaluation

3.1 Description of relevant GPS networks

3.1.1 Campaign-type GPS network in Greece and southern Bulgaria

An extensive record of campaign-type data for the period 1993–2003 was available. It was processed in previous studies [Hollenstein, 2006; Hollenstein et al., 2008a]. Besides the GGL several other institutes contributed to the data record [Gilbert et al., 1994; Denys et al., 1995; Clarke et al., 1998; McClusky et al., 2000]. All these campaigns were re-evaluated in the course of this thesis. Moreover, the data set has been considerably extended compared to Hollenstein et al. [2008a] by including campaigns carried out between 2004 and 2009 and older campaigns not yet consistently processed with the GGL data (e.g., Kotzev et al. 2006 (data downloaded from UNAVCO)). The campaign-type network evaluated is shown in Figure 3.1. Further details related to particular campaign-type sites can be found in the appendix.

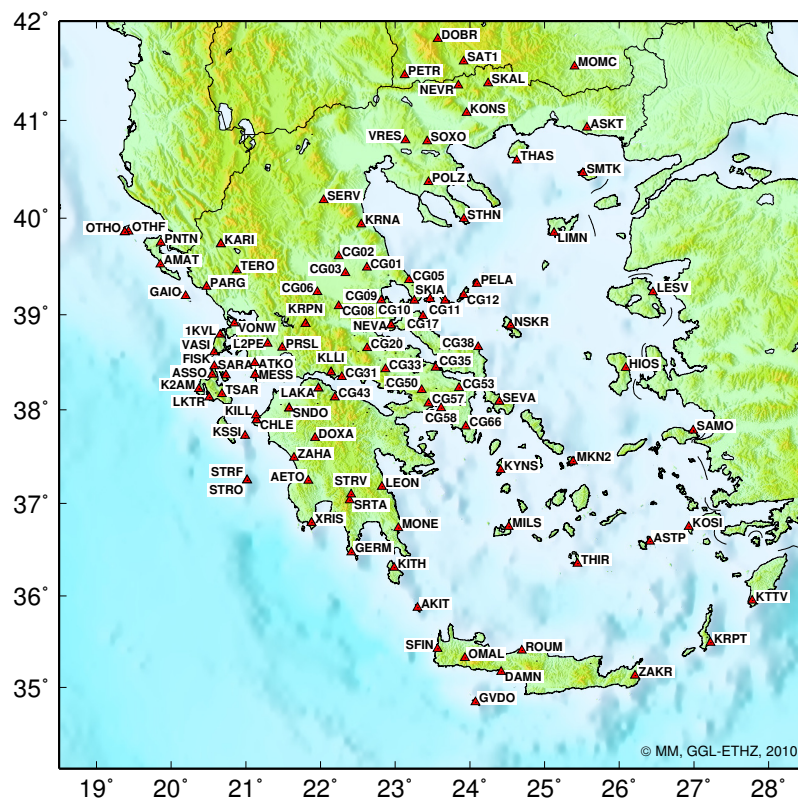


Figure 3.1: Evaluated campaign-type GPS network in Greece and southern Bulgaria for the time period 1993–2009.

3.1.2 Continuous GPS networks in Greece

An increasing number of continuous GPS sites is operated in Greece. CGPS sites whose data was evaluated in this thesis are shown in Figure 3.2. The continuous HELLAS GPS network was initiated in 1995 [Peter, 2000]. It consists of 22 stations at present. The sites DION, ARSA and NEAP are operated by the National Technical University of Athens (NTUA). The National Observatory of Athens (NOA) has commenced to establish a continuous GPS network with two sites (RLS_, VLSM) in the Ionian Sea region in 2006. Additional sites have been installed in the years 2007 and 2008 leading to a network consisting of 9 sites [Ganas, 2009]. Data of seven NOA sites was processed. However, rates were only derived for sites RLS_ and VLSM due to the limited time-span of site operation. The MIT has operated two continuous GPS sites in the Southeast Aegean sea since 2005. Data of both sites, TILO and KATC, were used in this thesis. Thus, four CGPS sites in the North Aegean sea (ALON, EFSS, LIMS, SMTZ) and five CGPS sites in the South Aegean sea (KALY, KATC, NEAP, NISI, TILO) were additionally included in the derived velocity solution compared to *Hollenstein et al.* [2008a].

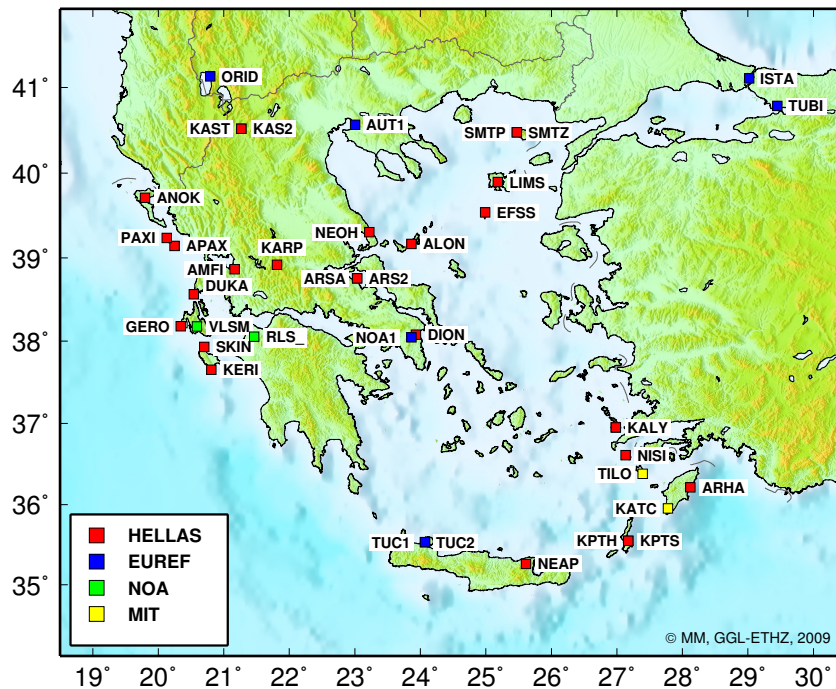


Figure 3.2: Evaluated continuous GPS network in Greece. Red squares depict HELLAS sites (operated by ETHZ and NTUA), blue squares depict EUREF sites, green squares depict sites operated by NOA, yellow squares depict sites operated by MIT.

3.1.3 IGS and EUREF sites

Up to 72 IGS [Dow *et al.*, 2009] and EUREF [Bruyninx, 2004] sites were included in the data evaluation (see Fig. 3.3) in order to align the GPS network to a reference frame, to obtain additional velocity information in regions adjacent to Greece and to assess the quality of the chosen processing strategy. Six EUREF sites are located in or close to Greece (AUT1, ISTA, NOA1, ORID, TUBI and TUC2; see Fig. 3.2). The density of both networks has considerably increased since the early nineties which made it possible to solve the tasks mentioned above.

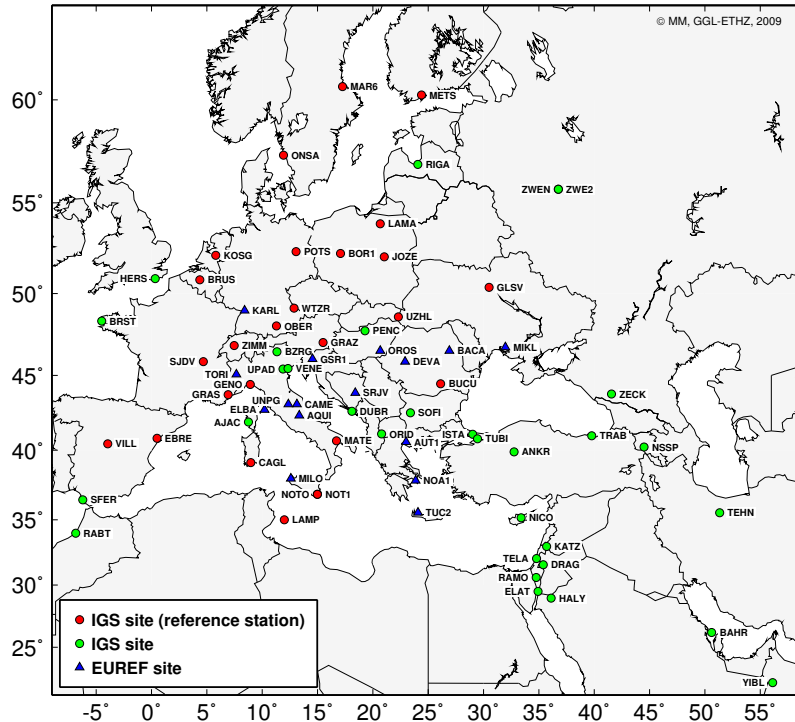


Figure 3.3: IGS and EUREF sites included in the GPS data processing. Green and red circles depict IGS sites. Red colored IGS sites are used as reference sites. Blue triangles depict EUREF sites.

3.2 Strategy of GPS data processing

The GPS data was evaluated using double difference observations. The Bernese GPS software 5.0 [Beutler *et al.*, 2007] was used for the processing. All bug-fixes and improvements up to release date 15 May 2009 were applied. The next section summarizes the processing scheme (see also Table 3.1 for a brief overview).

The processing was based on daily sessions. For days where campaign-type data was available two solutions were calculated: one without and one including the campaign-type data. A sampling rate of 30 seconds was selected throughout all processing steps. To achieve a robust processing routine, demanding only few reviewing, data files of continuous GPS sites containing less than 12 hours of observation time or large data gaps were rejected. Exceptions were made for selected sites in Greece (e.g., campaign-type measurements of sites GERO and DUKA after 2003). The data was evaluated several times in order to exclude data from the processing which is corrupted due to site specific tracking problems. Tracking problems of IGS and EUREF sites are mostly indicated by respective station mails. The Bernese GPS software 5.0 does not provide the functionality to handle different coordinate/velocity pairs for subsequent time windows per site. This functionality was added script-based.

The modeled observable was the ionosphere-free linear combination of double difference carrier phase. Baselines were automatically formed by the maximum observation strategy. Sites with suboptimal tracking behavior leading to a high number of ambiguities were forced to be involved in only one baseline. During the ambiguity resolution the frequencies L1 and L2 were used except for baselines including L2-squaring type receivers where L5 and L3 were used. In general, ambiguities were resolved using the quasi-ionosphere-free (QIF) strategy. The SIGMA strategy was only applied to baselines with L2-squaring type receivers. The minimum elevation angle was set to 3° (10°

Purpose/program	Main task
Preparation of products	
INI	Compilation of relevant a priori coordinates/velocities
COOVEL	Propagation of a priori coordinates to specific epoch
POLUPD	Preparation of earth orientation parameters
PRETAB, ORBGEN	Preparation of precise orbit information
Data import	
RNXGRA	Selection and exclusion of rinex files
RXOBV3	Data import into bernese format
Data preprocessing	
CODSPP	Computing the corrections for synchronizing the receiver clocks with respect to GPS time
SNGDIF	Forming baselines from zero-difference observation files
MAUPRP	Detecting and resolving cycle slips, removing outliers, adding multiple ambiguities for the phase observation files
GPSEST, RESRMS, SATMRK	Removing outliers
Ambiguity resolution	
GPSEST	Ambiguity resolution
Final solution	
GPSEST	Generation of normal equation
ADDNEQ2	Normal equation inversion, definition of the geodetic datum

Table 3.1: Main processing steps of the Bernese GPS software 5.0 selected for the data evaluation.

during ambiguity resolution). An elevation-dependent weighting was applied by using the function $\cos^2(z)$.

Zenith path delays were estimated in one hour intervals for each station. In addition, for each day two tilt angles defining the direction of the minimum zenith path delay were estimated. A priori values for the zenith path delays were obtained using the Saastamoinen model in combination with the "DRY NEILL" mapping function. Final troposphere parameters were derived using the "WET NEILL" mapping function [Neill, 1996].

Ocean tide loading model coefficients were calculated using the web service at <http://www.oso.chalmers.se/~loading/>. The obtained values are based on the model FES2004 [Letellier, 2004].

Absolute antenna phase center corrections were applied. These corrections are principally based on the model release "igs05_1525.atx". For eight sites individually calibrated correction patterns were used which are available from EUREF. However, numerous GPS antenna types, mainly older ones, have not been absolutely calibrated. For a few antennas used at campaign-type sites even the correct type is unknown. Therefore, a processing with absolute antenna phase center correction models could only partly be realized.

Compared to the data processing described in Hollenstein [2006] several new or enhanced modeling features were used in this thesis. Some of the model changes are related to the employment of a newer version of the Bernese GPS software. Most important are the correction of the error in modeling the solid earth tides, the consideration of ocean tide loading effects, the introduction of gradients related to the calculation of tropospheric delays and the use of absolute antenna phase center correction models. These improvements enhance the quality of parameter estimation and allow the definition of the geodetic datum by a less rigorous mathematical transformation. Temporal variations of parameters describing the quality of the processing are quantifiable (e.g., σ a posteriori or percentage of resolved ambiguities (Fig. A.1 and A.2)). Finally, the derived coordinates which are of main interest in this thesis are not completely unaffected by systematic signals. Systematic signals in position time series and the corresponding reduction are addressed in chapter 3.4.6.

3.3 Definition of the geodetic datum

All the daily solutions and the final combined solution also including the campaign-type data were aligned to the reference frame IGS05 (*IGSmail*: 5447, 5455). IGS05 is the IGS realization of ITRF2005 [Altamimi *et al.*, 2007]. For the derivation of IGS05 only GPS measurements were used. IGS05 is based on absolute antenna phase center correction models and is aligned to ITRF2005. IGS05 is realized by coordinates and velocities of 139 core sites. Discontinuities in coordinate time series are taken into account (per site: one position/velocity pair for each time period without offsets, no constraints between parameters of different sections).

IGS final orbits and earth orientation parameters (EOPs) derived in different ITRF realizations (ITRF91, ITRF92, ITRF93, ITRF94, ITRF96, ITRF97, IGS00, IGb00) were transformed into IGS05 in this thesis. The transformation was accomplished by the program TRNFSP3N [Kouba, 2002] as described in Hollenstein [2006]. The transformation parameters IGb00 to IGS05 including the switch from relative to absolute antenna phase center correction models were published in *IGSmail* 5455. The number of subsequent transformations required for orbit and EOP information derived in the 1990s led to a set of orbits and EOPs with limited consistency. The employment of reprocessed orbits and EOPs [Steigenberger *et al.*, 2006] instead of the IGS final orbits/EOPs for the time period 1994-2003 improves the consistency of the products. However, CODE (Center for Orbit Determination in Europe) orbits and EOPs had to be used for the year 1993 since no reprocessed products were available for this time. The improvement of the results by using reprocessed orbits instead of IGS final orbits is outlined in chapter 3.6.2.

The daily solutions were aligned to IGS05 by imposing a no-net-translation condition on the derived coordinates of a set of reference sites with respect to those published in the IGS cumulative solution. In contrast, the final campaign solution was aligned to IGS05 by imposing a no-net-translation condition on coordinates and velocities during the combination of the normal equations in the Bernese GPS software subprogram ADDNEQ2. Between 1993 and 2009 the set of reference sites has changed due to commissioning or decommissioning of sites or due to temporal malfunctions of equipment of particular sites. The locations of the reference sites are shown in Figure 3.3. Time periods for which particular sites are used as reference sites are shown in Figure 3.4.

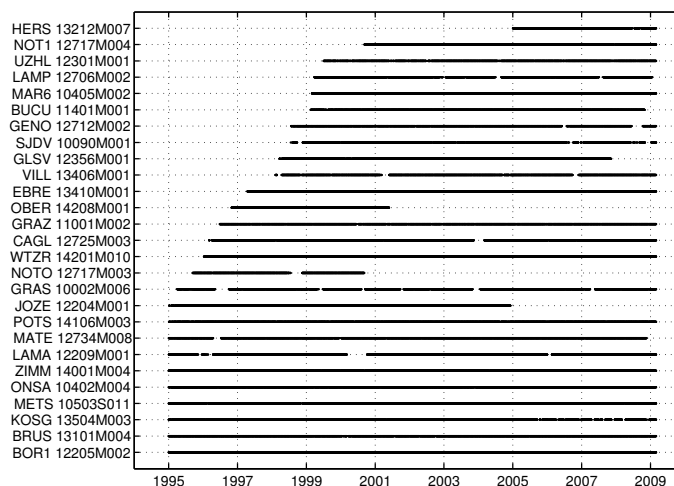


Figure 3.4: Temporal overview of the use of IGS sites as reference sites.

In order to align the final campaign solution to IGS05 the set of reference sites was slightly modified compared to the one used for the daily solutions. As the no-net-translation condition is imposed on coordinates and velocities without weighting in the Bernese subprogram ADDNEQ2, large

residuals of coordinates and velocities of short segments (up to about two years) strongly influence the solution. Therefore, sites were not used as reference sites on these segments.

Coordinates and velocities of particular reference sites were extracted from the IGS combined solution. Only coordinates and velocities starting from 1998 are published in this solution due to missing availability and/or lower quality of data before this date. For reprocessing purposes within the IGS all available segments of the IGS reference sites were made available in IGS05_repro.snx [R. Ferland, personal communication, 2007]. Therefore, the following approach was chosen for the definition of the geodetic datum:

- Coordinates and velocities of required segments of reference sites before 1998 and short segments at the beginning of the combined solution were extracted from IGS05_repro.snx.
- All other coordinates and velocities are based on the IGS combined solution published in IGS09P06.snx.

More detailed information with respect to the used reference sites is listed in appendix A.1.

3.4 Velocity estimation of CGPS sites

3.4.1 Introduction

The available rinex files were processed in daily sessions using the Bernese GPS software (see chapter 3.2). The main results of the GPS processing are the normal equations and, in particular, geocentric coordinates and their corresponding formal accuracies. Rates of all CGPS sites were derived based on their position time series. These time series were analyzed and processed according to the scheme described in the following chapters. The effort made in this field allows for an accurate velocity estimation and improves the detection and quantification of earthquake related displacements. Furthermore, it allows the assessment and interpretation of non-stochastic signals. The Bernese subprogram ADDNEQ2 was not used for the final estimation of rates of CGPS sites. This program is capable to estimate site velocities based on the combination of normal equations but provides only a constant velocity model. Nevertheless, rates of sites operational for more than 4 years estimated based on their position time series and by using ADDNEQ2 are comparable at a few tenths of a millimeter.

Rates of CGPS sites were estimated based on their position time series by performing the following three steps:

1. Detection of discontinuities (chapter 3.4.2), outliers (chapter 3.4.3) and exclusion periods (chapter 3.4.4)
2. Reduction of systematic signals of a regional scale which are obvious in GPS position time series (chapter 3.4.6)
3. Estimation of site velocities (chapter 3.4.5) and scaling of corresponding formal accuracies (chapter 3.4.7)

The scheme of the processing steps is outlined in Figure 3.5. *Raw* time series are based on daily position estimates as derived by the GPS processing. Time series are called *improved* after the performance of the outlier detection and the reduction of systematic signals. Detected outliers, discontinuities and exclusion periods related to time series of particular CGPS sites were accordingly applied to the combination of normal equations (chapter 3.5). The corresponding information was included in the files used by the Bernese software subprogram ADDNEQ2.

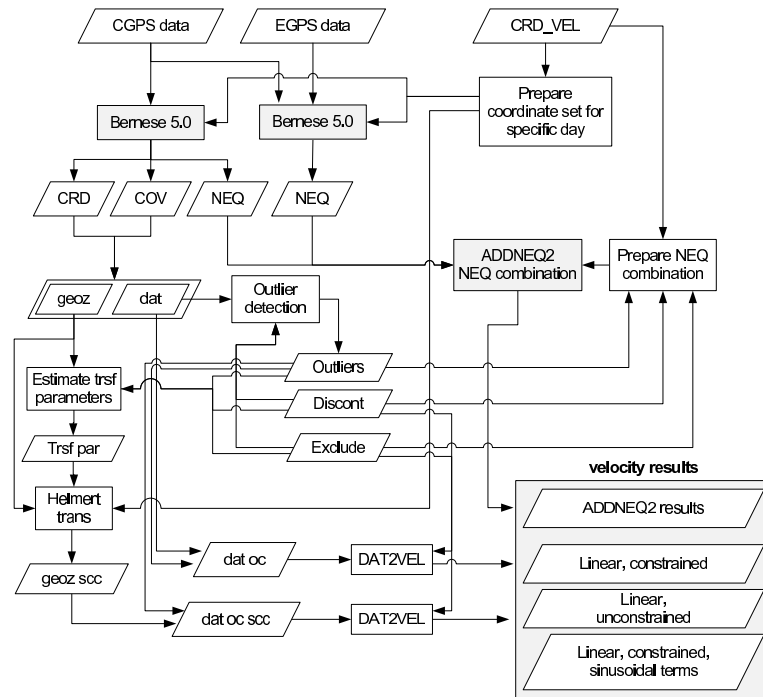


Figure 3.5: GPS processing scheme. White parallelograms denote data files, white rectangles PERL or MATLAB scripts. Used abbreviations: CRD_VEL: a priori site coordinates/velocities; Discont: file with the dates of particular discontinuities; Exclude: file with the dates of particular exclusion periods; Outliers: file containing the dates of detected outliers; CRD, COV: geocentric coordinates of daily solutions and their covariances; NEQ: Normal equation; geoz: time series in geocentric system; dat: time series in topocentric system; oc: outlier corrected; scc: improved time series, Trsf par: parameters used with respect to the reduction of systematic signals common to all sites (chapter 3.4.6).

3.4.2 Discontinuities in position time series

Discontinuities were introduced in time series according to the scheme shown in Table 3.2. If a discontinuity was found in one coordinate component an offset was introduced in the other two components as well. Time periods of a continuous site without discontinuities are denoted sections 1..k. All offsets introduced in the GPS time series are listed in appendix A.2.

Event	Criterion
Antenna change	Always (unless the introduction of an offset prevents the estimation of rates; in particular: site KALY).
Receiver/firmware change	If causing an offset.
Nearby earthquake	If causing an offset.
Other reasons (partly unknown)	If causing an offset.

Table 3.2: List of events possibly causing discontinuities in position time series and relevant criteria for modeling an offset.

3.4.3 Removing outliers

Outliers in time series were detected and removed by applying a moving median filter on detrended time series. Each coordinate component was treated separately. However, when an outlier was

detected in one coordinate component also the estimates of the other two coordinate components were flagged as outliers. Following this concept minimum assumptions were made with respect to the actual site motion.

The procedure works as follows. First, the time series are detrended and the residuals d_t with respect to a linear trend are calculated (component-by-component)

$$d_t = (x_k + v \cdot t) - l_t \quad (3.1)$$

where v is the respective velocity component, x_k is the axis intercept in section k and l_t is the observable. For each 61 days interval $[t - 30 \dots t + 30]$ within a section k the median of the values d_t is determined and the residual r_t

$$r_t = d_t - \text{median}[d_{int}] \quad (3.2)$$

is derived. A RMS value is calculated to determine the noise level of the respective time series.

$$RMS = \sqrt{\frac{\sum r_t r_t}{n - 1}} \quad (3.3)$$

The number of position estimates in the respective time series is denoted by n . The criterion for an outlier is defined as

$$|r_t| \geq 5 \cdot RMS \quad (3.4)$$

The algorithm is iterative as the RMS decreases when outliers are marked. Multiple outliers within a few days and a magnitude several times larger than the noise level can be found by using the algorithm above. Longer lasting outlier periods e.g. related to equipment malfunction have to be marked separately as exclusion periods (chapter 3.4.4).

3.4.4 Exclusion periods

An exclusion period denotes a time interval in which positions were derived for a particular CGPS site but were not used for the estimation of rates. For instance, unstable antenna monumentation can be a reason for the definition of an exclusion period. Defined exclusion periods for CGPS sites are listed in Table A.4.

3.4.5 Estimation of velocities and offsets

Three types of velocity estimation were considered. All coordinate components (North, East and Up) were treated individually. Correlations between the components were not considered.

1. Identical constant velocity \mathbf{v} in all sections 1.. k and k axis intercepts \mathbf{x}_i (Fig. 3.6 (a))

$$\mathbf{x}(t) = \mathbf{x}_i + \mathbf{v} \cdot t \quad (3.5)$$

2. Constant velocity \mathbf{v}_i and axis intercept \mathbf{x}_i per section (Fig. 3.6 (b))

$$\mathbf{x}(t) = \mathbf{x}_i + \mathbf{v}_i \cdot t \quad (3.6)$$

3. Identical constant velocity \mathbf{v} plus sinusoidal terms with annual and semiannual periods ($\omega_m = 2\pi \cdot m \frac{1}{365.25}$) in all sections 1.. k plus k axis intercepts \mathbf{x}_i (Fig. 3.6 (c))

$$\mathbf{x}(t) = \mathbf{x}_i + \mathbf{v} \cdot t + \sum_{m=1}^2 (\mathbf{a}_m \sin \omega_m t + \mathbf{b}_m \cos \omega_m t) \quad (3.7)$$

The last term of Eq. (3.7) can be rearranged to the form $A \cos(\omega t - \phi)$. Amplitude $A_{m,n}$ and phase lag $\phi_{m,n}$ can be calculated component-by-component by

$$A_{m,n} = \sqrt{a_{m,n}^2 + b_{m,n}^2} \quad \phi_{m,n} = \arctan \frac{a_{m,n}}{b_{m,n}} \quad (3.8)$$

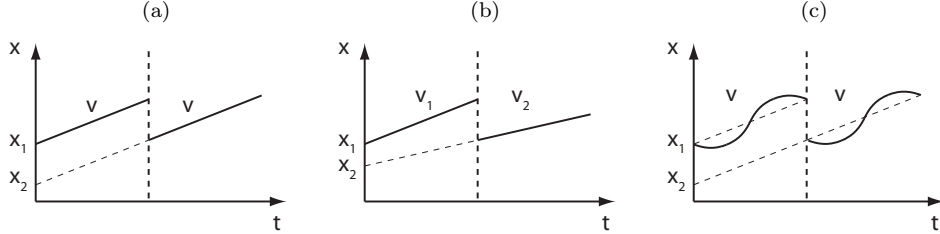


Figure 3.6: (a) Sketch of Eq. (3.5). (b) Sketch of Eq. (3.6). (c) Sketch of Eq. (3.7).

The assumption of a constant velocity is appropriate for most of the compiled time series. Exceptions are the sites TUBI, ISTA (postseismic relaxation related to the Izmit earthquake in 1999 [Ergintav *et al.*, 2002]) and AQU1. Superimposed annual oscillations can be found at several sites, mostly expressed at site PAXI (appendix B.4). The velocity estimation based on models 1 (Eq. 3.5) and 3 (Eq. 3.7) reveals very similar results for time series longer than 4 years (Fig. 3.7 (a)). In general, the final velocities were calculated based on model 1 unless the application of model 3 improved the WRMS of one component by at least 20%. Only velocities of sites having been operated for more than 30 months were used for geodynamic interpretations. Model 2 (Eq. 3.6) was used to investigate velocities in consecutive sections temporally separated by an earthquake.

If an earthquake occurs in a time period when a specific site is not operating a velocity model is required for the accurate estimation of the corresponding displacements. The above described velocity models are sufficient for this task. Most differences between offsets calculated with models 1 and 3 ($\Delta \mathbf{x} = \mathbf{x}_{k+1}(t) - \mathbf{x}_k(t)$) are smaller than 2 mm (Fig. 3.7 (b)). Larger differences are encountered between offsets estimated by models 1 and 2 (Fig. 3.7 (c)). This is partly related to the less accurate velocity estimation based on data of short intervals. The model used for estimating the final offsets of a specific site is identical with the applied velocity model. The actually employed model is indicated for each continuous site in appendix C.2. Moreover, a comparison of derived earthquake displacements for CGPS sites in Greece depending on the applied velocity model is shown in Table 6.4.

Time series of particular sites were treated separately. Exceptions are successor sites in close distance to the old station (ARSA-ARS2, KAST-KAS2, KPTH-KPTS, SMTP-SMTZ, TUC1-TUC2). Data of these sites (maximum site separation: 1.3 km) were combined for the velocity estimation.

3.4.6 Reduction of apparent scale changes of the processed GPS network

The employed models of the Bernese GPS software lead to seasonal variations in processing related parameters such as the σ a posteriori or the percentage of resolved ambiguities (Figs. A.1 and A.2 in the appendix). This suggests some model deficiencies which affect the obtained coordinates as well. The estimation of site velocities based on Eq. (3.7) revealed a dependency of amplitude and phase shift of the annual sinusoidal term on site location (Fig. 3.8). The annual sinusoidal term is the most pronounced one in all three coordinate components. This is also valid for continuous sites in Greece: In Figure 3.9 the weighted common-mode signal for continuous sites in Greece is shown. The main frequencies of the common-mode signal are depicted in Fig. 3.10. This observation can

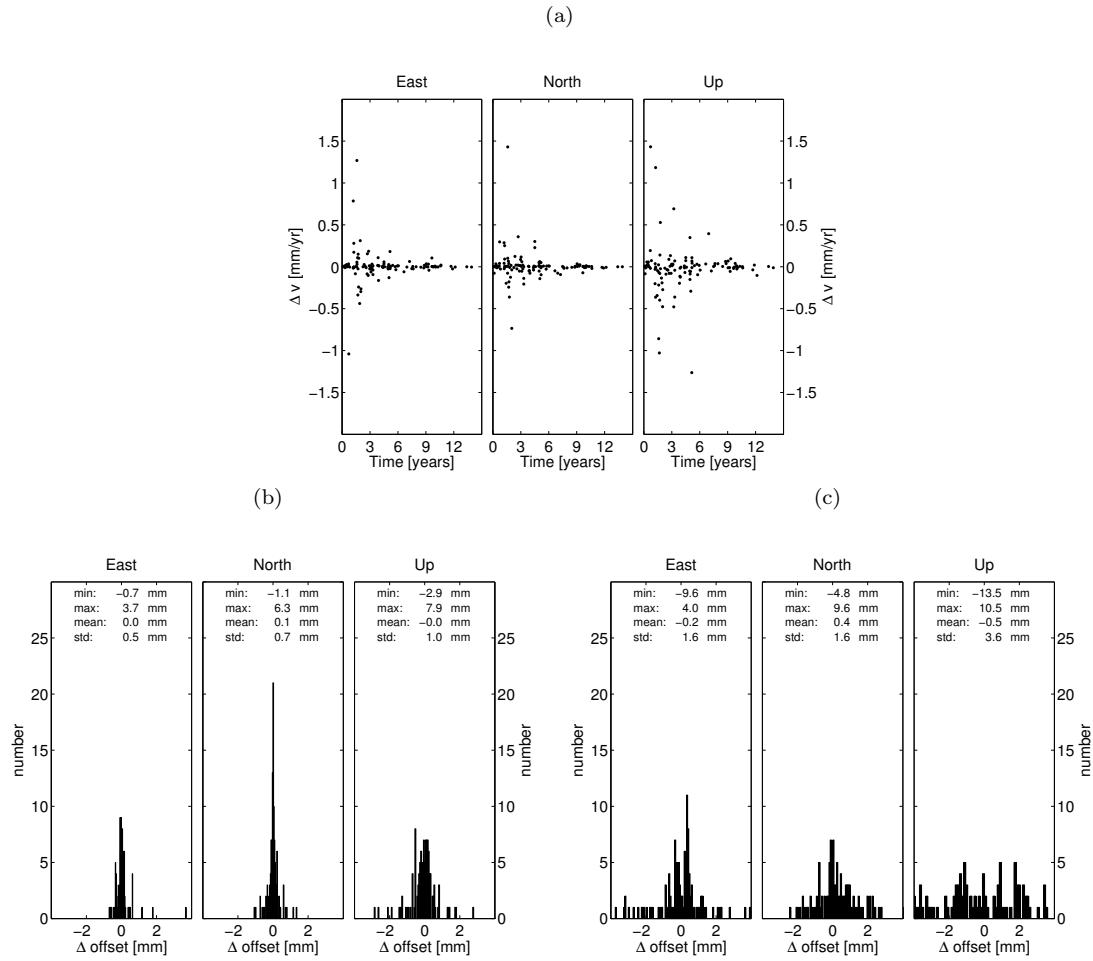


Figure 3.7: (a) Differences of velocities between model 1 (Eq. 3.5) and model 3 (Eq. 3.7) as function of the length of the time series. (b) Histograms of the differences of the offsets estimated by using model 1 and model 3. The statistic is based on 120 values. (c) Histograms of the differences of the offsets estimated by using model 1 and model 2. Values exceeding $|10 \text{ mm}|$ in the east and north components, respectively, and $|25 \text{ mm}|$ in the up component are considered as outliers and not used for the statistics (4 values in total). The statistic is based on 120 values.

be related to an apparent periodic change of scale. This artifact is not removed by aligning the GPS network to the reference frame by imposing a no-net-translation condition on a set of reference sites without the estimation of a scale.

Signals in GPS coordinate time series with annual and semiannual periods were reported by several authors (e.g., *Dong et al.* 2002; *Ray et al.* 2008). The signals reflect inadequately modeled or even unmodeled non-tectonic processes such as atmospheric and oceanic loading effects or local hydrology. Significant contributions to the signals likely arise from the modeling of tropospheric delays (e.g., *Tregoning and Herring* 2006). Additional effects related to the GPS technique may lead to periodic signals at annual and semiannual periods as well (e.g., errors in satellite orbits, antenna phase center modeling, site multipath). *Penna and Stewart* [2003] showed how unmodeled signals with periods near 12 and 24 hours can be aliased to signals with annual and semiannual periods in daily processing. However, the assessment of particular effects based on a regional network is difficult as the signals found in the coordinate time series are not independent of the strategy of aligning the network to a specific reference frame. A trend to a reduction of systematic

signals in coordinate time series can be expected in the near future since GPS processing techniques are constantly improved (e.g., application of atmospheric loading [Tregoning and Watson, 2009], Vienna mapping function [Boehm et al., 2006], higher-order ionospheric corrections [Fritsche et al., 2005]).

The detection of tectonic signals such as earthquake displacements, pre- and postseismic signals and transient motions requires the identification of processing induced signals. The velocity estimation as well can be skewed by systematic error signals. Periodic signals with annual and semiannual periods are negligible in time series longer than 4.5 years. In contrast, annual and semiannual signals should be modeled when using time series shorter than 4.5 years but longer than 2.5 years [Blewitt and Lavallée, 2002]. Several time series compiled in this thesis have data gaps leading to an inaccurate estimation of periodic signals. Additionally, the GPS network is temporally not homogeneous (e.g., increasing number of sites) suggesting non-stationary signals. Therefore, a spatial improvement was applied. The used algorithm is based on a Helmert transformation and the assumption that site motion is linear. Only data of sites was selected for this algorithm which show no pronounced signals (appendix A.4). Sites in Greece were not used at all. First, the linear geocentric motion of each selected site i was estimated and the residuals $\mathbf{r}_{geoz,i}(t)$ of the daily GPS positions $\mathbf{x}_i(t)$ with respect to this motion were calculated.

$$\mathbf{x}_{lin,i}(t) = \mathbf{x}_{k,i} + \mathbf{v}_{k,i} \cdot t \quad (3.9)$$

$$\mathbf{r}_{geoz,i}(t) = \mathbf{x}_i(t) - \mathbf{x}_{lin,i}(t) \quad (3.10)$$

The parameter t denotes time, $\mathbf{x}_{k,i}$ and $\mathbf{v}_{k,i}$ denote the estimated axis intercept and velocity, respectively, for section k and $\mathbf{x}_{lin,i}(t)$ denote the modeled positions. The parameters of a Helmert transformation (3 translations: T_x, T_y, T_z ; 3 rotations: R_x, R_y, R_z ; one scale: m) were estimated for each day in a least-squares adjustment minimizing the geocentric residuals $\mathbf{v}_{geoz}(t)$.

$$\mathbf{v}_{geoz,i} + \mathbf{r}_{geoz,i}(t) = f(\mathbf{x}_i(t), \mathbf{T}(T_x, T_y, T_z), \mathbf{R}(R_x, R_y, R_z, m)) \quad (3.11)$$

The formal accuracy of the daily positions was considered in the stochastic model to account for the larger scattering in the vertical component in contrast to the horizontal components.

The derived coordinates of every single day were transformed using the obtained parameters. Subsequently, the daily solutions were finally aligned to ITRF2005 by imposing a not-net-translation condition on the set of reference sites. Only few constraints were imposed on the parameter estimation of the Helmert transformation due to the individual estimation of the site velocities. EUREF sites which are not included in the IGS combined solution can be used in addition to IGS sites. Moreover, for IGS sites discontinuities not applied in the IGS solution can be taken into account. The estimated scale is between -2 and +2 ppb and its periodicity becomes more distinct since the year 2000 (Fig. 3.11). This might be directly related to the increasing number of sites included in the processing and the concurrent spatial enlargement of the GPS network. Note that the estimated scale leads only to marginal changes in the height components since the scale is highly correlated with the translation parameters.

The applied algorithm reduces annual and semiannual signals mainly in the east and north components while the improvements are smallest in the up component (Fig. 3.8 (b), (d) and (f)). This holds for sites in Greece as well (Table 3.3, Fig. 3.12). Figures 3.9 and 3.10 show the improvement by means of the common-mode signal. The large improvement in the up component is probably somewhat accidental as the phases of the annual signal in the height components are less coherent. The effect of the application of the described method on position time series is shown by the time series of sites ARHA and KERI (Fig. A.4). The application of the algorithm leads to small changes in velocities: about 1/10 mm/yr on average for time series lasting for more than four years and some few 1/10 mm/yr for shorter time series. Compared to Hollenstein [2006] time series were not improved in this thesis by the subtraction of a common-mode signal deduced from data of continuous sites in Greece. The common-mode signal is largest between 1996 and 2000 when only 2 to 5 sites were operational and consequently not very reliable.

Version	East		North		Up	
	WRMS [mm]	A_{ω_1} [mm]	WRMS [mm]	A_{ω_1} [mm]	WRMS [mm]	A_{ω_1} [mm]
OC	1.6	1.0	1.8	1.8	5.6	1.8
OC ScC	1.5	0.7	1.5	0.8	5.2	1.6

Table 3.3: Average WRMS of position estimates of CGPS sites in Greece with respect to a linear motion model extended by annual and semiannual sinusoidal terms and average amplitude A_{ω_1} of the annual sinusoidal term. OC: Outlier corrected time series; OC ScC: Outlier corrected time series which were improved using the procedure described in chapter 3.4.6. The improvement is largest in the north component. CGPS sites used for this comparison: alon, aut1, arha, arsa, dion, duka, efss, gero, kaly, karp, kast, keri, kpts, kpth, lims, neoh, nisi, noa1, rls_, smtz, tuc1, tuc2 and vlsm.

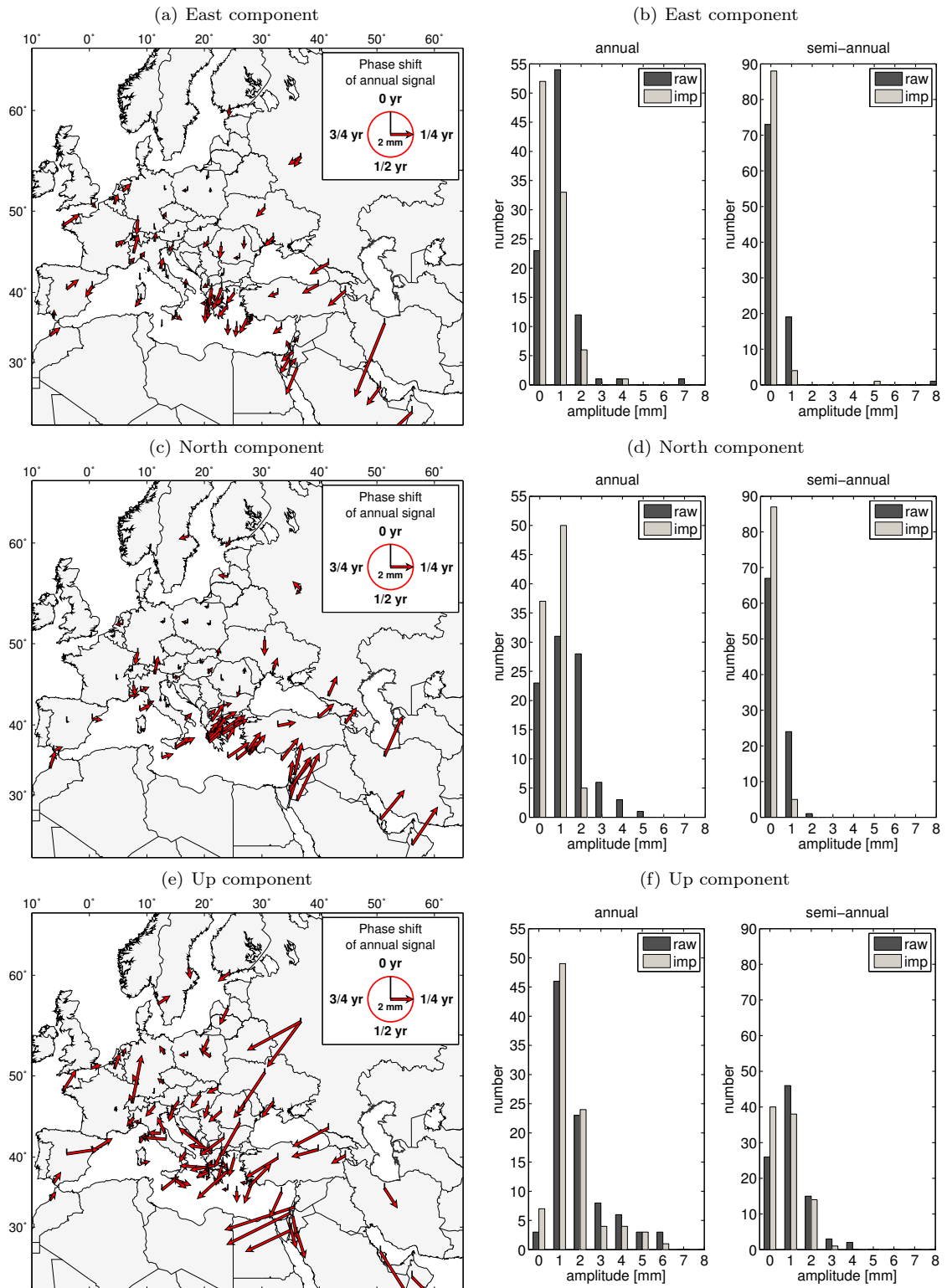


Figure 3.8: Amplitude (length of red arrows) and phase lag (azimuth of red arrows) of annual sinusoidal signals estimated from raw time series of each continuous GPS site. (a) east component (c) north component (e) up component. Histogram of amplitudes of annual and semiannual sinusoidal terms of raw and improved time series (93 samples in total). (b) east component (d) north component (f) up component. Note the different scales applied in the histogram pairs. imp: improved.

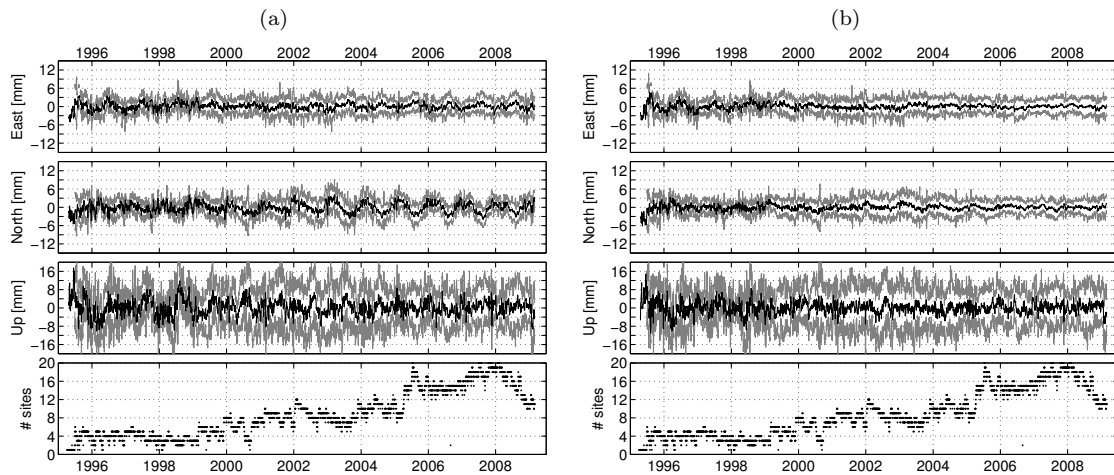


Figure 3.9: (a) Weighted common-mode signal of raw time series and (b) improved time series, respectively, calculated from all continuous sites in Greece. The black line depicts the common-mode signal in the three coordinate components. The gray lines depict the 95% confidence interval. "# sites" denotes the number of sites contributing to the common-mode signal on a particular day. The improvement largely reduces annual signals (Table 3.3). Remaining signals in (b) are largest in the period 1995–2000 related to the limited number of sites in that time.

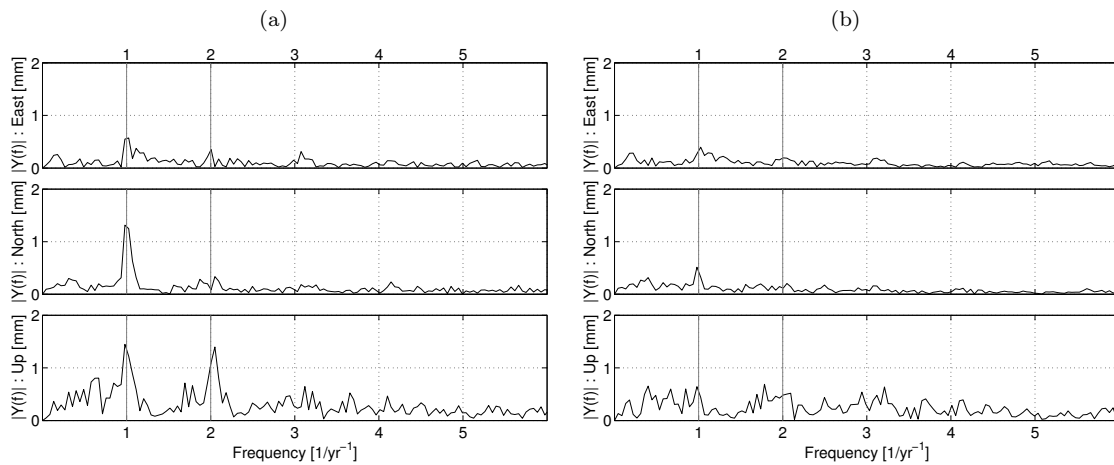


Figure 3.10: Single-sided amplitude spectra of the common-mode signals shown in Fig. 3.9 ((a) raw time series, (b) improved time series). The gray lines depict annual and semiannual periods, respectively. Annual and semiannual periods are almost inexistent in the common-mode signals derived based on improved time series.

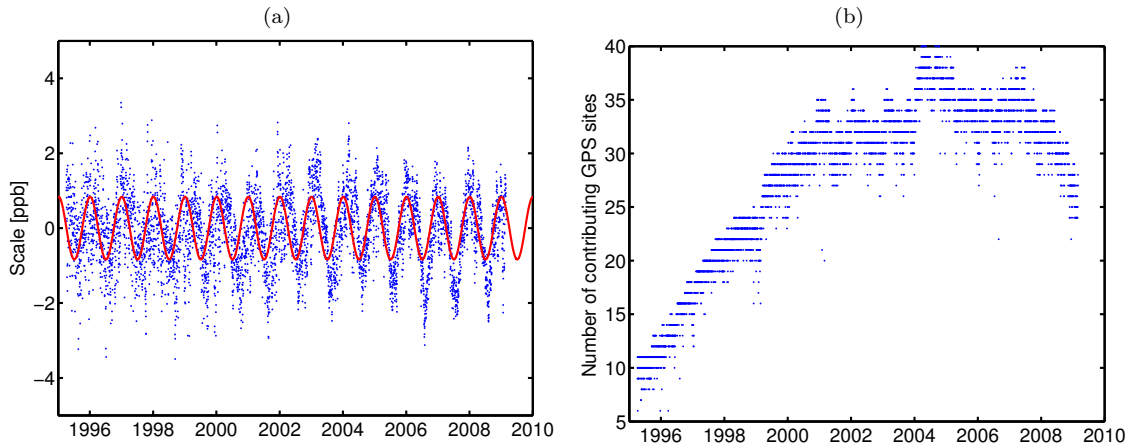


Figure 3.11: (a) Estimated scale of the network. The red line indicates the fit of a sine function with an annual period. The fit to the scale is not optimal as it is not entirely periodic. (b) Number of sites used for the estimation of the Helmert parameters.

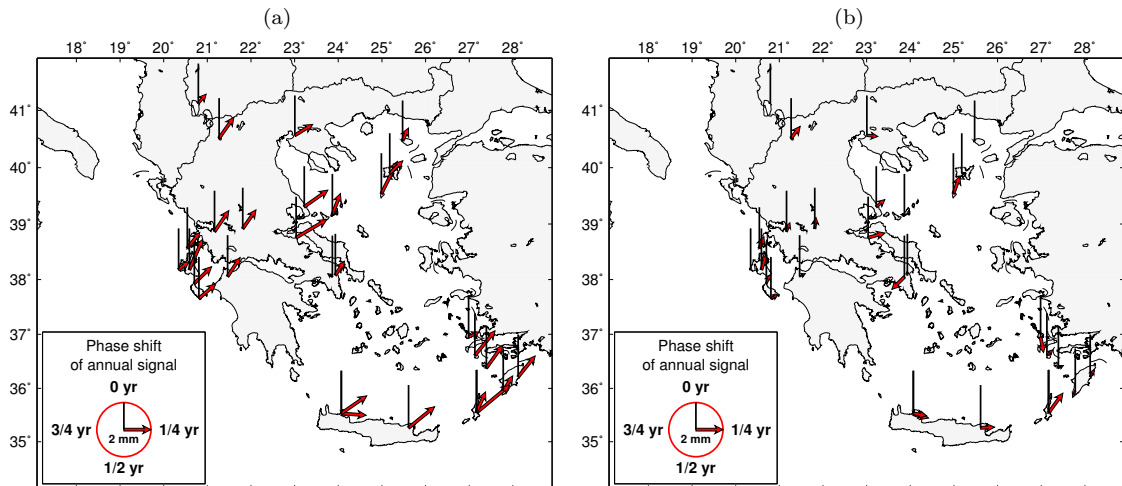


Figure 3.12: Amplitudes (length of red arrows) and phase lags (azimuth of red arrows) of annual sinusoidal signals estimated from the north components of raw (a) and improved (b) time series of continuous GPS sites in Greece.

3.4.7 Scaling of formal errors of velocities

The velocity estimation based on coordinate time series (chapter 3.4.5) and the combination of normal equations (chapter 3.5) is based on a white noise error model. Many authors (e.g., *Zhang et al.* 1997; *Mao et al.* 1999; *Williams et al.* 2004; *Langbein* 2008) have shown that a major part of the error budget in GPS derived velocities consists of colored noise. Consequently, temporal correlations have to be taken into account in the parameter estimation process, or the resulting formal errors have to be scaled in order to obtain realistic accuracies. In this thesis the latter procedure was applied.

Hollenstein [2006] carried out an autocovariance analysis in order to derive scaling factors for formal accuracies corresponding to velocity estimates of CGPS sites. The scaling factors were found to depend on time series length and data characteristics (completeness). Coefficients of a linear function were estimated to determine scaling factors as a function of the length of time series. A similar procedure was applied in order to review the validity of these factors for accuracies of rates derived in this thesis. The analysis is based on improved time series. Only two functions were considered to fit the autocovariance functions (AKF) in order to simplify the procedure.

$$\Gamma(\tau) = a_1 \cdot e^{-\frac{\tau^2}{b_1^2}} + a_2 \cdot e^{-\frac{\tau}{b_2}} \quad (3.12)$$

$$\Gamma(\tau) = a_1 \cdot \frac{b_1^2}{b_1^2 + \tau^2} + a_2 \cdot e^{-\frac{\tau}{b_2}} \quad (3.13)$$

The parameters $a_{1,2}$ and $b_{1,2}$ were estimated for each time series in two steps. First, the parameters a_1 and b_1 were derived with the elements $\tau = 1..l$ where l is the fifth negative element of the AKF. If the subtraction AKF (elements 1..7) minus the first term of the fitting function yields more than 2 positive elements also the parameters of the second term of the function (a_2, b_2) were estimated based on these positive differences. Equation (3.12) fits the autocovariance functions better than Eq. (3.13) on average.

Equations (3.12) and (3.13) and the corresponding site specific parameters $a_{1,2}$ and $b_{1,2}$ were used to fill two fully occupied weight matrices \mathbf{P} for each site. The scaling factors are equal the ratio between the accuracy derived when considering realistic covariances and the formal accuracy derived with a white noise model. Scaling factors were calculated for both approximation functions (Eq. (3.12) or (3.13)) and two velocity models (linear motion, linear motion combined with annual- and semiannual sinusoidal terms). The scatter of the obtained scaling factors is large (Fig. 3.13 (a)). It varies only little depending on the used approximation function and the used velocity model. A weak dependency of the scaling factors on time series length is revealed (Fig. 3.13 (a)). Scaling factors corresponding to the motion model estimating rates in combination with annual and semiannual signals are slightly smaller than those corresponding to a linear motion model (Fig. 3.13 (b)). These observations led to the following procedure: A single trend function was estimated on the basis of the scaling factors (based on Eq. (3.12) and the constant velocity model) of all three velocity components. This function (Table 3.4) is adequate for both velocity models. It is comparable with the trend function derived by *Hollenstein* [2006]: Its y-axis intercept is larger by 1.5 and its slope is less steep by 0.14.

The scaling factors for formal errors originating from the combination of normal equations were derived after comparing these formal errors with the ones obtained from time series compilation. On average, formal errors of campaign-type sites derived based on the combination of normal equations are 15 times smaller. The formal errors were multiplied with this factor. Temporal correlation was not considered since campaign-type measurements are usually separated by more than one year. All used factors are compiled in Table 3.4.

Scaling factors for formal errors corresponding to rates of CGPS sites are derived from coordinate residuals with respect to a particular mathematical model. Error fractions causing no residuals

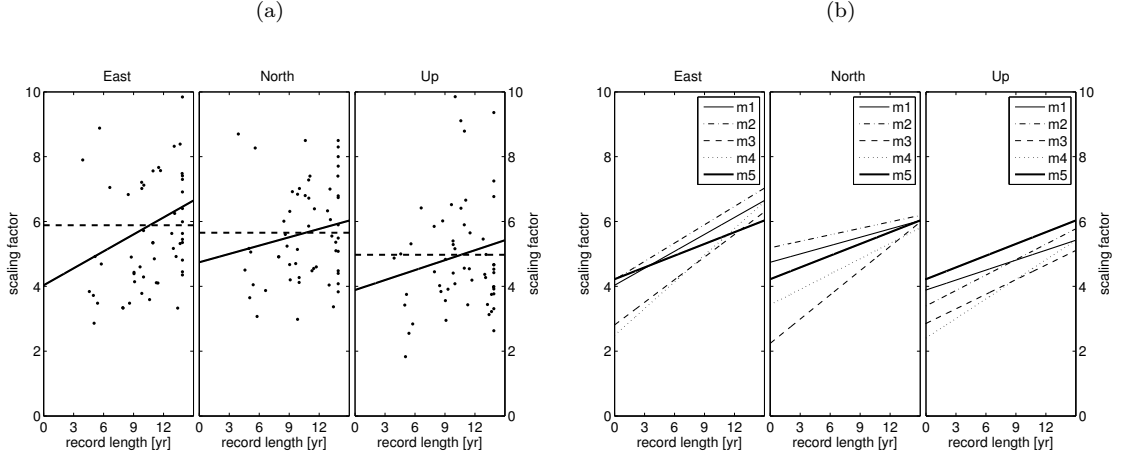


Figure 3.13: (a) Individual scaling factors for formal accuracies of rates of CGPS sites (based on Eq. (3.12) and a linear motion model). The dashed line represents the average, the continuous line a linear trend (m1 in (b)). (b) Trend functions of scaling factors. Notation: F1: Eq. (3.12); F2: Eq. (3.13)); v1: linear motion (Eq. (3.5)); v2: constant velocity plus annual and semiannual sinusoidal terms (Eq. (3.7)). Depicted trend functions: m1: F1+v1; m2: F2+v1; m3: F1+v2; m4: F2+v2; m5: F1+v1, optimal trend function estimated based on scaling factors of all three velocity components.

Applied to	Factor
Accuracies of rates of CGPS sites	$f = 4.22 + 0.12 \cdot T$
Accuracies of rates of campaign-type sites	$f = 15$

Table 3.4: Scaling factors used to derive realistic accuracies for velocities. T: length of time series [years].

such as for instance quasi linear non-tectonic site motions are not part of the error. *King and Williams* [2009] analyzed velocity differences of sites located close to each other ($\ll 1\text{km}$). While on average rates in all three components vary by about 0.1 mm/yr , some velocity pairs differ by up to 0.5 mm/yr . This means that scaling factors derived from autocovariance analysis likely yield too optimistic accuracies if site velocities are interpreted to represent a wider area. The resulting residuals derived by the combination of normal equations, which is used to derive velocities of campaign-type sites, lead to a scaling of all errors due to an increasing σ a posteriori of the inversion. The procedure of using one factor for scaling all velocity errors of campaign-type sites is a general approach. Indeed, it leads to inadequate accuracies for a few sites (compare e.g. chapter 3.6.3). Though, it is reasonable as for these sites significant parts of the error are hardly random and, therefore, difficult to quantify.

3.5 Velocity estimation of campaign-type GPS sites

Velocities of campaign-type sites were derived based on the combination of normal equations using the Bernese subprogram ADDNEQ2. All derived normal equations containing campaign-type data and the complementary normal equations of days where only data of continuous sites was available were combined. The program ADDNEQ2 estimates one position and velocity pair for each site and does not account for discontinuities. Therefore, the inclusion of discontinuities was realized by renaming the sites after each discontinuity. Except for reference sites all set-up velocities of a site were constrained to the same value. Position outliers detected in continuous GPS time series and position estimates during exclusion periods were removed before the combination of the

normal equations. CGPS sites with obvious non-linear systematic signals in their respective time series were excluded from the combination. Campaign-type and CGPS sites whose data do not cover at least 3 years were omitted. Formal accuracies of the derived rates were multiplied with a constant factor in order to account for the systematic underestimation of errors in GPS processing (chapter 3.4.7).

Velocities of continuous sites with a long data record (> 4 years) do not significantly differ depending on whether they were derived based on their position time series or the combination of normal equations. On average the rates for such sites in Greece differ by 0.13 mm/yr for each horizontal and 0.58 mm/yr for the vertical component, respectively. Rates of nearby CGPS and campaign-type GPS sites (< 8.5 km) agree well (Table B.3). Consequently, both velocity sets can be combined.

3.6 Factors affecting the velocity estimates

3.6.1 Tracking performance of GPS sites

Tracking performance of GPS sites such as e.g. satellite visibility has a significant effect on the repeatability of position estimates and, therefore, limits the ability to detect signals in time series. Tracking performance depends on site environment, monumentation and measuring equipment. Figure 3.14 (a) shows the very limited tracking performance of site ANOK (obstruction by trees) leading to large scatter in the corresponding coordinate time series. Figures 3.14 (b) and (c) show the increase in the C1 noise/multipath level $mpp1$ at site NEOH due to the installation of a radio emitter. The value $mpp1$ is derived by

$$mpp1 = C_1 - L_1 \cdot \lambda_1 - 2 \cdot \Delta_{iono,1} \quad (3.14)$$

$$\Delta_{iono,1} = (L_1 \cdot \lambda_1 - L_2 \cdot \lambda_2) / (f_1^2 / f_2^2 - 1) \quad (3.15)$$

where C is the code measurement, L is the phase measurement, f and λ are the frequency and the wavelength, respectively, of the carrier wave and Δ_{iono} is the ionospheric delay expressed in meters. The indices 1,2 denote the respective GPS carrier wave, respectively. The mean of all $mpp1$ values in a time period without cycle slips is subtracted from the values in this period. The installation of the emitter affects the up component of the coordinate time series most (appendix D). Measuring characteristics of sites being part of the evaluated CGPS network in Greece are heterogeneous contributing to the differences in the achieved coordinate repeatability (Table C.2). Therefore, the application of common-mode filtering seems less appropriate. Obviously, time series of sites with unfavorable measuring performance do not significantly improve when corresponding data is reprocessed using enhanced models.

3.6.2 Used orbits and earth orientation parameters

Between 1993 and 2009 several improvements have been achieved in GPS processing models used by the IGS analysis centers as well as in the combination strategy applied by the IGS analysis center coordinators. Concurrently, the numbers of satellites and GPS stations have increased and several subsequent reference frames have been realized. These efforts have enhanced the accuracy of products like satellite orbits, earth orientation parameters (EOPs) and site coordinates and velocities. Therefore, time series of IGS products are inhomogeneous and inconsistent [Steigenberger *et al.*, 2006].

The IGS initiated a data reprocessing campaign leading to an improved set of products between 1994 and 2008 in order to remove the lack of consistency [Ray, 2010]. Final combined products are

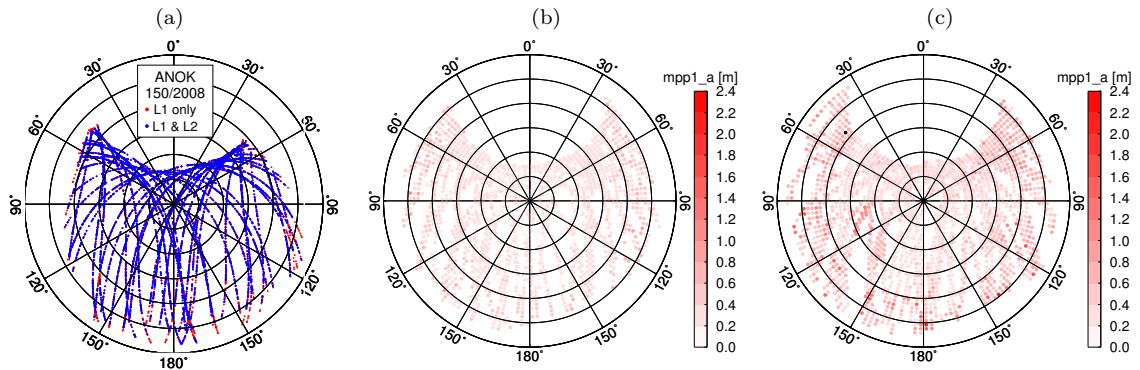


Figure 3.14: (a) Skyplot of site ANOK on 150/2008 (Date: DOY/YEAR). Problems in signal tracking due to a suboptimal antenna environment (obstruction by trees) is obvious. Blue: L1 and L2 tracked; red: L1 tracked only. (b) Noise level (C1) at site NEOH on 001/2004. (c) Noise level (C1) at site NEOH on 179/2007. The increase in the noise level is caused by the nearby installation of a radio emitter. The receiver/antenna configuration is identical in (b) and (c). The parameter *mpp1_a* is an average of the absolute *mpp1*-values in a $2.5^\circ \times 2.5^\circ$ sector.

available since early 2010 [IGSmail 6136]. Reprocessed orbits and EOPs were derived earlier by TU Munich and TU Dresden [Steigenberger *et al.*, 2006]. A later version of this data set comprehending products for the period 1994–2006 was available at <http://isdg.gfz-potsdam.de/gps-pdr>. An additional processing of the GPS data of the period 1994–2003 was performed using these products instead of IGS final products. Afterward, the effect of improved products on coordinate time series of a regional network was analyzed.

Especially in the early years of the measurements (1993–1998), several systematic signals are present in the obtained raw coordinate time series when employing IGS final products. For instance, such artifacts degrade the retrieval of co- and postseismic signals in GPS time series (see for an example the time series of station KERI: Fig. 3.15). The use of reprocessed orbits and EOPs enhances the quality of the obtained results. This effect is most significant in the time period 1994 to 1998. After 1998 the improvement is less remarkable. The decrease of the sigma a posteriori values is shown in Figure 3.16. Figure 3.17 shows the improved repeatability of position estimates in time series by means of RMS values. This RMS is based on daily residuals of all CGPS sites related to the linear trend. Figure 3.15 shows two raw time series of site KERI whereas IGS final orbits/EOPs and reprocessed orbits/EOPs were used for the processing. The use of reprocessed orbits largely reduces the difference between the rates before and after the 1997 Strofades earthquake (epicenter located ~ 40 km south of KERI). The results obtained based on reprocessed products and time series improvement confirm that the interseismic velocity did not significantly differ before and after this earthquake (Table 6.2; cmp. Hollenstein [2006]).

Several recently developed modeling techniques were used for the reprocessing of TU Munich and TU Dresden. These include absolute antenna phase center correction modeling, satellite specific z-values for its center of mass and second and third order ionospheric corrections. The geodetic datum was imposed by a no-net-rotation with respect to IGB00 (set of up to 99 station coordinates and velocities given in the IGS internal realization IGS03P33_RS106.snx). In IGSmail 5447 and 5455 two parameter sets were released for a Helmert transformation between IGB00 and IGS05 whereas the latter one also takes into account the change from relative to absolute antenna phase center corrections. The published transformation parameters were not rated to be optimal for the required transformation because of the modeling techniques used in the reprocessing. Therefore, the orbits and EOPs were not transformed. Assuming that a Helmert transformation (7 parameters and their rates) describes the transition between both systems but datum definition is only achieved by a

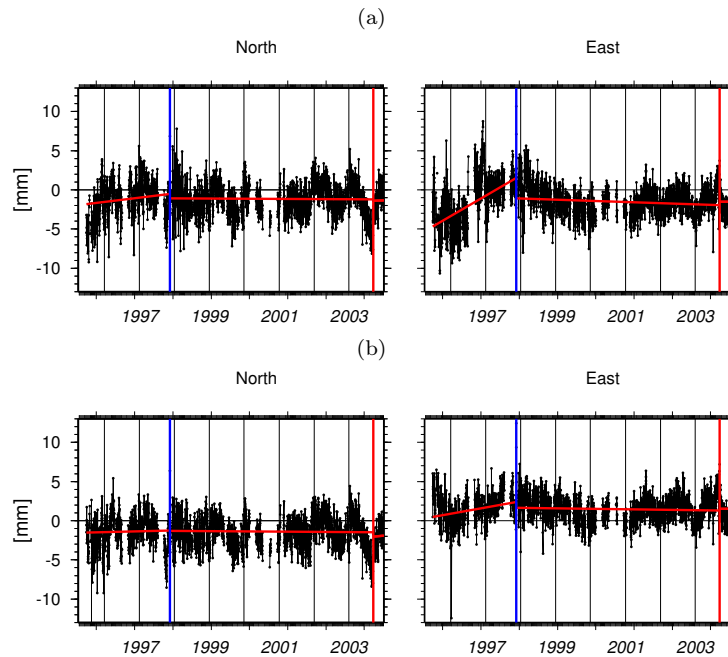


Figure 3.15: Detrended raw time series of site KERI in the period 1995–2003. The red lines indicate the residual velocity in the particular sections. The blue vertical line depicts the 1997 Mw 6.6 Strofades earthquake, the red vertical line an antenna change in 2003. (a) IGS final orbits/EOPs were used. Rates before and after the 1997 Strofades earthquake differ by -0.6 ± 0.6 mm/yr and -2.8 ± 0.6 mm/yr in the north and east components, respectively. (b) Reprocessed orbits/EOPs were used. Rates before and after the 1997 Strofades earthquake differ by -0.2 ± 0.5 mm/yr and -0.9 ± 0.4 mm/yr in the north and east components, respectively.

no-net-translation condition, the resulting error on velocities can be assessed. For this purpose the published parameter set for transforming IGB00 into IGS05 coordinates (relative to relative PCVs) was used. The scale and its temporal change were set to zero. The no-net-translation condition absorbs a large part of the error. Remaining systematic errors for each velocity component do not exceed $1/10$ mm/yr for sites in Greece and $3/10$ mm/yr for sites BHR and TEHN (Fig. 3.18). In contrast, an apparent scale drift of 0.1 ppb/yr in the processing would change the velocity of site BHR in the order of 0.27 mm/yr in each horizontal component and 0.13 mm/yr in the vertical component (Fig. 3.18). Rates of sites in Greece would not change by more than $2/10$ mm/yr. Strain rate calculation in Greece is not affected by this error source as the differential errors are insignificant in this region. Rates of sites in Greece for the period 1995–2003 change by a few tenths of a millimeter on average and by 1 mm/yr at most depending on the used orbits/EOPs (Table 3.5). The reduction of artifacts in coordinate time series and reference frame issues may cause this effect.

The obtained results demonstrate the benefit of reprocessed orbits and EOPs for regional networks. The detection of short-term signals lasting several days to months is enhanced in the period 1994–1998. The effect on long-term rates is less significant. The final GPS results derived in this thesis are based on the processing using reprocessed products for the period 1994–2003.

3.6.3 Campaign-type data of the years 1993 and 1994

Campaign-type position estimates of the year 1993 deviate significantly more from a linear motion than estimates of following years (Fig. 3.19). The processing of data of the year 1993 started not

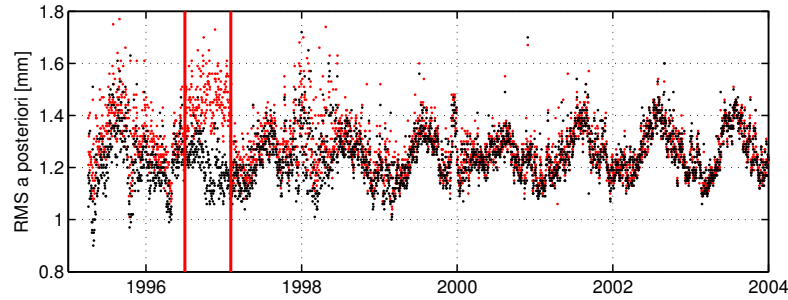


Figure 3.16: Daily σ a posteriori values of the GPS processing using IGS final orbits/EOPs (depicted as red points) and reprocessed orbits/EOPs (depicted as black points). Red lines indicate two model changes relevant for IGS products: 182/1996: start of estimating the earth rotation parameters including rates; 033/1997: inclusion of length of day.

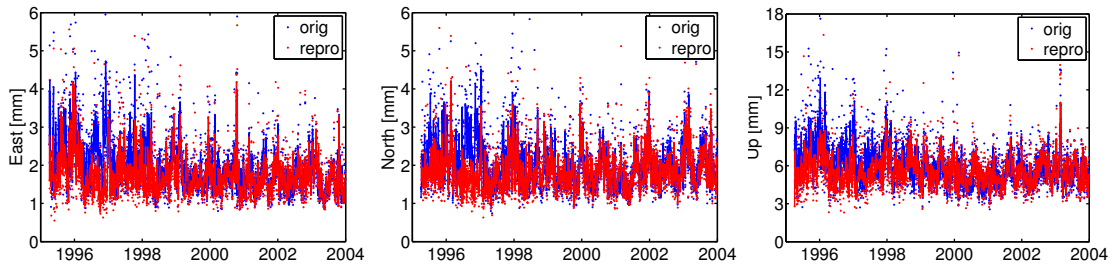


Figure 3.17: RMS of daily position estimates of CGPS sites with respect to a linear trend in the period 1995–2004. Blue dots: processing with IGS final orbits/EOPs; red dots: processing with reprocessed orbits/EOPs. The blue and red lines depict the median filtered RMS time series ($n = 5$).

from RINEX files but from manually screened single-difference files prepared by *Mueller* [1996]. No reprocessed orbits and EOPs are available for the year 1993. A smaller number of GPS satellites, less precise orbit and EOP information, few reference sites (~ 5) and, for particular sites, short measuring windows per day are the main reasons for these residuals. In parts, this is also true for data from the year 1994. Consequently, campaign-type sites with a short monitoring period and a high percentage of occupations in the years 1993 and 1994 are reduced reliable. The scaled accuracies calculated during the combination of normal equations only partly reflect these biases. Recently carried out campaigns permit to exclude measurements of the years 1993 and 1994 for selected sites. Table 3.6 lists the sites for which measurements in the years 1993 and 1994 were omitted for the selective solution. In Figure 3.20 the velocity differences between a complete and a selective solution are shown. Large differences are found for sites whose velocities are based on a short measuring period when excluding the 1993/1994 data and/or strongly depend on 1993 and 1994 data.

Nevertheless, all estimates were included in the final velocity solution. In general, the influence of 1993 and 1994 data is small provided three or more measurements from later years are available. Formal errors of campaign-type position estimates are larger in the years 1993 and 1994 on average than in subsequent years because of their dependency on the number of phase observations. In addition, most sites with large velocity differences between the solution types are occupied only twice when data before 1995 is omitted. Corresponding campaign-type sites have to be reoccupied in order to improve the accuracy of their rates.

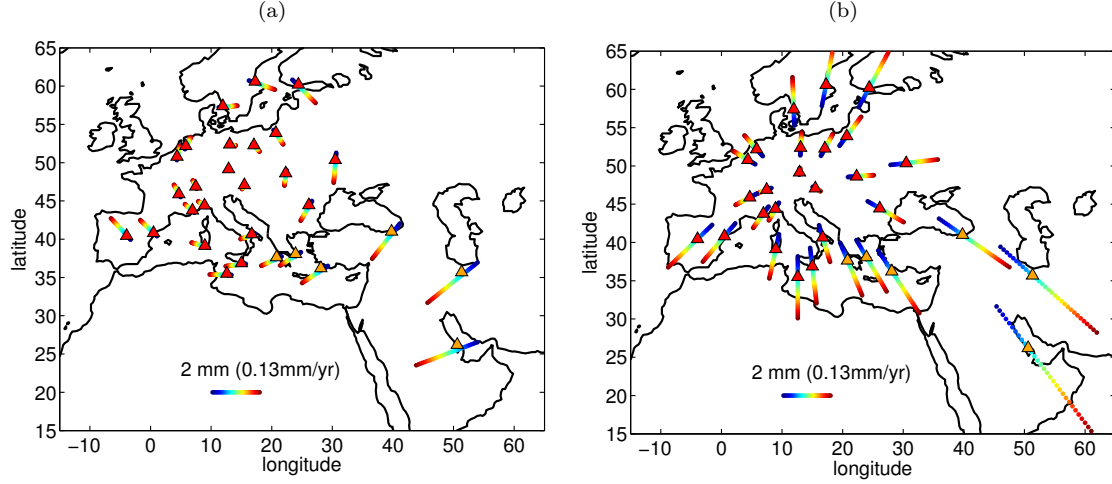


Figure 3.18: (a) Errors of site velocities if two assumptions are met: First, translation and rotation rates are non-zero in the Helmert transformation between the reference frame of used orbits and EOPs and the reference frame in which the coordinates of the reference sites are given. Second, the datum definition is achieved by imposing a no-net-translation condition. In the figures a scale is indicated showing 2 mm which corresponds to a velocity of 0.13 mm/yr over a period of 15 years. Red triangles indicate used reference sites, orange triangles other sites. Used rates: $\dot{T}_x = 0.04$ cm/yr; $\dot{T}_y = -0.07$ cm/yr; $\dot{T}_z = 0.18$ cm/yr; $\dot{\omega}_x = -0.0033$ mas/yr; $\dot{\omega}_y = 0.0001$ mas/yr; $\dot{\omega}_z = 0.0161$ mas/yr. (b) Only a scale rate is used: $\dot{s}c=0.1$ ppb/yr. The influence of the errors on strain rate calculation in Greece is insignificant for both cases.

Site	Data	Δv_e [mm/yr]	Δv_n [mm/yr]	Δv_{up} [mm/yr]	Remarks
AMFI	07/1995 - 12/2003	-0.96	-0.19	-0.39	data gaps, offsets
ANOK	06/2001 - 12/2003	0.16	-0.05	-0.17	
APAX	04/1995 - 12/2003	0.26	-0.09	-0.07	data gaps, offsets
ARHA	11/2000 - 12/2003	0.21	-0.12	0.66	data gaps
ARSA	11/2001 - 12/2003	0.00	-0.09	-0.52	data gaps
DION	04/1995 - 12/2003	0.32	-0.22	0.19	offsets
DUKA	04/1995 - 02/2002	0.00	-0.10	-0.43	data gaps, offsets
GERO	06/1995 - 12/2003	0.08	-0.14	0.25	data gaps, offset
KARP	02/2000 - 12/2003	0.18	-0.06	0.24	
KAST	02/1996 - 12/2003	0.11	-0.06	0.31	data gaps, offset
KERI	06/1995 - 12/2003	0.11	-0.08	-0.02	data gaps, offsets
KPTH	02/2001 - 07/2003	0.04	0.03	0.92	data gaps
NEOH	01/2002 - 12/2003	-0.08	-0.08	-0.06	
ORID	07/2000 - 12/2003	0.26	-0.11	0.50	data gap, offset
PAXI	07/1995 - 12/2000	0.14	-0.20	0.40	data gaps, offset
SKIN	06/1995 - 12/2003	0.12	-0.03	0.08	data gaps, offset
TUC1	08/1997 - 01/2003	0.35	-0.21	0.12	data gaps, offset
max		0.35	-0.03	0.92	
min		-0.96	-0.22	-0.52	
mean		0.08	-0.11	0.16	
std		0.29	0.07	0.37	

Table 3.5: Differences of rates ($v_{repro} - v_{orig}$) for CGPS sites in Greece. Only data of the period 1995–2003 was taken into account. The time series were not improved prior to the velocity estimation which is based on a constant velocity model. The time span of data is indicated as month/year. Only data gaps lasting several days are listed.

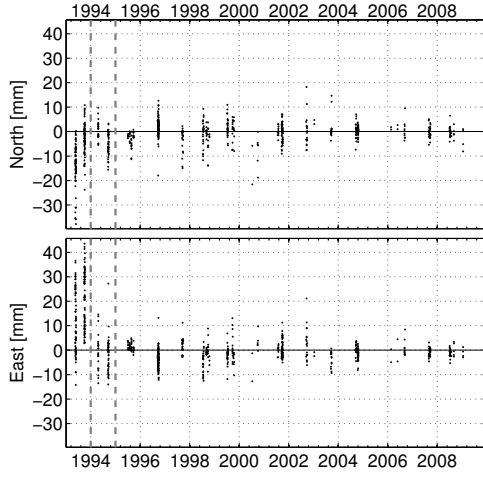


Figure 3.19: Residuals in the north and east components with respect to a linear motion of the campaign-type sites included in the final solution. Residuals in the years 1993 and 1994 are largest. Gray dashed lines highlight these years.

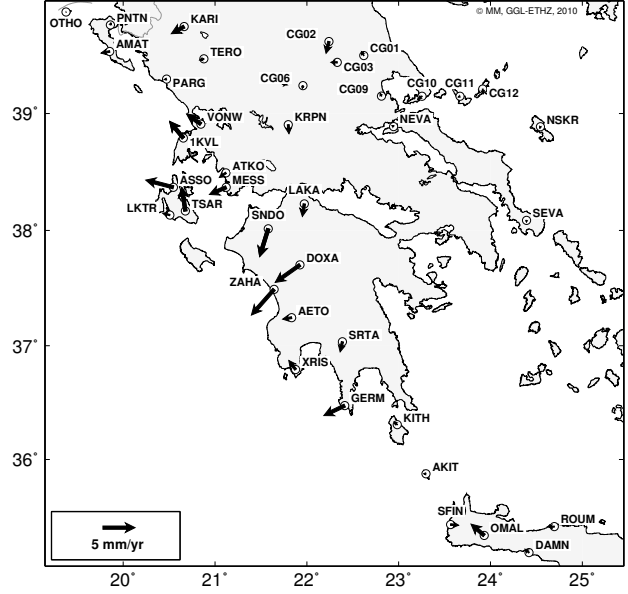


Figure 3.20: Differences in site velocity between a complete solution and a solution neglecting measurements in the years 1993 and 1994 ($v_{complete} - v_{selective}$). The differences in rates reach up to 5 mm/yr.

Site	Occupations				Site	Occupations			
	[year]	[n]	[year]	[n]		[year]	[n]	[year]	[n]
1KVL	93-94	3	98-02 03-09	4 2	LAKA	93	2	01-06	2
AETO	94	1	98-02	5	LKTR	93-94	2	99-06	4
AKIT	93	1	98-06	3	MESS	93	1	98-01	2
AMAT	93	1	99-06	2	NEVA	93	1	96-04	4
ATKO	93	1	98-01	3	NSKR	93	1	96-99 01-08	2 4
ASSO	93-94	3	99-02 03	2 1	OMAL	93	1	96-01	3
CG01	93	1	99-08	3	OTHO	93-94	2	95-02	4
CG02	93	1	98-01	3	PARG	93-94	2	98-07	4
CG03	93	1	99-04	2	PNTN	94	1	96-06	4
CG06	93	1	99-07	3	ROUM	93-94	2	96-03	5
CG09	93	1	99-07	3	SEVA	93	1	96-07	5
CG10	93	1	99-08	3	SFIN	93-94	2	98-01	2
CG11	93	1	01-07	3	SNDO	93	2	98-01	2
CG12	93	1	01-08	3	SRTA	93	1	98-02	3
DAMN	93	1	98-04	3	TERO	93	1	98-08	4
DOXA	93	1	98-01	2	TSAR	93-94	2	99-02 03	2 1
GERM	93	1	98-01	3	VONW	93-94	2	98-01 03	2 1
KARI	93-94	4	96-02	6	XRIS	93-94	4	96-04	8
KITH	93-94	2	96-06	4	ZAHA	93	1	98-01	2
KRPN	93	2	98-04	5					

Table 3.6: Number (n) and period of site occupations in the years 1993, 1994 and after 1994. The site NSKR was affected by the 2001 Mw 6.4 Skyros earthquake and the sites 1KVL, ASSO, TSAR and VONW were affected by the 2003 Mw 6.2 Lefkada earthquake. Site occupations before and after these earthquakes are listed separately.

3.7 Concluding remarks

This chapter describes the selected GPS data evaluation strategy. The main goal of this task was the estimation of consistent and accurate velocities for sites in Greece. The work was initiated by previous studies (e.g., *Peter 2000*; *Hollenstein et al. 2006*). New pre-conditions and possibilities for improvements were investigated and applied. The use of the Bernese GPS software 5.0 required the reprocessing of the whole data set to achieve a consistent solution. Several routines were developed in GPS data processing. These include the application of site specific information (e.g., handling of discontinuities, exclusion of outliers, modeling of periodic terms) and the reduction of systematic signals in time series. The (re-)processing of the GPS data between 1993 and 2009 led to a consistent velocity solution for Greece. The main findings are the following:

- The use of the Bernese GPS software 5.0 providing enhanced modeling features improved the obtained results compared to those in *Hollenstein et al. [2008a]*. However, coordinate time series still exhibit seasonal signals depending on the location of a site with respect to the reference sites. These artifacts were reduced by up to 30% by the application of a spatial filter.
- Results of regional GPS networks profit from the use of reprocessed orbits and EOPs. The repeatability of position estimates in time series improves most for the time period 1994 to 1998 concurring with a reduction of artifacts which could be misinterpreted as tectonic signals. However, the effect on the velocity estimation of complete and sufficiently long (>5 years) time series is only in the order of a few 1/10 mm. The quality of time series of sites whose tracking performance is low remain insufficient for geodynamic analysis. Reprocessed IGS orbits and EOPs are available since early 2010. In case regular IGS reprocessing activities become standard the latest products should be used whenever this data set is reprocessed.
- The scaling of formal errors of velocities estimated based on coordinate time series is necessary to account for temporal correlations. However, additional error sources exist which depend on the evaluation strategy. These effects are non-random and difficult to describe formally. Several of them such as the use of different sets of orbits/EOPs and the applied velocity model were analyzed. The influence on site velocities can amount to several tenths of a millimeter and exceed the formal errors indicated. Similar considerations apply for rates of campaign-type sites depending largely on data from 1993.

4 Kinematic field in Greece (1993–2009)

4.1 Introduction

The newly derived velocity field in Greece is significantly improved compared to previous solutions. A longer data record (1993–2009) was homogeneously processed and the network was extended by several continuous and campaign-type sites. While the main pattern of the horizontal velocity field in Greece is well-known (e.g., *Kahle et al.* [1995]; *Clarke et al.* [1998]; *Cocard et al.* [1999]; *McClusky et al.* [2000]; *Avallone et al.* [2004]; *Reilinger et al.* [2006]; *Hollenstein et al.* [2008a]) the network densification and additional site occupations provide a more detailed and reliable kinematic field mainly in three regions: along the North Aegean trough and especially at its western termination, in the southeast Aegean sea and in central Greece. Longer lasting time series enhance the accuracy and reliability of the results of many GPS sites. In addition, the derivation of vertical rates for 21 CGPS sites establishes an important step towards a three-dimensional velocity field.

In this chapter the new results are presented and analyzed. A block model is derived providing a structure of the kinematic field in Greece. Corresponding results are discussed in chapter 4.3. The kinematic field of the North Aegean domain and the Hellenic trench system are outlined in detail in chapters 4.4 and 4.5, respectively. Vertical rates in the reference frame IGS05 are discussed in chapter 4.6.

Horizontal and vertical rates are listed in Tables C.1, C.2 and C.3. The obtained horizontal site velocities in Greece relative to Eurasia are shown in Figure 4.1. Horizontal rates of sites located in Europe, North Africa and the Middle East are depicted in Figure B.3. Vertical rates are shown in Figures 4.16 and 4.17.

4.2 Euler vector and estimation of a pole of rotation for Eurasia (ITRF2005)

The horizontal components of a topocentric velocity \mathbf{v}_i can be written as a function of the Earth's radius r_E , the spherical coordinates (ϕ_i, λ_i) and the corresponding Euler vector $\mathbf{\Omega} = (\omega_x, \omega_y, \omega_z)^T$ given in a geocentric system.

$$\mathbf{v}_i^{topo} = \begin{pmatrix} v_n \\ v_e \end{pmatrix}_i = r_E \cdot \begin{pmatrix} \sin \lambda & -\cos \lambda & 0 \\ -\sin \phi \cos \lambda & -\sin \phi \sin \lambda & \cos \phi \end{pmatrix}_i \cdot \begin{pmatrix} \omega_x \\ \omega_y \\ \omega_z \end{pmatrix} \quad (4.1)$$

The Euler vector $\mathbf{\Omega}$ can be estimated based on site velocities by a least-squares adjustment. A test of the standardized residuals can be applied in order to decide which site velocities can be described by the same Euler vector.

A pole of rotation for Eurasia was derived iteratively based on rates of IGS and EUREF sites and using the mathematical principle described by Eq. (4.1). After each iteration the site with the largest standardized velocity residual outside the confidence interval (95% level) was excluded for the following iteration (cmp. *Hollenstein* 2006). In this thesis, whenever velocities are indicated

Pole	ϕ [°]	λ [°]	ω [°/Myr]
This thesis	56.28 ± 0.50 N	96.12 ± 1.09 W	0.266 ± 0.002
<i>Altamimi et al.</i> [2007]	56.33 ± 0.55 N	95.98 ± 0.97 W	0.261 ± 0.003
<i>D'Agostino et al.</i> [2008]	55.04 ± 0.36 N	98.06 ± 0.36 W	0.257 ± 0.001

Table 4.1: Poles of rotation for Eurasia (ITRF2005) derived from CGPS data.

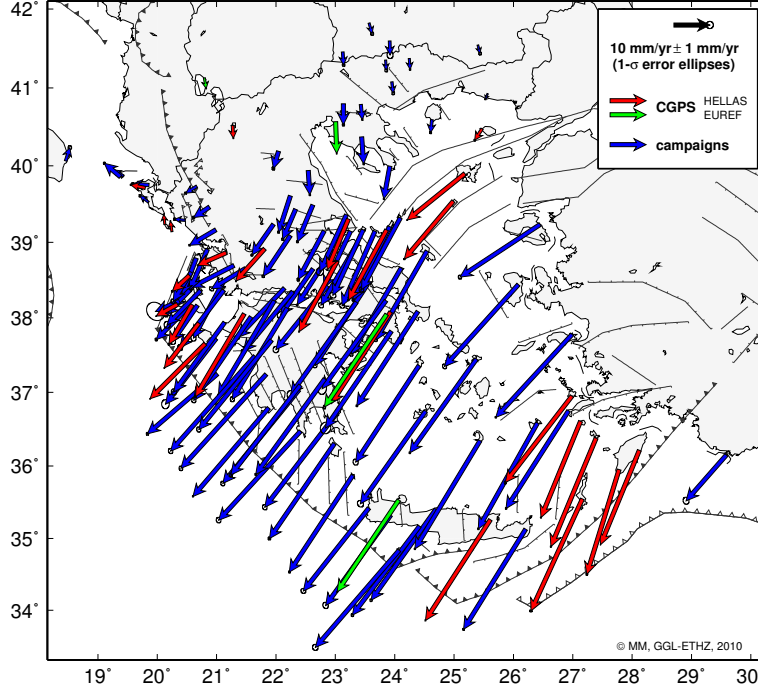


Figure 4.1: Horizontal velocities for the period 1993–2009 in Greece relative to Eurasia.

in an Eurasian-fixed frame the estimated pole of rotation given in Table 4.1 was used. Details related to the calculation are found in appendix B.1. *Altamimi et al.* [2007] and *D'Agostino et al.* [2008] derived slightly different Euler poles for Eurasia using a different set of site velocities (for a comparison see Table 4.1). The difference between the pole derived by *Altamimi et al.* [2007] and the pole derived in this thesis is statistically not significant. The difference in rates amounts to 0.28 and 0.50 mm/yr in the north and east components, respectively, for sites in Greece (Fig. B.1). Nubian plate motion whenever used in this thesis is described by the corresponding Euler pole for Nubia derived by *Altamimi et al.* [2007] (see App. B.2).

4.3 Kinematic block model for Greece

Block models are used to separate slowly from more rapidly deforming parts of the lithosphere. Block models for Greece have already been presented earlier (e.g., *McClusky et al.* 2000; *Nyst and Thatcher* 2004; *Reilinger et al.* 2006), though based on a less accurate data set. The intention of this chapter is not the identification of physical microplates but a first-order mathematical description of the velocity field based on a simple kinematic model. It was not attempted to completely subdivide the area into a number of blocks similar to the approaches of *Nyst and Thatcher* [2004], *Reilinger et al.* [2006] and *Floyd et al.* [2010]. Rapidly deforming regions such as western Turkey,

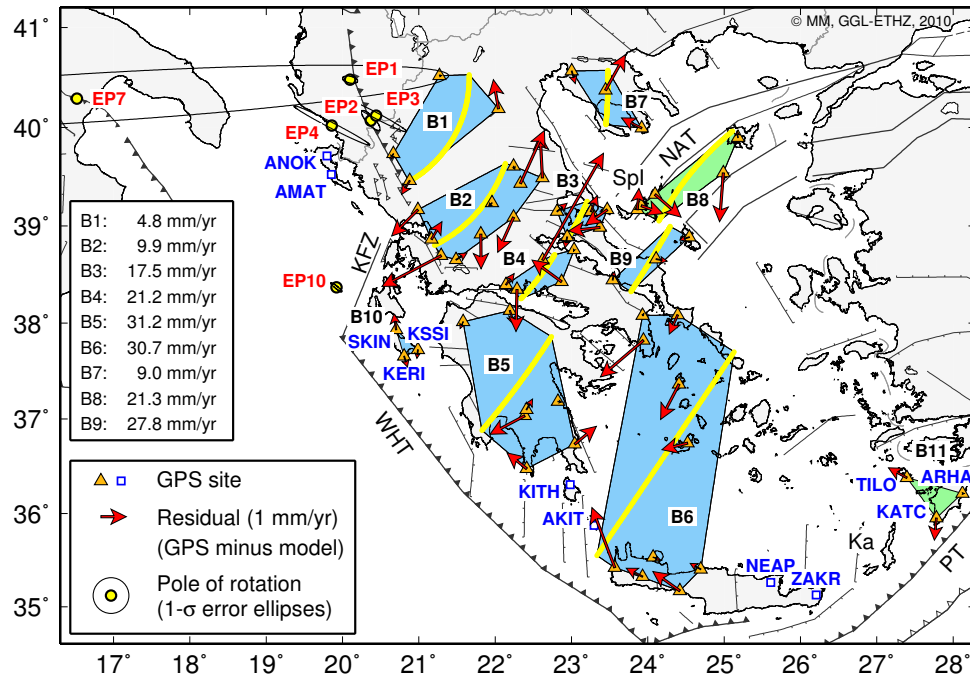


Figure 4.2: Slowly deforming areas in Greece are indicated as shaded polygons (blue: cw rotating, green: ccw rotating). Sites belonging to a particular block are shown as orange triangles. Additional GPS sites mentioned in the text are depicted by blue squares. Residuals of site velocities with respect to the block motion are below 2.5 mm/yr (exception: CG20). For blocks B1 to B9 the yellow line denotes the trace of a short arc of rotational motion. The curvature of the arc is an indication for the distance to the Euler pole. The corresponding rates are indicated on the left side. The Euler poles for blocks in northwestern Greece are indicated as yellow circles. The other ones are located outside the Figure. Ka: Karpathos, KFZ: Kefalonia fault zone, NAT: North Aegean trough, PT: Pliny trench, Spl: Sporades Islands, WHT: West Hellenic trench.

Lefkada and Kefalonia were not covered by blocks at all.

The assignment of a site to a particular block is based only on statistics and does not need to be unambiguous. There are several regions in Greece in which GPS site velocities have small residuals with respect to a block motion ($< 2.5 \text{ mm/yr}$; see Fig. 4.2 and Table 4.2). The corresponding Euler poles were derived by using Eq. (4.1). Most of the blocks are statistically not significant at a 95% confidence level (standardized residuals or F-test) despite the low residuals. The concept of rigid areas *sensu stricto* is hardly possible in Greece as there are no larger regions without any reported seismicity or active fault systems. Small strain rates within the blocks may lead to significant strain energy after several hundreds or thousands of years which can be released during intermediate earthquakes. As an example the 1995 Ms 6.6 Kozani-Grevena (northwestern Greece) earthquake occurred within block B1 [Hatzfeld *et al.*, 1997; Chatzipetros *et al.*, 1998; Stiros, 1998]. However, the kinematic block model shows that a large part of ongoing deformation is bound to distinct areas. This is supported by low seismicity associated with the defined blocks over the last thirty years (cmp. Fig. 4.2 and Fig. 4.3).

The largest regions with block-like behavior are found on the Peloponnesos and in the southwestern Aegean sea (blocks B5 and B6, respectively; compare also McClusky *et al.* [2000]). The extent of block B6 towards Antikythera (site AKIT) and Kithera (site KITH) slightly downgrade the statistical significance but residuals of these sites with respect to block B6 are below 1.5 mm/yr . Similarly, residuals of sites on eastern Crete (NEAP, ZAKR) with respect to block B6 are below 1.8 mm/yr . Extending block B5 towards south would lead to large residuals at KITH and AKIT

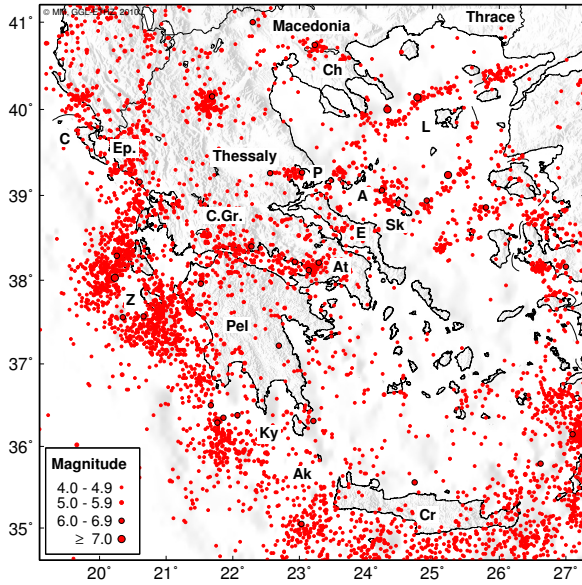


Figure 4.3: Seismicity ($M \geq 4$) in Greece for the period 1973–2009 [NEIC catalog, 2009]. In general, the blocks defined in Table 4.2 and shown in Fig. 4.2 correspond to regions of low seismicity. A: Alonissos, Ak: Antikythera, At: Attica, C: Corfu, Ch: Chalkidiki, C.Gr.: Central Greece, Cr: Crete, E: Evia, Ep: Epirus, Ky: Kythera, L: Limnos, P: Pelion, Sk: Skyros, Z: Zakynthos.

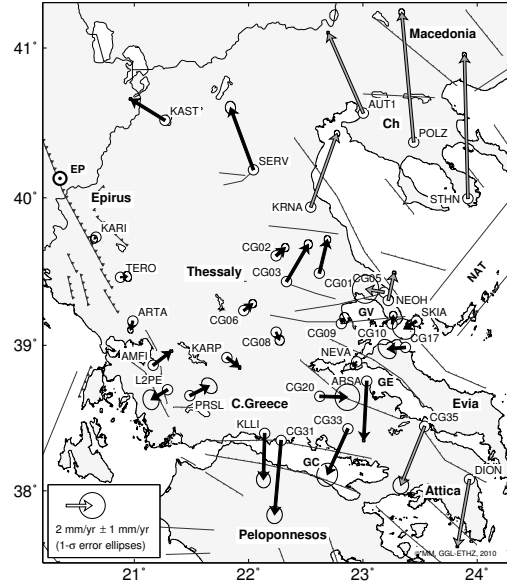


Figure 4.4: Velocity residuals of sites in northwestern Greece with respect to the Euler pole EP ($\lambda_P = 159.65^\circ\text{W}$, $\phi_P = 40.13^\circ\text{S}$, $\omega_P = 3.81^\circ$). Residuals of sites used for the estimation of the Euler pole are depicted by black arrows. Further residuals are depicted by gray arrows. Ch: Chalkidiki, GC: Gulf of Corinth, GE: Gulf of Evia, GV: Gulf of Volos, NAT: North Aegean trough.

(residuals: 4.8–7.0 mm/yr) pointing to considerable deformation between these blocks (see Fig. 4.15 and 5.2 (b)).

CW rotation of central Greece relative to Eurasia was discussed in previous GPS studies [Avallone *et al.*, 2004; Nyst and Thatcher, 2004]. An extended analysis of this feature is presented in this thesis based on more recent GPS data. The region of Epirus, Thessaly and central Greece rotate quite coherently clockwise around Euler poles located in southern Albania. Four poles of rotation (EP1, EP2, EP3 and EP4) were found to describe the motion of this region. These Euler poles are located within an angular distance of 0.5° . Their angular velocities differ by $2.1^\circ/\text{Myr}$. Despite considerable seismicity in Epirus (Fig. 4.3) the residuals of sites on Corfu (ANOK and AMAT) are below 2 mm/yr with respect to the northwesternmost block B1. This suggests little deformation in this area. The rate of site CG20 is rather doubtful. CG20 is part of block B4 owing to its location although its rate better fits to block B2 (residuals: 1.4 mm/yr and 4.8 mm/yr, respectively). Its influence on the Euler pole EP4 is small (0.1° in location, $0.16^\circ/\text{Myr}$ in angular velocity). Several versions of the block definition in mainland Greece provide a comparable fit to the GPS rates. In case a single Euler pole would be estimated for all the sites in northwestern Greece (blocks B1, B2 and B3), the largest residual would amount to 3.7 mm/yr (site: SERV). Maximum residuals amount to 3.7 mm/yr for sites CG31 and CG20 when a single Euler pole is estimated for blocks B2 and B4 and sites CG01, CG02 and CG03 are omitted. The largest residual with respect to a single Euler pole for blocks B1, B2, B3 and B4 amounts to 5.8 mm/yr (site: CG31). The residuals with respect to this Euler pole ($\lambda_P = 159.65^\circ\text{W}$, $\phi_P = 40.13^\circ\text{S}$, $\omega_P = 3.81^\circ$) witness ongoing N-S extension in western Thessaly and across the Gulf of Evia (Fig. 4.4). A clear correlation with faults remains difficult except for the Gulf of Evia. The distribution of the residuals corroborates the findings of Goldsworthy *et al.* [2002] derived based on geomorphology, earthquake distribution and

geodetic measurements that extension is larger in the East than in the West of mainland Greece. The general result of a rather coherent cw rotation of NW Greece does not change depending on the particular block definition.

Block	λ_P [°]	ϕ_P [°]	ω_P [°/Myr]	F-test	Site	λ_S [°]	ϕ_S [°]	r_n [mm/yr]	r_e [mm/yr]	w_n	w_e
B1	-159.90	-40.48	2.07	1.97	KARI	20.66	39.73	0.20	0.09	0.51	0.29
	± 0.10	± 0.04	± 0.16	[2.21]	KAST	21.27	40.52	-0.01	-0.08	-0.15	-1.59
					SERV	22.04	40.19	-1.14	0.20	-1.80	0.37
					TERO	20.88	39.46	0.54	0.32	1.05	1.01
B2	-159.63	-40.07	3.58	17.18	AMFI	21.16	38.86	-0.69	-0.41	-2.52	-0.90
	± 0.12	± 0.10	± 0.32	[1.62]	ARTA	20.99	39.17	1.03	1.03	1.17	1.25
					CG01	22.62	39.49	-1.71	0.09	-1.53	0.09
					CG02	22.24	39.61	0.12	-0.05	0.10	-0.05
					CG03	22.33	39.43	-2.08	-0.94	-1.53	-0.75
					CG06	21.96	39.24	0.13	0.13	0.10	0.11
					CG08	22.24	39.09	1.37	0.62	0.91	0.42
					KARP	21.81	38.92	1.36	-0.01	2.64	-0.04
					L2PE	21.29	38.70	1.21	2.33	0.38	0.91
					PRSL	21.49	38.66	-0.27	-0.43	-0.11	-0.17
B3	-159.56	-40.12	3.92	2.06	CG09	22.81	39.15	-0.32	-0.39	-0.61	-0.84
	± 0.40	± 0.16	± 0.59	[2.01]	CG10	23.25	39.15	-0.63	-0.25	-1.90	-0.77
					CG17	23.37	38.99	0.14	1.23	0.14	1.26
					NEVA	22.94	38.89	0.43	0.09	1.80	0.57
					SKIA	23.47	39.16	0.60	0.85	0.57	0.71
B4	-160.14	-40.02	4.17	4.74	ARSA	23.03	38.76	0.05	0.02	0.69	0.36
	± 0.50	± 0.20	± 0.66	[2.01]	CG20	22.62	38.65	-4.20	-2.39	-1.92	-1.16
					CG31	22.28	38.35	1.65	0.04	1.30	0.03
					CG33	22.87	38.43	-0.85	1.16	-0.44	0.68
					KLLI	22.14	38.40	-0.44	-0.32	-0.41	-0.30
B5	-166.26	-41.78	2.03	1.23	CG43	22.19	38.13	0.59	-0.19	0.77	-0.37
	± 0.91	± 0.41	± 0.19	[1.79]	GERM	22.41	36.47	-0.62	0.77	-0.74	1.16
					LEON	22.82	37.18	0.02	-0.14	0.12	-0.81
					MONE	23.04	36.74	-0.70	-0.85	-0.88	-1.26
					SNDO	21.58	38.01	0.26	0.12	0.38	0.22
					SRTA	22.39	37.03	0.73	1.37	1.05	2.26
					STRV	22.41	37.10	-0.42	-0.24	-0.73	-0.47
B6	125.55	-44.00	0.33	3.11	CG66	23.94	37.82	1.44	1.69	0.50	0.66
	± 9.23	± 2.73	± 0.03	[1.62]	DAMN	24.42	35.17	-0.76	1.06	-1.06	1.75
					DION	23.93	38.08	-0.08	-0.05	-0.71	-0.70
					KYNS	24.41	37.36	1.38	0.72	0.91	0.57
					MILS	24.52	36.75	0.26	1.01	0.16	0.67
					OMAL	23.93	35.32	-0.33	0.64	-0.21	0.48
					ROUM	24.69	35.40	-0.23	0.41	-0.34	0.75
					SEVA	24.39	38.09	0.75	0.33	1.78	0.88
					SFIN	23.57	35.42	-2.36	0.90	-1.94	0.74
					TUC2	24.07	35.53	0.09	-0.27	0.46	-2.52
B7	-163.48	-40.29	0.87	28.50	AUT1	23.00	40.57	0.49	-0.14	1.54	-0.58
	± 4.87	± 0.33	± 0.62	[2.60]	POLZ	23.44	40.37	-1.40	-0.78	-1.06	-0.70
					STHN	23.92	39.99	-0.40	0.79	-0.63	1.43
B8	27.58	37.56	3.56	20.27	ALON	23.86	39.17	-0.84	-0.06	-1.15	-0.08
	± 0.26	± 0.23	± 0.37	[2.01]	CG12	23.91	39.21	0.31	-0.85	0.19	-0.59
					EFSS	24.99	39.54	1.92	0.15	2.44	0.22
					LIMS	25.18	39.90	-0.25	0.04	-1.77	0.24
					PELA	24.09	39.32	0.89	-1.02	0.27	-0.34
B9	-169.24	-43.68	1.29	0.65	CG35	23.54	38.45	-0.33	-0.07	-1.08	-0.18
	± 3.97	± 1.15	± 0.35	[2.60]	CG38	24.11	38.66	0.08	-0.43	0.23	-1.40
					NSKR	24.54	38.89	0.11	0.37	0.55	1.66
B10	-160.08	-38.37	11.01	15.45	KERI	20.81	37.65	0.42	-0.13	1.72	-1.60
	± 0.08	± 0.05	± 0.95	[2.60]	KSSI	20.99	37.72	0.34	0.04	0.07	0.01
					SKIN	20.70	37.94	-0.63	0.09	-1.73	1.68
B11	32.56	34.62	3.70	10.59	ARHA	28.12	36.21	0.00	-0.07	0.01	-1.14
	± 0.61	± 0.23	± 0.50	[2.60]	KATC	27.78	35.95	0.87	0.08	0.99	0.11
					TILO	27.39	36.38	-0.39	0.72	-1.31	1.35

Table 4.2: Details of the slowly deforming blocks used to characterize the kinematic field in Greece. λ_P , ϕ_P and ω_P define the Euler vectors by means of its longitude, latitude and angular velocity. The numbers beneath denote the respective 1- σ accuracies. F-test denotes the test statistics based on a Fisher distribution. The values in square brackets correspond to the 95% confidence interval based on the particular degree of freedom. λ_S , ϕ_S are the longitude and latitude of the site. r_n and r_e are the residuals (model - observation), north and east components, respectively. w_e and w_n are the standardized residuals.

The coherent rotation of northwestern Greece is limited to the south by the Gulf of Corinth where N-S extension of up to 300 nstrain/yr is encountered (chapter 5.3). This is probably related to the collision of the Apulian domain with Greece/Albania north of the Kefalonia fault zone and the retreat of the Nubian slab south of it.

In Northern Greece the south components of GPS velocities at about equal latitudes are larger on Chalkidiki (AUT1: 8.9 mm/yr) than in western Macedonia (KAST: 3.6 mm/yr) and in Thrace (THAS: 3.6 mm/yr) (Fig. 4.6 (a)). Small residuals of sites on Chalkidiki (AUT1, POLZ and STHN) with respect to an Euler pole located in southern Italy (EP7) suggests that the southward motion of Chalkidiki can be interpreted in terms of a slow cw rotation similar to the rotation of northwestern Greece. Residuals of sites on Chalkidiki with respect to EP1 do not exceed 3 mm/yr indicating little deformation in northwestern Greece. Blocks B3 and B7 indicate N-S extension (~ 8 mm/yr) between Chalkidiki and Pelion. The GPS derived angular velocities for northwestern Greece ($\sim 2\text{--}4^\circ/\text{Myr}$) and Chalkidiki ($\sim 0.9^\circ/\text{Myr}$) correspond with rates obtained from paleomagnetism. *Van Hinsbergen et al.* [2005] determined a clockwise rotation for northwestern Greece of $\sim 10^\circ$ since 4 Myr ago. Moreover, the Chalkidiki peninsula has rotated 30° in the last 40 Myr while in Thrace no rotation has been observed in the last 30 Myr [*Kissel and Laj*, 1988].

Since seismicity belts ($M \geq 4$) are observed along the North Aegean trough, the Agios Efstratios fault and within the Skyros basin (Fig. 4.5 (b)), an additional Euler pole was estimated for the islands located in between. The location of these islands (Limnos (L), Agios Efstratios (AE), Pelagonissi (P) and Alonissos (A)) is shown in Fig. 4.6 (a). Although the Euler pole is statistically not significant (F-test), all velocity residuals are below $|2.0$ mm/yr|. The residuals are relatively small compared to differential rates across the NAT reaching more than 20 mm/yr. It is suggested that the seismicity belts define a slowly deforming, block-like zone (block B8) and that seismotectonic processes are predominantly bounded to the borders of it. The extent of this block-like area to the East is uncertain. The corresponding Euler pole located at 27.58°E , 37.56°N predicts a velocity with a direction of 252° in the Saros basin (26.4°E , 40.5°N). This is close to 261° , the orientation of the Ganos fault [*Yaltirak and Alpar*, 2002], and in agreement with predominant strike-slip structures combined with normal components along the Saros trough. Moreover, GPS rates of *McClusky et al.* [2000] on the Biga peninsula are reasonably represented by this block motion (residuals: SUBA: ~ 2.7 mm/yr; SEVK: ~ 4.1 mm/yr; for site locations see Fig. 4.9).

NE-SW extension in the order of 6 mm/yr is calculated between block B8 (Alonissos, Limnos) and block B9 (Skyros, Central Evia). South of the NAT the general sense of rotation relative to Eurasia changes along a diffuse line between the Sporades islands and Karpathos from counterclockwise east of this line to clockwise west of it. Interseismic rates observed on Skyros fit better with the cw rotating domain (block B9). The observed velocity difference between blocks B8 and B9 is partly reflected by the coseismic displacements related to the 2001 Mw 6.4 Skyros event. NNE-SSW extension in the order of ~ 3 mm/yr is indicated by blocks B5 and B9 across Central Greece/Attica.

Finally, the GPS velocities suggest pronounced rotations in two areas of very local dimensions: The sites SKIN, KERI and KSSI indicate cw rotation of Zakynthos in the order of $11^\circ/\text{Myr}$ (largest residual at site SKIN: 0.7 mm/yr). CCW rotation ($3.7^\circ/\text{Myr}$) is indicated for the islands of Rhodes and Tilos by the sites ARHA, KATC and TILO (largest residual at site TILO: 0.9 mm/yr).

4.4 Kinematic field and modeling in the North Aegean domain

4.4.1 Kinematic field

The North Aegean domain forms part of the plate contact between the Eurasian and Anatolian/Aegean plates. Kinematically it separates the regions of Macedonia and Thrace, moving southward by 4 mm/yr, from the Aegean microplate moving southwestward by 30 mm/yr, relative to the Eurasian plate. The tectonic framework of the Aegean sea is controlled by the interaction between Eurasia, Anatolia and Nubia (Fig. 4.5 (a)). Extensional processes in the Aegean microplate are closely related to the retreat of the Nubian slab [Le Pichon and Angelier, 1979]. These extend northwards into F.Y.R.O.M. and Southern Bulgaria [Kotzev *et al.*, 2006; Burchfiel *et al.*, 2006, 2008]. The North Anatolian fault (NAF) separates the Anatolian plate from the Eurasian plate [Sengör, 1979; Sengör *et al.*, 2005]. It splits into three branches west of 31°E. The three branches are witnessed by seismicity belts in the North Aegean sea (Fig. 4.5 (b)). The northern branch is kinematically and seismically the most active one while the southern ones are less distinct [Straub *et al.*, 1997; Kiratzi, 2002].

Investigations of tectonic structures in the North Aegean sea revealed wide-spread fault patterns. The NE-SW and ENE-WSW trending faults accommodate predominantly right-lateral strike-slip motion. Similarly oriented faults bounding the basins are also associated with normal faulting [Koukouvelas and Aydin, 2002]. NW-SE trending faults are found at the western and northern part of the Sporades basin [Laigle *et al.*, 2000; Koukouvelas and Aydin, 2002; Papanikolaou *et al.*, 2006] and along the southwestern margin of the Skyros basin [Taymaz *et al.*, 1991; Ganas *et al.*, 2005]. These faults accommodate normal and occasional left-lateral slip. The North Aegean trough (NAT) comprises the Sporades and the Saros basins (1500 m and 600 m deep, respectively). The latter is located adjacent to the Ganos fault. The Saros basin is bounded by ENE-WSW trending faults. According to seismic studies the southern boundary appears as a normal fault while the northern one acts as the western continuation of the Ganos fault [Yaltirak and Alpar, 2002; Karabulut *et al.*, 2006]. Kiratzi [2002] revealed a smooth change in the orientation of the least compressive stress component σ_3 from western Turkey (N35°E) towards central Greece (nearly N0°E). Towards Evia and the Greek mainland microearthquake data shows that shear deformation as observed along the NAT transforms into normal faulting [Hatzfeld *et al.*, 1999; Kiratzi, 2002]. Crustal thickness in the North Aegean sea is estimated to be in the range of 24–30 km [Tirel *et al.*, 2004; Sodoudi *et al.*, 2006]. This is attributed to ongoing extensional processes.

Right-lateral strike-slip motion is the dominating deformation style along the North Aegean trough. Differential motion across the NAT decreases from NE to SW from ~20 mm/yr between Samothraki and Limnos to ~7 mm/yr along the Sporades basin (Fig. 4.6). The change of differential motion is closely related to a 35 degrees bending of the NAT. No strike-slip fault trace is observed towards northern Evia [Papanikolaou *et al.*, 2006]. It is of interest whether this is also supported by the GPS data. GPS velocities at the western termination of the NAT are rather uniformly directed (~205° relative to Eurasia). The kinematic field at the western termination of the NAT between Pelion and the Sporades islands is shown in Figure 4.7 (a) relative to block B8 and in Figure 4.7 (b) relative to block B3 (see chapter 4.3 and Fig. 4.6 (b)). Rotational components found in Thessaly have to be considered when accurately estimating strike-slip motion between the Sporades islands and Pelion.

GPS velocities indicate N-S extension from southwestern Bulgaria towards Pelion. In particular, the sites PETR and VRES indicate 2.2 ± 0.6 mm/yr extension across central Macedonia, the sites VRES and AUT1 indicate 3.0 ± 0.4 mm/yr extension across the Mygdonian graben (differences in north components), and the sites STHN and NEOH suggest extension between Chalkidiki and Pelion amounting to 6.5 ± 0.2 mm/yr (baseline lengthening). In addition, baseline lengthening of

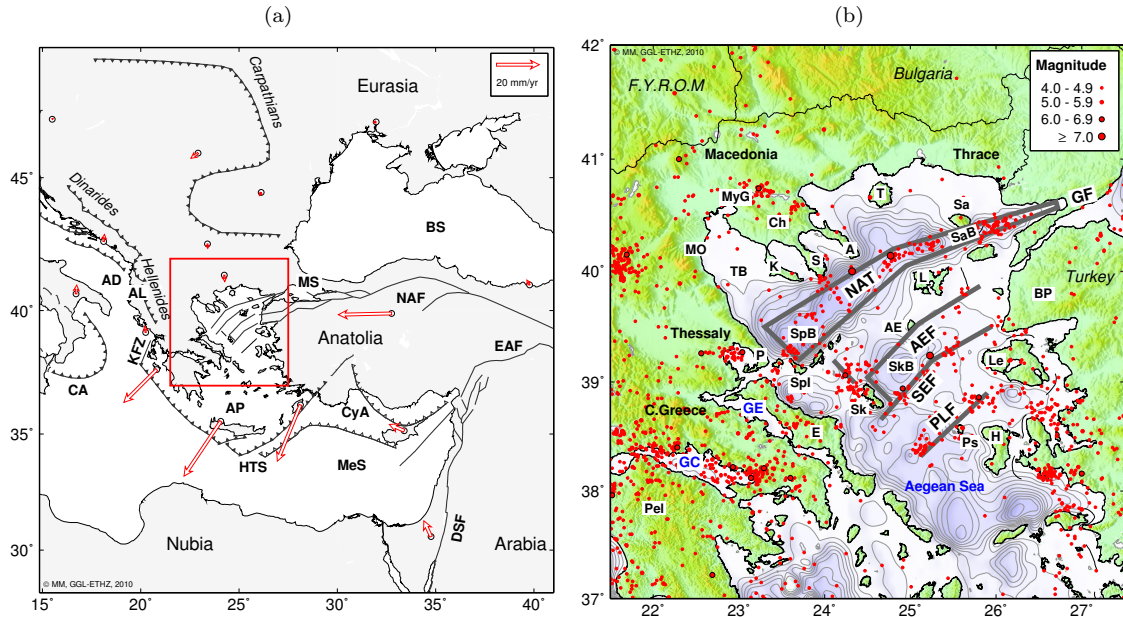


Figure 4.5: (a) Tectonic framework of the Eastern Mediterranean. The red arrows denote GPS rates relative to Eurasia (derived in this thesis). The area depicted as red square is enlarged in (b). (b) Seismicity ($M \geq 4$) in the North Aegean region in the period 1973–2009 [NEIC catalog, 2009]. The gray lines denote major seismicity belts. The North Aegean trough (NAT), the Agios Efstratios fault (AEF) and the Skyros-Edremit fault (SEF) are considered to be extended branches of the NAF. The equidistance of isobaths amounts to 100 m. A: Athos peninsula, AD: Apulian domain, AE: Agios Efstratios, AEF: Agios Efstratios fault, AL: Albania, AP: Aegean Plate, BP: Biga peninsula, BS: Black sea, CA: Calabrian arc, Ch: Chalkidiki peninsula, CyA: Cyprus arc, DSF: Dead Sea fault, E: Evia, EAF: East Anatolian fault, GC: Gulf of Corinth, GE: Gulf of Evia, GF: Ganos fault, H: Hios, HTS: Hellenic trench system, K: Kasandra peninsula, KFZ: Kefalonia fault zone, L: Limnos, Le: Lesvos, MO: Mount Olympus, MyG: Mygdonian graben, NAF: North Anatolian fault, NAT: North Aegean trough, P: Pelion, Pel: Peloponnesos, PLF: Psara-Lesvos fault, Ps: Psara, S: Sithonia peninsula, Sa: Samothraki, SaB: Saros basin, SEF: Skyros-Edremit fault, Sk: Skyros, SkB: Skyros basin, SpB: Sporades basin, SpI: Sporades islands, T: Thasos, TB: Thermaikos basin.

5.0 ± 0.3 mm/yr is observed between Sithonia (STHN) and Thasos (THAS).

The 1978 earthquake series near Thessaloniki whose largest event had a magnitude M_s 6.5 [Papazachos et al., 1979; Soufleris and Stewart, 1981] was located on the Mygdonian graben. Geodetic measurements revealed an average extension rate of 5.7 ± 1.3 mm/yr across the graben for the period 1979 to 1994 [Martinod et al., 1997]. The velocity solution (1993–2009) derived in this thesis also indicates extension but of smaller amount (3.0 ± 0.4 mm/yr). Martinod et al. [1997] suggest that the rates may also contain postseismic signals related to the 1978 event. Based on seismicity Papazachos et al. [2001] derived a long-term extension rate between 0.8–3.4 mm/yr depending on the E-W location along the structure. The GPS data of this study does not discern between strain accumulation or fault slip. The Mygdonian graben belongs to a larger extensional province extending from Central Bulgaria [Kotzev et al., 2006] to Pelion which is geodetically well documented. This extensional domain is also reflected in seismic records and witnessed by large earthquakes (e.g., 1904 M_s 7.8 Southern Bulgaria [Meyer et al., 2002], 1923 M_s 6.4 offshore Kasandra, 1930 M_s 6.0 offshore Pelion [Ambraseys and Jackson, 1990], 1978 M_s 6.5 Thessaloniki [Papazachos et al., 1979]).

South of Agios Efstratios (EFSS) the kinematic field indicates shear deformation and extension. Towards Skyros (NSKR) differential motion of 7.9 ± 0.5 mm/yr is found (baseline lengthening). The

residual of site LESV with respect to block B8 is $|13.7 \text{ mm/yr}|$. Most of this velocity difference is probably accommodated by strike-slip on the Agios Efstratios and Skyros-Edremit faults.

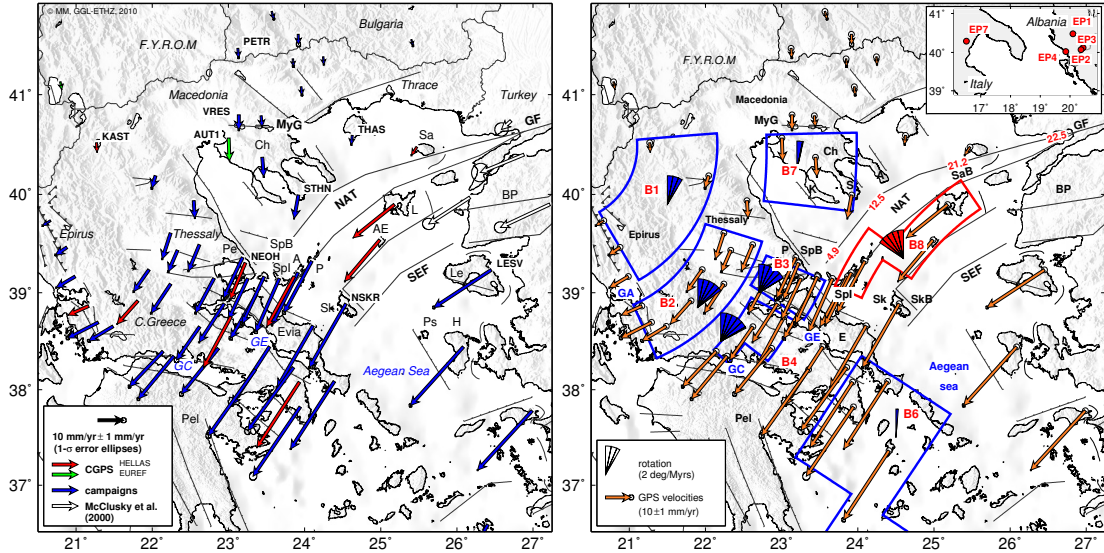


Figure 4.6: (a) Horizontal velocities in the North Aegean domain relative to Eurasia. White arrows originate from data of *McClusky et al.* [2000] transformed to ITRF2005. A: Alonissos, AE: Agios Efstratios, BP: Biga peninsula, Ch: Chalkidiki, SEF: Skyros-Edremit fault, GC: Gulf of Corinth, GE: Gulf of Evia, H: Hios, L: Limnos, Le: Lesvos, NAT: North Aegean trough, P: Pelagonissi, Pe: Pelion, Ps: Psara, Sa: Samothraki, Sk: Skyros, SpI: Sporades islands. (b) First-order structuring of the kinematic field relative to Eurasia in the North Aegean domain. The blue and red blocks denote slowly deforming areas. The size of curvature indicates the distance to the location of the Euler pole. The angular velocity is proportional to the angle of the circle sectors (blue: cw rotating, red: ccw rotating). The inset shows Euler poles (EP) belonging to blocks B1, B2, B3, B4 and B7 located in southern Italy and Albania. The Euler poles are listed in Table 4.2. The numbers along the NAT indicate the amount of strike-slip motion as derived in chapter 4.4.2. A: Athos peninsula, BP: Biga peninsula, Ch: Chalkidiki peninsula, E: Evia, GA: Gulf of Arta, GC: Gulf of Corinth, GE: Gulf of Evia, GF: Ganos fault, K: Kassandra peninsula, MyG: Mygdonian graben, NAT: North Aegean trough, P: Pelion, Pel: Peloponnesos, S: Sithonia peninsula, SaB: Saros basin, Sk: Skyros, SkB: Skyros Basin, SpB: Sporades basin, SpI: Sporades islands, SEF: Skyros-Edremit fault.

4.4.2 Slip rates and locking depths along the North Aegean trough

Description of the used model

The strain analysis conducted in chapter 5.3 revealed the NAT as a primary strike-slip structure although significant extensional components were derived along the Saros basin. In the following, strike-slip parameters of the NAT are analyzed from the Ganos fault to the Sporades islands. The investigation focuses on the locking depth and the slip rate of the NAT assuming that the fault is completely locked. The fault properties provide useful constraints in terms of seismic hazard assessment. The two-dimensional model of a buried screw dislocation in an elastic half-space was applied [*Weertman and Weertman, 1964; Savage and Burford, 1973*]. The model relates fault-parallel motion v_{par} at distance x from the fault to a constant fault motion v_0 , the difference in fault parallel motion across the fault v_1 and the fault's locking depth W (Fig 4.8). The shear strain

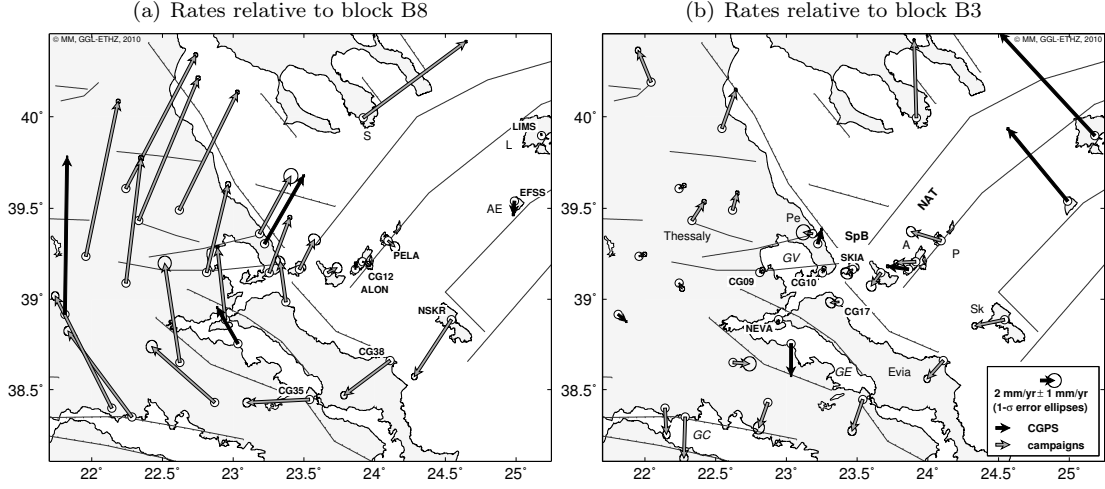


Figure 4.7: (a) Horizontal velocity field at the western termination of the NAT relative to block B8 (EP8: $\varphi_P=37.56^\circ\text{N}$, $\lambda_P=27.58^\circ\text{E}$, $\omega_P=3.56^\circ/\text{Myr}$) derived using the sites ALON, CG12, EFSS, LIMS, PELA (see chapter 4.3). (b) Horizontal velocity field relative to block B3 (EP3: $\varphi_P=-40.12^\circ\text{N}$, $\lambda_P=-159.56^\circ\text{E}$, $\omega_P=3.92^\circ/\text{Myr}$) derived by the sites CG09, CG10, CG17, NEVA and SKIA (see chapter 4.3). Scale and measuring type for (a) and (b) see inset in (b). A: Alonissos, AE: Agios Efstratios, GC: Gulf of Corinth, GE: Gulf of Evia, GV: Gulf of Volos, L: Limnos, P: Pelagonissi, Pe: Pelion, S: Sithonia peninsula, Sk: Skyros, SpB: Sporades basin.

rate $\dot{\epsilon}_{12}$ is analytically derived from v_{par} .

$$v_{par}(x) = v_0 + v_1 \cdot \left(\frac{1}{2} - \frac{1}{\pi} \arctan \left(\frac{x}{W} \right) \right) \quad (4.2)$$

$$\dot{\epsilon}_{12}(x) = \frac{1}{2} \frac{\partial v_{par}}{\partial x} = -\frac{v_1}{2\pi} \cdot \frac{W}{W^2 + x^2} \quad (4.3)$$

The fault characteristics were analyzed by depicting four profiles P1 to P4 as shown in Fig. 4.9 (a). The parameters for profile P1 were estimated using the GPS rates of *Straub et al.* [1997] (Fig. 4.9 (b)) whereas the ones for P2 to P4 were derived based on data obtained in this study. Fault characteristics of the Ganos segment of the NAF (P1) were formerly analyzed by *Motagh et al.* [2007] using a comparable approach.

There are enough sites to estimate the three model parameters for cross-sections over the Ganos

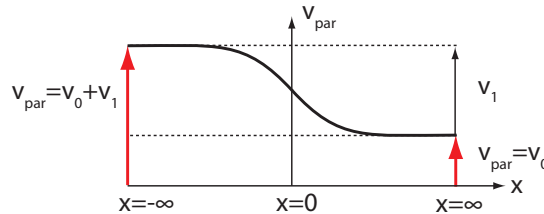


Figure 4.8: Parameters employed in Eq. (4.2) and (4.3). v_{par} denotes the fault-parallel velocity. v_0 is the fault-parallel velocity component which is assumed constant along the cross-section. v_1 is the difference in fault-parallel velocity across the fault. The fault is located at $x = 0$.

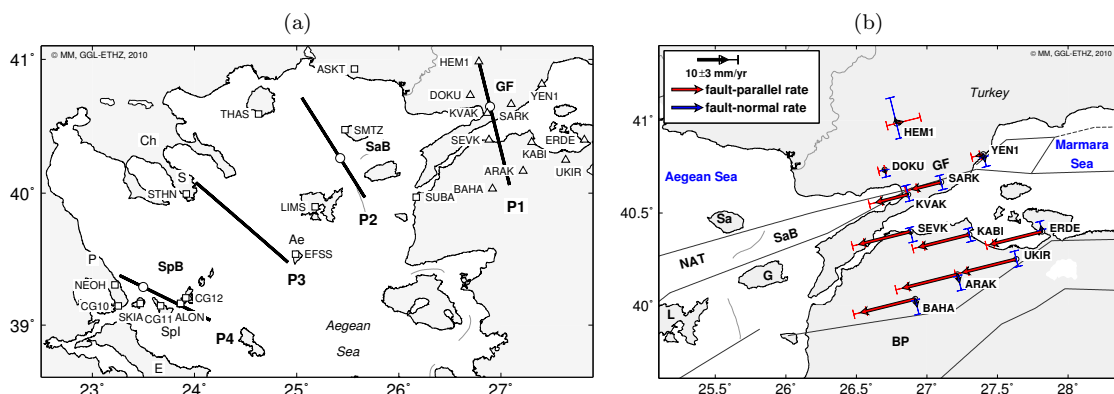


Figure 4.9: (a) Locations of the profiles across the NAT. Rates of sites depicted as squares are given in ITRF05. They were derived in this study, except for SUBA (data of *McClusky et al.* [2000]). Sites depicted as triangles originate from *Straub et al.* [1997]. Their respective velocities are given in ITRF94 relative to Istanbul. White circles indicate the assumed fault locations in cross-sections P1, P2 and P4. (b) GPS rates across the Ganos fault (data from *Straub et al.* [1997]). The rates are given relative to Istanbul. The error bars depict the 1- σ confidence interval. AE: Agios Efstratios, BP: Biga peninsula, Ch: Chalkidiki peninsula, E: Evia, GF: Ganos fault, G: Gökçeada, L: Limnos, NAT: North Aegean trough, P: Pelion, S: Sithonia Peninsula, Sa: Samothraki, SaB: Saros basin, SpB: Sporades basin, SpI: Sporades islands.

Profile	Slip v_1 [mm/yr]	Locking depth W [km]	WRMS [mm/yr]
P1	22.5 ± 6.7	8.9 ± 6.2	0.4
P2	21.2 ± 0.4	5.6 ± 0.8	0.4
P3	12.5 ± 0.2	n.a.	n.a.
P4	4.9 ± 1.0	17.7 ± 7.3	0.6

Table 4.3: Fault-parallel slip rates v_1 and locking depths W at the defined cross-sections along the NAT. The standard deviations are derived by a sensitivity analysis. The weighted root mean squares (WRMS) indicate the quality of the fit.

fault (P1), between Limnos and Samothraki (P2) and between the Sporades islands and Pelion (P4). For profile P3 located between Agios Efstratios and Sithonia only a slip rate was estimated as there are only three sites located near this profile. The fault-parallel velocities used in profiles P2 - P4 are the tangential velocity components referring to a small circle centered at 37.56°N , 27.58°E corresponding to the location of Euler pole B8 (see Table 4.2). The velocities of EFSS and LIMS were employed for both profiles P2 and P3.

The fault location ($x = 0$) was only estimated for profile P1. For profile P2 the fault location was defined by considering that strike-slip motion is attributed to faults in the north of the Saros basin [*Yaltirak and Alpar*, 2002; *Karabulut et al.*, 2006]. For profile P4 it was set according to seismicity and GPS velocities. The parameters were obtained by solving the global optimization problem by applying a simulated annealing algorithm. Standard deviations of the estimated parameters were derived numerically by a sensitivity analysis (appendix F.1). The results for profiles P1, P2 and P4 are shown in Figures 4.10 (a)-(f) and listed in Table 4.3.

The results reveal the following: Maximum shear strain rates between 400 and 600 nstrain/yr are derived for profiles P1 and P2. Maximum shear strain rates for profile P4 do not exceed 50 nstrain/yr (Fig. 4.10 (d)-(f)). The Saros segment of the NAT (profile P2) shows similar strike-slip motion as the Ganos fault (profile P1) in the order of 21 mm/yr. Fault coupling on P2 is slightly weaker than on P1 (P1: $W=8.9\pm 6.2$ km, P2: $W=5.6\pm 0.8$ km). For P3 a differential fault parallel motion of 12.5 mm/yr is derived from rates of the sites STHN, LIMS and EFSS between

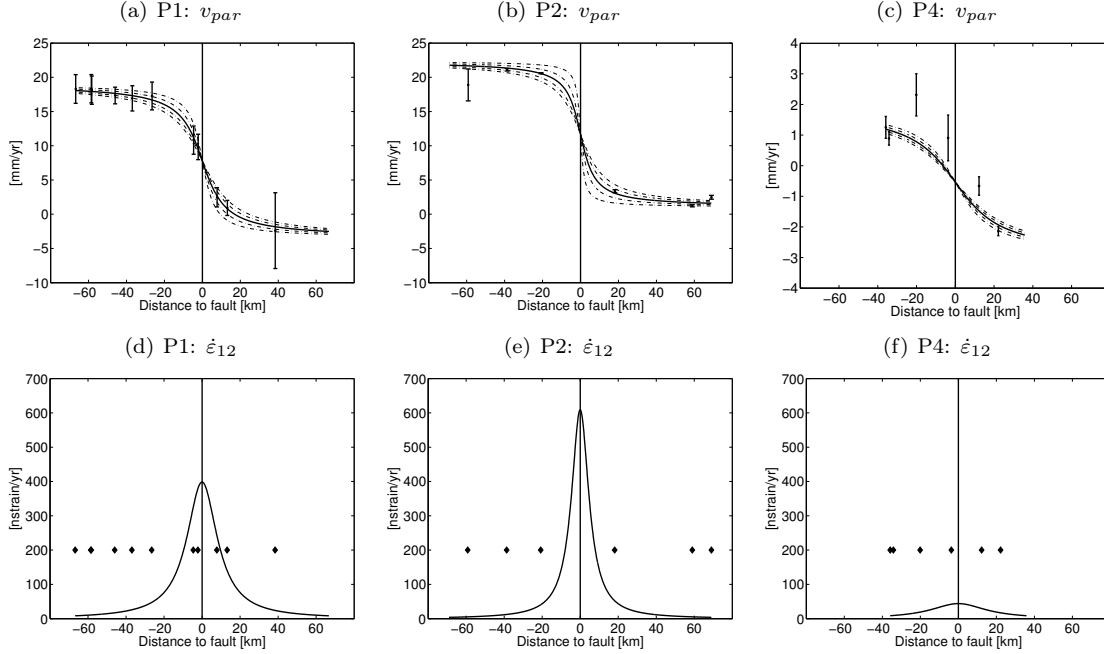


Figure 4.10: Fault parallel rates v_{par} across (a) profile P1 (Ganos segment of the NAF), (b) profile P2 (Agios Efstratios - northeastern Greece) and (c) profile P4 (Sporades islands - Pelion). Additionally, the figures show the rates along the cross-sections for the same velocity difference but varying locking depths (step size 2 km). The accuracy of the GPS rates is indicated by the 1- σ confidence interval. Note the different scale in Figure (c) compared to Figures (a) and (b). Shear strain rate $\dot{\epsilon}_{12}$ (d) across profile P1, (e) profile P2 and (f) profile P4. The black diamonds indicate the GPS site locations along the cross-sections.

Agios Efstratios and Sithonia. Further southwest at profile P4 the NAT terminates where the kinematic field merges into the rotational velocity field of Thessaly/Central Greece. To obtain a reasonable value for shear deformation this rotation (described by block B3, 3.9 mm/yr velocity difference between sites NEOH and ALON) has to be subtracted from the site velocities relative to Eurasia. The resulting parameter v_1 is 4.9 ± 1.0 mm/yr, and the corresponding locking depth W is 17.7 ± 7.2 km. The analytical model does not reveal concentrated strike-slip deformation towards Northern Evia for Profile P4 but rather diffuse shear strain extending over a width of 40–60 km. Moving the fault location about 10 km towards NW along profile P4 would lead to almost no coupling and to a reduction of the fault-parallel velocity difference to 3.1 mm/yr. The values for slip across profiles P3 and P4 amounting to 12.5 mm/yr and 4.9 mm/yr, respectively, agree well with the NE-SW extension indicated by the rates of sites STHN and NEOH (~ 6.5 mm/yr).

The derived locking depths are in agreement with the predominant depths of earthquakes in the North Aegean sea which are reported to be shallow (< 15 km) (Hatzfeld *et al.* [1999]; Kiratzi [2002]; see also Fig. 4.11). Karabulut *et al.* [2006] investigated the 2003 Mw 5.7 Saros earthquake sequence which consisted of strike-slip events. The slip patch of the main event is located in a depth between 15 and 20 km.

High values of heat flow (> 100 mWm $^{-2}$) are observed between the Saros and Sporades basins [Fytikas and Kolios, 1979]. This could be an indication for a weaker crust in that area compared to the west and east and be a reason for the shallow locking depth along the Saros basin.

Locking depths W and fault slip rates v_1 have been estimated across several cross-sections along the North Anatolian fault (NAF) (e.g., Wright *et al.* [2001]; Meade *et al.* [2002]; Motagh *et al.* [2007]; Walters *et al.* [2011]). The parameter v_1 was found to be approximately constant from

east to west (20–26 mm/yr), while W varies between 6 and 25 km. This means that the NAT is kinematically a continuation of the NAF up to the peninsula of Chalkidiki. Further southwest the NAT bends and NW-SE trending normal faults between the Chalkidiki peninsula and Pelion likely reduce right-lateral strike-slip motion on NE-SW trending faults along the Sporades basin.

Seismic hazard is high along the NAT. *Jenny et al.* [2004] expect a Mw 7.2–7.7 event every 100–500 years in the North Aegean domain. *Papanikolaou and Papanikolaou* [2007] estimate the maximum earthquake size for the southern marginal fault of the Sporades basin between Mw 7.1 and Mw 7.6 depending on the rupture length.

The application of the model of a buried screw dislocation in an elastic half-space yields changing slip rates along the NAT. Accordingly, rates of strain accumulation for strike-slip earthquakes are not constant along the NAT in case the fault is completely locked. The seismic moment is calculated by $M = \mu \cdot W \cdot L \cdot u$ where μ is the rigidity, W is the locking depth, L is the rupture length and u is the average displacement. Both parameters u and L depend on v_1 if assuming the rupture length L equal the surface rupture length L_S and implying the empirical relationship $\log u = -1.43 + 0.88 \cdot \log L_S$ [*Wells and Coppersmith*, 1994]. Therefore, the accumulated seismic moment M increases more rapidly with time in the east of the NAT than in the west (about factor 6 if μ is kept constant). The Saros-Marmara earthquake in 1912 had a magnitude M 7.4 [*Ambraseys and Finkel*, 1987]. The estimated fault parameters for profile P1 yield a comparable magnitude for a 146 year period (time since the preceding major earthquake in 1766) and a rigidity μ of 28 GPa. *Janssen et al.* [2009] concluded based on a study of low-magnitude seismicity that the eastern part of the Ganos fault is partly creeping. The creep rate remains to be quantified. Two large strike-slip earthquakes occurred on the NE-SW trending fault along the Sporades basin between profiles P2 and P3 in 1982 (Mw 6.5) and 1983 (Mw 6.7) [*Taymaz et al.*, 1991; *Kiratzi and Louvari*, 2003]. A time period of 87–120 years is required to produce a Mw 6.7 event in case the fault is fully locked and aseismic deformation is negligible (slip: 12.5 mm/yr, W : 5–10 km).

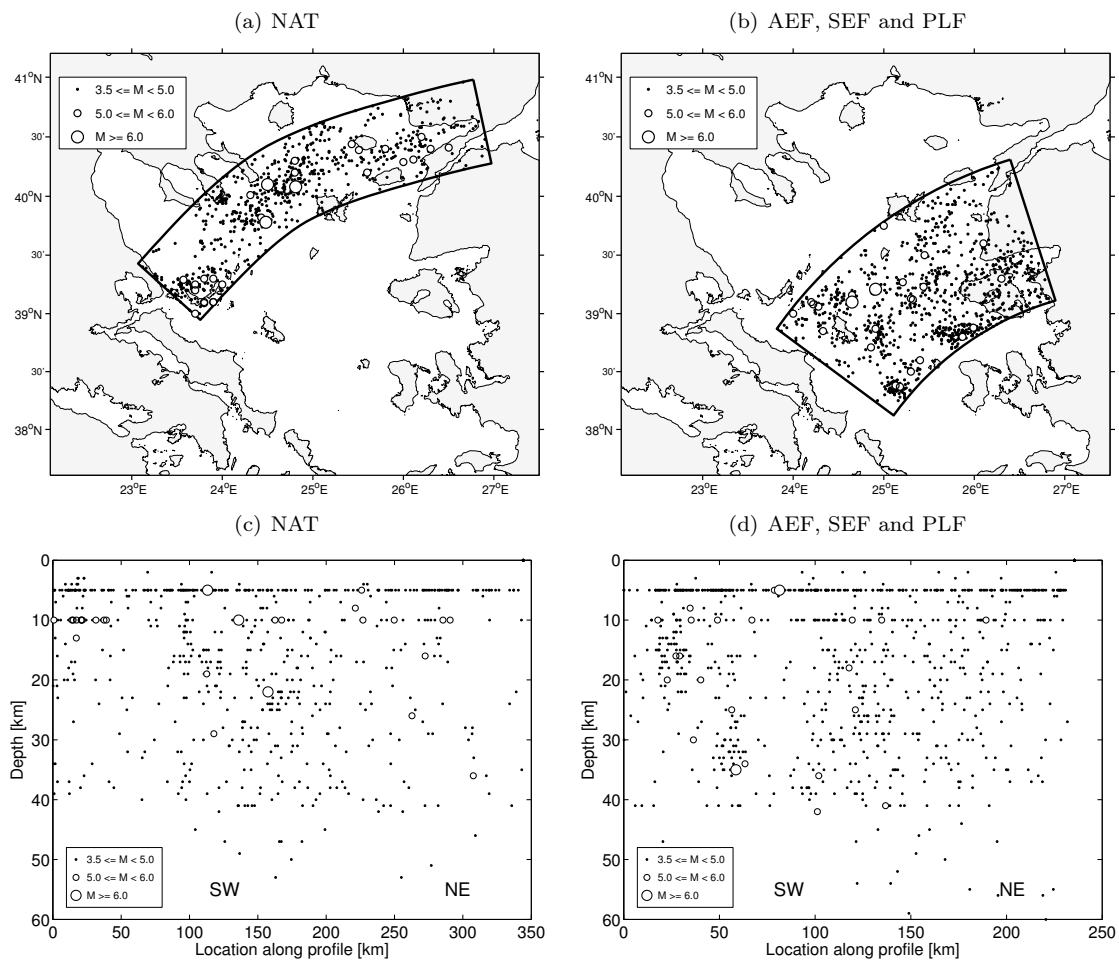


Figure 4.11: Seismicity ($M \geq 3.5$) according to the revised earthquake catalog published by the National Observatory of Athens [Papanastassiou *et al.*, 2001] in the area of the major NE-SW trending structures of the North Aegean domain for the period 1950–2000. (a) Selected earthquakes located close to the North Aegean trough. (b) Selected earthquakes located close to the Agios Efstratios fault (AEF), the Skyros-Edremit fault (SEF) and the Psara-Lesvos fault (PLF). (c) Focal depths of selected earthquakes located close to the NAT. (d) Focal depths of selected earthquakes located close to the AEF, SEF and PLF.

4.5 Kinematics along the Hellenic trench system

4.5.1 Ionian islands, Western Greece and NW Peloponnesos

The region comprising the Ionian islands, southwestern mainland Greece and the NW Peloponnesos exhibits distinct kinematic patterns (Fig. 4.12 (a)). The Kefalonia fault zone (KFZ), a dextral strike-slip fault, separates two tectonic regimes: little convergence between the Apulian domain and Greece/Albania in the north and rapid subduction associated with rollback of the Nubian slab in the south. Rates on Paxi, located north of the KFZ, deviate only by 3 mm/yr from Eurasian and Nubian plate motion, respectively (Nubian plate motion defined by an Euler pole derived by *Altamimi et al.* [2007]; see appendix B.2). The Kefalonia fault zone is the major structure accommodating shear strain rates of up to 200 nstrain/yr (chapter 5.3). Only small fault-perpendicular velocity components remain when transforming the velocities of sites on Kefalonia and Lefkada in a Nubian fixed frame (v_p below $|4 \text{ mm/yr}|$ and $|2 \text{ mm/yr}|$ for sites on Lefkada and Kefalonia, respectively, when assuming a fault azimuth of 200° ; see Fig. 4.12 (c)). It can be surmised from this observation that the location of the KFZ moves concurrently with the Nubian plate and is not stable with respect to Eurasia.

The GPS rates in the Nubian fixed frame on Lefkada and Kefalonia clearly indicate plate coupling along the KFZ. Fault-parallel and fault-perpendicular rates with respect to a straight fault and a segmented fault were analyzed (Fig. 4.13). Fault-parallel rates NW of the KFZ are not precisely known and approximated by the rates encountered on Paxi. The fit of the fault-parallel rates with the velocity profile expected for a locked transform fault [*Savage and Burford, 1973*] is better when taking into account the different orientations of the Lefkada and Kefalonia segments of the KFZ. This corroborates results of previous studies where the fault orientation of the KFZ was analyzed by means of focal mechanisms [*Lowari et al., 1999; Benetatos et al., 2005*]. Fault-slip and locking depth amount to $19.2 \pm 0.7 \text{ mm/yr}$ and $10.8 \pm 0.9 \text{ km}$, respectively, for the segmented fault (Table 4.4). Correspondingly, maximum shear strain rates are in the order of 280 nstrain/yr. GPS derived fault-parallel rates of sites VASI and 1KVL both located on Lefkada are clearly larger than the modeled rates with respect to a segmented fault. This might imply weaker coupling on the Lefkada segment than on the Kefalonia segment or a more north directed Lefkada segment.

Earthquakes with $M_w \geq 6$ produced slip between 1.3–1.7 m on the Lefkada segment since 1869 corresponding to slip rates of 9.8–12.8 mm/yr (depending on the used scaling relations [*Mai and Beroza, 2000; Wells and Coppersmith, 1994*] and the assumption that the 1948 earthquakes ruptured different fault segments). However, the comparison of the geodetic results with seismicity is difficult due to the unknown amount of slip produced by earthquakes with magnitude $M_w < 6$. Furthermore, *Benetatos et al.* [2007] modeled slip corresponding to the 2003 $M_w 6.2$ Lefkada earthquake at a depth of 10–25 km.

E-W to ENE-WSW compression and right-lateral shear strain is observed between Kefalonia and NW Peloponnesos (see chapter 5.3). In NW Peloponnesos, GPS velocities deviate only by 3 mm/yr from Peloponnesos block motion described by block B5 (Fig. 4.12 (b)). The 2001 $M_w 6.4$ NW Peloponnesos earthquake (chapter 6.5.4) was located in this region which primarily exhibits strike-slip faulting [*Kiratzi and Lowari, 2003*]. Directions of site velocities relative to Nubia slightly change from Kefalonia (GERO: 203° , VLMS: 194°) to Zakynthos (SKIN: 202° , KERI: 213°) and SW Peloponnesos (AETO, ZAHA, XRIS, GERM: 212° – 215°). The corresponding rates increase from north to south: VLMS: 15.8 mm/yr, KERI: 23.4 mm/yr, XRIS: 34.4 mm/yr. Rates of sites on Zakynthos suggest clockwise rotation of $11 \pm 1^\circ/\text{Myr}$. Shear strain rates do not exceed 50 nstrain/yr between southeastern Kefalonia and southern Zakynthos.

Large-scale clockwise rotation on mainland Greece is transformed into southwestward motion within a zone reaching from the Gulf of Arta to the Gulf of Corinth. The Katouna fault is

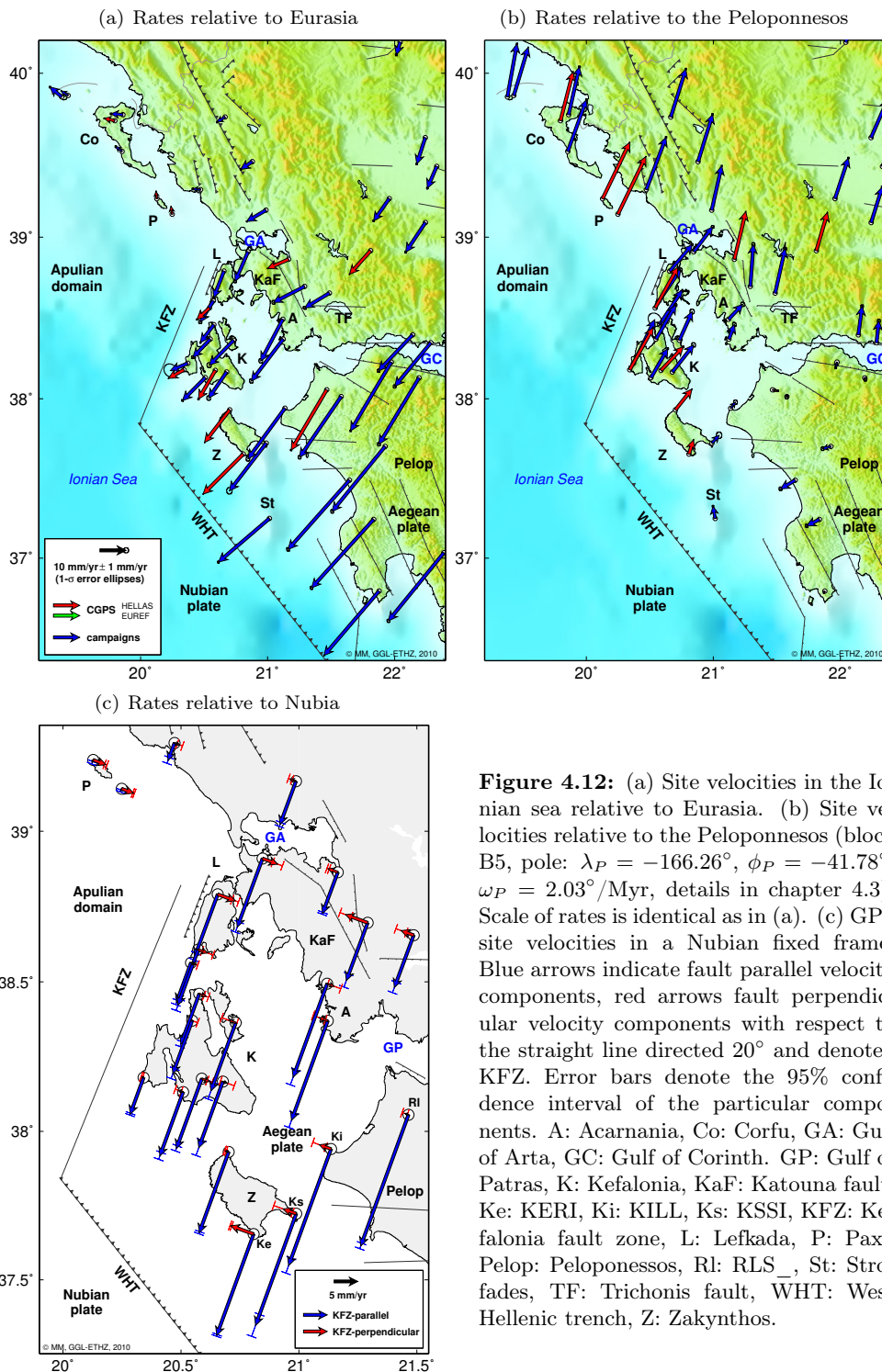


Figure 4.12: (a) Site velocities in the Ionian sea relative to Eurasia. (b) Site velocities relative to the Peloponnesos (block B5, pole: $\lambda_P = -166.26^\circ$, $\phi_P = -41.78^\circ$, $\omega_P = 2.03^\circ/\text{Myr}$, details in chapter 4.3). Scale of rates is identical as in (a). (c) GPS site velocities in a Nubian fixed frame. Blue arrows indicate fault parallel velocity components, red arrows fault perpendicular velocity components with respect to the straight line directed 20° and denoted KFZ. Error bars denote the 95% confidence interval of the particular components. A: Acarnania, Co: Corfu, GA: Gulf of Arta, GC: Gulf of Corinth. GP: Gulf of Patras, K: Kefalonia, KaF: Katouna fault, Ke: KERI, Ki: KILL, Ks: KSSI, KFZ: Kefalonia fault zone, L: Lefkada, P: Paxi, Pelop: Peloponnesos, Rl: RLS_, St: Strofadis, TF: Trichonis fault, WHT: West Hellenic trench, Z: Zakynthos.

most likely the western limit of the rotational domain of mainland Greece. GPS rates indicate distinct left-lateral and extensional motion on the Katouna fault. Previously, the Katouna fault was identified as a horst-graben structure [Haslinger *et al.*, 1999] which probably links the Gulf of Arta and the Trichonis lake by left-lateral strike-slip motion [Brooks *et al.*, 1988]. There are no

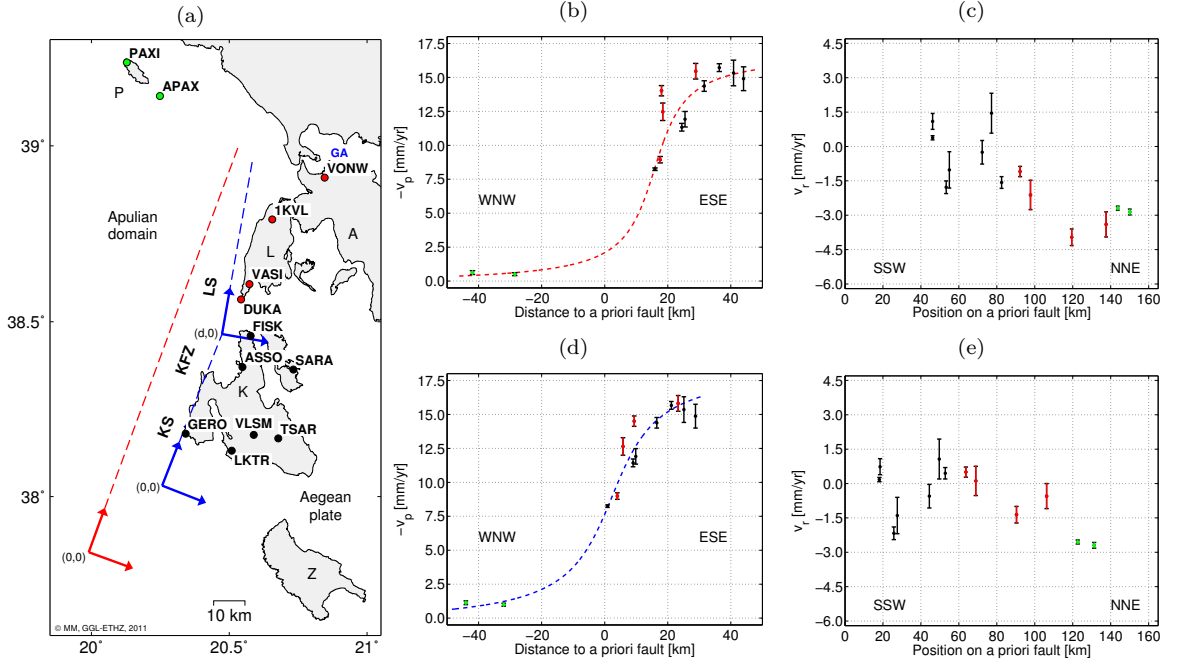


Figure 4.13: Analysis of GPS rates along the KFZ with respect to a Nubian fixed frame. Rates of sites on Lefkada/Acarmania are colored red, those on Kefalonia black and those on Paxi green. (a) A priori locations of the faults. The red dashed line depicts a fault directed 20° , the blue dashed line depicts a segmented fault directed 21.4° and 9.9° , respectively. The sites on Kefalonia (except FISK) are associated with the Kefalonia segment and the sites on Paxi and Lefkada plus site FISK are associated with the Lefkada segment. A: Acarmania, GA: Gulf of Arta, K: Kefalonia, KFZ: Kefalonia fault zone, KS: Kefalonia segment, L: Lefkada, LS: Lefkada Segment, P: Paxi, Z: Zakynthos. (b) Fault-parallel rates with respect to the straight a priori fault. The dotted line denotes the velocity trend for a locked fault. Its parameters are listed in Table 4.4. The accuracy of the GPS rates is indicated by the $1\text{-}\sigma$ confidence interval. (c) Fault-perpendicular rates with respect to the straight a priori fault. (d) Fault-parallel rates with respect to the segmented a priori fault. (e) Fault-perpendicular rates with respect to the segmented a priori fault.

Model	v_1 [mm/yr]	W [km]	dx [km]	$WRMS$ [mm/yr]
Straight fault	17.1 ± 1.6	7.4 ± 2.9	15.8 ± 0.6	0.8
Segmented fault	19.2 ± 0.7	10.8 ± 0.9	2.3 ± 0.4	0.5

Table 4.4: Parameters of the dislocation model applied to the KFZ. The model corresponds to Eq. (4.2) except that the fault location ($x = 0$) was estimated. The corresponding velocity profiles are depicted in Figure 4.13. v_1 denotes the fault-parallel slip rate, W denotes the locking depth and dx denotes the distance between the estimated fault location and its a priori location (positive towards ESE). $WRMS$ denotes the weighted root mean square based on the residuals between the model and the GPS rates. The calculation of standard deviations of the parameters is described in appendix F.1.

GPS sites revealing the kinematic field in the area between the Trichonis graben and the Gulf of Corinth. *Kiratzis et al.* [2008] describes a NW-SE oriented left-lateral shear zone connecting the extensional structures of the Trichonis and Corinth grabens.

GPS derived strain rates indicate predominantly E-W compression between the central Ionian islands and NW Peloponnesos (chapter 5.3). This could be related to strain accumulation related to subduction of the Nubian slab. *Laigle et al.* [2002] located the gently dipping ($\sim 3^\circ$) interplate boundary 10 km west of Zakynthos at a depth of 10–13 km. The authors argue for a completely

locked subduction interface west of Zakynthos (width ~ 50 km). Trenchward components of rates of sites RLS_, KILL, KSSI and KERI plus the vertical rate of KERI were used to determine the parameters of a dislocation model describing strain accumulation at subduction zones [Savage, 1983] (description in appendix F.2). The two-dimensional modeling and the ill-defined problem (five observations, six model parameters) are suboptimal. Nonetheless, the modeling can show if the measurements generally agree with a locked plate interface. Two model version were considered: In version A site velocities are projected to direction 225° and in version B the magnitudes of the rates are used. The minimum of the objective function $\mathbf{p}^T \cdot (\mathbf{l} - \mathbf{f})^2$ was searched by a simulated annealing algorithm (\mathbf{p} denotes the weights of the measurements; \mathbf{f} is based on Eq. (F.2) and (F.3)). The minimum of the objective function is not distinct leading to considerable variation in the obtained parameter sets. Large correlations exist between several model parameters (e.g., between the downwidth s and the position c along the profile of the locked plate interface). Figure 4.14 shows the trench-perpendicular, the vertical velocity components and the corresponding locked plate interface for numerous parameter sets of model versions A and B. The location and width of the locked plate interface corresponding to the parameters providing the best fit for the two model versions are very similar. The optimal parameters for version A are $s = 113.5$ km, $s_1 = 61.1$ km, $c = 43.6$ km $\alpha = 9.6^\circ$, $b = 17.9$ mm/yr and $u_0 = 28.5$ mm/yr and those for version B are $s = 163.1$ km, $s_1 = 111.1$ km, $c = 91.1$ km, $\alpha = 6.3^\circ$, $b = 20.3$ mm/yr and $u_0 = 29.5$ mm/yr. Both model versions indicate maximum vertical rates between Zakynthos and western Peloponnesos. GPS derived vertical rates in this area would improve the significance of the model results. The optimal parameter sets suggest a depth of the plate interface between 10 and 19 km. Moreover, the eastern termination of the locked plate interface seems to be located between Zakynthos and western Peloponnesos. *Serpetsidaki et al.* [2010] located the largest events of the 2006 earthquake series SE of Zakynthos at a depth of 13 km (cmp. chapter 6.5.3). They interpreted the earthquakes to be events on the plate interface which they assumed 2–5 km above the location revealed by the dislocation models. GPS rates in combination with this model approach do not rule out a locked subduction interface near Zakynthos as outlined by *Laigle et al.* [2002]. However, the derived rates of strain accumulation related to a locked plate interface have to be interpreted as an upper bound. A part of differential motion indicated by the used sites is most likely attributed to shear strain rates [Kiratzi and Louvari, 2003].

In summary, the main features of the kinematic field in western Greece are pronounced NNE-SSW extension and left-lateral shear strain between the Gulfs of Arta and Corinth along the Katouna and Trichonis faults, distinct right-lateral shear strain along the KFZ, E-W to ENE-WSW compression and right-lateral shear strain between Kefalonia and NW Peloponnesos and dextral shear strain and cw rotation between Kefalonia and Zakynthos. A locked subduction interface east of Zakynthos cannot be ruled out based on geodetic estimates.

4.5.2 Southern Peloponnesos and South Aegean sea

The Peloponnesos and the southwestern Aegean sea move quite coherently as two quasi-rigid blocks south-southwestward towards the Hellenic trench as already stated in previous work (e.g., *McClusky et al.* [2000]). Peloponnese block motion (block B5) predicts slightly larger westward rates at the southern Peloponnesos than block B6 describing the southwestern Aegean sea (Fig. 4.15, chapter 4.3). This points to arc-parallel extension in this section of the West Hellenic arc as indicated by *Hollenstein et al.* [2008a]. GPS sites AETO, SRTA and STRV indicate E-W extension across N-S trending normal faults in the southwest of the Peloponnesos. Baseline lengthening between AETO and SRTA is 2.4 ± 0.8 mm/yr and between AETO and STRV 4.0 ± 0.7 mm/yr, respectively. These N-S trending fault structures were seismically active in the past and likely accommodated earthquakes of magnitude Ms 7.2 [*Lyon-Caen et al.*, 1988; *Armijo et al.*, 1991]. Rates of sites DOXA and ZAHA which are located north of AETO may include some systematic parts (see Fig. 3.19) whereby the extent of extensional processes is not completely evident. In contrast to

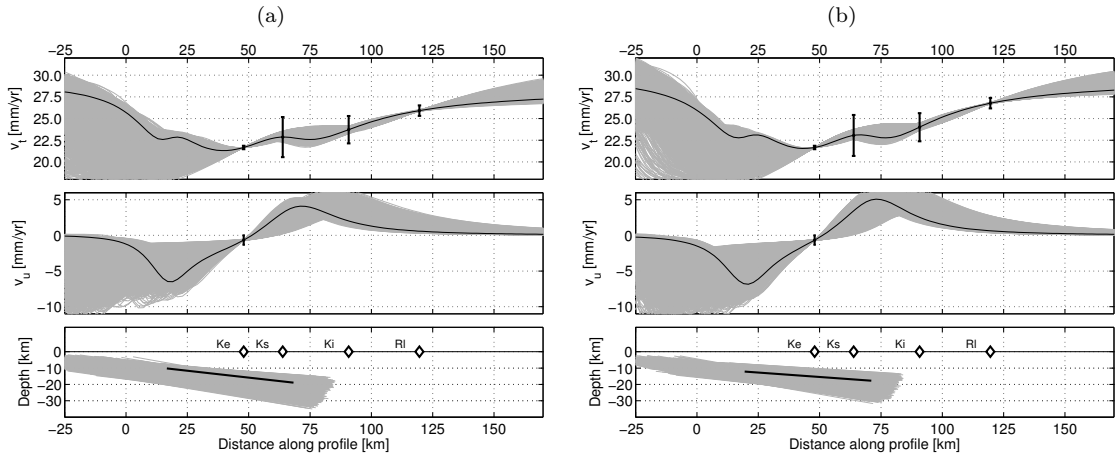


Figure 4.14: Dislocation model for a locked subduction interface near Zakynthos. The black lines correspond to the model parameters providing the best fit. The gray lines correspond to the first 80% of the parameter sets sorted in order of the resulting fit. (a) Site velocities projected to direction 225° . Optimal parameters: $s = 113$ km, $s1 = 61$ km, $\alpha = 9.6^\circ$ and $b = 17.9$ mm/yr (meaning of parameters: appendix F.2.) (b) Absolute value of site velocities. Optimal parameters: $s = 163$ km, $s1 = 111$ km, $\alpha = 6.3^\circ$ and $b = 20.3$ mm/yr. Ke: KERI, Ks: KSSI, Ki: KILL, Rl: RLS_ (see Figure 4.12 (c) for site locations). v_t : trenchward velocity, v_u : vertical component of the velocity. The accuracy of the rates is indicated by the 95% confidence interval.

extensional processes in the North velocities of sites located in southern Peloponnesos (GERM, XRIS) fit well to the Peloponnesse block motion (chapter 4.3).

Rates of GPS sites in the Southeast Aegean sea deviate from the Southwest Aegean block (B6) motion by about 6–10 mm/yr. Their relative direction is to the southeast (Fig. 4.15 (a)). This motion is nearly perpendicular to the Pliny trench. The residuals of the rates of the site on Kastelorizo (KSZO) with respect to block B11 indicate left-lateral strike-slip and plate convergence of 3.4 and 3.5 mm/yr, respectively, on the Pliny trench near Rhodes. The Euler pole of block B11 is similar within the 1σ confidence interval to the one derived for southwestern Anatolia estimated by *Reilinger et al.* [2006].

Pronounced NNW-SSE extension of 150 nstrain/yr takes place between the islands of Kos and Nisyros (Fig. 5.6). Nisyros island is an active volcano of the South Aegean volcanic arc (Fig. 2.2). A period of seismic unrest was observed between 1996–1998 possibly related to the inflation of a magma chamber [*Sachpazi et al.*, 2002]. Uplift between 1995 and mid 1998 and consecutive subsidence till 2000 (both in the order of a few centimeters) were revealed by *Sykioti et al.* [2003] and *Lagios et al.* [2005] using DinSAR. The CGPS site on Nisyros indicates subsidence of 7.4 ± 0.5 mm/yr in the measuring period 2002–2008. The derived vertical rate and the horizontal rates do probably not correspond to the long-term rates. The continuation of the monitoring will reveal more details concerning the relation between volcanic activity and deformation.

GPS sites on Santorini (THIR) and Astipalea (ASTP) deviate by 4–5 mm/yr from the southwest Aegean block (B6) motion (Fig. 4.15). *Bohnhoff et al.* [2006] report clusters of microseismicity between Santorini and Amorgos and interpret these features as related to volcanic activity. At least one large extensional earthquake is reported in this area. The 1956 Mw 7.6 earthquake at the southwestern tip of the island of Amorgos (strike: 39° , dip: 58° , rake: -88°) [*Okal et al.*, 2009] is in agreement with the present-day interseismic velocities on Mykonos, Astipalea and Santorini. Though, the cause for 4.5 mm/yr compression between Santorini and northern Crete remains unclear. Local deformation processes cannot be excluded. *Stiros et al.* [2010] observed baseline lengthening (~ 10 cm) between the island of Nea Kammeni (the center of the caldera of the Santorini

volcano) and the island of Therasia (located 4–5 km to the NW) in the time period 1994–2000 using electronic distance meter measurements.

The GPS data reveals arc-parallel extension between the southern tip of the Peloponnese and the island of Kythera and between eastern Crete and the islands of Karpathos and Rhodes (80 nstrain/yr and 90 nstrain/yr, respectively (Fig. 4.15 (b)); cmp. *Hollenstein 2006; Hollenstein et al. 2008a*). The GPS derived arc-parallel lengthening rate is below 2.5 mm/yr between Kythera (KITH) and eastern Crete (ZAKR). Seismicity studies concur with geodetic results. They revealed arc-parallel extension in the Aegean plate (depth < 20 km) in western Crete and between eastern Crete and Karpathos [*Benetatos et al., 2004; Bohnhoff et al., 2005*]. *Caputo et al. [2010]* recently estimated based on structural investigations a minimum average WNW-ESE surface lengthening-rate of 2.2 mm/yr across the island of Crete during the last 13 kyr. This is comparable with present-day geodetic data.

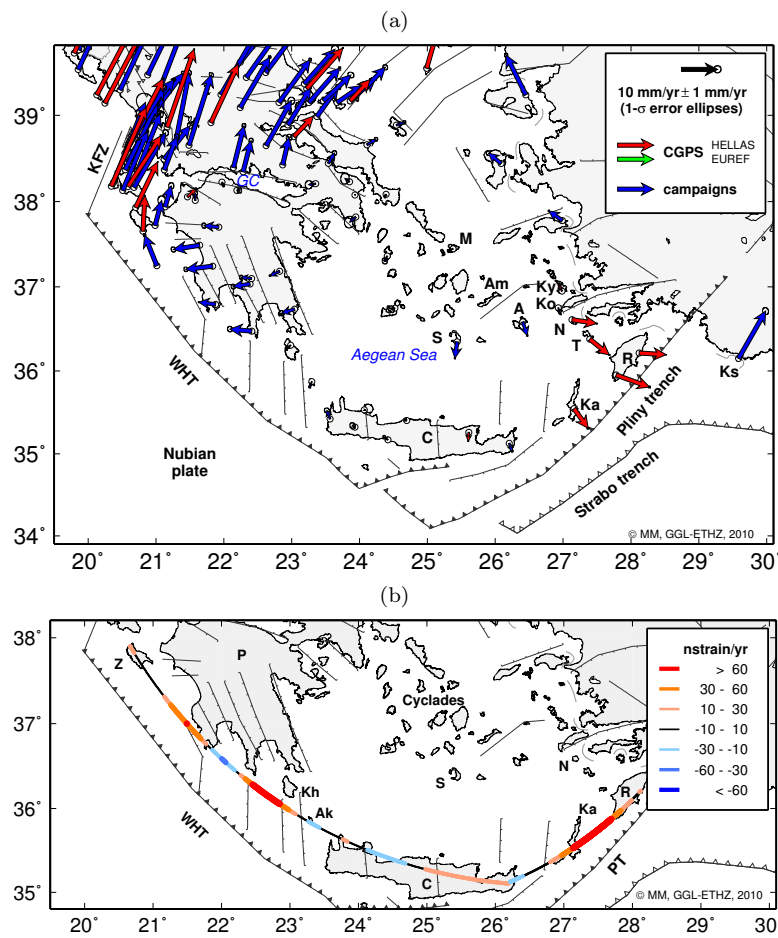


Figure 4.15: (a) Site velocities relative to the southern Aegean sea (block B6, pole: $\lambda_P = 125.55^\circ\text{E}$, $\phi_P = -44.00^\circ\text{N}$, $\omega_P = 0.33^\circ/\text{Myr}$, details in chapter 4.3). (b) Arc-parallel extension/compression along two small circles [C1: center: 26.78°E , 40.48°N ; C2: 24.04°E , 39.09°N]. The small circle C1 optimally fits the GPS sites closest to the West Hellenic arc. The small circle C2 optimally fits the GPS sites closest to the Pliny trench. The strain rates are identical to those in Fig. 5.2. Red colors denote extension and blue colors denote compression. A: Astipalea; Ak: Antikythera, Am: Amorgos, C: Crete; Ka: Karpathos; Ko: Kos; Kh: Kythera, Ky: Kalymnos; Ks: Kastelorizo; M: Mykonos, N: Nisyros; P: Peloponnese, PT: Pliny trench, R: Rhodes, S: Santorini; T: Tilos. GA: Gulf of Corinth. KFZ: Kefalonia fault zone, WHT: West Hellenic trench, Z: Zakinthos.

4.6 Vertical motion in Greece

Vertical rates with respect to IGS05 are interpreted for CGPS sites with a data record longer than four years and for the sites AUT1 and NEOH. The accurate estimation of vertical rates is challenging. The scattering in the vertical component of the position estimates amounts to 4–6 mm on average. Events such as antenna changes or instrument malfunctions leading to data gaps reduce the achievable accuracy. In addition, the rates depend on the strategy how the network is aligned to IGS05 (chapter 3.3) and on the mode of velocity estimation (chapter 3.4). The RMS of the difference between vertical rates indicated by IGS05 (IGS09P06.snx) and derived by this processing is 0.83 mm/yr. The mean difference is -0.21 mm/yr, the median -0.28 mm/yr. The alignment of a regional network to an ITRF and accompanying the accuracy of vertical rates may be enhanced by using globally distributed reference sites [Legrand *et al.*, 2010]. This matter, not analyzed in this thesis, has to be examined in the future.

Figure 4.16 shows vertical rates obtained for sites in Europe. The largest vertical rates are found in Scandinavia (3.7–8.2 mm/yr) most likely related to postglacial rebound. Uplift is also observed in the central Alps though at smaller rates (2.1–2.5 mm/yr). Rates are either smaller or less coherent in other regions.

The obtained vertical rates for Greece are in the range -1 to 2 mm/yr (Fig. 4.17). The significance of the results allows only the formulation of trends. Moderate uplift rates are observed at sites located on the South Aegean islands amounting to 0.3–1.9 mm/yr. Sites in southern F.Y.R.O.M. (ORID) and on mainland Greece (ARSA, DION, KAST, KARP) indicate uplift of about 1.5 mm/yr. Vertical motion on the Ionian islands varies between -1 and 0.5 mm/yr. The distinct velocity difference between the northern and central Ionian islands described by *Hollenstein et al.* [2008a] is not evidenced in the extended data set used in this thesis. Vertical rates are below |0.7 mm/yr| in the North Aegean sea. Significant subsidence of 7.4 mm/yr is observed at site NISI on Nisyros between October 2002 and October 2008. It is tempting to relate this observation to the active volcano on Nisyros but has to be further investigated.

The derived results are not finally conclusive for assessing the vertical motion in Greece. This is mainly due to the small signals, but also to the uneven and sparse coverage of CGPS sites. No vertical rates are available for many regions such as the Peloponnesos and the central Aegean sea. Isolated observations are difficult to interpret in terms of tectonics as processes such as e.g. faulting may cause rather local vertical signals. Relative vertical rates between closely located sites are most accurate since errors of the reference frame and of the alignment of the regional network to the ITRF are negligible. GPS derived vertical motions represent present-day interseismic velocities which do not have to agree with long-term geological rates. Anyhow, the results yield some few constraints on present-day tectonic processes such as e.g. strain accumulation near faults (chapter 4.5.1) or isostatic adjustment. Further efforts are necessary to enhance the accuracy of CGPS height estimates and to achieve a spatial densification of vertical rates derived by geodetic methods in general (CGPS, leveling, InSAR).

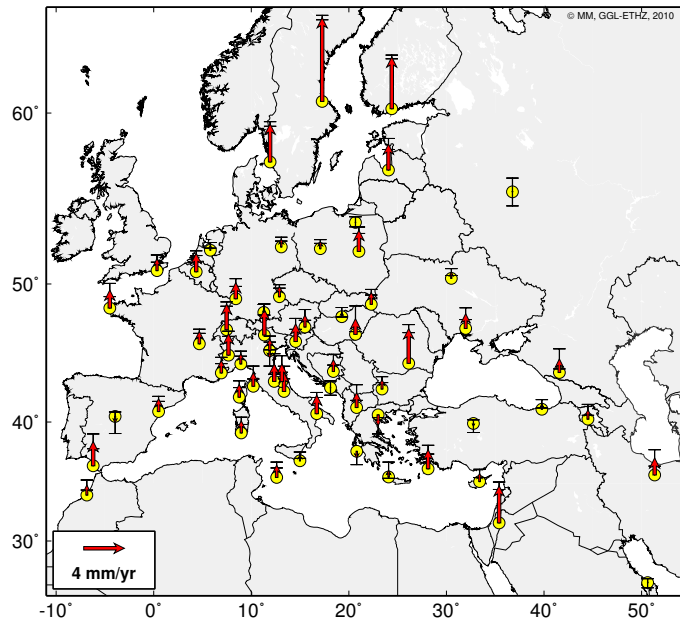


Figure 4.16: Vertical rates of sites in Europe, North Africa and the Middle East with respect to IGS05. The accuracy of the vertical rates is indicated by the 95% confidence interval. Vertical rates are shown only for sites with time series longer than 4 years.

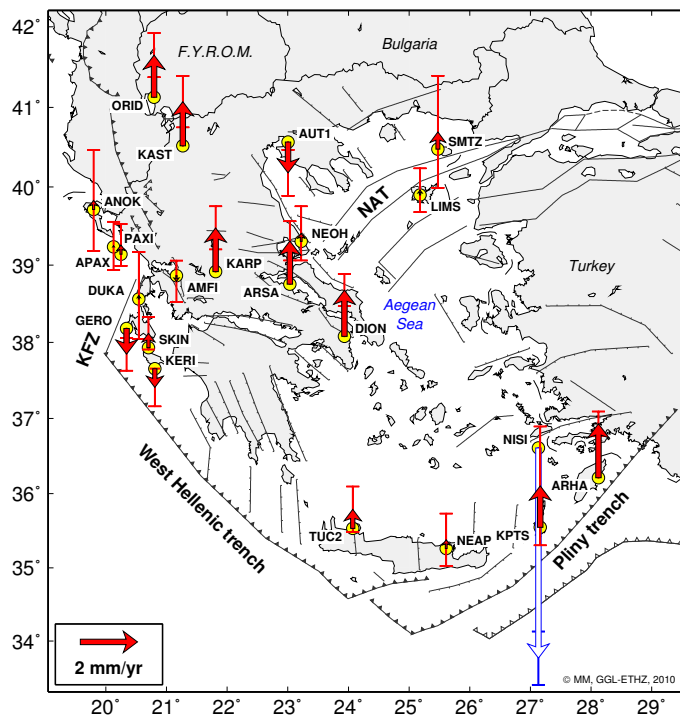


Figure 4.17: Vertical rates of CGPS sites in Greece with respect to IGS05. The vertical motion of site NISI is depicted by a blue arrow because changes in rates were reported on the island of Nisyros in the period 1995–2000. The accuracy of the vertical rates is indicated by the 95% confidence interval. Vertical rates are shown only for sites with time series longer than 4 years and for sites AUT1 and NEOH. KFZ: Kefalonia fault zone, NAT: North Aegean trough.

4.7 Concluding remarks

The derived kinematic field reveals new aspects and refinements of present-day crustal motion in Greece. It was analyzed in terms of kinematic block modeling and the application of dislocation models. In summary, the most important findings are the following.

- Northwestern and central Greece rotate rather coherently cw and are slowly deforming. Deformation in western Thessaly and across the Gulf of Evia is evident by means of block modeling. The motion of Chalkidiki might also be interpreted as cw rotation but with smaller rates than encountered in northwestern and central Greece. A slowly deforming and ccw rotating region is identified comprising the islands of Limnos, Agios Efstratios and Alonissos (block B8).
- Strike-slip motion along the NAT diminishes from the Ganos fault to the Sporades islands from 21 mm/yr to less than 5 mm/yr. Locking depths are between 5 and 18 km.
- The region around the central Ionian islands exhibits distinct kinematic patterns: Large-scale clockwise rotation encountered on mainland Greece is transformed into southwestward motion between the Gulfs of Arta and Corinth along the Katouna fault. Strike-slip motion in the order of 19.2 mm/yr and a locking depth of about 11 km were derived for the KFZ. A locked subduction interface west of Zakynthos cannot be ruled out by GPS rates. However, additional measurements and modeling are required in order to derive conclusive results.
- Vertical rates were derived for 21 sites in Greece. The rates are in a range between -1 and 2 mm/yr. Only trends can be formulated (e.g., uplift on the islands along the eastern Hellenic arc and on mainland Greece) but they have to be verified in terms of their spatial significance.

Although the kinematic field was generally enhanced, it remains weakly constrained in several regions (e.g., Chalkidiki peninsula, Gulf of Arta and Katouna fault, NW Peloponnesos). A more extensive set of GPS rates would provide substantial refinements of the kinematic field and more detailed constraints for tectonic models. Especially, this applies for vertical rates. For instance, extended knowledge of vertical crustal motion on the central Ionian islands and NW Peloponnesos might improve the understanding of deformations related to the plate boundary. Moreover, corresponding efforts would contribute to a better assessment of seismic hazard.

5 Strain rates derived by using the method of collocation

5.1 Least-squares collocation

Least-squares collocation is a parameter estimation technique. Residuals consist of both noise and systematic parts implying that functional relations are not entirely known. Collocation also allows for prediction. In this thesis collocation is used for the derivation of a strain rate field and for specifying kinematic boundary conditions in the context of the finite element method. A detailed description of the method is given in *Moritz* [1973]. In the following, only the main aspects are noted. The system of linearized observation equations can be written as

$$\mathbf{A}\mathbf{x} + \mathbf{B}\mathbf{v}' - \mathbf{w} = \mathbf{0} \quad (5.1)$$

where

$F()$	is the deterministic model
\mathbf{A}	is the design matrix of the adjustment (linearized deterministic model)
$\mathbf{x}_0 + \mathbf{x}$	is the vector of the unknown parameters
\mathbf{B}	$= (\mathbf{I}_{n,n} \quad \mathbf{0}_{n,p} \quad \mathbf{I}_{n,n})$
\mathbf{s}, \mathbf{s}'	are the signals on the observations and on the predictions, respectively
\mathbf{n}	is the noise on the observations
\mathbf{v}'	$= (\mathbf{s}_{1,n} \quad \mathbf{s}'_{1,p} \quad \mathbf{n}_{1,n})^T$
\mathbf{w}	is the difference between the observations \mathbf{l} and $F(\mathbf{x}_0)$

\mathbf{I} denotes the identity matrix and n and p denote the numbers of observations and predictions, respectively. With the covariance matrices $\mathbf{C}_{ss} = cov(s, s)$, $\mathbf{C}_{ss'} = cov(s, s')$, $\mathbf{C}_{nn} = cov(n, n)$ and the least-squares condition

$$\mathbf{n}^T \mathbf{C}_{nn}^{-1} \mathbf{n} + \mathbf{s}^T \mathbf{C}_{ss}^{-1} \mathbf{s} = min \quad (5.2)$$

the interesting quantities are obtained by

$$\mathbf{k} = \mathbf{D}^{-1}(\mathbf{l} - \mathbf{A}\mathbf{x}) \quad \text{with} \quad \mathbf{D} = \mathbf{C}_{nn} + \mathbf{C}_{ss} \quad (5.3)$$

$$\mathbf{x} = (\mathbf{A}^T \mathbf{D}^{-1} \mathbf{A})^{-1} \mathbf{A}^T \mathbf{D}^{-1} \mathbf{l} \quad (5.4)$$

$$\mathbf{n} = \mathbf{C}_{nn} \mathbf{k} ; \quad \mathbf{s} = \mathbf{C}_{ss} \mathbf{k} ; \quad \mathbf{s}' = \mathbf{C}_{s's} \mathbf{k} \quad (5.5)$$

5.2 Velocity and strain rate fields calculation implemented in the program 'strain'

The software STRAIN calculates a kinematic field in 2D based on distributed GPS velocities by using least-squares collocation. It was developed by M. Cocard and Y. Peter and is based on studies of *Danuser et al.* [1993], *Straub* [1996], *Kahle et al.* [2000] and *Peter* [2000]. The continuous field of

strain rates and differential rotations is deduced from the predicted signal \mathbf{s}' . The matrices \mathbf{C}_{ss} and $\mathbf{C}_{s's}$ are built with a correlation function r depending on the distance d between two points, the correlation length d_0 and the accuracy of the signal σ_0 .

$$r = \sigma_0^2 \cdot \frac{d_0^2}{d_0^2 + d^2} \quad (5.6)$$

No functional model is implemented in the program ($\mathbf{A} = \mathbf{0}$). The results are largely controlled by the accuracy of the GPS velocities σ_n , the accuracy of the signal σ_0 and the correlation length d_0 . The parameters σ_0 and d_0 are constants in the calculations. Large variations in site separation and a non-uniform site distribution are unfavorable. The use of a correlation length which is not optimal with respect to local site distribution may cause artifacts or inadequately strong smoothing of the signals.

The program reports the following quantities and the corresponding accuracies:

- Horizontal rates v_e, v_n in the east and north components, respectively.
- Principal axes and corresponding eigenvalues $\dot{\epsilon}_1, \dot{\epsilon}_2$ of the strain rate tensor.
- Differential rotation rates.

Dilatation rates ($\dot{\epsilon}_1 + \dot{\epsilon}_2$) and maximum shear strain rates $\frac{1}{2} \cdot |\dot{\epsilon}_1 - \dot{\epsilon}_2|$ plus corresponding accuracies are calculated based on the program output. The unit for strain is nstrain. 1 nstrain corresponds to a change in length of 1 mm on a distance of 1000 km.

5.3 Strain rates and differential rotations in Greece

The strain rate field for the area of Greece was calculated by using the program STRAIN. The accuracy of GPS velocities was introduced in the program as listed in Tables C.1, C.2 and C.3. The accuracy of the GPS rates of *McClusky et al.* [2000] was scaled by a factor 2. The correlation length was set to 110 km because at least three GPS sites are located within this distance for more than 97% of the area. In general, only the CGPS site was used if a CGPS site is closely located to a campaign-type site (cmp. Table B.3, exception: CG12). The accuracy of the signal σ_0 was then chosen to reach a σ a posteriori close to 1. It was set to 5 mm/yr. The calculation yields a σ a posteriori of 1.71 and a S/N ratio of 6.01. As aforementioned, the method itself has not been improved during this thesis. However, enhanced velocity data was used in comparison to *Hollenstein et al.* [2008a]. The results benefit from the increased number of GPS stations (e.g., in the North Aegean sea and in the Southeast Aegean sea) and updated velocities of several sites (e.g., CG17, KLLI, CG33). In contrast to *Hollenstein et al.* [2008a] no Nubian plate motion was introduced as the grade of coupling between Nubia and the overriding Aegean plate is little known. In general, results should not be interpreted at locations not surrounded by GPS sites (e.g., near the West Hellenic trench). Figure 5.1 is shown to facilitate the reference to tectonic structures and geographic features mentioned in the following section. The derived results for Greece are presented in Figures 5.2 to 5.5. More detailed strain rate fields were calculated for the region around the central Ionian islands and the Southeast Aegean sea using a shorter correlation length of 60 km. Corresponding results are shown in Figures 5.6 and 5.7.

The most striking features of the deformation field in Greece are the following: Large dextral shear strain rates along the NAT (up to 150 nstrain/yr) and along the KFZ (up to 200 nstrain/yr), sinistral shear strain rates along the Katouna fault (~ 200 nstrain/yr) and pronounced extension of up to 300 nstrain/yr in the Gulf of Corinth. Small strain rates (< 50 nstrain/yr) are encountered in western Macedonia, in Thrace, on the eastern Peloponnesos and in the southwestern Aegean sea. These results confirm and refine to a large extent findings of previous studies [*Peter, 2000; Hollenstein, 2006; Hollenstein et al., 2008a*].

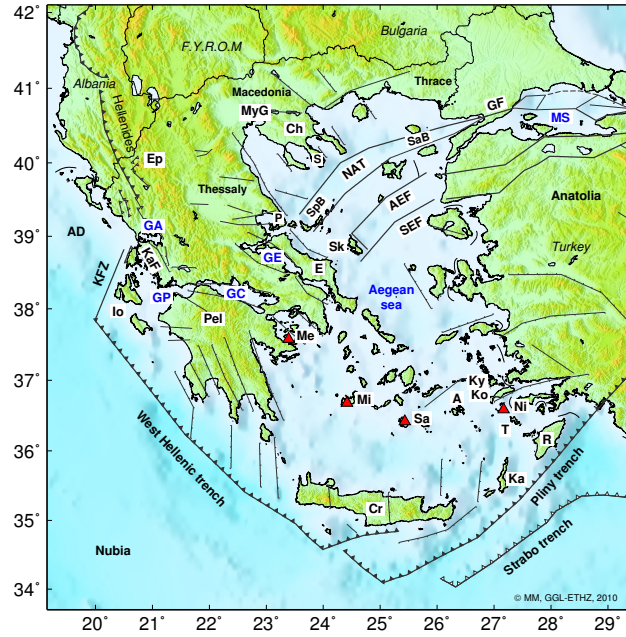


Figure 5.1: Map depicting the geographic and tectonic features discussed in this chapter. The South Aegean volcanic arc is depicted as red triangles (Me: Methana, Mi: Milos, Sa: Santorini, Ni: Nisyros). AD: Apulian domain, A: Astipalea, AEF: Agios Efstratios fault, Ch: Chalkidiki, Cr: Crete, E: Evia, Ep: Epirus, GA: Gulf of Arta, GC: Gulf of Corinth, GE: Gulf of Evia, GP: Gulf of Patras, Io: Ionian islands, Ka: Karpathos, KaF: Katouna Fault, KFZ: Kefalonia fault zone, Ko: Kos, Ky: Kalymnos, MS: Marmara sea, MyG: Mygdonian graben, NAT: North Aegean trough, P: Pelion, Pel: Peloponnesos, R: Rhodes, S: Sithonia, Sk: Skyros, SpB: Sporades basin, SaB: Saros basin, SEF: Skyros-Edremit fault, T: Tilos.

In addition, the results provide several important new insights:

- Large NNW-SSE extension of up to 150 nstrain/yr between Kalymnos and Tilos and predominant E-W extension between Karpathos and Rhodes (Fig. 5.2 (b), Fig. 5.6 (a)). Assuming that the rates observed on Nisyros are representative for the island even larger WNW-ESE extension (280 nstrain/yr) is derived between Kos and Nisyros (Fig. 5.6 (b)).
- Shear strain rates diminish along the NAT from the Saros basin towards the Sporades islands and Pelion from 150 to 75 nstrain/yr (Fig. 5.3 (b) and (d)).
- NNE-SSW extension between Pelion and Sithonia and between Skyros and Agios Efstratios amounting to 100 nstrain/yr (Fig. 5.2 (c) and Fig. 5.3 (a) and (c)).
- NNE-SSW extension of up to 100 nstrain/yr on the Chalkidiki peninsula and in central Macedonia (Fig. 5.2 (b) and (c) and Fig. 5.3 (a) and (c)).

Figures 5.3 (c) and (d) show the strain rates projected on fault structures. N-S to NE-SW extensional strain dominates from central northern Greece to the Gulf of Corinth and in central western Turkey. The signal s' describes the displacement rate and decreases with increasing distance to GPS sites. Compression along the Hellenic trench is for this reason since no rates are introduced for the Nubian plate motion. This feature should not be interpreted. The calculated strain rates provide some implications for the NAT: There is shear strain and extension (160 and 70 nstrain/yr, respectively) on ENE-WSW oriented faults along the Saros basin but almost only shear strain (100 nstrain/yr) on NE-SW oriented faults along the Sporades basin. N-S to NNE-SSW directed extension (100 nstrain/yr) within the Sporades basin is more likely related to E-W to ESE-WNW trending faults. In addition, the GPS based strain analysis suggests a left-lateral strike-slip component on all NW-SE trending faults along the western shoreline of the North Aegean sea. The

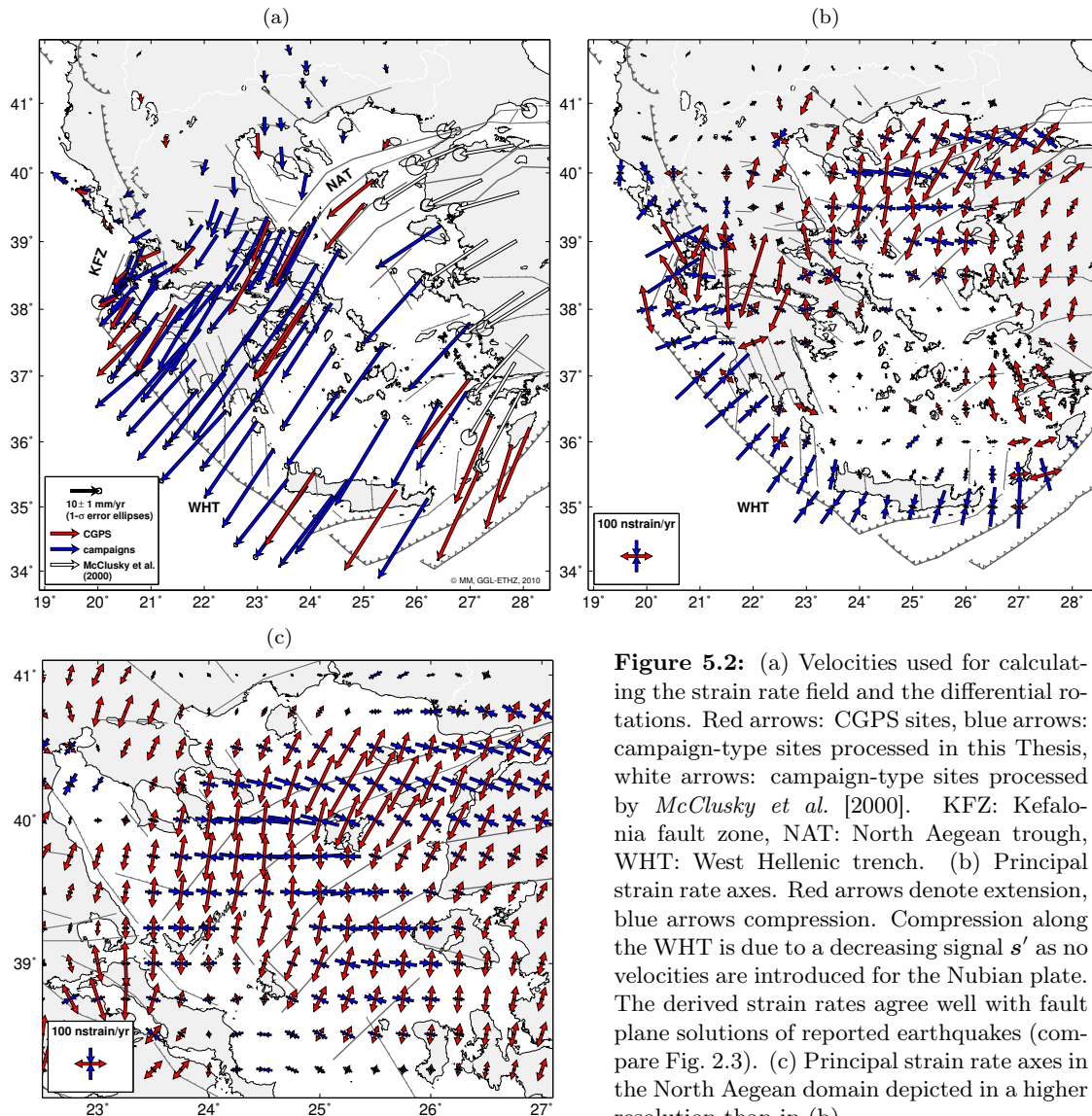


Figure 5.2: (a) Velocities used for calculating the strain rate field and the differential rotations. Red arrows: CGPS sites, blue arrows: campaign-type sites processed in this Thesis, white arrows: campaign-type sites processed by *McClusky et al.* [2000]. KFZ: Kefalonia fault zone, NAT: North Aegean trough, WHT: West Hellenic trench. (b) Principal strain rate axes. Red arrows denote extension, blue arrows compression. Compression along the WHT is due to a decreasing signal s' as no velocities are introduced for the Nubian plate. The derived strain rates agree well with fault plane solutions of reported earthquakes (compare Fig. 2.3). (c) Principal strain rate axes in the North Aegean domain depicted in a higher resolution than in (b).

calculated shear strain rates south of Limnos towards Hios along the AEF and SEF are smaller than along the NAT. Shear strain is not extending towards east and west. Almost only NE-SW to NNE-SSW extension is encountered along the eastern Aegean shoreline between 38.5°N and 39.5°N. Fault plane solutions of earthquakes in the period 1976–2010 agree well with the principal axes of the derived strain rate field (compare Fig. 2.3 and Figure 5.2 (b)).

The 2001 Mw 6.4 Skyros earthquake (chapter 6.4.2) occurred between Skyros and the Sporades islands which is an area of predominant NNE-SSW extension (Fig. 5.2 (c)). The strike of the sinistral strike-slip earthquake was approximately 150° [*Melis et al.*, 2001; *Benetatos et al.*, 2002; *Ganas et al.*, 2005]. GPS based strain rates indicate about 60 nstrain/yr of left-lateral shear strain on a NNW-SSE trending fault where the earthquake occurred. This is only slightly less (~30 nstrain/yr) than encountered on the NE-SW trending right-lateral strike-slip fault northeast of Skyros. *Ganas et al.* [2005] suggested that the 1967 Ms 6.6 (normal faulting) and the 2001 Mw 6.4 Skyros events occurred on en-echelon faults. GPS based strain rates are considerably smaller to the southwest of this line than to the northeast. Moreover, the sense of rotation relative to

Eurasia changes from east to west from ccw to cw. In this context, a connection between the Agios Efstratios and the Skyros-Edremit faults, accommodating about 10 mm/yr of dextral strike-slip in total (chapter 7.4), and, at their southwestern termination, NNW-SSE trending fault structures accommodating sinistral strike-slip and NNE-SSW extension is likely.

Large differential rotations relative to Eurasia are derived along the western Hellenic trench (up to 8°/Myr cw rotation), along the Pliny trench (up to 4°/Myr ccw rotation) and along the NAT towards Central Greece (up to 6°/Myr cw rotation) (Fig. 5.5 (a)). CCW rotation ($\sim 2^\circ$ /Myr) on the Chalkidiki peninsula disagrees with the finding derived in chapter 4.3 suggesting cw rotation. However, no tectonic features (i.e., the Mygdonian graben) are considered by the applied collocation method. Moreover, differential rotations are not identical with rotations around Euler poles since they describe rotations around local rotation axes. Therefore, cw rotation of the Chalkidiki peninsula relative to Eurasia remains plausible.

The formal errors of the estimated strain rates depend amongst others on the relation between the correlation length and the site spacing. The errors of the dilatation are smallest in the region of the central Ionian islands and in Thessaly where the site spacing is considerably smaller than the correlation length (Fig. 5.4). The formal accuracy decreases in regions with large site separation. Most parts of the area with formal errors larger than 80–100 nstrain/yr are located in northwestern Greece and in the Aegean sea. The formal error of the maximum shear strain rate is smaller than the formal error of the dilatation by a factor 2. The spatial distribution of the formal errors of the differential rotations is similar. Corresponding errors ($1-\sigma$) are in the range 0.7°/Myr to 4.1°/Myr (Fig. 5.5 (b)).

More detailed strain rate fields were calculated for the regions of the Southeast Aegean sea and the central Ionian islands. The calculations were performed by using a correlation length of 60 km and a σ_0 of 5 mm/yr. The results are discussed in the following.

Rates on the island of Nisyros might be influenced by very local effects related to active volcanism (chapter 4.5.2). Therefore, the velocity of site NISI was not used for the calculations shown in Figures 5.2 to 5.5. Two local strain rate fields were calculated for the Southeast Aegean sea to assess the influence of the rates of site NISI on the strain rate results. The velocity of site NISI was used only for the calculation of the second strain rate field. The results of the first calculation reveal N-S to NW-SE extension of up to 150 nstrain/yr between Kalymnos and Tilos (Fig. 5.6 (a)). Moreover, only small strain rates (<50 nstrain/yr) are encountered in the area between the sites on Tilos and Rhodes (cmp. block B11 in chapter 4.3). It seems that N-S to NW-SE extension is localized between Kalymnos and Tilos and does not extend towards the Pliny trench. The inclusion of the rates of site NISI in the second calculation causes an increase of the extension rates between Kalymnos, Kos and Nisyros to 280 nstrain/yr (Fig. 5.6 (b)). Both horizontal principal strain rates are positive in this area. Only a dense and preferably continuous GPS network can provide a more accurate and time-dependent strain rate field between Kalymnos, Tilos and Bodrum.

The strain rate field in the region comprising the central Ionian islands, Western Greece and NW Peloponnesos was slightly refined compared to *Hollenstein* [2006] (Fig. 5.7). The most striking features are: extension and sinistral shear strain (240 nstrain/yr and 275 nstrain/yr, respectively) between the Gulfs of Arta and Corinth along the Katouna fault, right-lateral shear strain along the KFZ (200 nstrain/yr) and E-W to ENE-WSW compression and shear strain (180 nstrain/yr and 70 nstrain/yr, respectively) between Kefalonia and NW Peloponnesos. The calculations reveal small deformation (<50 nstrain/yr) but large cw rotation ($\sim 11^\circ$ /Myr) between Zakynthos and Kefalonia. Strain rates on NW Peloponnesos are moderate (~ 50 nstrain/yr) compared to the KFZ or the Gulf of Corinth. The most extensional strain rate axes directed NW-SE to NNW-SSE are larger by 30–50 nstrain/yr between Zakynthos and Strofades if the rates of site STRO instead of those of site STRF (Table C.3) were used for the strain rate calculation. This does not change the conclusions.

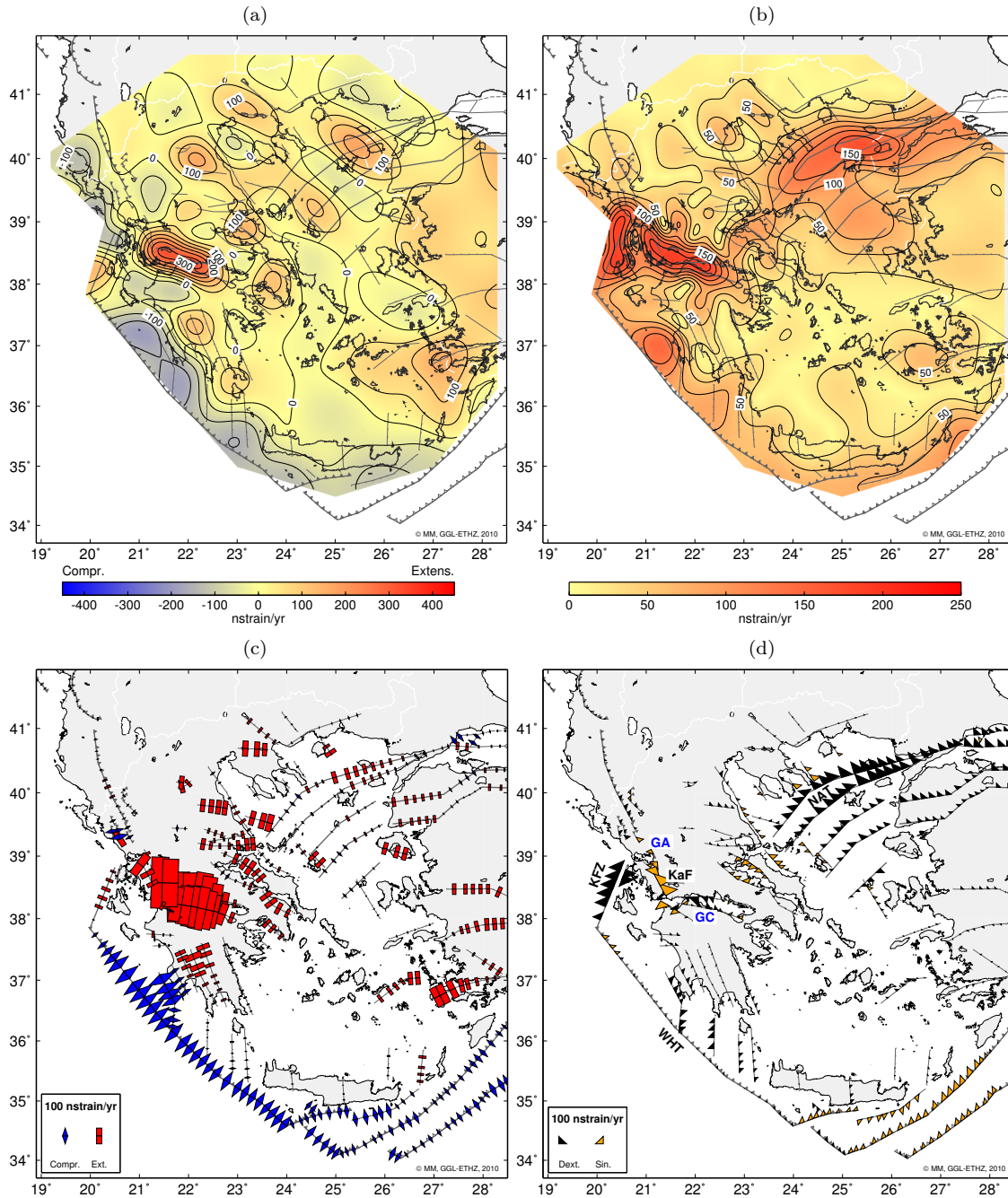


Figure 5.3: (a) Dilatation rates ($\dot{\epsilon}_1 + \dot{\epsilon}_2$). Maximum extension takes place across the Gulf of Corinth (300 nstrain/yr). (b) Maximum shear strain rates ($\frac{1}{2}|\dot{\epsilon}_1 - \dot{\epsilon}_2|$). Largest shear strain rates are found in a zone extending from the Gulf of Corinth to the Gulf of Arta, along the KFZ (~ 175 nstrain/yr, respectively) and along the NAT (up to 150 nstrain/yr). (c) Normal strain rates in respective fault coordinate system (blue rhombi indicate compression and red bars extension). The calculation suggests normal faulting components for the majority of the faults in Greece and western Turkey. Again, compression along the WHT is due to a decreasing signal s' towards SW as no velocities are introduced for Nubia. (d) Shear strain rates in respective fault coordinate system (black triangles denote dextral and orange triangles sinistral shear strain rates). Dextral shear strain rates along the NAT and the KFZ and sinistral shear along the Katouna fault are the most dominant features. NAT: North Aegean trough, GA: Gulf of Arta, GC: Gulf of Corinth, KaF: Katouna fault, KFZ: Kefalonia fault zone, WHT: West Hellenic trench.

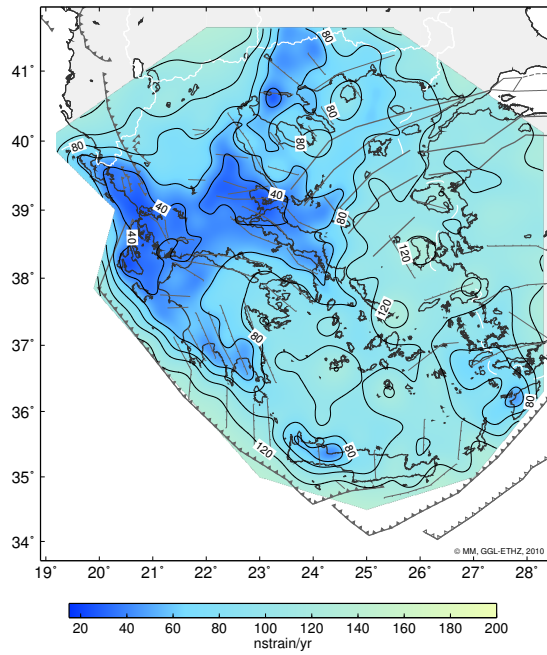


Figure 5.4: 1- σ accuracies for the dilatation. The accuracies for the maximum shear strain rates can be obtained by multiplying the indicated values with the factor 0.5.

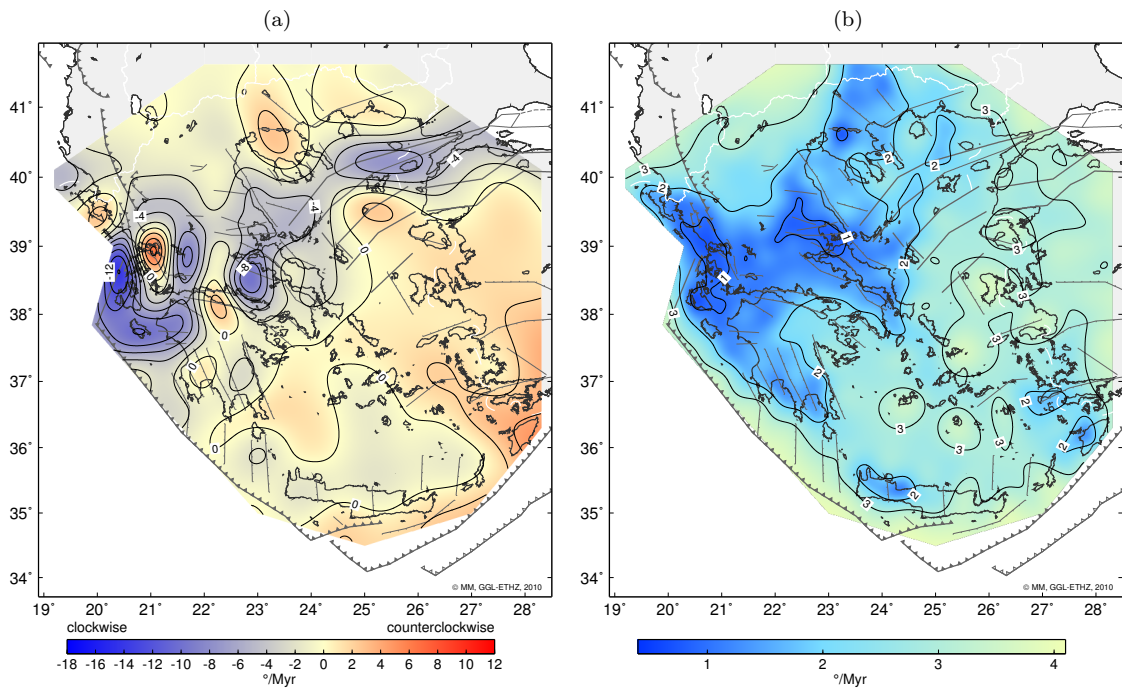


Figure 5.5: (a) Differential rotation relative to Eurasia. Large differential rotations are derived along the western (up to 8°/Myr cw rotation) and the eastern (up to 4°/Myr ccw rotation) termination of the WHT and along the NAT towards Central Greece (up to 6°/Myr cw rotation). In the central and southwest Aegean sea and on the Peloponnesos rotations are small. (b) Corresponding 1- σ accuracies of differential rotations.

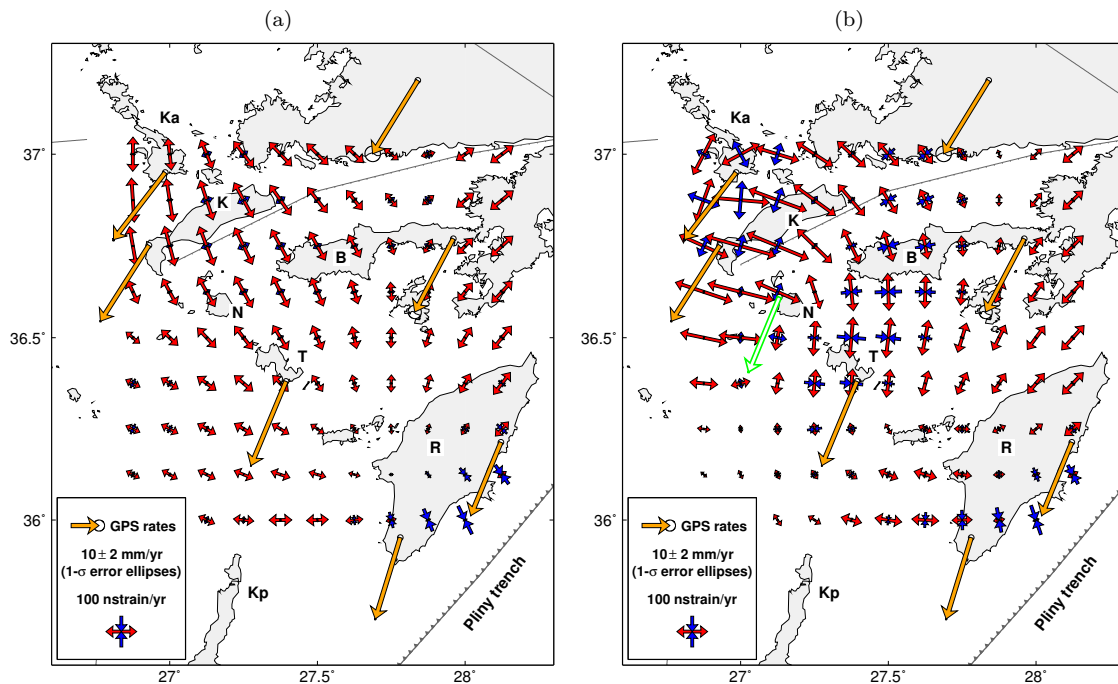


Figure 5.6: Strain rates in the Southeast Aegean sea. (a) Rates of the site on Nisyros not included in the calculation. (b) Rates of the site on Nisyros included in the calculation. The collocation is based on a correlation length of 60 km and a σ_0 of 5 mm/yr. Note that all principal strain rate axes are positive between Nisyros and Kalymnos and that strain rates are below 50 nstrain/yr between the sites on Tilos and Rhodes. B: Bodrum peninsula, K: Kos, Ka: Kalymnos, Kp: Karpathos, N: Nisyros, R: Rhodes, T: Tilos.

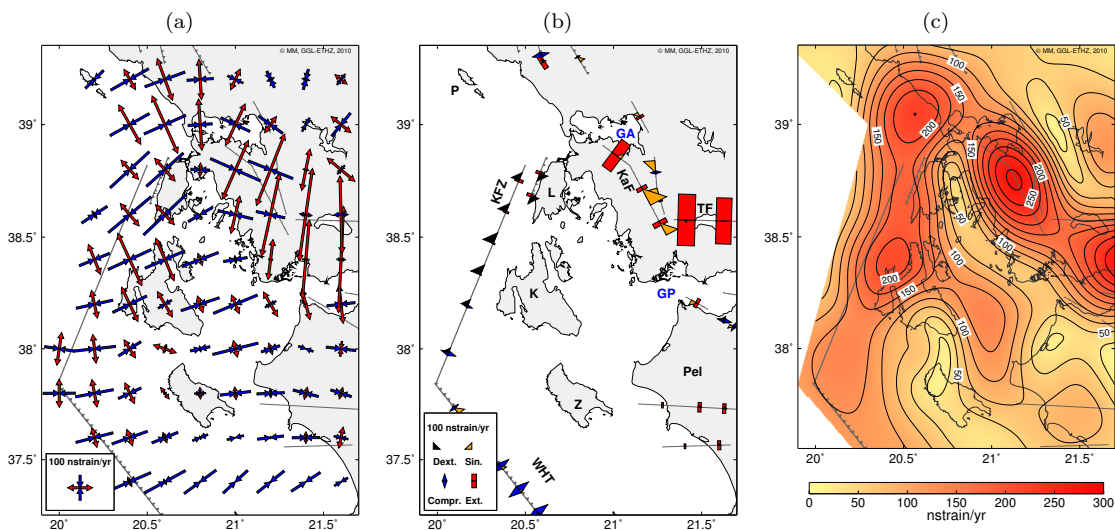


Figure 5.7: (a) Strain rates near the central Ionian islands. A correlation length of 60 km and a σ_0 of 5 mm were used for the calculations. The central Ionian islands are surrounded by tectonic structures accommodating large differential motions. Red arrows depict extension, blue arrows depict compression. (b) Strain rates with respect to fault geometry. Orange triangles depict sinistral shear strain rates and black triangles depict dextral shear strain rates. Red bars depict extension and blue rhombi depict compression. GA: Gulf of Arta, GP: Gulf of Patras, K: Kefalonia, KaF: Katouna fault, KFZ: Kefalonia fault zone, L: Lefkada, P: Paxi, Pel: Peloponnesos, TF: Trichonis fault, WHT: West Hellenic trench, Z: Zakynthos. (c) Maximum shear strain rates: $\frac{1}{2}|\dot{\epsilon}_1 - \dot{\epsilon}_2|$.

5.4 Concluding remarks

The method of collocation was applied to compute the strain rate field. In brief, the conducted analysis is summarized.

- The strain rate calculation based on the method of collocation is an inversion technique which depends only on GPS data. It is free from geophysical hypotheses. The method is suitable for the analysis of a velocity field by the interpolation of the rates and the determination of corresponding deformation and rotation rates.
- Several important refinements of the present-day deformation field in Greece were derived: N-S to NNW-SSE extension of up to 150 nstrain/yr between Kalymnos and Tilos, diminishing shear strain rates along the NAT from the Saros (150 nstrain/yr) to the Sporades basin (75 nstrain/yr), NNE-SSW extension amounting to 100 nstrain/yr between the Chalkidiki peninsula and Pelion, which extends towards central Macedonia, and between Skyros and Agios Efstratios. Fault related implications were derived for the NAT. In particular, higher rates of normal faulting are suggested on ENE-WSW trending faults along the Saros basin than on NE-SW trending faults along the Sporades basin.
- The dependency of the numerical results on the correlation length and the use of a radial-symmetric covariance function are the most important shortcomings of the method since site spacing is quite variable. In general, features of the strain rate field with local dimensions compared to the correlation length might be smoothed. Artifacts in the strain rate field may arise in regions where site spacing is larger than the correlation length.
- The interpretation of the obtained strain rates in terms of tectonics is not straightforward because the applied method is based on a two-dimensional continuum. The development of the method towards the implementation of fault structures was abandoned in favor of the employment of the finite element method.

6 Seismic signals in GPS time series

6.1 Introduction

Over the last 15 years several strong earthquakes occurred in Greece - a couple of them in close distance to campaign-type or continuous GPS sites. This chapter gives a summary of the earthquakes for which significant displacements were detected in GPS time series. GPS derived site displacements are listed in Table 6.1. Displacements related to particular earthquakes are compared with dislocations of a basic analytical dislocation model. The comparison of GPS derived displacements and modeled dislocations enables an assessment of earthquake source parameters. Moreover, the calculated dislocations are used in order to rate the reliability of velocities which are possibly affected by an earthquake but are based on data not allowing for the accurate estimation of a corresponding displacement.

6.2 Estimation of earthquake displacements

Displacements of GPS sites related to earthquakes were estimated based on continuous and campaign-type position time series. The displacements for CGPS sites were derived using Eq. (3.5) or Eq. (3.7) according to the selected motion model. Displacements of campaign-type sites were derived using Eq. (3.5). In case a campaign-type site was occupied only once after an earthquake, the displacement is equal the residual of the derived position after the earthquake with respect to the linear motion based on position estimates before the earthquake.

It is assumed that annual rates are constant. However, the analysis of interseismic rates of site KERI corresponding to sections without earthquakes and antenna changes based on Eq. (3.6) revealed the following: Significant differences (95% confidence level) exist for rates of different sections in the east and up components, respectively (Table 6.2, Fig. B.6). All the sections are shorter than 2.6 years except section 2. Rates of sections 1–4 vary by maximum 1.3 mm/yr, 0.7 mm/yr and 3.6 mm/yr in the east, north and up components, respectively. Similar applies for site DION (Table 6.3, Fig. 6.2). Small changes in rates cannot be ruled out for these sites but the data is not conclusive in order to accept the hypothesis of rate changes.

A comparison of estimated earthquake displacements of CGPS sites depending on the applied velocity model is listed in Table 6.4. Most of these displacement vectors only slightly vary depending on the used model. Larger differences (>1 mm in a horizontal and >2 mm in a vertical component, respectively) are related to short sections (<2.1 years) and/or data gaps.

6.3 Analytical surface dislocation model

The analytical surface dislocation model derived by *Okada* [1985] was used to calculate earthquake dislocations. The employed program was written by P. Cervelli. The model provides surface dislocations due to slip on inclined rectangular shear and tensile faults in an elastic half-space. The model requires the specification of the following parameters (Fig. 6.1): position of the earthquake,

Earthquake	Site	Lon [°]	Lat [°]	GPS			R	Okada model		
				East [mm]	North [mm]	Up [mm]		East [mm]	North [mm]	Up [mm]
Strofades 1997 11 18	KERI	20.808	37.655	-10 ± 1	-17 ± 1	-1 ± 1	a_1			
	STRF	21.014	37.250	11 ± 1	-117 ± 1	83 ± 3	b			
	STRO	21.016	37.250	-12 ± 11	-115 ± 8	67 ± 30	b			
Athens 1999 09 07	DION ¹	23.933	38.079	-4 ± 1	0 ± 1	1 ± 1	a_1	-0.4	0.3	0.9
Skyros 2001 07 26	CG38	24.109	38.661	-16 ± 4	-17 ± 7		b	-3.3	-9.8	-0.9
	NSKR	24.543	38.887	-58 ± 7	14 ± 3		b	-13.9	2.9	0.1
	DION ¹	23.933	38.079	-1 ± 1	-3 ± 1	-3 ± 1	a_1	-0.5	-1.8	-0.5
Lefkada 2003 08 14	IKVL	20.656	38.791	-8 ± 7	-78 ± 7	45 ± 9	b	-3.4	-7.3	-0.7
	APAX	20.249	39.141	-5 ± 1	6 ± 1	-1 ± 1	a_2	-2.4	3.8	0.2
	ASSO	20.548	38.371	5 ± 4	-32 ± 9		c	3.6	-7.2	4.9
	DUKA	20.543	38.564	-49 ± 1	-49 ± 1	-22 ± 3	a_1	-3.5	-9.1	-3.5
	FISK	20.577	38.460	-4 ± 2	-36 ± 2		b	-0.7	-6.4	-0.0
	SKIN	20.702	37.931	0 ± 1	-2 ± 1	3 ± 1	a_3	1.0	-2.4	0.1
	VASI	20.573	38.607	12 ± 2	-43 ± 6		c	-2.2	-12.0	1.6
	VONW	20.846	38.910	-20 ± 2	-22 ± 6		c	-8.1	-5.3	-3.2
Zakynthos 2006 04 03–19	KERI	30.123	30.123	-10 ± 1	-2 ± 1	8 ± 1	a_1			
NW Peloponnesos 2008 06 08	KERI	20.808	37.655	4 ± 1	1 ± 1	-3 ± 1	a_1	4.1	1.7	0.0
	KILL	21.136	37.941	15 ± 1	0 ± 1		b	14.1	2.8	-4.2
	RLS	21.465	38.056	-4 ± 1	8 ± 1	12 ± 1	a_2	-3.2	13.1	15.1
	SKIN	20.702	37.931	3 ± 2	0 ± 1		a_1	4.6	0.8	0.0
	SNDO	21.580	38.014	-5 ± 7	-8 ± 4		c	-2.9	-0.5	-0.8
Rhodes 2008 07 15	ARHA	28.121	36.214	-1 ± 1	-2 ± 1	0 ± 1	a_1			

Table 6.1: GPS derived coseismic displacements (\pm standard deviation) in the period 1995–2009. Vertical displacements are only indicated for CGPS sites and selected campaign-type sites. Dislocations computed by the application of an Okada model are indicated in the last three columns (corresponding model parameters are listed in Tables 6.5 and 6.7). R indicates how the displacements were derived: a_1 : offset according to Eq. (3.5); a_2 : offset according to Eq. (3.7); a_3 : estimation procedure described in caption of Figure 6.5; b : offsets according to Eq. (3.5) based on campaign-type time series; c : Linear motion derived from position estimates of campaign-type time series before the earthquake propagated to the date of the first site occupation after the earthquake. ¹ See chapters 6.4.1 and 6.4.2 for more details concerning these displacements. A comparison of estimated earthquake displacements of CGPS sites depending on the applied velocity model is listed in Table 6.4.

depth, strike, dip, rake, fault length, fault width and the average displacement on the rupture plane. A Poisson’s ratio of 0.25 is used for all the calculated models.

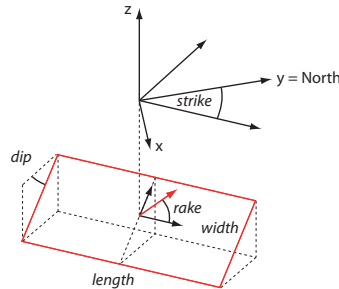


Figure 6.1: Sketch of the geometry of the Okada model. The red rectangle depicts the rupture plane. The red arrow depicts the motion of the hanging wall with respect to the footwall.

Section	Time period	T	East				North				Up			
			v	σ_v	σ_c	Δ	v	σ_v	σ_c	Δ	v	σ_v	σ_c	Δ
1	49896–50768	2.39	-14.8	0.4	1.5	3	-15.5	0.4	1.7	-	-1.5	1.2	4.9	3
2	50771–52892	5.81	-15.4	0.1	1.4	4	-15.3	0.1	1.4	-	-0.9	0.3	4.6	3
3	52894–53828	2.56	-15.7	0.3	1.2	1,4	-15.3	0.3	1.2	-	2.1	1.0	4.1	1,2
4	53846–54586	2.03	-14.4	0.3	1.1	2,3	-15.9	0.3	1.2	-	-0.5	1.2	4.1	-
5	54710–54890	0.49	-16.7	2.4	1.0	-	-11.9	2.2	1.0	-	-1.9	9.1	4.0	-
All	49896–54890	13.67	-15.3	0.1	1.4	-	-15.3	0.1	1.4	-	-0.7	0.3	4.5	-

Table 6.2: Rates of site KERI estimated based on Eq. (3.6) (rates for sections 1–5) and Eq. (3.5) (rate based on data of all sections, denoted by *All*). Time period is indicated by the modified Julian date. T indicates the length of the sections in years. v and σ_v denote the estimated rate and the corresponding scaled accuracy. Both values are indicated in [mm/yr]. σ_c denotes the coordinate precision indicated in [mm]. Δ denotes sections whose rates significantly differ from the rate of the particular section (95% confidence level). Only two pairs of rates significantly differ in case that the October 2005 earthquake (cmp. chapter 6.5.3) is modeled as an additional offset (East: sections 2 \leftrightarrow 4, Up: sections 2 \leftrightarrow 3).

Section	Time period	T	East				North				Up			
			v	σ_v	σ_c	Δ	v	σ_v	σ_c	Δ	v	σ_v	σ_c	Δ
1	49825–50378	1.51	-15.1	1.1	2.4	3	-21.8	1.1	2.5	2,3,4	-5.8	3.3	7.1	4
2	50379–51427	2.87	-15.4	0.3	1.7	3,4	-24.5	0.3	1.7	1,3,4	0.9	0.9	5.5	-
3	51428–52115	1.88	-18.4	0.5	1.6	1,2,4	-26.2	0.5	1.6	1,2	1.0	1.7	5.4	-
4	52116–54890	7.59	-16.5	0.1	1.9	2,3	-25.5	0.1	1.8	1,2	1.7	0.3	5.5	-
All	49825–54890	13.87	-16.5	0.1	2.0	-	-25.4	0.1	1.9	-	1.6	0.3	5.7	1

Table 6.3: Rates of site DION estimated based on Eq. (3.6) (rates for sections 1–4) and Eq. (3.5) (rate based on data of all sections, denoted by *All*). Time period is indicated by the modified Julian date. T indicates the length of the sections in years. v and σ_v denote the estimated rate and the corresponding scaled accuracy. Both values are indicated in [mm/yr]. σ_c denotes the coordinate precision indicated in [mm]. Δ denotes sections whose rates significantly differ from the rate of the particular section (95% confidence level).

Site	EQ	R	Constrained			Constrained + terms				Unconstrained			
			East [mm]	North [mm]	Up [mm]	East [mm]	North [mm]	Up [mm]	East [mm]	North [mm]	Up [mm]		
APAX	L		-4.5	4.8	1.0	-4.5	5.7	-1.4	*	-4.6	5.7	-1.2	
ARHA	R	(a)	-1.3	-1.9	-0.4	*	-1.2	-2.0	-0.5		-2.5	-2.8	1.0
DION	A		-3.9	0.3	1.5	*	-3.9	0.2	1.6		-3.7	-0.2	3.1
DION	Sk		-1.2	-2.7	-2.5	*	-1.2	-2.8	-2.6		0.8	-1.8	-2.3
DUKA	L	(b)	-48.7	-49.4	-21.8	*	-48.8	-48.7	-19.7		-45.4	-46.9	-18.1
KERI	St		-10.3	-17.2	-0.9	*	-10.2	-17.2	-0.9		-10.8	-17.1	0.7
KERI	Z		-9.6	-2.2	8.3	*	-9.6	-2.3	8.4		-10.1	-1.5	4.8
KERI	P		3.6	1.4	-4.2	*	3.9	1.6	-4.1		3.3	0.5	-3.8
RLS	P		-1.9	7.0	9.4		-3.7	7.6	12.0	*	-0.1	7.0	8.5
SKIN	P	(c)	2.7	0.2	-0.1	*	3.0	-0.0	-0.2		2.4	0.0	4.7

Table 6.4: Comparison of estimated earthquake displacements depending on the applied velocity model for CGPS sites. *Constrained* denotes the estimation based on Eq. (3.5). *Constrained + terms* denotes the estimation based on Eq. (3.7). *Unconstrained* denotes the estimation based on Eq. (3.6). The displacements marked with a star are listed in Table 6.1. The earthquakes (EQ) causing the displacements are discussed in subsequent chapters (A: 1999 Athens, L: 2003 Lefkada, P: 2008 NW Peloponnesos, R: 2008 Rhodes, Sk: 2001 Skyros, St: 1997 Strofades, Z: 2006 Zakynthos). Remarks (R): (a) Only 214 days of data available after the earthquake. (b) The rates before and after the 2003 Lefkada earthquake do not differ significantly (95% confidence level). (c) Only 180 days of data available after the earthquake.

6.4 Earthquakes in the Aegean domain

6.4.1 1999 Ms 5.9 Athens earthquake

The Ms 5.9 Athens earthquake (location: 23.60°E, 38.12°N [NEIC catalog, 2009]) occurred on 7 September 1999 in a region of low seismicity [Papadopoulos, 2002]. The fault plane solution pointing to a normal faulting event is in general agreement with NE-SW extensional strain rates (50–80 nstrain/yr) derived across Attica/Central Greece (Fig. 5.2 (b)). Near the epicenter of the earthquake five campaign-type GPS sites (CG35, CG50, CG53, CG57, CG58) and one continuous GPS site (DION) are located (Fig. 6.3). Coseismic displacements cannot be inferred from the campaign-type data. The detrended time series of site DION indicates a displacement of 4 mm towards west between a few days before and after the event (Fig. 6.2 (a) and (c)). A conspicuous signal in the time series of DION prior to the Athens earthquake was already mentioned by Hollenstein [2006].

Dislocations were calculated based on a dislocation model (Okada [1985], see chapter 6.3) in order to check the plausibility of coseismic displacements at site DION. The location and orientation of the rupture plane, the seismic moment ($1.6 \cdot 10^{18}$ Nm) and the average slip were set according to Baumont *et al.* [2004]. Length and width of the fault were set to equal the seismic moment because variable slip is modeled on the rupture plane in the respective study (Table 6.5). The Okada model reveals horizontal surface dislocations between 6 and 14 mm for sites CG35, CG50, CG53, CG57 and CG58 and 0.5 mm for site DION (Fig. 6.3). The Athens earthquake significantly downgrades the reliability of rates of closely located campaign-type sites. In particular, the results of the Okada model point to a smaller north component of the velocity of CG35 and to a smaller east component of the velocity of CG50 (1 mm/yr, respectively). The campaign-type sites CG57 and CG58 which are located closest to the earthquake were not used for analyses in this thesis.

The residual of the modeled dislocation at site DION with respect to the GPS derived displacement amounts to 3.5 mm in magnitude and 40° in direction, respectively. However, DION is located in an area where dislocation vectors are very sensitive to changes in fault strike (Fig. 6.3 (inset)). Directions agrees within 10° when assuming a fault strike of 107°. The occurrence of a coseismic slip at site DION related to the Athens earthquake is not conclusively proven based on the modeling. Due to the scatter in the time series it remains open if the GPS derived displacement is rather a transient motion (Fig. 6.2 (c)). Indeed, postseismic slip on the fault plane lasting a few days till 2.5 years has been detected by Atzori *et al.* [2008] using InSAR. Moreover, they reported the absence of significant preseismic slip. The temporal characteristics of the displacement at DION are not entirely resolved. The simple introduction of a discontinuity in the GPS time series of DION at the time of the earthquake largely reduces the influence of the observed slip on the interseismic velocity. The velocity changes due to the modeling of this discontinuity by 0.34 and 0.02 mm/yr in the east and north components, respectively.

Earthquake	Lon [°]	Lat [°]	Depth [km]	Strike [°]	Dip [°]	Rake [°]	Length [km]	Width [km]	Slip [m]
1999 Ms 5.9 Athens	23.58	38.12	9.5	112	60	-84	13	11	0.36
2001 Mw 6.4 Skyros	24.34	39.05	8.0	150	70	10	20	10	0.64
2008 Mw 6.4 NW Peloponnesos	21.52	37.99	18.0	210	82	175	15	12	0.74

Table 6.5: Parameters used for the Okada models. The parameters for the Athens earthquake are based on Baumont *et al.* [2004] (more details in the text). The parameters for the Skyros earthquake were published by Ganas *et al.* [2005]. The parameters for the NW Peloponnesos earthquake were published by Ganas *et al.* [2009].

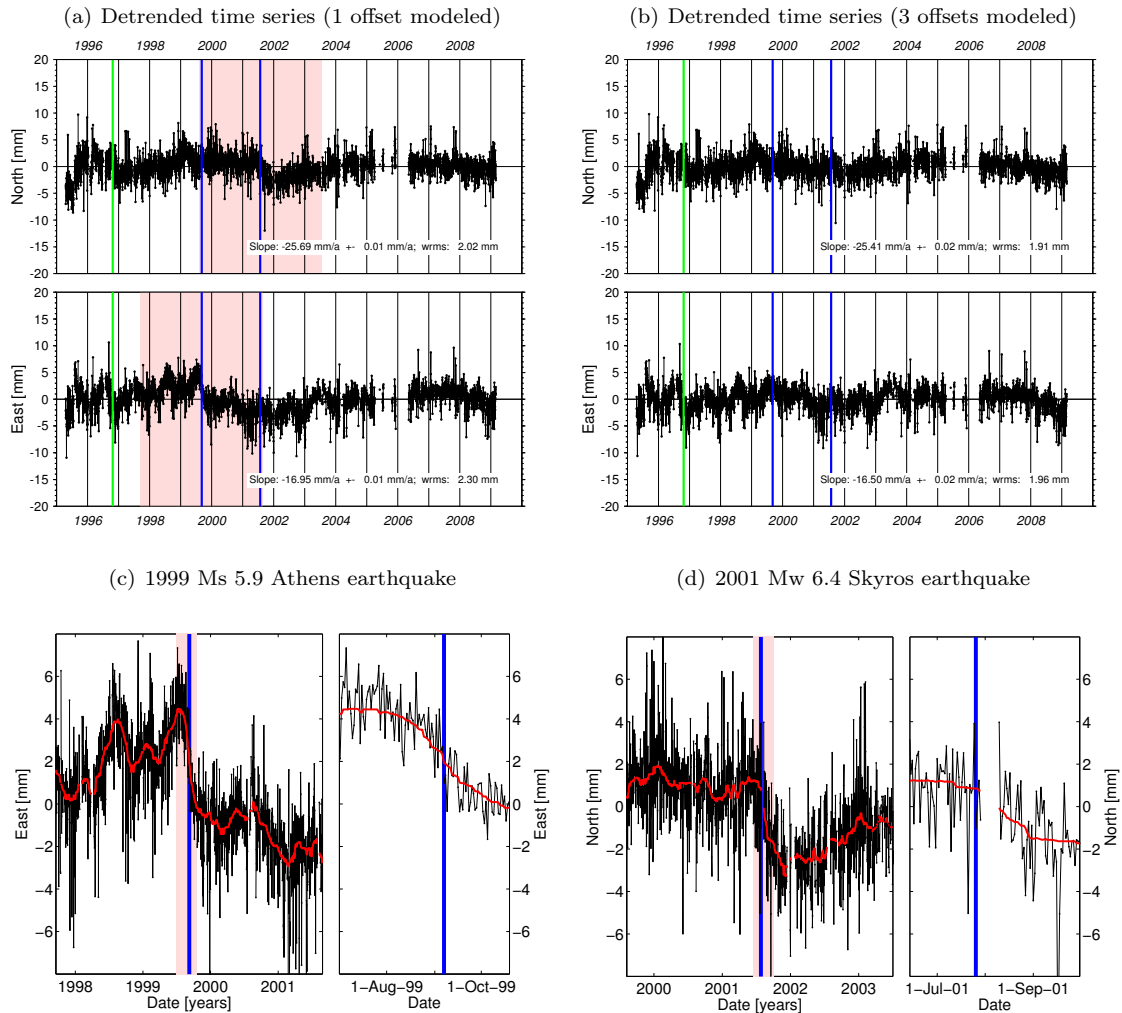


Figure 6.2: (a) Improved and detrended time series of site DION. Only the offset related to an antenna change in the year 1997 is modeled (green vertical line). The blue lines depict the 1999 Ms 5.9 Athens and the 2001 Mw 6.4 Skyros earthquakes. The red shaded areas are enlarged in (c) and (d). (b) Detrended time series of DION. The offset related to an antenna change in the year 1997, and additionally the offsets related to the 1999 Athens earthquake and the 2001 Skyros earthquake are modeled. The introduction of two additional offsets changes the interseismic velocity by 0.28 mm/yr and 0.45 mm/yr in the north and east components, respectively. (c) Magnifications of the east component depicted in (a) centered on the 1999 Athens earthquake. The red line depicts the median filtered (60 days window) time series. The interpretation of the displacement (~ 4 mm to the west) in terms of co- and postseismic motion is not unambiguous. (d) Magnifications of the north component depicted in (a) centered on the 2001 Skyros earthquake. No instantaneous offset is visible immediately after the earthquake but a southward motion of about 3 mm is observed within the following 60 days.

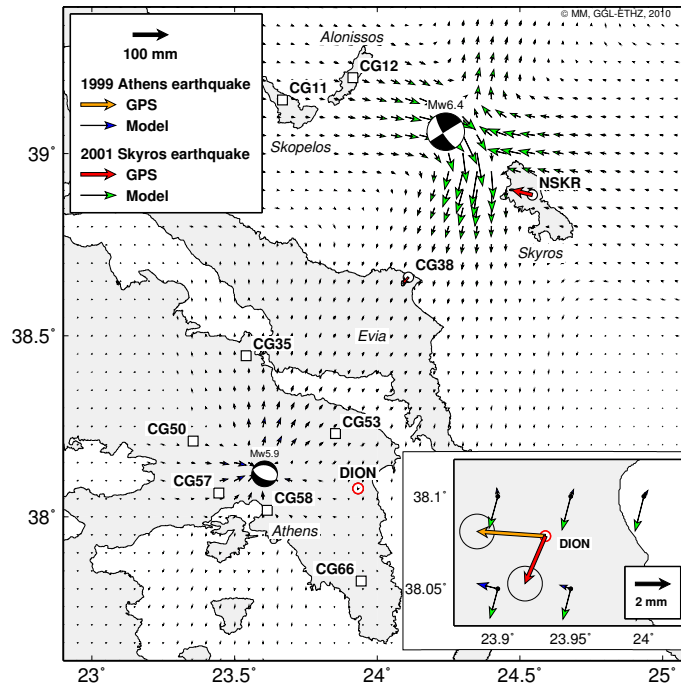


Figure 6.3: Modeled surface dislocations for the 1999 Ms 5.9 Athens earthquake (blue arrows) and the 2001 Mw 6.4 Skyros earthquake (green arrows). The GPS derived displacement at site DION related to the 1999 Athens earthquake is depicted as orange arrow. The GPS derived displacements at sites CG38, DION and NSKR related to the 2001 Skyros earthquake are depicted as red arrows. The inset depicts the GPS derived displacements at site DION and the modeled dislocations at neighboring grid points. The GPS derived displacements are larger (factor 1.5–10) than the modeled ones. While the directions agree well for the Skyros earthquake, the directions largely differ for the Athens earthquake. However, for the Athens earthquake the directions of the modeled dislocations change remarkably in the area around DION (from 280° to 45°). A slight variation in the strike angle of the Okada model would improve the fit. Note the different scale of the displacements applied in the inset. The error ellipses corresponding to the GPS displacements depict the $1\text{-}\sigma$ confidence region. The parameters used for the Okada models are listed in Table 6.5. Fault plane solutions of the Athens and Skyros earthquakes: Louvari and Kiratzi [2001] and CMT catalog [2011], respectively.

Earthquake	Site	Lon [°]	Lat [°]	<i>Hollenstein et al.</i> [2008b]		This thesis	
				East [mm]	North [mm]	East [mm]	North [mm]
Mw 6.4 Skyros 2001-07-26	CG38	24.109	38.661	-26 ± 10	-26 ± 12	-16 ± 4	-17 ± 7
	NSKR	24.543	38.887	-74 ± 10	9 ± 11	-58 ± 7	14 ± 3
Mw 6.2 Lefkada 2003-08-14	1KVL	20.656	38.791	-21 ± 9	-69 ± 10	-8 ± 7	-78 ± 7
	DUKA	20.543	38.564	-40 ± 2	-39 ± 2	-49 ± 1	-49 ± 1
	FISK	20.577	38.460	-10 ± 8	-33 ± 8	-4 ± 2	-36 ± 2

Table 6.6: Comparison of GPS derived displacements published in *Hollenstein et al.* [2008b] and displacements derived in this thesis using additional data. The differences are not significant on the 95% confidence level except for site DUKA.

6.4.2 2001 Mw 6.4 Skyros earthquake

The Mw 6.4 Skyros earthquake (location: 24.24°E, 39.06°N [*NEIC catalog*, 2009]) occurred on 26 July 2001. The sinistral strike-slip event was located on the Skyros fault which strikes approximately NW-SE, perpendicular to the North Aegean trough (see Fig. 6.3) [*Melis et al.*, 2001; *Ganas et al.*, 2005]. The earthquake corresponds with the strain rate field derived in chapter 5.3 which indicates moderate left-lateral shear and extension for a fault striking approximately 150°.

Hollenstein et al. [2008b] derived coseismic displacements from repeated GPS measurements performed at the sites NSKR and CG38. They compared the results with an analytical dislocation model (Table 6.5). Additional measurements carried out in the years 2007 and 2008 led to slightly different displacements compared to those derived in *Hollenstein et al.* [2008b]. The differences are not significant on the 95% level but accuracy and reliability of the estimates improved (Table 6.6). However, the new results do not better fit the modeled dislocations. The GPS derived displacements are larger than the modeled dislocations by a factor 2–4.5. The agreement in direction is within 25°.

The difference between observed displacements and calculated dislocations can be associated with a suboptimal modeling of the earthquake (magnitude of slip, dimensions and location of the rupture plane) and/or the presence of significant postseismic displacements during the following two months.

It can be expected from the Okada model that the islands of Skopelos and Alonissos were displaced by the earthquake by 7–16 mm towards ESE. Therefore, measurements of sites CG11 and CG12 prior to the earthquake were omitted for the calculation of interseismic velocities. No coseismic displacements were derived for these two sites since the only measurements of these sites before the earthquake were performed in 1993 (cmp. chapter 3.6.3). According to the analytical model coseismic displacements are found as far as site DION (~2 mm towards SSW, see Fig. 6.3 and Table 6.1). The 2001 Skyros earthquake is visible in the north component of the detrended time series of DION (Fig. 6.2) although not as a sharp offset but as transient motion within the following 60 days. A data gap starting 4 days after the earthquake and lasting 11 days might indicate site-specific irregularities. However, only about one-third of the motion is attributed to this time period. The derived displacement is similarly directed as the coseismic dislocation based on the Okada model but is larger by a factor 2 (Fig. 6.3 and Table 6.1). The displacement is modeled by an offset in the time series in order to derive a most accurate interseismic velocity for site DION. The rates change due to this additional discontinuity by 0.23 and 0.29 mm/yr in the east and north components, respectively.

In conclusion, the 1999 Athens and the 2001 Skyros earthquakes most likely influenced the time series of DION. *Hollenstein* [2006] already mentioned signals possibly related to the two earthquakes but did not further elaborate this topic. The signals retrieved in this thesis are small (<4 mm).

Their temporal characteristics remain partly indistinct. The modeling of offsets associated with the two earthquakes changes the interseismic rates by 0.45 and 0.28 mm/yr in the east and north components, respectively. These differences are larger than the indicated errors of the long-term rates by a factor 2–5. The dependency of the estimated offsets of site DION on the applied velocity model is outlined in Table 6.4. The differences are partly above the margin of errors but are not substantial with respect to the derived conclusions.

6.4.3 2008 Mw 6.4 Rhodes earthquake

The 2008 Mw 6.4 earthquake on 15 July 2008 was located in the southwestern part of Rhodes (location: 27.86°E, 35.80°N, depth: 52 km [*NEIC catalog*, 2009]). A plane striking $\sim 265^\circ$ and dipping $\sim 85^\circ$ was identified as the most likely rupture plane for the strike-slip earthquake [*Zahradnik et al.*, 2008]. The kinematic and strain rate fields in the SE Aegean sea are discussed in chapters 4.5.2 and 5.3, respectively. Left-lateral shear strain and compression along the Pliny trench correspond with the earthquake mechanism. A rather small displacement was observed for site ARHA (East: -1 ± 1 mm, North: -2 ± 1 mm, Up: 0 ± 1 mm). No data is available from the closest located site KATC to derive a coseismic displacement.

6.5 Earthquakes in the Ionian sea

6.5.1 1997 Mw 6.6 Strofades earthquake

The Mw 6.6 Strofades earthquake (location: 20.66°E, 37.57°N, depth: 33 km [*NEIC catalog*, 2009]) on 18 November 1997 was located 20 km southwest of Zakynthos. The earthquake is best modeled by two sources. Both events had reverse-faulting mechanisms. The second event followed the first one by ~ 9 s in a distance of 30 km directed ESE. It had a larger strike-slip component and a two times larger seismic moment [*Kiratzi and Lowari*, 2003]. The event is sparsely discussed in literature.

No additional geodetic data is available compared to *Hollenstein* [2006] that would provide new insights into the associated displacement field. Site STRF moved 118 mm to the south and was uplifted by 83 mm. Site KERI moved 20 mm towards SSW and subsided by 1 mm (Tab. 6.1 and Fig. 6.10). Dislocations were calculated by using an elastic dislocation model assuming two subevents separated by 30 km. The location of the first event was set identical to the location of the single source event published in *NEIC catalog* [2009]. The modeled dislocations at sites KERI and STRF are by magnitudes too small suggesting, given the applicability of the model, a too deep location of the rupture plane. The locations of the subevents are uncertain. The Institute of Geodynamics of the National Observatory of Athens located the earthquake (single source) 38 km farther SSW compared to the USGS at 5 km depth. A corresponding moment tensor was not published. A depth of 5 km for a thrusting-type earthquake west of Zakynthos is more plausible with respect to seismic profiles (e.g., *Laigle et al.* [2002]). It was refrained from indicating modeled dislocations due to sparse knowledge of the earthquake parameters.

The observed uplift (~ 8 cm) at site Strofades is well confirmed by independent tide-gauge measurements [*Hollenstein et al.*, 2006]. However, a direct link to elastic dislocations is questionable. *Stiros* [2005] explained the large uplift by faulting in the crystalline basement causing a reorganization of overlying evaporites and a consecutive piston-type uplift of the overburden.

	Lon [°]	Lat [°]	Depth [km]	Strike [°]	Dip [°]	Rake [°]	Length [km]	Width [km]	Slip [m]
Subevent 1	20.575	38.770	17.5	12	81	174	25	15	0.175
Subevent 2	20.450	38.475	17.5	20	63	-179	15	15	0.140

Table 6.7: Parameters employed for modeling the two largest subevents of the 2003 Mw 6.2 Lefkada earthquake.

6.5.2 2003 Mw 6.2 Lefkada earthquake

The Mw 6.2 Lefkada earthquake occurred on the Lefkada segment of the Kefalonia fault zone on 14 August 2003. It is optimally modeled by multiple consecutive subevents. The largest two events were right-lateral strike-slip earthquakes separated by approximately 30 km (Fig. 6.4) [Benetatos *et al.*, 2005, 2007; Zahradnik *et al.*, 2005].

Additional data of continuous and campaign-type sites located on the Ionian islands have been evaluated compared to Hollenstein *et al.* [2008b]. This effort enabled an improved estimation of the coseismic displacements at the sites 1KVL, DUKA and FISK. Differences between the values obtained in this study and the values derived by Hollenstein *et al.* [2008b] are within the margins of error except for site DUKA (Tables 6.1 and 6.6). In addition, a small displacement of the CGPS site SKIN associated with the Lefkada earthquake was derived (2 mm directed south, Fig. 6.5). The displacement is hardly significant. The time series of SKIN exhibits conspicuous signals beginning about one year prior to this event and ending at the end of 2003 (appendix B.5). A relation between these signals and the earthquake is speculative.

Modeling of the Lefkada earthquake by an Okada model reveals a suboptimal fit whether employing a single event or two subevents [Hollenstein *et al.*, 2008b]. The resulting dislocations by modeling this event with two sources is shown in Figure 6.4. Position, strike, dip, rake and seismic moment of the two subevents were set according to Benetatos *et al.* [2005]. The length, width and depth of the rupture planes correspond approximately with those found by Benetatos *et al.* [2007]. The slip was set to fit the seismic moments corresponding to Mw 6.0 and Mw 5.8 earthquakes, respectively. The used parameters are listed in Table 6.7. The calculated dislocations are too small by a magnitude compared with GPS derived displacements on Lefkada and Kefalonia. The slip directions agree within 27°. The spatial extent of the displacement field is fairly well determined by the model (see the displacements of sites APAX, GERO, LKTR and SKIN). However, the calculated dislocations are less sensitive to variations in the model parameters with increasing distance to the earthquake (cmp. chapter 6.5.4). The GPS derived displacements with respect to the Lefkada earthquake are based on measurements obtained about one month after the event. The discrepancy between model and observations suggests that significant fractions of the observed displacements are not associated with the two mainshocks and are of postseismic nature.

6.5.3 2006 Zakynthos earthquake series

Six earthquakes with magnitudes between Mw 5.0 and Mw 5.7 occurred south of Zakynthos between 3 and 19 April 2006 [NEIC catalog, 2009]. They were all of thrusting-type mechanism (Fig. 6.10). During this period of increased seismic activity the site KERI located on the south-western tip of the island moved 10 ± 1 mm to WSW [East: -10 ± 1 mm; North: -2 ± 1 mm; Up: 8 ± 1 mm]. The displacement cannot exactly be associated with particular earthquakes due to the noise in the time series and the short time lag between the events (Fig. 6.6). However, it seems that most of the displacement in the east component occurred between 11 and 13 April when three earthquakes with magnitudes Mw 5.5–5.7 were reported. Data of the campaign-type site KSSI indicates a displacement in the order of 28 ± 8 mm towards NE. This estimate is based on measurements

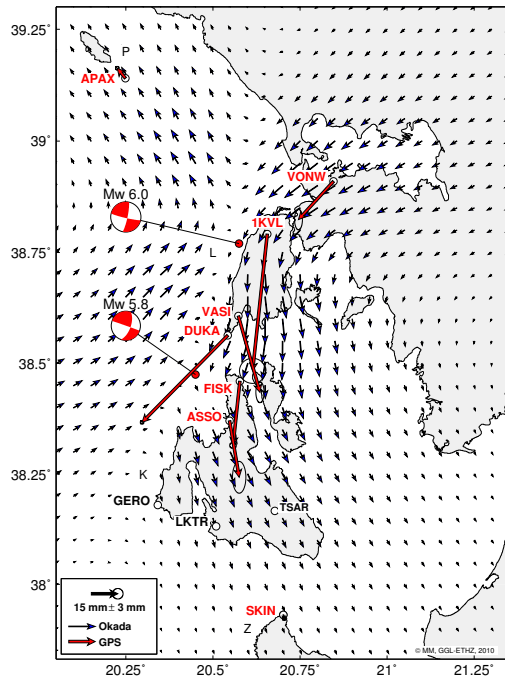


Figure 6.4: Comparison of the modeled dislocation field (blue arrows) and GPS derived coseismic displacements (red arrows) related to the Mw 6.2 Lefkada earthquake. The parameters used for modeling the two subevents are listed in Table 6.7. The depicted fault plane solutions of the two major subevents were derived by *Benetatos et al.* [2005]. The error ellipses depict the 1- σ confidence region. K: Kefalonia, L: Lefkada, P: Paxi, Z: Zakynthos.

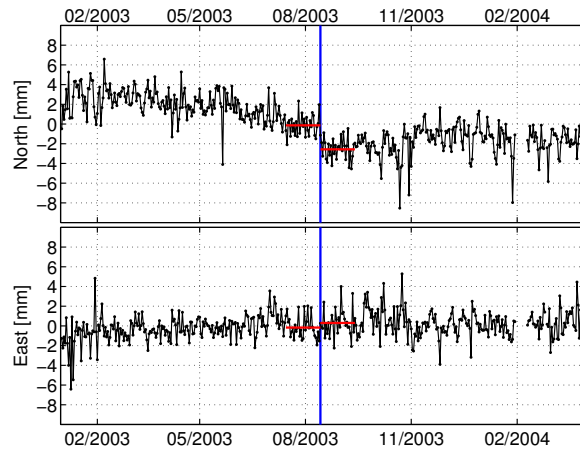


Figure 6.5: Time series of the north and east components (linear trend removed), respectively, of site SKIN between January 2003 and March 2004 (see Fig. B.6 (a) for the complete time series). The blue line depicts the 2003 Mw 6.2 Lefkada earthquake. The red horizontal lines depict the average positions over 30 days before and after the earthquake. The difference between the average positions indicates a displacement of -2 ± 1 mm and 1 ± 1 mm in the north and east components, respectively.

carried out in the years 1999, 2002 and 2006 (May 22–23).

The same area was already struck by a Mb 4.9 and a Mw 5.6 earthquake on October 18, 2005 [*EMSC catalog*, 2009]. No data of site KERI is available for the relevant days due to a 60 days lasting data gap. If an additional offset related to these reverse faulting earthquakes is modeled in the time series of KERI a small displacement amounting to -2 ± 1 mm, 1 ± 1 mm and 4 ± 1 mm in the east, north and up components, respectively, is obtained. Concurrently with this model change the displacement related to the April 2006 earthquakes slightly changes to -8 ± 1 mm, -3 ± 1 mm and 5 ± 1 mm in the east, north and up components, respectively. The long-term rates of KERI only change by 0.04 mm/yr, -0.02 mm/yr and -0.10 mm/yr in the east, north and up components, respectively. It is possible that the October 2005 earthquakes caused a small displacement towards ENE at site KERI. The October 2005 earthquakes might be closely related to the seismic sequence in April 2006.

The earthquake series south of Zakynthos is likely related to ongoing subduction processes. *Serpentidaki et al.* [2010] recently relocated the events of the earthquake series. They located the three largest earthquakes in a depth of about 13 km and interpreted them to have occurred on the interplate subduction boundary. Thrusting type earthquakes in this depth are in agreement with the supposed location of the plate interface beneath southern Zakynthos [*Laigle et al.*, 2002]. The reported depth (~ 13 km) of the thrusting-type earthquakes and the west-southwestward displacement of site KERI suggest relative motion between the overriding and the subducting plate.

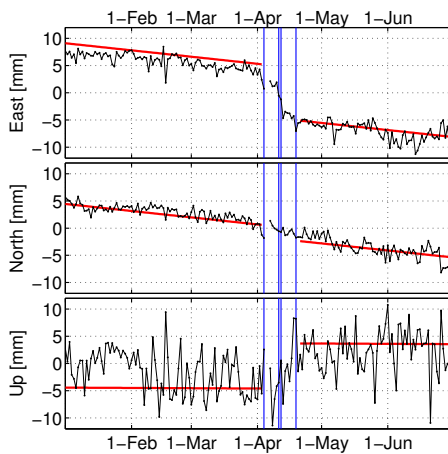


Figure 6.6: Time series of site KERI in the first half of 2006. The blue lines indicate events of the earthquake series with magnitudes between Mw 5.0 and Mw 5.7. The site moved 10 ± 1 mm to the west-southwest and was uplifted by 8 ± 1 mm during this time. The red lines depict linear site motion estimated based on data of the period 1995–2009.

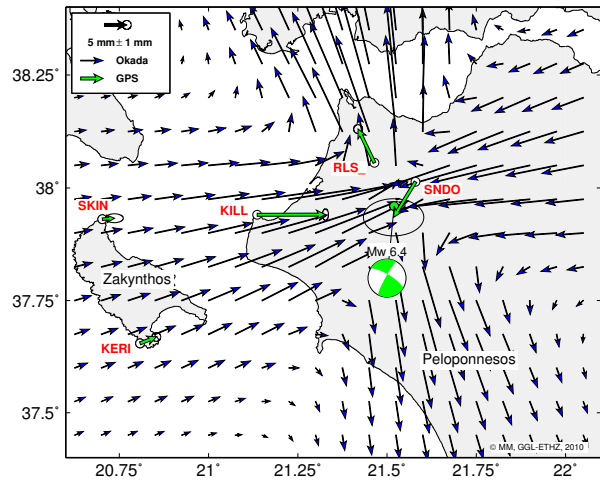


Figure 6.7: Comparison of the modeled dislocation field (blue arrows) and GPS derived coseismic displacements (green arrows) related to the Mw 6.4 NW Peloponnesos earthquake. The parameters used for the Okada model are listed in Table 6.5. The depicted fault plane solution and its position are extracted from *CMT catalog* [2011] and *NEIC catalog* [2009], respectively. The error ellipses depict the 1- σ confidence region.

The GPS derived slip at site KERI, including the uplift, is in agreement with the dislocation model describing strain accumulation at subduction zones employed in chapter 4.5.1. It is not clear to which extent the displacement at site KSSI is compatible with this interpretation. An artifact in the measuring process at site KSSI cannot be excluded due to the number of available measurements.

6.5.4 2008 Mw 6.4 NW Peloponnesos earthquake

The Mw 6.4 NW Peloponnesos earthquake on 8 June 2008 was located at 37.96°N , 21.52°E [*NEIC catalog*, 2009]. It was a right-lateral strike-slip event, the fault plane trending NE-SW [*Ganas et al.*, 2009]. Fault plane solutions of previous earthquakes on the NW Peloponnesos also indicate strike-slip faulting (*Kiratzis and Lowari* [2003]; cmp. Fig. 6.11). The derived velocity solution provides coseismic displacements for the campaign-type sites KILL and SNDO and for the continuous sites KERI, RLS_ and SKIN (Table 6.1). In Figure 6.7 these displacements are compared with dislocations derived with an analytical model based on parameters published by *Ganas et al.* [2009] (Table 6.5). The agreement between GPS displacements and calculated dislocations is within 2 mm in magnitude and within 11° in direction for the sites KERI, KILL and SKIN. A less optimal fit results for the sites RLS_ and SNDO which are located at shorter distances to the rupture plane. The GPS derived displacement for site RLS_ is smaller than the calculated dislocation by 5.0 mm. They agree within 13° in direction. The difference between observed and modeled displacements at site SNDO amounts to 6.4 mm in magnitude and 49° in direction, respectively. The site is located close to the northeastward prolongation of the rupture plane where dislocations are very sensitive to variations in fault location and strike. Moreover, the accuracy of the GPS displacement for SNDO is low (7 mm and 4 mm in the east and north components, respectively).

Parameter		Range	Steps	Optimal set
Length	[km]	6–25	20	14
Width	[km]	4–25	22	11
Depth	[km]	16–30	15	24
Dip	°	62–90	8	78
Strike	°	200–230	11	212
Rake	°	175	-	-
Slip	[m]	0.24–1.24	21	1.19
Longitude	°	21.52	-	-
Latitude	°	37.99	-	-

Table 6.8: Parameter space employed for the sensitivity analysis. Steps denote the number of discrete values within the defined range. The parameter set providing the best fit is indicated in the last column.

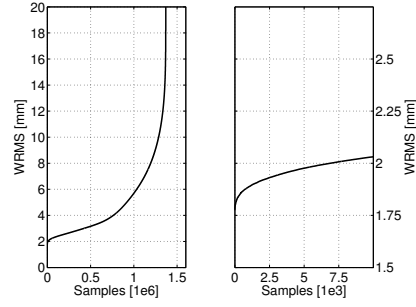


Figure 6.8: WRMS of all $1.4 \cdot 10^6$ samples and the WRMS of the 10^4 best samples.

It was analyzed if the variation of some of the Okada parameters indicated by *Ganas et al.* [2009] provides a better fit to the GPS derived displacements. A search space was defined by setting lower and upper limits for the parameters (Tab. 6.8). A large number of Okada models was calculated by systematically exploring the parameter space. The earthquake location and the rake were kept constant. Parameter sets were rejected when defining physically impossible models, indicating a moment magnitude considerably different from $M_w 6.4$ ($|M_w - 6.4| > 0.1$) or describing a rupture plane with $W > L$. The weighted RMS was calculated based on the model residuals whereas the up component was included only for CGPS sites (Fig. 6.8). The parameter sets and the corresponding displacements of the 10^4 best models are shown in Figure 6.9 (a) and (b).

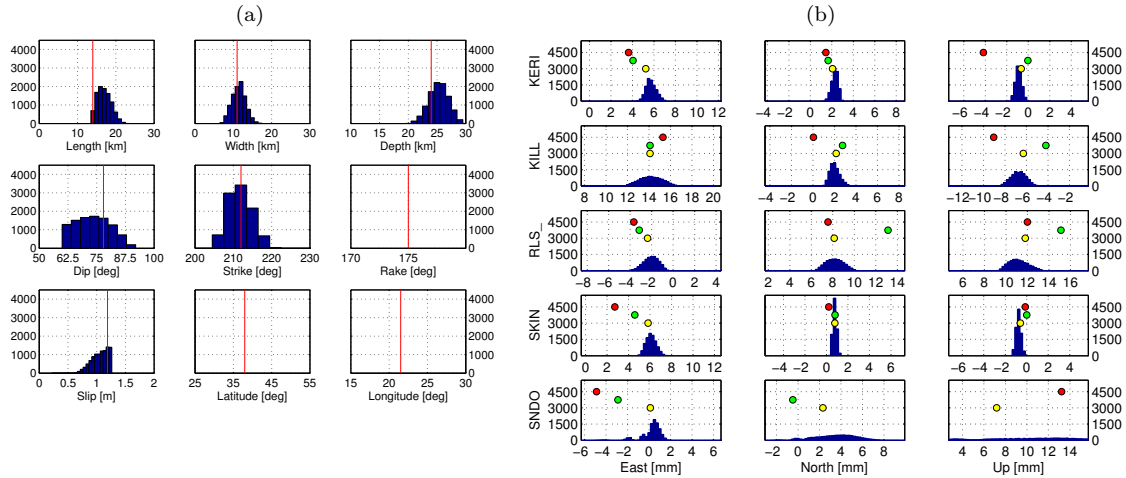


Figure 6.9: (a) Histograms of the parameter values corresponding to the parameter sets providing the 10^4 best fitting models. The earthquake location (longitude, latitude) and the rake were kept constant. The parameter values of the optimal model are depicted as red lines. (b) Resulting dislocations at the GPS sites KERI, KILL, RLS, SKIN and SNDO by using the parameter sets depicted in (a). The red circles depict GPS derived displacements, the green circles depict dislocations calculated with the parameters listed in Table 6.5 and the yellow circles depict the dislocations resulting from the best parameter set derived.

The optimal parameter set obtained do not largely differ from the values derived by *Ganas et al.* [2009] except for the earthquake depth and the slip. Nonetheless, it provides a slightly better fit to the geodetically derived displacements (WRMS: 1.8 mm compared with 2.6 mm). Dislocations at short distances to the earthquake are most sensitive to variations in the Okada parameters. The optimal earthquake depth is 24 km depending largely on the displacement of site RLS_. Modeled dislocations on Zakynthos located at distances of ~ 70 km from the earthquake are quite

insensitive to this parameter. Varying the earthquake depth between 12 and 24 km while keeping the other parameters of *Ganas et al.* [2009] constant changes the displacement at site KERI by less than 0.6 mm. The unbalanced distribution of the GPS sites with respect to the rupture plane is likely the cause of large correlations between the dip angle and the depth considering the 10^4 best parameter sets ($\rho_{corr} = -0.62$). The contribution of SNDO to the WRMS is small due to the low accuracy of its displacement. Rake angles of 170° and 180° instead of 175° do not lead to largely different conclusions.

The number and spatial distribution of the available GPS displacements are not sufficient to substantially improve the Okada parameters. *Feng et al.* [2010] already noted that the earthquake depth required for an optimal fit to the displacement of site RLS_ is not consistent with results of seismic studies. Only few of the relocated aftershocks occurred below 22 km depth [*Ganas et al.*, 2009]. Therefore, *Feng et al.* [2010] argued that the 3 km thick flysch layer located in the middle of the earthquake region acts as a near-surface decoupling agent. In contrast, the displacement of site KILL reasonably agrees with the modeled dislocation derived by using the parameters of *Ganas et al.* [2009]. The local deviations from the predicted displacement field supports the existence of structural differences in the earthquake region.

6.5.5 Comparison of seismicity and interseismic strain rates

Coseismic displacements related to four earthquakes in the region of the Ionian sea were obtained between 1997 and 2008 (Fig. 6.10 (a)). The focal mechanisms of the Lefkada and the Zakynthos earthquakes correspond with the kinematic and strain rate fields discussed in chapters 4.5.1 and 5.3, respectively. The 2003 Mw 6.2 Lefkada earthquake occurred along the KFZ where right-lateral shear strain rates of up to 200 nstrain/yr were derived (Fig. 6.10 (b)). The 2006 Zakynthos earthquakes (Mw 5.0–5.7) were reverse faulting events. They occurred in a zone where GPS rates point to compression. In contrast, the mechanism of the Mw 6.4 NW Peloponnesos earthquake is less clearly indicated in the strain rate field as only moderate shear strain rates (<50 nstrain/yr) are encountered on the NW Peloponnesos (Fig. 6.10 (b)). The location of the two subevents of the 1997 Strofades earthquake are not surrounded by GPS sites. A comparison of the earthquake mechanisms and the geodetic strain rates is not possible.

Roumelioti et al. [2007] relocated earthquakes in western Greece having occurred in the period 2000–2005 by merging phase data of three different seismic catalogs. The results show several features which are not indicated by the GPS derived strain rate field. For instance, they observed an almost complete absence of epicenters between Kefalonia and Acarnania and only few seismicity around the Gulf of Arta and along the Katouna fault. A NW-SE trending seismic alignment between southern Kefalonia and the westernmost tip of the Peloponnesos may point to occasional left-lateral strike slip. There is not yet clear seismic evidence for sinistral strike-slip in this area [*Roumelioti et al.*, 2004] but it can be surmised from the strain rate field (Fig. 6.10 (b)).

Horizontal projections of P-axes of earthquakes in the upper crust (depth < 20 km) are directed E-W to NE-SW along the KFZ and the westernmost WHT while the T-axes are directed N-S along the Gulf of Corinth [*Kiratzis and Louvari*, 2003; *Benetatos et al.*, 2004]. In addition, the maximum compressive stress axis on NW Peloponnesos is directed 273° [*Konstantinou et al.*, 2011]. This is in good agreement with the geodetically derived strain rates (Fig. 6.10 (b)). The close vicinity (~ 100 km) of the extensional zone between the Gulfs of Arta and Corinth and the possibly locked subduction interface west of Kefalonia and Zakynthos poses the question of the involved dynamics. Compression between NW Peloponnesos and Kefalonia (Fig. 6.10 (b)) and strike-slip faulting along the western Peloponnesos (Fig. 6.11) might indicate faster retreat of the Nubian slab south of Zakynthos than north of it.

Site KERI was displaced by three earthquakes between 1997 and 2008 (inset in Fig. 6.10 (a)). The

subduction related thrusting-type earthquakes (1997 Strofades and 2006 Zakynthos) moved the site towards the trench (20 mm directed 211° and 10 mm directed 257° , respectively). The directions of these displacements are not very different from the direction of the interseismic velocity (225°). The NW Peloponnesos earthquake (strike-slip faulting) caused a displacement in opposite direction (4 mm directed 69°).

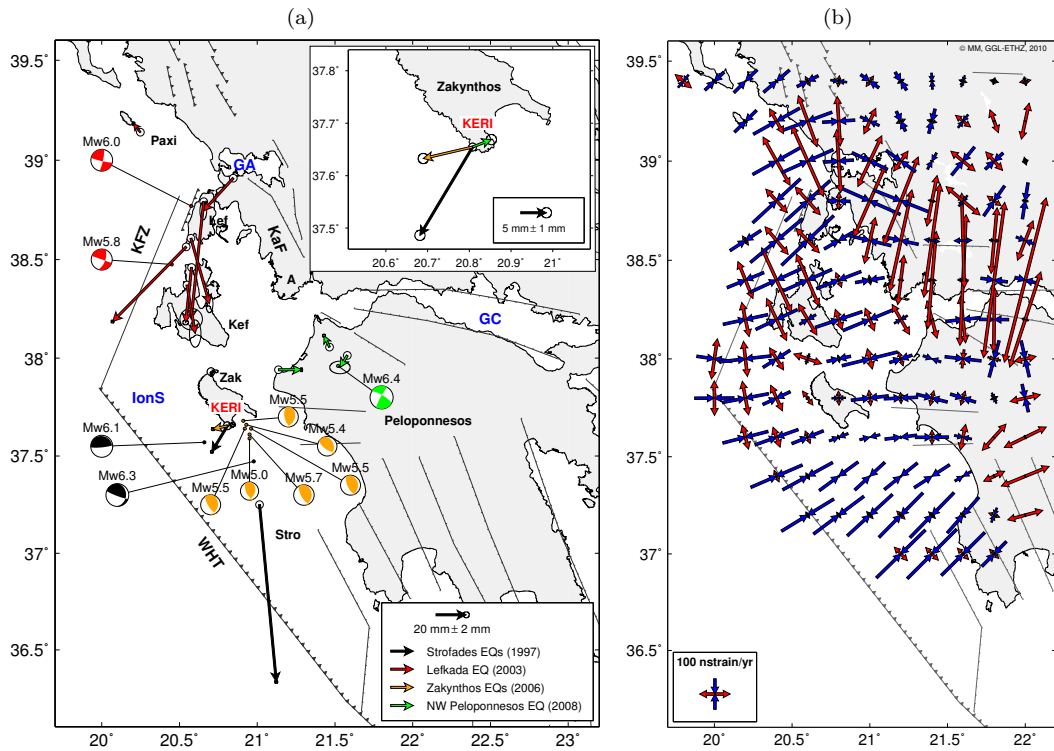


Figure 6.10: (a) Compilation of GPS derived coseismic displacements in the Ionian sea region in the period 1995–2008. The colors of the displacements correspond to the colors of the particular fault plane solutions (FPS). The inset shows displacements of site KERI on Zakynthos which was displaced by three earthquakes (1997 Strofades, 2006 Zakynthos, 2008 NW Peloponnesos). The error ellipses depict the $1\text{-}\sigma$ confidence region. Positions and FPS of the Zakynthos and NW Peloponnesos earthquakes were extracted from *NEIC catalog* [2009] and *CMT catalog* [2011], respectively. The position of the first subevent of the Strofades earthquake was extracted from the *NEIC catalog*. The distance to the second subevent and the FPS of both subevents were extracted from *Kiratzí and Louvarí* [2003]. Positions and FPS of the Lefkada subevents were derived by *Benetatos et al.* [2005]. A: Acarnania, GA: Gulf of Arta, GC: Gulf of Corinth, IonS: Ionian sea, KaF: Katouna Fault, Kef: Kefalonia, KFZ: Kefalonia fault zone, Lef: Lefkada, Stro: Strofades island, WHT: West Hellenic trench, Zak: Zakynthos. (b) Principal axes of the GPS derived strain rate field near the central Ionian islands for the period 1993–2009 (cmp. Fig. 5.7). A correlation length of 60 km and a σ_0 of 5 mm were used for the calculations. Red arrows depict extension, blue arrows depict compression.

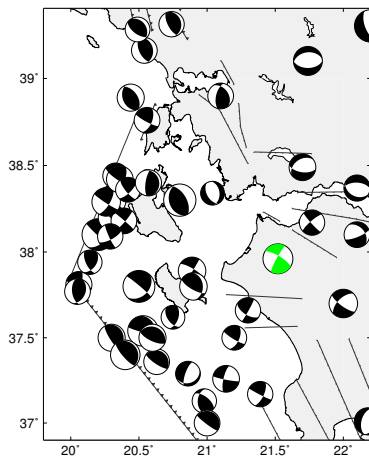


Figure 6.11: Fault plane solutions (FPS) in the region of the central Ionian islands determined by waveform modeling and by first motion polarities [*Kiratzí and Louvarí* [2003] and references therein]. The FPS represent earthquakes between 1953 and 1999. The green FPS depicts the 2008 NW Peloponnesos earthquake. Its position and FPS were extracted from *NEIC catalog* [2009] and *CMT catalog* [2011], respectively.

6.6 Concluding remarks

The analysis of seismic signals in continuous and campaign-type GPS time series in Greece led to the following conclusions:

- Displacements related to the 2006 Zakynthos earthquake series, the 2008 NW Peloponnesos earthquake and the 2008 Rhodes earthquake were derived in this thesis in addition to the displacements related to earthquakes already discussed in former studies. GPS derived coseismic displacements provide constraints for the three-dimensional rupture process of the mainshock and the aftershocks.
- In general, the fault plane solutions of the earthquakes discussed correspond with the derived strain rate field. The 1999 Athens and the 2008 NW Peloponnesos earthquakes occurred in areas of moderate strain rates (40–80 nstrain/yr). A further increase in accuracy and spatial resolution of strain rate estimates could improve seismic hazard assessment.
- The accuracy and reliability of the displacements depend largely on the frequency of available position estimates. Daily position estimates from continuous GPS yield significantly better results than campaign-type GPS. The difficulty of separating coseismic and postseismic displacements is inherent in both measurement types though at different levels. Position estimates at high frequencies (>1 Hz) would improve the separation between co- and postseismic signals and possibly provide new insights into the earthquake rupture process.
- The comparison of GPS derived displacements with dislocations calculated by using an elastic dislocation model is expedient. Model dislocations reasonably agree with GPS derived displacements for the 2008 NW Peloponnesos earthquake. The fit is less optimal for the 1997 Strofades, the 2001 Skyros and the 2003 Lefkada earthquakes. Numerous reasons may cause a poor fit between observations and modeled dislocations (e.g., geodetic estimates including postseismic motion, inaccurate earthquake parameters, geologic structures not compatible with an elastic halfspace). The improvement of earthquake parameters based on geodetic estimates was analyzed for the 2008 NW Peloponnesos earthquake. The parameter set was not substantially enhanced due to the small number of accurate GPS displacements and the in parts large distances between the GPS sites and the earthquake center. The comparison of GPS derived displacements and dislocations calculated by using the Okada model supports the existence of structural inhomogeneities in the region of the NW Peloponnesos earthquake.
- The presence of co- and postseismic signals at site DION related to the 1999 Athens and the 2001 Skyros earthquakes was investigated. Though the temporal characteristics of the signals are not entirely resolved, a relation to the earthquakes is highly suggested. The distinction between coseismic and postseismic motion remains challenging when displacements are in the range of the scatter.

7 Finite element models

7.1 Finite element method

7.1.1 Basic theory

The finite element method (FEM) is a powerful tool for solving problems in continuums described by differential equations and boundary conditions imposed on the unknown function or functions. The continuum is divided into a finite number of parts (elements) whose behavior is specified by a finite number of parameters. The solution of the complete system as an assembly of its elements follows precisely the same rules as those applicable to standard discrete systems. FEM is applied in many fields of science and engineering. The corresponding theory is a wide area and extensively discussed in various textbooks. FEM is used in this thesis to derive displacements, strains and stresses as a result of imposed displacements at the model border. Only the basic principles related to this approach shall be outlined in this chapter. The following explanations (including chapter 7.1.2) are based on *Zienkiewicz and Taylor [2000]*.

In principle, FEM is used for problems where a function \mathbf{u} is searched which satisfies a certain set of differential equations in a 'domain' Ω (volume, area, etc.) with certain boundary conditions on the boundaries Γ of the domain (Fig. 7.1):

$$\mathbf{A}(\mathbf{u}) = (A_1(\mathbf{u}) \ A_2(\mathbf{u}) \ \dots)^T = \mathbf{0} \quad \text{in } \Omega \quad (7.1)$$

$$\mathbf{B}(\mathbf{u}) = (B_1(\mathbf{u}) \ B_2(\mathbf{u}) \ \dots)^T = \mathbf{0} \quad \text{on } \Gamma \quad (7.2)$$

The finite element process seeks the solution in the approximate form

$$\mathbf{u} \sim \hat{\mathbf{u}} = \sum_{i=1}^n N_i \mathbf{a}_i = \mathbf{N} \mathbf{a} \quad (7.3)$$

where N_i are shape functions prescribed in terms of independent variables (such as the coordinates, etc.) and \mathbf{a}_i are the unknown parameters (in our case: the displacements). The unknown

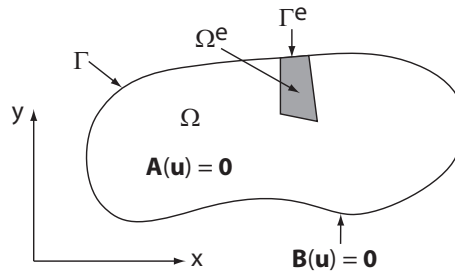


Figure 7.1: Problem domain Ω and boundary Γ . The shaded polygon depicts one element.

parameters \mathbf{a}_i are obtained from the equation

$$\int_{\Omega} \mathbf{G}_j(\hat{\mathbf{u}})d\Omega + \int_{\Gamma} \mathbf{g}_j(\hat{\mathbf{u}})d\Gamma = \mathbf{0} \quad j=1 \text{ to } n \quad (7.4)$$

where \mathbf{G}_j and \mathbf{g}_j are known functions or operators. These integral forms permit the approximation to be obtained element by element, providing the functions \mathbf{G}_j and \mathbf{g}_j are integrable,

$$\int_{\Omega} \mathbf{G}_j d\Omega + \int_{\Gamma} \mathbf{g}_j d\Gamma = \sum_{e=1}^m \left(\int_{\Omega_E} \mathbf{G}_j d\Omega + \int_{\Gamma_E} \mathbf{g}_j d\Gamma \right) = \mathbf{0} \quad (7.5)$$

where Ω_E is the domain of each element and Γ_E its part of the boundary. One procedure to find the approximation in integral forms like Eq. (7.5) is the determination of variational functionals for which stationarity is sought.

The variational principle specifies a scalar quantity (functional) Π , which is defined by an integral form

$$\Pi = \int_{\Omega} F \left(\mathbf{u}, \frac{\partial \mathbf{u}}{\partial x}, \dots \right) d\Omega + \int_{\Gamma} E \left(\mathbf{u}, \frac{\partial \mathbf{u}}{\partial x}, \dots \right) d\Gamma \quad (7.6)$$

where \mathbf{u} is the unknown function and E and F are specified differential operators. The solution to the continuum problem is a function \mathbf{u} which makes Π stationary with respect to arbitrary changes $\delta \mathbf{u}$. Thus, for a solution to the continuum problem, the variation is

$$\delta \Pi = 0 \quad (7.7)$$

Inserting the trial function expansion Eq. (7.3) into Eq. (7.6) yields

$$\delta \Pi = \frac{\partial \Pi}{\partial \mathbf{a}_1} \delta \mathbf{a}_1 + \frac{\partial \Pi}{\partial \mathbf{a}_2} \delta \mathbf{a}_2 + \dots + \frac{\partial \Pi}{\partial \mathbf{a}_n} \delta \mathbf{a}_n \quad (7.8)$$

This being true for any variations $\delta \mathbf{a}$ yields a set of equations

$$\frac{\partial \Pi}{\partial \mathbf{a}} = \begin{pmatrix} \frac{\partial \Pi}{\partial \mathbf{a}_1} \\ \vdots \\ \frac{\partial \Pi}{\partial \mathbf{a}_n} \end{pmatrix} = \mathbf{0} \quad (7.9)$$

from which the parameters \mathbf{a}_i are found.

According to the definitions of Eqs. (7.6) and (7.7) stationarity can be expressed, after performing some differentiations, by

$$\delta \Pi = \int_{\Omega} \delta \mathbf{u}^T \mathbf{A}(\mathbf{u})d\Omega + \int_{\Gamma} \delta \mathbf{u}^T \mathbf{B}(\mathbf{u})d\Gamma = 0 \quad (7.10)$$

The equation above must be true for any variations $\delta \mathbf{u}$ and thus

$$\mathbf{A}(\mathbf{u}) = \mathbf{0} \quad \text{in } \Omega \quad (7.11)$$

$$\mathbf{B}(\mathbf{u}) = \mathbf{0} \quad \text{in } \Gamma \quad (7.12)$$

7.1.2 Displacement-based finite element analysis

In a general three-dimensional continuum the equilibrium equations of an elementary volume can be written in terms of the components of the symmetric cartesian stress tensor as

$$\begin{pmatrix} A_1 \\ A_2 \\ A_3 \end{pmatrix} = \begin{pmatrix} \frac{\partial \sigma_x}{\partial x} + \frac{\partial \tau_{xy}}{\partial y} + \frac{\partial \tau_{xz}}{\partial z} \\ \frac{\partial \sigma_y}{\partial y} + \frac{\partial \tau_{xy}}{\partial x} + \frac{\partial \tau_{yz}}{\partial z} \\ \frac{\partial \sigma_z}{\partial z} + \frac{\partial \tau_{xz}}{\partial x} + \frac{\partial \tau_{yz}}{\partial y} \end{pmatrix} + \begin{pmatrix} b_x \\ b_y \\ b_z \end{pmatrix} = \mathbf{0} \quad (7.13)$$

where $\mathbf{b} = [b_x, b_y, b_z]^T$ stands for the body forces acting per unit volume. In solid mechanics the six stress components are a function of the components of the displacements

$$\mathbf{u} = [u, v, w]^T \quad (7.14)$$

Therefore, Eq. (7.13) corresponds to Eq. (7.11). Accordingly, inserting Eq. (7.13) into the first integral of Eq. (7.10) yields

$$\int_{\Omega} \delta \mathbf{u}^T \mathbf{A}(\mathbf{u}) d\Omega = \int_{\Omega} \left[\delta u \left(\frac{\partial \sigma_x}{\partial x} + \frac{\partial \tau_{xy}}{\partial y} + \frac{\partial \tau_{xz}}{\partial z} + b_x \right) + \delta v (A_2) + \delta w (A_3) \right] d\Omega = 0 \quad (7.15)$$

Integrating this equation by parts and rearranging yields

$$\int_{\Omega} \delta \boldsymbol{\varepsilon}^T \boldsymbol{\sigma} d\Omega - \int_{\Omega} \delta \mathbf{u}^T \mathbf{b} d\Omega - \int_{\Gamma} \delta \mathbf{u}^T \mathbf{t} d\Gamma = 0 \quad (7.16)$$

where $\delta \mathbf{u}$ are virtual displacements, $\delta \boldsymbol{\varepsilon}$ are virtual strains and \mathbf{t} are forces acting per unit area of the surface Γ . Virtual strains are related to virtual displacements by

$$\partial \varepsilon_{ij} = \frac{1}{2} (\partial u_{i,j} + \partial u_{j,i}) \quad (7.17)$$

Equation (7.16) is the three-dimensional equivalent virtual work statement. It is valid for non-linear as well as linear stress-strain (or stress-rate of strain) relations. Moreover, Eq. (7.16) can be considered as the variation of the total potential energy E_{pot} which is the sum of the strain energy of the system and the potential energy of the external loads. The total potential energy must be stationary ($\delta E_{pot} = 0$) to ensure an equilibrium. The total potential energy is minimum at the equilibrium configuration for linear elastic bodies [Reddy, 2002].

Remarks:

1. If the differential equations (7.1) and (7.2) are linear and can be written as

$$\mathbf{A}(\mathbf{u}) \equiv \mathbf{L}(\mathbf{u}) + \mathbf{p} = \mathbf{0} \quad \text{in } \Omega \quad (7.18)$$

$$\mathbf{B}(\mathbf{u}) \equiv \mathbf{M}(\mathbf{u}) + \mathbf{t} = \mathbf{0} \quad \text{on } \Gamma \quad (7.19)$$

then the approximating equation system will yield a set of linear equations of the form

$$\mathbf{K} \mathbf{a} + \mathbf{f} = \mathbf{0} \quad \text{with} \quad \mathbf{K}_{ij} = \sum_{e=1}^m \mathbf{K}_{ij}^e \quad \text{and} \quad \mathbf{f}_i = \sum_{e=1}^m \mathbf{f}_i^e \quad (7.20)$$

2. In an isotropic, linear-elastic medium Eq. (7.16) is a linear function of the displacements \mathbf{u} . The stress $\boldsymbol{\sigma}$ depends on the elastic moduli (i.e., the Young's modulus E and the Poisson's ratio ν), the strain $\boldsymbol{\varepsilon}$, the initial strains $\boldsymbol{\varepsilon}_0$ and the initial stresses $\boldsymbol{\sigma}_0$. The strain $\boldsymbol{\varepsilon}$ is a linear function of the displacements \mathbf{u} .

$$\underbrace{\begin{pmatrix} \sigma_{xx} \\ \sigma_{yy} \\ \sigma_{zz} \\ \sigma_{xy} \\ \sigma_{yz} \\ \sigma_{zx} \end{pmatrix}}_{\boldsymbol{\sigma}} = \frac{E}{1-\nu-2\nu^2} \underbrace{\begin{pmatrix} 1-\nu & \nu & \nu & 0 & 0 & 0 \\ \nu & 1-\nu & \nu & 0 & 0 & 0 \\ \nu & \nu & 1-\nu & 0 & 0 & 0 \\ 0 & 0 & 0 & 1-2\nu & 0 & 0 \\ 0 & 0 & 0 & 0 & 1-2\nu & 0 \\ 0 & 0 & 0 & 0 & 0 & 1-2\nu \end{pmatrix}}_D \cdot (\boldsymbol{\varepsilon} - \boldsymbol{\varepsilon}_0) + \boldsymbol{\sigma}_0 \quad (7.21)$$

$$\underbrace{\begin{pmatrix} \varepsilon_{xx} \\ \varepsilon_{yy} \\ \varepsilon_{zz} \\ \varepsilon_{xy} \\ \varepsilon_{yz} \\ \varepsilon_{zx} \end{pmatrix}}_{\boldsymbol{\varepsilon}} = \begin{pmatrix} \frac{\partial}{\partial x} & 0 & 0 \\ 0 & \frac{\partial}{\partial y} & 0 \\ 0 & 0 & \frac{\partial}{\partial z} \\ \frac{\partial}{\partial y} & \frac{\partial}{\partial x} & 0 \\ 0 & \frac{\partial}{\partial z} & \frac{\partial}{\partial y} \\ \frac{\partial}{\partial z} & 0 & \frac{\partial}{\partial x} \end{pmatrix} \cdot \begin{pmatrix} u \\ v \\ w \end{pmatrix} = \mathbf{S} \cdot \mathbf{u} \quad (7.22)$$

With Eq. (7.3) we obtain for the variables \mathbf{K} and \mathbf{f} of Eq. (7.20)

$$\mathbf{K} = \int_{\Omega} \mathbf{N}^T \mathbf{S}^T \mathbf{D} \mathbf{S} \mathbf{N} d\Omega = \int_{\Omega} \mathbf{C}^T \mathbf{D} \mathbf{C} d\Omega \quad (7.23)$$

$$\mathbf{f} = - \int_{\Omega} \mathbf{N}^T \mathbf{b} d\Omega - \int_{\Omega} \mathbf{C}^T \mathbf{D} \boldsymbol{\varepsilon}_0 d\Omega + \int_{\Omega} \mathbf{C}^T \boldsymbol{\sigma}_0 d\Omega - \int_{\Gamma} \mathbf{N}^T \mathbf{t} d\Gamma \quad (7.24)$$

7.2 Physical properties of a model lithosphere

7.2.1 Introductory notes

Various rheological behaviors (deformational response to applied loads) are attributed to the numerous rock types. The type of response depends not only on the specific rock but also on parameters such as temperature, pressure and time [Ranalli, 1987]. At low pressure and room temperature most rocks are brittle. They deform elastically until they fail by fracture. At confining pressures near the brittle strength of the rock, a transition from brittle to ductile behavior occurs. Creep processes become important at temperatures near the melt temperature [Turcotte and Schubert, 2002]. In contrast to oceanic plates the composition and thermal structure of continental domains are not yet fully resolved [Jackson, 2002; Burov, 2007]. The three main deformation processes in the lithosphere are elasticity, brittle failure and ductility. The processes are outlined in chapters 7.2.2 to 7.2.4 in the scope required for the developed models. An elementary temperature model is described in chapter 7.2.5 since creep processes depend largely on temperature. More extensive discussions of deformation processes and rheologic models are found in various textbooks.

7.2.2 Elasticity

In an elastic body strains are proportional to applied stresses and independent of loading rates. In isotropic elastic solids the principal axes of strain $\boldsymbol{\varepsilon}$ and stress $\boldsymbol{\sigma}$ coincide. The strain-stress relation in an isotropic, linear-elastic solid can be formulated by

$$\varepsilon_{ij} = \frac{1+\nu}{E} \sigma_{ij} - \frac{\nu}{E} \sigma_{kk} \delta_{ij} \iff \sigma_{ij} = \frac{E\nu}{(1+\nu)(1-2\nu)} \varepsilon_{kk} \delta_{ij} + \frac{E}{(1+\nu)} \varepsilon_{ik} \quad (7.25)$$

where repeating indices mean summation, δ denotes the Kronecker's operator, E denotes the Young's modulus and ν denotes the Poisson's ratio [Fridtjov, 2008].

7.2.3 Brittle failure

In a tectonic context failure of materials such as rocks occurs mostly related to shear fracture. Brittle strength of rocks depends on pressure and increases with depth. Several empirical laws describe the onset of brittle-plastic deformation for given conditions [Burov, 2007]. In principle, a yield criterion is formulated which defines when a material behaves purely elastically and when the material starts to yield leading to plastic strains. If $f(\boldsymbol{\sigma})$ is a scalar-valued function of the stress tensor $\boldsymbol{\sigma}$ then the yield criterion for elastic-perfectly plastic materials is according to Fridtjov [2008]:

$$\begin{aligned} f(\boldsymbol{\sigma}) &= 0 \Rightarrow \text{yielding may start} \\ f(\boldsymbol{\sigma}) &< 0 \Rightarrow \text{elastic behavior} \\ f(\boldsymbol{\sigma}) &> 0 \Rightarrow \text{not acceptable} \end{aligned} \quad (7.26)$$

Plastic flow occurs when yielding starts. The general flow rule has the form

$$d\boldsymbol{\varepsilon}^p = d\lambda \frac{\partial f}{\partial \boldsymbol{\sigma}} \quad (7.27)$$

where $d\boldsymbol{\varepsilon}^p$ is the plastic strain increment [Fridtjov, 2008]. The parameter $d\lambda$ is an unknown, constant scalar for the case of a perfectly plastic material and a scalar-valued function of the state of stress $\boldsymbol{\sigma}$, the hardening parameters κ_i , and of the stress increment tensor $d\boldsymbol{\sigma}$ in the case of a hardening material.

Brittle behavior of rocks is often described by the friction angle ϕ and the cohesion C_{MC} of the Mohr-Coulomb model. Nonetheless, the Drucker-Prager yield criterion is used for the finite element modeling in this thesis since the software *ABAQUS* allows only the use of this model in combination with rate effects.

Drucker-Prager yield criterion

The Drucker-Prager yield criterion depends on the mean normal stress σ_m , the friction angle β , the cohesion C_{DP} , and the second and third invariants of the deviatoric stress $\boldsymbol{\sigma}'$. Before discussing the Drucker-Prager yield criterion these parameters are explained (based on Fridtjov [2008] if not referenced otherwise).

The mean normal stress σ_m is equal the negative equivalent pressure stress p . It is a function of the first principal stress invariant I_1 .

$$\sigma_m = -p = \frac{1}{3}(\sigma_{11} + \sigma_{22} + \sigma_{33}) = \frac{1}{3}\text{tr}(\boldsymbol{\sigma}) = \frac{1}{3}I_1 \quad (7.28)$$

The deviatoric stress tensor $\boldsymbol{\sigma}'$ is derived from the stress tensor $\boldsymbol{\sigma}$ by

$$\boldsymbol{\sigma}' = \boldsymbol{\sigma} - \left(\frac{1}{3}\text{tr}(\boldsymbol{\sigma})\right) \mathbf{I} \quad (7.29)$$

where \mathbf{I} denotes the identity matrix. The second and third deviatoric stress invariants J_2 and J_3 are scalars. They are obtained by

$$J_2 \equiv \frac{1}{2}(\text{norm } \boldsymbol{\sigma}')^2 = \frac{1}{2}\boldsymbol{\sigma}' : \boldsymbol{\sigma}' = \frac{1}{2}\sigma'_{ij}\sigma'_{ij} = \frac{1}{2}\left[\boldsymbol{\sigma} : \boldsymbol{\sigma} - \frac{1}{3}(\text{tr}(\boldsymbol{\sigma}))^2\right] \quad (7.30)$$

$$J_3 \equiv \det \boldsymbol{\sigma}' \quad (7.31)$$

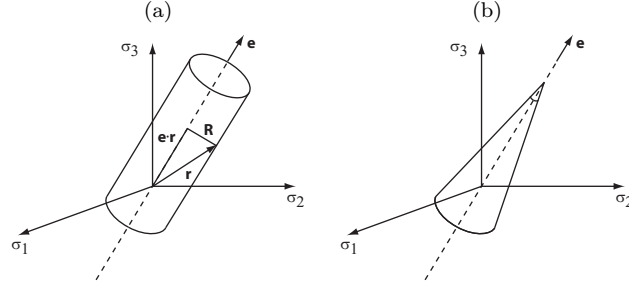


Figure 7.2: (a) Mises yield surface and (b) Drucker-Prager yield surface in the principal stress space.

The sign “:” denotes the scalar product of two tensors of 2. order. The norm (magnitude) of the tensor $\boldsymbol{\sigma}'$ is obtained by

$$\text{norm } \boldsymbol{\sigma}' = \|\boldsymbol{\sigma}'\| = \sqrt{\boldsymbol{\sigma}' : \boldsymbol{\sigma}'} = \sqrt{\text{tr}(\boldsymbol{\sigma}'\boldsymbol{\sigma}'^T)} = \sqrt{\sigma'_{ij}\sigma'_{ij}} \quad (7.32)$$

The Drucker-Prager yield criterion can be considered as an extension of the Mises yield criterion (Fig. 7.2). Both criteria are functions of the Mises equivalent stress which can be expressed by

$$\begin{aligned} \sigma_{vM} &= \sqrt{\frac{3}{2}\boldsymbol{\sigma}' : \boldsymbol{\sigma}'} = \sqrt{3J_2} \\ &= \frac{1}{\sqrt{2}}\sqrt{(\sigma_{11} - \sigma_{22})^2 + (\sigma_{22} - \sigma_{33})^2 + (\sigma_{11} - \sigma_{33})^2 + 6(\sigma_{12}^2 + \sigma_{23}^2 + \sigma_{13}^2)} \end{aligned} \quad (7.33)$$

The Mises yield surface is a circular cylinder of radius R . The orientation of the cylinder in the stress space is given by the vector $\boldsymbol{e} = 1/\sqrt{3} \cdot [1 \ 1 \ 1]^T$. A stress point on the yield surface with the radius vector $\boldsymbol{r} = [\sigma_1 \ \sigma_2 \ \sigma_3]^T$ has to satisfy the equation

$$\boldsymbol{r} \cdot \boldsymbol{r} - (\boldsymbol{e} \cdot \boldsymbol{r})^2 = R^2 \quad (7.34)$$

Thus, the Mises yield criterion in the principal stress space is written as

$$3J_2 = \sigma_1^2 + \sigma_2^2 + \sigma_3^2 - \sigma_1\sigma_2 - \sigma_2\sigma_3 - \sigma_3\sigma_1 = f_y^2 \iff \text{yielding may start} \quad (7.35)$$

In contrast to the Mises yield criterion the Drucker-Prager yield criterion depends not only on the stress differences but also on the first principal stress invariant I_1 . It describes the increasing strength of rocks with increasing depth and is written as

$$f = \alpha I_1 + \sqrt{J_2} = k \quad (7.36)$$

where α and k are positive constants at each point of the material [Drucker and Prager, 1952]. In the used finite element software package ABAQUS [ABAQUS, 2009] the Drucker-Prager yield criterion is defined as

$$f = t - p \tan \beta - C_{DP} = 0 \iff \text{yielding may start} \quad (7.37)$$

where

$t = \frac{1}{2}\sigma_{vM} \left[1 + \frac{1}{K} - \left(1 - \frac{1}{K} \right) \left(\frac{J_3}{\sigma_{vM}} \right) \right]$	and
$p = -\sigma_m = -\frac{1}{3}tr(\boldsymbol{\sigma})$	is the equivalent pressure stress
β	is the slope of the linear yield surface in the p-t-stress plane and is commonly referred to as the friction angle of the material
C_{DP}	is the cohesion of the material
K	is the ratio of the yield stress in triaxial tension to the yield stress in triaxial compression and, thus, controls the dependence of the yield surface on the value of the intermediate principal stress.

The parameter K was set to 1 and thus t equals σ_{vM} . A reasonable match between the Drucker-Prager model (β , C_{DP}) and the Mohr-Coulomb model (ϕ , C_{MC}) in plane strain can be obtained by

$$\tan \beta = \frac{9 \cdot \sin \phi}{\sin \phi \tan \psi + \sqrt{3} \cdot (9 - \tan^2 \psi)} \quad \text{and} \quad C_{DP} = \frac{(9 - \tan \beta \tan \psi) \cdot C_{MC} \cdot \cos \phi}{\sqrt{3} \cdot (9 - \tan^2 \psi)} \quad (7.38)$$

where ψ denotes the dilatancy angle [ABAQUS, 2009]. The dilatancy ψ indicates the change in volume associated with shear distortion of an element in the material. The dilatancy angle for rocks is in the range of 0° to 20° . It vanishes at high confining pressures [Vermeer and de Borst, 1984]. It was set to zero in the particular models.

7.2.4 Ductile deformation

Ductile deformation denotes the ability of materials to deform irreversibly without fracturing. It can be classified according to the strain-rate–stress dependency. Dislocation creep is most relevant for geodynamic analysis in the lithosphere with temperatures in the range of 300°C to 1300°C [Burov, 2007]. The relationship between strain rate $\dot{\epsilon}$ and deviatoric stress σ' for dislocation creep is given by

$$\dot{\epsilon}_{xx} = -\dot{\epsilon}_{yy} = A \left(\frac{\sigma'}{G} \right)^n \left(\frac{b}{h} \right)^m e^{-\frac{E_a + pV_a}{RT}} \quad (7.39)$$

where A denotes the preexponential factor, G denotes the shear modulus, h denotes the grain size, b denotes the lattice spacing, E_a denotes the activation energy, p denotes the pressure, V_a denotes the activation volume, R denotes the gas constant and T denotes the temperature [Turcotte and Schubert, 2002]. Typical values for n and m are 3.5 and 0, respectively.

In ABAQUS creep can be defined as power-law model. Parameters found in literature have to be transformed accordingly.

$$\dot{\bar{\epsilon}}^{cr} = A\bar{q}^n t^m \quad (7.40)$$

$\dot{\bar{\epsilon}}^{cr}$ denotes the uniaxial equivalent strain rate $\left(\sqrt{\frac{2}{3}\dot{\epsilon}^{cr} : \dot{\epsilon}^{cr}} \right)$, \bar{q} denotes the uniaxial equivalent deviatoric stress, t denotes the total time at this point, and A , n and m denote variables defined as functions of temperature. \bar{q} denotes the Mises equivalent stress σ_{vM} if isotropic creep behavior is defined [ABAQUS, 2009].

7.2.5 Temperature in the continental lithosphere

Rheology of rocks is strongly related to temperature. The dominant thermal processes in the continental crust and lithosphere are radiogenic heat production and conductive heat transport to

the surface [Turcotte and Schubert, 2002]. The great age of the continental lithosphere allows to neglect time-dependent effects in general. An elementary temperature distribution is used in this thesis. It is based on the model of one-dimensional steady state heat conduction with volumetric heat production. The heat production rate H can be assumed being a function of the surface radiogenic heat production rate per unit mass H_0 , depth y and a length scale h_r .

$$H = H_0 e^{-\frac{y}{h_r}} \quad (7.41)$$

The formula above can be inserted into the energy conservation equation

$$0 = k \frac{d^2 T}{dy^2} + \rho H \quad (7.42)$$

where k is the coefficient of thermal conductivity, T is the temperature and ρ is the density. Integrating this differential equation twice using the particular boundary conditions

$$q = -k \frac{dT}{dy} = q_m \quad \text{for } y \rightarrow \infty \quad \text{and} \quad T = T_0 \quad \text{for } y = 0 \quad (7.43)$$

yields the steady-state temperature profile in the continental crust

$$T = T_0 + \frac{q_m y}{k} + \frac{\rho H_0 h_r^2}{k} (1 - e^{-\frac{y}{h_r}}) \quad (7.44)$$

where T_0 is the surface temperature and q_m is the heat flux at great depth. The surface heat flow q_0 is a linear function of the surface radioactive heat production rate in case that an exponential depth dependence of radioactivity is assumed ($q_0 = q_m + \rho h_r H_0$). A temperature profile of the continental lithosphere corresponding to Eq. (7.44) is shown in Fig 7.5 (a).

7.3 Interaction between the overriding and the subducting plate at the central Hellenic trench

7.3.1 Geodetic constraints

The mode of interaction between the Aegean and the Nubian plates is under debate. The grade of coupling between both plates and the rate of slab retreat are not precisely known. A mainly aseismic convergence between both plates is suggested when comparing seismicity along the trench with geodetic rates and/or deformation (e.g., Jackson and McKenzie 1988; Jenny et al. 2004). Nonetheless, Ganas and Parsons [2009] argue for a highly coupled plate boundary. The characteristics and especially the grade of coupling of ongoing subduction possibly vary along the Hellenic trench system. For instance, Laigle et al. [2002, 2004] argue for a locked plate interface along the Ionian island segment while the plate interface along western Crete cannot maintain complete coupling. Coupling along the central Ionian islands cannot be ruled out by the GPS data (see chapter 4.5.1). Archaeological and geological investigations revealed uplift of the Hellenic arc islands from Rhodes to southern Peloponnesos during the Holocene (e.g., Lambeck [1995]). Besides coseismic effects, in particular the AD 365 earthquake SW of Crete (e.g., Pirazzoli et al. 1996; Stiros 2001; Shaw et al. 2008; Papadimitriou and Karakostas 2008; Stiros 2010), also gravitational forces may have contributed to this uplift [Snopek et al., 2007].

GPS data provides several constraints for the overriding plate along the central Hellenic trench. These include:

- A trenchward velocity of the Aegean plate in the order of 30–32 mm/yr (Fig. 7.3).

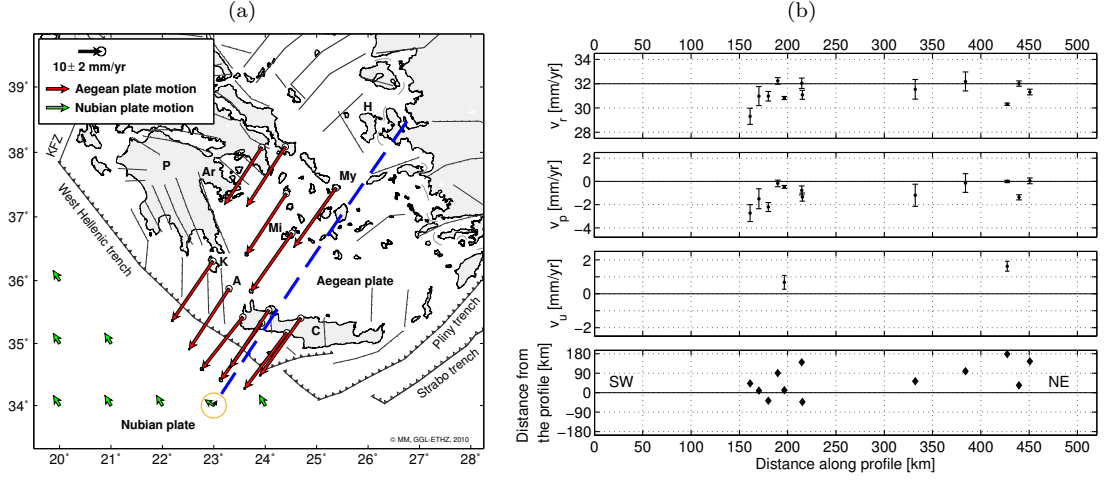


Figure 7.3: Geodetically derived Aegean and Nubian plate motion used as constraints for the Hellenic subduction. (a) Red arrows depict GPS site velocities located on the slowly deforming part of the Aegean plate. The error ellipses depict the 1- σ confidence region. Green arrows depict the motion of the Nubian plate [Altamimi *et al.*, 2007]. Nubian plate motion at $\lambda = 23.0^\circ\text{E}$, $\varphi = 34.0^\circ\text{N}$ is split into a fault-perpendicular and a fault-parallel velocity component amounting to 2.4 and 4.6 mm/yr, respectively. The dashed blue line depicts the location of the NE-SW cross-section modeled by FEM (chapter 7.3.2). Total plate convergence between the Aegean and Nubian plates amounts to 34.5 mm/yr along the dashed line. A: Antikythera, Ar: Argos, K: Kythera, C: Crete, H: Hios, KFZ: Kefalonia fault zone, Mi: Milos, My: Mykonos, P: Peloponnesos. (b) Trenchward v_r , trench-parallel v_p and vertical v_u (sites: TUC2, DION) rates of the GPS sites depicted in (a). The error bars depict the 1- σ confidence interval.

- Small deformation ($\frac{1}{2}|\varepsilon_1 - \varepsilon_2| < 40$ nstrain/yr and $|\varepsilon_1 + \varepsilon_2| < 40$ nstrain/yr) between the Cyclades and western Crete and little arc-parallel lengthening (< 2.5 mm/yr) between Kythera and eastern Crete (Figs. 4.15 (b) and 5.2 (b)).
- Small vertical rates ($|v_{up}| < 2.0$ mm/yr) on islands near the Hellenic trench (Fig. 4.17).

Moreover, block models derived from GPS velocities suggest a north-northwestward directed Nubian plate motion of 5 mm/yr near the Hellenic trench [Altamimi *et al.*, 2007]. Southwest of Crete ($\lambda = 23.0^\circ\text{E}$, $\varphi = 34.0^\circ\text{N}$), the Nubian plate motion relative to Eurasia can be split into a trenchward and a trench-parallel motion of 2.4 mm/yr and 4.6 mm/yr, respectively (Fig. 7.3 (a)).

7.3.2 Developed finite element model

Introduction

An elementary finite element (FE) model was set up by using the software ABAQUS to investigate present-day velocities and deformation rates at the surface in the region of the Southwest Aegean sea depending on subsidence rates of the Nubian slab. Finite element modeling is a common tool in geodynamics and in particular for the analysis of subduction zones (e.g., *Buiter et al.* 2002; *Hampel and Pfiffner* 2006; *Kellner* 2007). *Giunchi et al.* [1996] and *Ganas and Parsons* [2009] used FE analysis for investigating the Hellenic trench system. The former modeled a N-S cross-section across the Hellenic trench located in central Crete while the latter investigated the Hellenic trench system on its entire length. Both used a different approach than applied in this thesis.

The FE model should reveal the sensitivity of velocities at the surface and the stress distribution in the model depending on the variation of parameters such as the subsidence rate of the Nubian

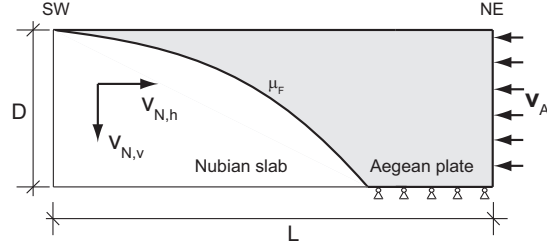


Figure 7.4: Schematic of the FE model geometry and the applied boundary conditions. D : model depth, L : length of the modeled cross-section, μ_F : friction coefficient of the Coulomb friction law applied on the contact surface, v_A : Aegean plate motion, $v_{N,h}$: horizontal velocity component of the Nubian slab, $v_{N,v}$: vertical velocity component of the Nubian slab.

slab and the coefficient of friction. The model inherently assumes two features: First, the velocity of the Aegean plate depends strongly on the retreat of the Nubian slab. Second, the crust and the upper mantle of the Aegean lithosphere are largely decoupled from the lower mantle. The motion of the Nubian slab is prescribed. The plausibility of the models is assessed by comparing the obtained displacement rates with GPS velocities. The aim of the modeling is the formulation of first-order constraints on the subduction process.

Model geometry and boundary conditions

The model space consists of a 600 km long and 125 km deep quasi two-dimensional section of the Aegean plate as shown in Fig. 7.3 (a). The cross-section is directed 213° corresponding to the direction of nearby GPS velocities in an Eurasia fixed frame. A schematic of the model is presented in Figure 7.4. The geometry of the Nubian slab was defined following *Meier et al. [2004]*. *Meier et al. [2004]* compiled the position of the plate boundary based on results of wide-angle seismics, surface wave analysis and receiver function studies. The slab geometry was kept basic in the FE model to ease computation. The dip of the downgoing slab increases from 16.2° at the surface to 25.1° in a depth of 125 km. The model geometry and the mesh of the Aegean plate are depicted in detail in Fig. G.1. Quadrilateral hexahedrons were selected as element types. In general, the size of the elements of the Aegean plate amounts to 2 km. A smaller size is employed along the contact surface to the Nubian plate.

The applied boundary conditions are shown in Fig. 7.4. Trenchward velocity v_A is imposed at the northeastern side of the Aegean plate. In addition, the Nubian slab motion v_N is prescribed. $v_{N,h}$ and $v_{N,v}$ are the horizontal and vertical velocity components of the Nubian slab, respectively.

$$\mathbf{v}_A = \begin{pmatrix} v_{A,h} \\ 0 \\ 0 \end{pmatrix} = \begin{pmatrix} 32 \\ 0 \\ 0 \end{pmatrix}; \quad \mathbf{v}_N = \begin{pmatrix} v_{N,h} \\ 0 \\ v_{N,v} \end{pmatrix} = \begin{pmatrix} -2.5 \\ 0 \\ v_{N,v} \end{pmatrix} \quad [\text{units: mm/yr}] \quad (7.45)$$

The parameter $v_{N,v}$ takes different values depending on the model version. The model extends to the island of Hios (Fig. 7.3 (a)). Nevertheless, v_A was set equal the rates observed on Mykonos. The Aegean plate is constrained at a depth of 125 km. No lateral (i.e., trench-parallel) motion is allowed. The interaction between the Nubian slab and the Aegean plate is modeled with a contact surface. The Coulomb friction law ($|\tau| = c_F \cdot |\sigma_n|$) is applied on this surface. The coefficient of friction c_F was assumed to be in the range 0.00–0.05 similar to other subduction zones (e.g., *Sobolev and Babeyko [2005]*). The dependency of the stress state on the friction coefficient was outlined e.g. by *Hassani et al. [1997]*.

Young's modulus	E	70	GPa
Poisson's ratio	ν	0.25	
Density	ρ	3000	kg m ⁻³
Cohesion	C_{MC}	10	MPa
Internal friction coefficient	ϕ	20–30°	
Dilatancy angle	ψ	0°	
Pre-exponential constant	A	0.008	MPa ⁻ⁿ s ⁻¹
Creep exponent	n	3.1	
Activation energy	Q	243000	Jmol ⁻¹
Surface temperature	T_0	273	K
Surface heat flow	q_0	50	mWm ⁻²
Thermal conductivity	k	3.35	Wm ⁻¹ K ⁻¹
Radiogenic heat production	ρH_s	1	μ Wm ⁻³
Heat production scale depth	h_r	10	km

Table 7.1: Parameters describing the rheology employed for the modeling of the cross-section. The parameters A , n and Q are defined in *Wilks and Carter* [1990].

Lithostatic pressure is established during the first analysis step (ABAQUS: GEOSTATIC analysis step) without causing deformations in the model. The boundary conditions described in Eq. (7.45) are applied at the beginning of the second analysis step. During the second analysis step a quasi-static stress analysis is performed. A quasi-static stress analysis is suitable for time-dependent material response if inertia effects are negligible. The second step covers a time period between 60'000 and 140'000 years depending on the model version. After this time approximately steady state conditions are established in the model where energy dissipation is nearly constant in subsequent increments (Fig. G.2). Results of the model versions are discussed for comparable modeling times. The respective times are indicated in Table 7.2. Model velocities are based on nodal displacements over 1000 years.

Adopted rheology

The Aegean plate is modeled with a brittle crust and a ductile upper mantle. Brittle failure is governed by a Drucker-Prager yield surface (Eq. 7.37). The angle of internal friction ϕ was set between 20° and 30° and the cohesion C_{MC} to 10 MPa. Ductile deformation is modeled by power-law creep according to Eq. (7.40) which is a function of deviatoric stress and temperature. The used parameters for creep represent lower crustal rocks [*Wilks and Carter*, 1990]. Temperature is modeled as a function of depth according to Eq. (7.44) and kept constant during the calculations. Hence, heat transfer between the colder Nubian slab and the Aegean lithosphere plus heat production due to frictional processes were neglected. Surface heat flow amounts to 30–52 mWm^{-2} southwest of Crete and 50–60 mWm^{-2} between southern Peloponnesos and Crete. Higher values are reported north of Crete (59–77 mWm^{-2}) and between Milos and Argos (114 mWm^{-2}) near the South Aegean volcanic arc (see Fig. 2.2 for the location of the South Aegean volcanic arc) [*Jongsma*, 1974; *Erickson et al.*, 1977]. *Erickson et al.* [1977] point out that the values obtained in the South Aegean are associated with uncertainty due to seasonal bottom water temperature variations. For the thermal conductivity k , the radiogenic heat production ρH_s and the heat production scale depth h_r average values were selected. The parameters describing the rheology used for modeling the Aegean plate are listed in Table 7.1. Figures 7.5 (a)-(c) depict the assumed temperature distribution in the lithosphere and the modeled strength of the lithosphere, respectively. The subducting Nubian slab is modeled as a rigid body.

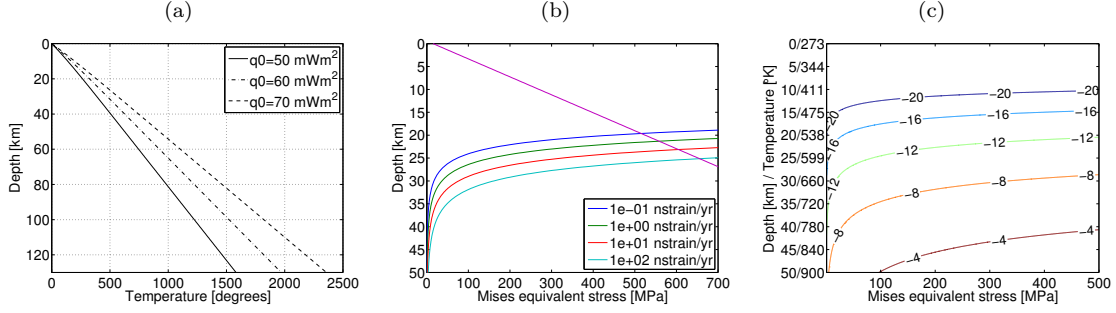


Figure 7.5: (a) Temperature profiles in the continental lithosphere according to Eq. (7.44). Used parameters: $T_0 = 0^\circ\text{C}$, $q_0 = 50, 60$ and 70 mWm⁻², $h_r = 10$ km, $k = 3.35$ Wm⁻¹K⁻¹ and $q_m = q_0 - \rho h_r H_0$. (b) Resulting strength of the lithosphere for the parameters listed in Table 7.1 (adopting $\phi = 30^\circ$). The line colored in magenta represents the brittle strength of the crust. The stress – strain rate relation represented by creeping behavior is depicted for different strain rates. (c) Creep strain rate in strain/yr as a function of Mises equivalent stress and depth/temperature for the parameters listed in Table 7.1.

Version		A	B	C	D	E	F	G	H	I	J	K	L
ϕ	[$^\circ$]	30	30	30	30	30	30	30	30	30	20	20	20
c_F	[-]	0.00	0.01	0.05	0.00	0.01	0.05	0.00	0.01	0.05	0.00	0.01	0.05
$v_{N,v}$	[mm/yr]	10	10	10	12	12	12	13	13	13	10	10	10
$WRMS$	[mm/yr]	1.1	1.3	0.8	1.5	1.7	1.1	1.8	2.0	1.3	1.1	1.3	0.8
$Time$	[kyr]	80	80	80	80	80	70	80	80	69	80	80	80

Table 7.2: Parameter values used for the calculated model versions. ϕ denotes the angle of internal friction, c_F denotes the coefficient of friction applied on the interplate interface and $V_{N,v}$ denotes the subsidence rate of the Nubian slab. The $WRMS$ is based on the residuals between horizontal GPS rates v_{GPS} and horizontal displacement rates v_{FEM} . Statistics are based on the GPS sites akit, damn, kyns, mils, mkn2, omal, roum, sfin, tuc2. $Time$ indicates the model time at which the results were extracted for discussion in the result section and for creating Figures 7.6, 7.7 and 7.8).

Results

The displacement rates of the model nodes, the slip rates on the contact surfaces and the stress state in the model are the primary results. Several model versions were calculated to investigate the sensitivity of the results depending on changing parameters such as the coefficient of friction c_F and the subsidence rate of the Nubian slab $v_{N,v}$ (Table 7.2). The increase of elastic strain energy in the model sharply reduces after about 25 kyr in case $c_F > 0$ (see Fig. G.2). Afterward, the models approximate nearly a steady state. The results remain to a minor degree time-dependent even at the end of the modeling period (see Fig. G.2). The limited level of detail allows only the interpretation of the main characteristics. Comparing the model results and the GPS rates it is noted: GPS data points to a slight reduction of horizontal rates towards the trench (~ 0.0 – 1.5 mm/yr) and small absolute uplift rates on Crete (0.3 – 0.6 mm/yr) (Fig. 7.3 (b)).

Trenchward and vertical velocities at the surface of the model depend largely on the geometry and the subsidence rate of the Nubian slab. Trenchward rates increase by 0.3 – 1.0 mm/yr towards SW if no friction is applied on the contact surface and the subsidence rate of the Nubian slab amounts to 10 – 13 mm/yr (Fig. 7.6 (a)). Setting $c_F = 0.05$ leads to trenchward rates decreasing by 0.7 – 1.0 mm/yr towards SW (Fig. 7.6 (b)). This is slightly in better agreement with the GPS rates (Table 7.2). The dependency of the vertical rates on the friction coefficient is distinct but the validation of the models is limited because of the small number of CGPS sites along the profile. Nonetheless, subsidence rates of the Nubian slab larger than 13 mm/yr produce clearly negative vertical rates near Crete which disagrees with geodetic estimates. The parameters employed in

versions C and L provide the best fit to the present-day GPS rates. In both models, the subsidence rate of the Nubian slab $v_{N,v}$ and the coefficient of friction c_F amount to 10 mm/yr and 0.05, respectively. Displacements depend only to a minor degree on the coefficient of internal friction ϕ (Fig. 7.6 (c) and (d)). Horizontal strain rates are moderate ($|\dot{\epsilon}| < 40$ nstrain/yr) in all model versions which is in agreement with the geodetically derived strain rates in the South Aegean sea (cmp. chapter 5.3).

The displacement rates in models with $c_F = 0.05$ on the interplate contact are considerably different from present-day GPS rates during the phase where friction prevents slip on the interplate contact (up to 20 mm/yr for horizontal rates; see Fig. G.2). Therefore, a highly coupled plate interface as suggested by *Ganas and Parsons [2009]* is not supported by this modeling approach. This finding concurs with the results recently outlined by *Reilinger et al. [2010]*.

The stress distribution and the displacement rates in the models largely depend on the applied friction (Fig. 7.7). In the model versions with $c_F > 0$ a distinct area of large Mises stresses extends from the plate interface (at about 30 km depth) to the surface (Fig. 7.7 (c) and (e)). These large Mises stresses are caused by variations in rates along the plate interface which in turn are due to a pressure and temperature dependent rheology. Maximum shear stresses caused by frictional forces on the plate interface are located at a similar depth.

Shaw et al. [2008] suggested that the AD 365 earthquake (Mw 8.3–8.5) located SW of Crete occurred on an intraplate fault rather than on the interplate interface. Their earthquake model is based on uplift observed along the coast of Crete which occurred synchronously with the AD 365 earthquake. The modeled earthquake produces 20 m of slip on a 100 km long rupture plane dipping 30° to the NE and reaching a depth of 45 km. They assume the AD 365 earthquake having been triggered by differences in slip rates on the plate interface above 30 km and beneath 70 km depth.

The stress drop of a dip-slip earthquake can be approximated by the equation

$$\Delta\sigma \approx \frac{8}{3\pi} \frac{M_0}{W^2 L} \quad (7.46)$$

where M_0 denotes the seismic moment and W and L denote the length and width, respectively, of the rupture plane [*Stein and Wysession, 2003*]. The earthquake parameters derived by *Shaw et al. [2008]* indicate a stress drop of 5.3 MPa. Considering fault parameters based on empirical scaling laws derived by *Mai and Beroza [2000]* and *Wells and Coppersmith [1994]* stress drops of 0.6 MPa and 2.6–2.8 MPa, respectively, are obtained for a Mw 8.3–8.5 earthquake. The maximum shear stress increases by ~ 0.9 – 1.0 kPa/yr in models C, F, I and L after a modeling period of 69–80 kyr. Time periods of 5.3–6.2 kyr, 0.6–0.7 kyr and 2.6–3.3 kyr, respectively, are required depending on the earthquake parameters to build-up stresses equal the calculated stress drops. However, the stress state in the model after 69–80 kyr only allows slip on a preexisting fault plane dipping 30° if the friction coefficient on this fault is relatively low ($c_F \approx 0.1$) (Fig. 7.8).

In summary, the modeling approach provides the following evidence for the central Hellenic trench: The GPS rates are in agreement with a largely uncoupled plate interface between the Aegean and Nubian plates. The models do not support a highly coupled plate interface. The calculated model versions point to a subsidence rate of the upper part of the Nubian slab amounting to 10–13 mm/yr. This parameter depends widely on the slab geometry. Models calculated with a friction coefficient $c_F = 0.05$ are in better agreement with GPS rates than models with smaller friction coefficients. Models with $c_F = 0.05$ exhibit high values of Mises stresses extending from the plate interface at 30 km depth to the surface. The occurrence of a Mw 8 earthquake (i.e., the AD 365 event) inside the Aegean plate is plausible. However, the recurrence time and the required stress state for slip on a gently dipping fault plane largely depend on fault friction and structural conditions and cannot definitively be answered with this approach.

The most important shortcomings of this modeling approach are the de facto two-dimensional model set up (neglecting e.g. trench-parallel displacements) and the elementary structural and

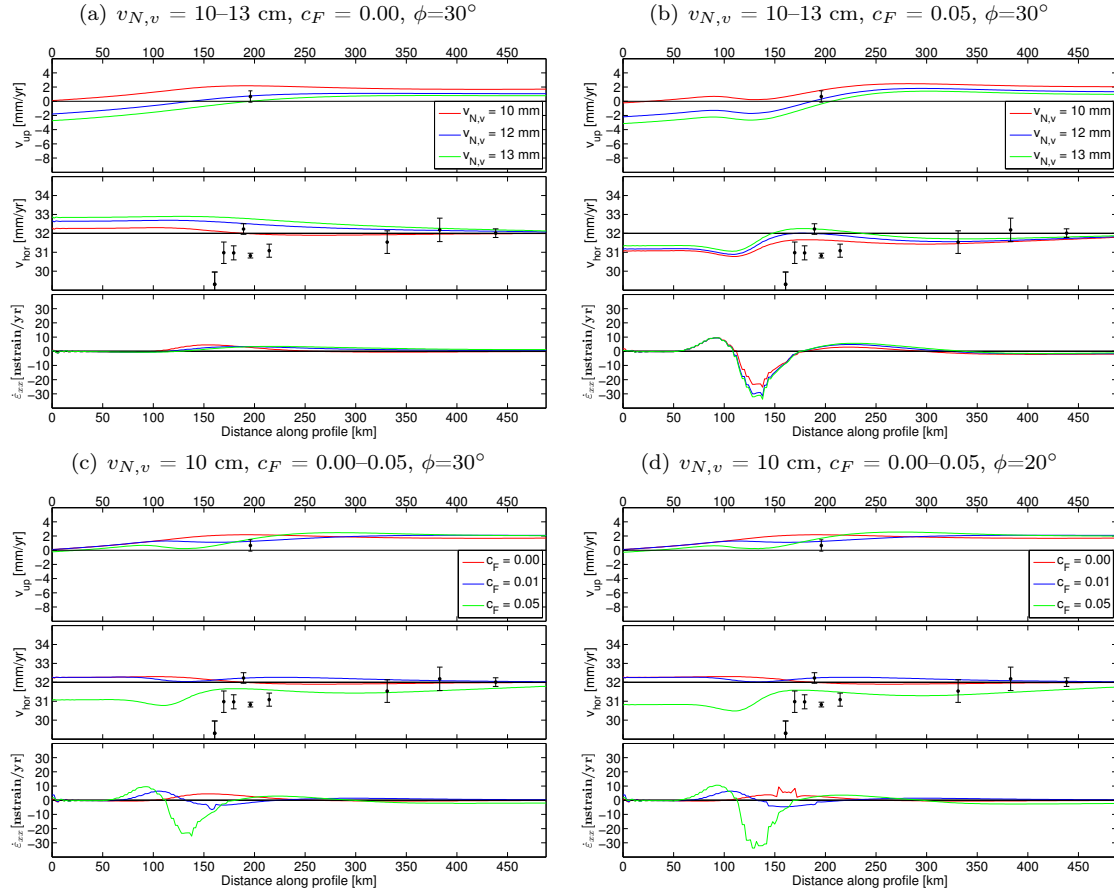


Figure 7.6: Vertical v_{up} and trenchward v_{hor} motion and normal strain rate ϵ_{xx} at the surface of the Aegean plate along the profile. $v_{N,v}$: vertical motion of the Nubian slab, c_F : coefficient of friction, ϕ : angle of internal friction. Rates of following GPS sites are shown: ak1t, damn, kyns, mils, mkn2, omal, roum, sfn, tuc2. The error bars depict the 1- σ confidence interval.

physical information implemented (e.g., temperature distribution). The extension of the FE model towards a three-dimensional set up would significantly increase its complexity and with it the number of parameters (e.g., trench-parallel variation in the subduction rate of the Nubian slab). The parameters are weakly constrained even in the two-dimensional case.

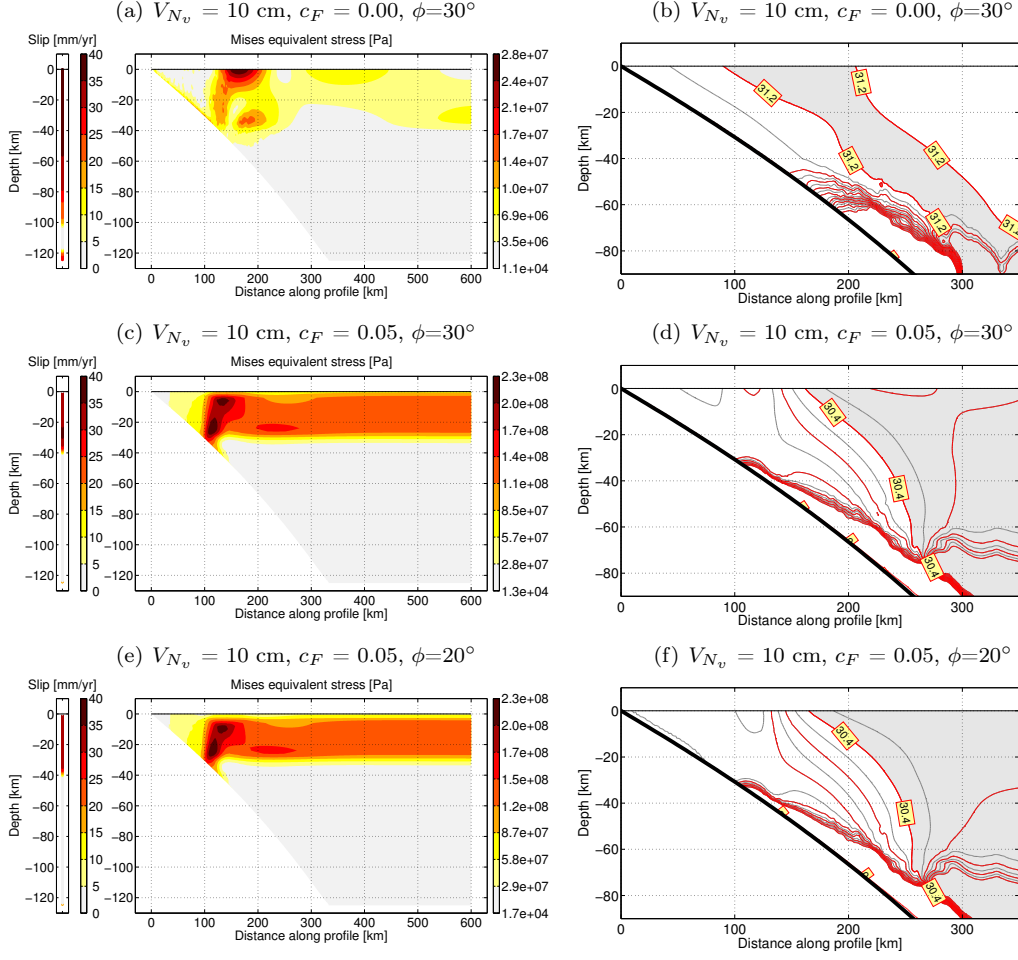


Figure 7.7: (a), (c) and (e) Slip rates along the subduction interface and Mises stresses in the FE model after a modeling period of 80 kyr. (b), (d) and (f) Slab-parallel displacement rates (assumed inclination of the slab: 17°) after a modeling period of 80 kyr. Unit: [mm/yr]. The equidistance of the contour lines amounts to 0.2 mm/yr. Displacement rates inside the shaded area are larger than the labeled value, rates outside the shaded area are smaller. $V_{N,v}$: vertical motion of the Nubian slab, c_F : coefficient of friction, ϕ : angle of internal friction.

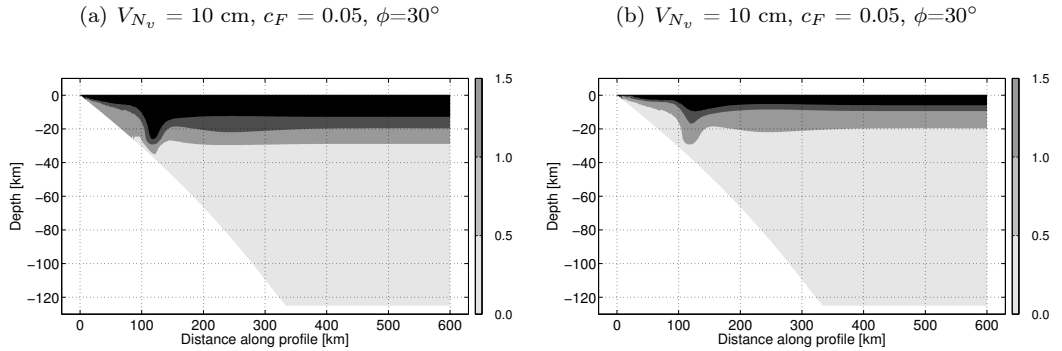


Figure 7.8: Ratio $c \cdot \sigma_n / \tau$ where c denotes the coefficient of friction on an imaginary fault plane dipping 30° and σ_n and τ denote the normal and shear stresses, respectively, on this fault plane. (a) $c = 0.1$ (b) $c = 0.2$. The ratio is larger than 1.5 in the black colored area. $V_{N,v}$: vertical motion of the Nubian slab, c_F : coefficient of friction applied on the subduction interface, ϕ : angle of internal friction.

7.4 3D finite element model of the North Aegean sea

7.4.1 Introduction

The extended GPS network in the North Aegean sea provides new evidence of the kinematic field in this region (chapter 4.4). Most of the active tectonic structures of the North Aegean domain are located offshore. Therefore, their characteristics are only weakly constrained by GPS. The calculation of the strain rate field (chapter 5) revealed NE-SW trending dextral shear and NNE-SSW extension as the main deformation styles. Strike-slip characteristics of the NAT were analyzed in terms of the model of a buried screw dislocation in an elastic half-space (chapter 4.4). Diminishing strike-slip rates along the NAT from the Ganos to the Sporades islands resulted from both modeling approaches. The dislocation model is based on an elastic rheology. Strain rate calculation based on the method of collocation implies rheologic information only inherently, namely in terms of the covariance function. Both methods do not consider stresses. In contrast, stress and rheology are vital parts in the formulation of the FE method.

An elementary FE model was set up to reveal additional insights into ongoing deformation processes of the North Aegean domain. The model is kept simple in terms of incorporated faults and used rheology. Differences between the modeled displacement rates and the observed GPS rates expose model deficiencies which may be interpreted in terms of distinct deformation processes. The investigations are aimed at shedding light on the following topics:

1. Dependency of the kinematic field on the imposed boundary conditions.
2. Amount of dextral strike-slip accommodated on ENE-WSW to NE-SW trending faults.
3. Identification of complementary deformation zones in addition to ENE-WSW to NE-SW trending dextral strike-slip faults.

7.4.2 Model set up

Geometry and rheology

The model covers the North Aegean sea, Thessaly, Macedonia and Thrace (Fig. 7.9 (a)). The depth of the model amounts to 40 km. Real geometry is mapped to model dimensions using a stereographic projection centered at 24°E, 39°N. Quadrilateral hexahedrons are used as element types. The mesh is finer along the curved contact surfaces (~2.5 km) and coarser in the north and southeast of the model (~7.0 km) (Fig. 7.9 (b)). The vertical resolution amounts to 2.5 km.

Three ENE-WSW to NE-SW trending faults accommodating mainly strike-slip motion are incorporated in the model: The North Aegean trough (NAT), the Skyros-Edremit fault (SEF) and the Psara-Lesvos fault (PLF). The Agios Efstratios fault (AEF) was not modeled due to its close distance to the SEF. Not all the faults are active in all the model versions. Model nodes of corresponding contact surfaces are tied together in case they are inactive.

The lithosphere in the model consists of an elastic material with a Young's modulus of 70 GPa and a Poisson's ratio of 0.25. No fault friction was applied on the contact surfaces as the model is intended to represent a steady-state model. In general, the onset of friction in the FE model would change the energy fractions (e.g., strain energy, frictional energy dissipation) and with it the displacements. However, the application of a friction law requires the modeling of a more realistic rheology because the maximum supported shear stress depends largely on pressure and temperature. Crustal heterogeneities and preexisting fault structures are probably vital features for the style and amount of crustal deformation in the North Aegean domain. The NAT which is

the predominant strike-slip fault is suggested to be a weak crustal zone at least along the Saros basin. This is supported by two aspects: First, the application of the model of a buried screw dislocation in an elastic half-space revealed locking depths in the range of 5 to 10 km. Second, high values of heat flow ($> 100 \text{ mWm}^{-2}$) [Jongsma, 1974] point to a relatively weak crust which supports only small shear stresses. Smaller heat flow values are reported near the SEF and the PLF. The crust is probably considerably stronger in this area. However, the omission of friction is reasonable for this elementary modeling approach.

Boundary conditions

It is assumed that a lithospheric block of regional dimension is driven by horizontal stresses at its border. Therefore, displacements are imposed as boundary conditions on the nodes located along the margin of the model. In addition, vertical motion is constrained to zero for nodes at the bottom of the model. The displacements at the model border were derived using the collocation approach [Straub, 1996; Peter, 2000] based on GPS site velocities located in close vicinity to the model border (Fig. 7.9 (a) and (b)). However, across the Ganos fault rates based on locking depth modeling instead of site velocities were employed in the collocation to reproduce the distinct velocity gradient related to this structure. The used rates marginally deviate from those corresponding to profile P1 as the sites ERDE, UKIR and YEN1 in the East were omitted for the calculations (Figs. 4.9 and 4.10) and the locking depth model was slightly adapted to the geometry of the FE model ($v_1 = 21.3 \text{ mm/yr}$ instead of $v_1 = 22.5 \text{ mm/yr}$, $W = 7.5 \text{ km}$ instead of $W = 8.9 \text{ km}$; the fault location ($x = 0$) is assumed 1.9 km southernly). Further, the fault-parallel rates were combined with fault-perpendicular rates. They have been transformed into ITRF2005 for reasons of consistency (chapter B.6). In the first analysis step (ABAQUS: GEOSTATIC analysis step) a lithostatic pressure state is established in the model corresponding to the applied body forces causing no deformations. Afterward, the applied boundary conditions are activated and the model starts to deform. The simulation time was set to 10'000 years which leads to maximum displacements of 250 m.

7.4.3 Results

Four versions were calculated with regard to the introduced faults (Fig. 7.9 (b)). In model A no faults were modeled. In models B–D three NE-SW directed faults were added. These were modeled following the trend of the seismicity belts as contact surfaces. In model B the North Aegean trough (NAT) was incorporated as strike-slip fault. Model C incorporates the NAT and the Skyros-Edremit fault (SEF) and model D the NAT, the SEF and the Psara-Lesvos fault (PLF). The calculated displacements were averaged to annual rates and compared to interseismic GPS velocities to assess the agreement.

Model A is calculated to derive the strain pattern solely caused by the applied kinematic boundary conditions. Residuals with respect to GPS velocities are shown in Figures 7.10 (a). Principal strain rate axes of the horizontal deformation field are shown in Figure 7.10 (b). They are collinear to the derived principal stresses due to the elastic rheology. The figure highlights three main regions: a zone of large strike-slip deformation in the northeast of the model related to the Ganos fault, a zone of predominantly NNE-SSW extension in the south and an area with low strain rates in the northwest. The direction of maximum extensional strain changes from NE-SW near the Ganos fault to almost N-S in Thessaly. This evidence is in good agreement with the seismically derived least compressive stress direction in the North Aegean sea [Kiritzi, 2002]. The slowly deforming area in northwestern Greece was also identified in chapter 4.3 by applying a kinematic block model. This feature is evident in all four model versions.

The incorporation of strike-slip faults in models B–D decouples different regions and decreases the

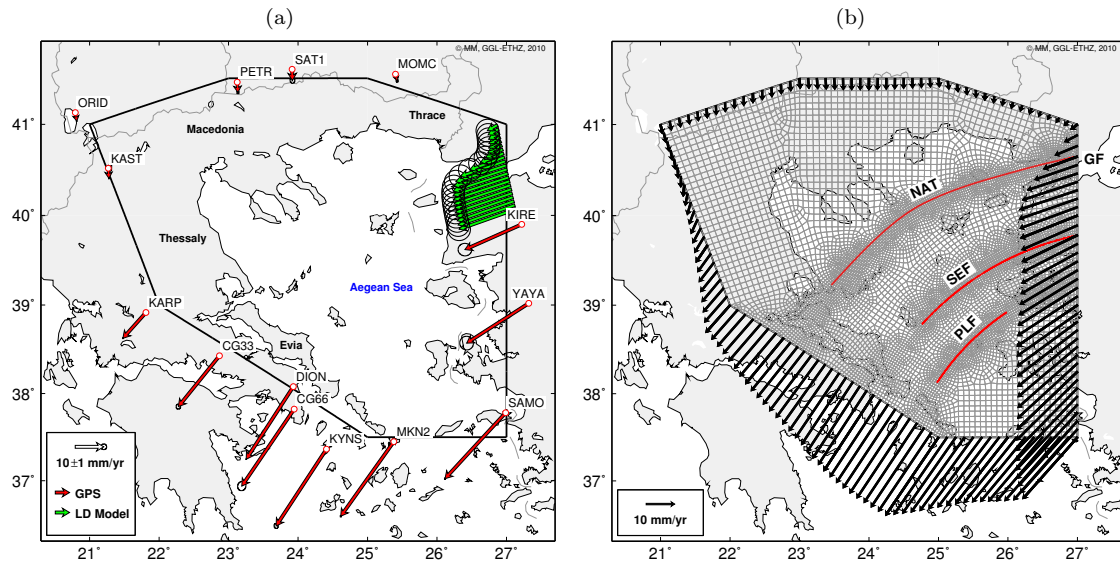


Figure 7.9: (a) Model dimensions (black line) and rates which are used to derive boundary conditions for the FE model. Based on these rates velocities at the model border are predicted using the method of collocation. Red arrows depict GPS site velocities. The green arrows correspond largely to the velocity profile derived for the Ganos fault. The rates were transformed to ITRF2005. The error ellipses depict the 1- σ confidence region. (b) Kinematic boundary conditions imposed on the nodes located at the border of the FE model (schematic illustration). The red lines indicate the introduced faults. The light gray lines depict the mesh of the model. The mesh is finer along the contact surfaces (~ 2.5 km) and coarser in the north and southeast of the model (~ 7 km). For all model versions the same mesh has been employed. In case that a contact surface was not active corresponding nodes have been tied together. NAT: North Aegean trough, GF: Ganos fault, PLF: Psara-Lesvos fault, SEF: Skyros-Edremit fault.

strain rates between the faults (Figures 7.10 (c)–(d), 7.11 (a)–(d)). The resulting right-lateral slip rates on the contact surfaces are depicted in Figures 7.10 (d), 7.11 (b) and (d) and maximum values are listed in Table 7.3. In model D maximum slip rates amounting to 20.9 mm/yr are calculated on the North Aegean trough. Smaller slip rates are concentrated on the southern faults, 9.7 mm/yr on the Skyros-Edremit fault and 4.0 mm/yr on the Psara-Lesvos fault, respectively. Slip rates on the NAT and the SEF vary only little in different model versions. The narrow deformation zone (~ 40 – 80 km wide) associated with the NAT derived in chapter 4.4.2 has two implications for the FE model: Modeling of the offshore located NAT as a simple contact surface does not lead to large residuals at closely located GPS sites and, conversely, the model does not reveal additional fault characteristics. East of 26.3° strike-slip motion on the NAT and SEF transforms from slip on the contact surfaces to shear deformation since continuous kinematic boundary conditions are applied along the model margin. Right-lateral strike-slip motion on the SEF is only 4 mm/yr towards western Anatolia [Aktug *et al.*, 2009]. The model indeed shows that strike-slip motion on the SEF is only to a minor extent due to transferred shear deformation from the east as the maximum slip rate on the SEF is about 10 mm/yr. Instead, shear at this location is related to the different sense of rotation at the eastern (ccw) and the western (cw) model border and N-S extension along the eastern margin (Fig. 5.2 (c)). Slip rates on the NAT derived by FE analysis are comparable with those calculated by the application of the model of a screw dislocation in an elastic half-space: 20.9 mm/yr compared to 21.2 mm/yr for profile P2, 16.8 mm/yr compared to 12.5 mm/yr for profile P3.

Slip on the SEF seems to be larger than on the AEF since maximum shear strain is observed south of the line Skyros-Lesvos in model B. However, both faults are located closely to each other and a part of the indicated slip on the SEF certainly has to be attributed to the AEF. Supposing

Model	RMS [mm/yr]	WRMS [mm/yr]	Maximum slip on faults		
			NAT [mm/yr]	SEF [mm/yr]	PLF [mm/yr]
A	2.4	2.5			
B	1.6	1.8	22.4		
C	1.3	1.4	21.0	10.3	
D	1.3	1.3	20.9	9.7	3.9

Table 7.3: Root mean square (RMS) and weighted RMS (WRMS) as indication for the fit between GPS rates and FEM displacement rates. The WRMS is based on the accuracy of GPS rates. The FEM displacement rates are treated as exact numbers. Maximum slip rates on the introduced faults. NAT: North Aegean trough, SEF: Skyros-Edremit fault, PLF: Psara-Lesvos fault. Model A incorporates no faults, model B the NAT, model C the NAT and the SEF and model D the NAT, the SEF and the PLF.

the reported 1968 Mw 6.8 (AEF) and the 1981 Mw 6.8 (SEF) [Taymaz *et al.*, 1991; Kiratzi and Louvari, 2003] are the maximum possible strike-slip events on these faults, recurrence intervals of 123–246 (4–8 mm/yr of slip) and 98–164 years (6–10 mm/yr of slip), respectively, are plausible (scaling relations after Mai and Beroza [2000]).

The western termination of the NAT is modeled a few kilometers north of Skiathos. Residuals in direction of the NAT (220°) of sites on Pelion, the Sporades islands and northern Evia differ by less than 1.3 mm/yr (versions C and D). Moderate shear strain rates in the order of 50 nstrain/yr are derived between Pelion and northern Evia corresponding to the results of the locking depth model (Fig. 7.12).

Models C and D are capable to reproduce about 90 percent of the observed GPS rates in the area of Limnos, Agios Efstratios and the Sporades Islands. The misfit between the model displacements and GPS rates (WRMS) decreases from model A (2.5 mm/yr) to model D (1.3 mm/yr) (Table 7.3). Residuals of sites located close to the model margin do not largely change since identical boundary conditions are applied in all four versions. The inclusion of the Psara-Lesvos fault in model D resulting in 4 mm/yr of dextral slip only marginally improves the fit compared to model C (RMS: 0.01 mm/yr, WRMS: 0.04 mm/yr) and does not greatly change the amount of calculated shear strain in this part of the model. The Psara-Lesvos fault is the least prominent NE-SW trending strike-slip structure in the North Aegean sea. The kinematic setting leading to strike-slip on the PLF is, in principle, comparable with that of the SEF. The model shows that dextral strike-slip on ENE-WSW and NE-SW trending faults is by far the prevailing deformation style in the North Aegean sea. This is supported by fault plane solutions of earthquakes in this region [Kiratzi, 2002; Taymaz *et al.*, 1991].

Since model C is considered to be the best version the further discussion is related to it. The residuals GPS rates minus averaged FEM displacement rates were analyzed in order to describe the deformation style of regions where the model only inadequately reproduces the GPS rates. Residual strain rates were derived by the method of collocation. There are four regions where residual strain rates of up to 100 nstrain/yr are encountered (Fig. 7.13): (1) NNE-SSW directed extensional residual strain is observed between the islands of Skyros, Agios Efstratios and Lesvos. The unmodeled extension between Agios Efstratios and Skyros (4.5 mm/yr) probably occurs partly as strike-slip on the Agios Efstratios fault and as normal faulting at the western scarp of the Skyros basin (see the 1967 Ms 6.6 and the 1968 Ms 7.0 events on Fig. 7.13 (a)). (2) NNE-SSW extension north of the Chalkidiki peninsula is most likely associated with the Mygdonian graben. (3) Residual strain rates in the northern Gulf of Evia are related to the residual of site ARSA (3.5 mm/yr) and can be explained by not modeled normal faults bounding the Gulf of Evia. (4) Residual strain rates in the Mount Olympus region are caused by the residual of site KRNA (3.3 mm/yr). Only small strain rates are encountered in this region which are probably related to NE-SW trending

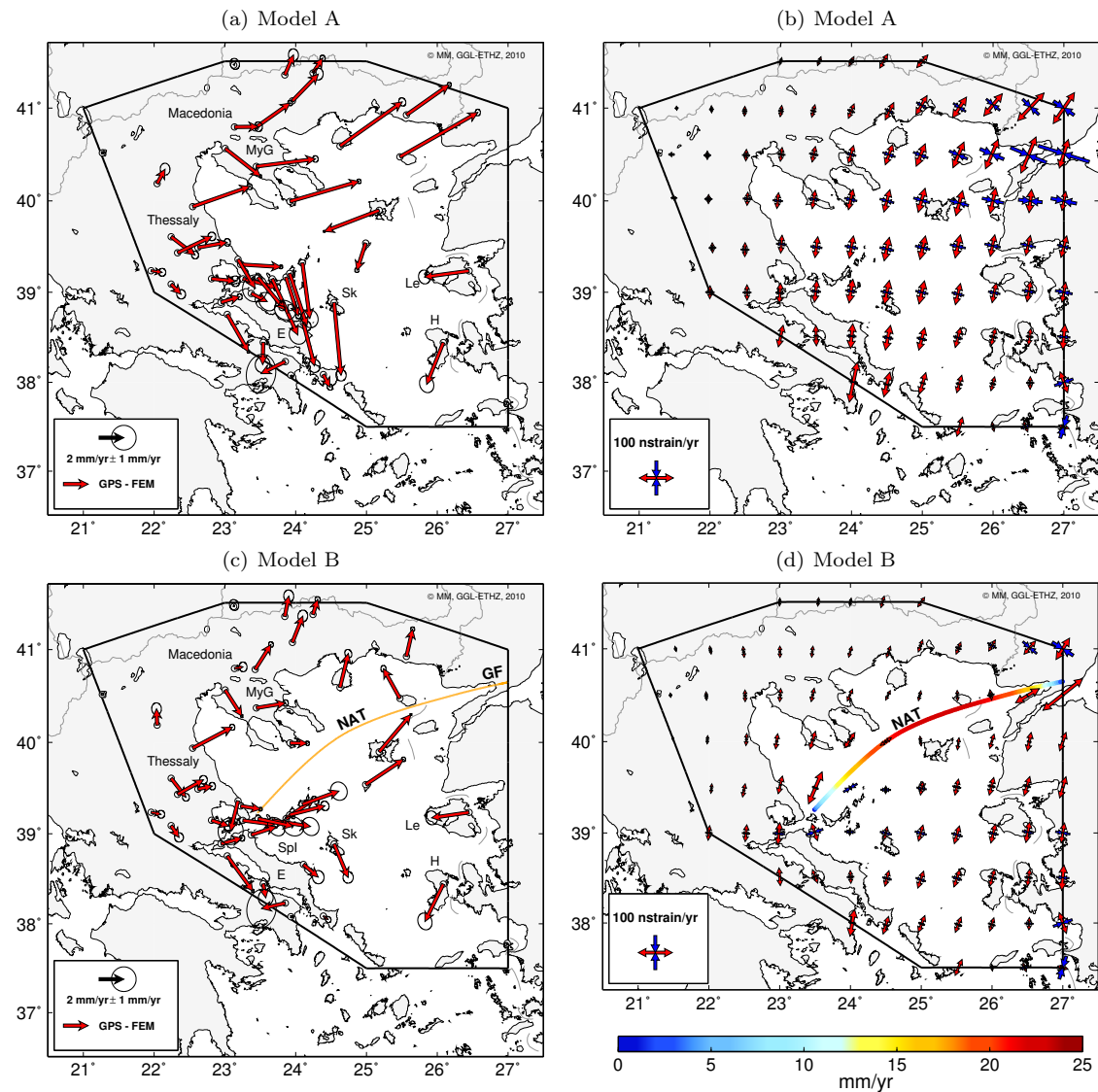


Figure 7.10: Results of FE modeling: (a) and (c) Residuals (GPS rates minus averaged annual FEM displacement rates) for models A (a) and B (c). The error ellipses depict the 1- σ confidence region. The orange line depicts the introduced fault in (c). (b) and (d) Principal strain rate axes and fault slip rates corresponding to the indicated color table (both annual averages) for models A (b) and B (d). Red arrows denote extension, blue arrows compression. Only selected principal strain rate axes are depicted following approximately a 1° grid spacing. No interpolation is applied. E: Evia, GF: Ganos fault, H: Hios, Le: Lesbos, MyG: Mygdonian graben, NAT: North Aegean trough, Sk: Skyros, Spl: Sporades islands.

normal faults northwest of Mount Olympus [Goldsworthy *et al.*, 2002] and NW-SE to E-W trending normal faults to the east and south of it [Caputo and Pavlides, 1993; Nance, 2010]

Strain rates in the North Aegean domain derived by FE analysis and derived by the method of collocation (chapter 5.3) do not yield identical results for all the regions (Fig. 7.13). The results of both methods indicate low strain rates in Thrace and between southern Evia and Samos (maximum shear strain rates: 30 nstrain/yr). A slowly deforming region comprising Limnos, Agios Efstration and the Sporades islands is obtained by the FE model. This feature is less evident in the GPS based strain rate field calculated by the method of collocation. However, this result is

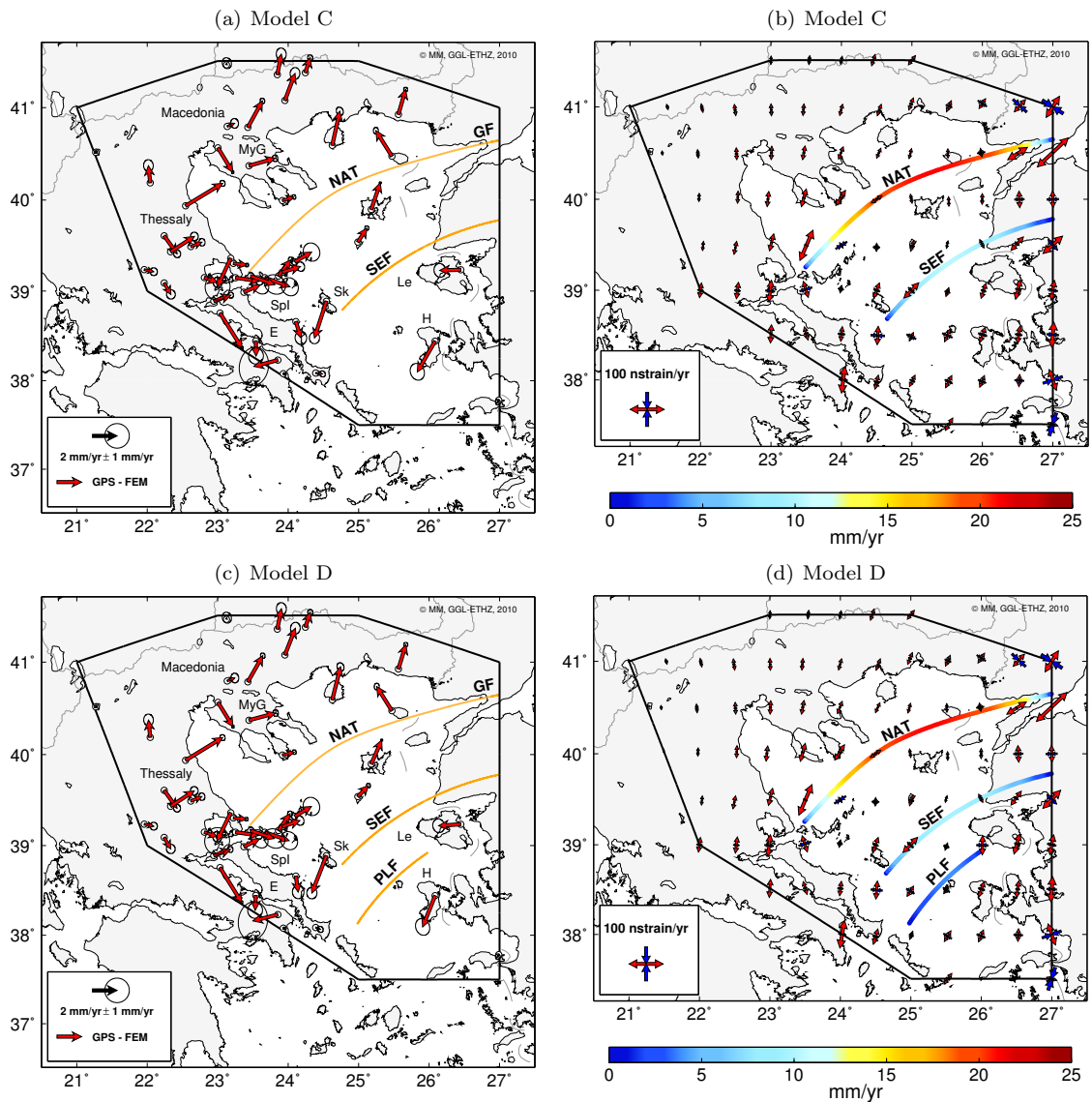


Figure 7.11: Results of FE modeling: (a) and (c) Residuals (GPS rates minus averaged annual FEM displacement rates) for models C (a) and D (c). The error ellipses depict the 1- σ confidence region. The orange lines depict the introduced faults in (a) and (c). (b) and (d) Principal strain rate axes and fault slip rates corresponding to the indicated color table (both annual averages) for models C (b) and D (d). Red arrows denote extension, blue arrows compression. Only selected principal strain rate axes are depicted following approximately a 1° grid spacing. No interpolation is applied. E: Evia, GF: Ganos fault, H: Hios, Le: Lesbos, MyG: Mygdonian graben, NAT: North Aegean trough, PLF: Psara-Lesvos trough, SEF: Skyros-Edremit fault, Sk: Skyros, Spl: Sporades islands.

corroborated by kinematic block modeling and by seismicity recorded in the last 30 years and, therefore, is plausible. Small strain rates (10–40 nstrain/yr) are derived by the FE model in entire Northwestern Greece. In contrast, GPS based strain rates show pronounced extension across the Mygdonian graben and shear strain and extension near Mount Olympus. Extension rates (100 nstrain/yr) across the Mygdonian graben are indicated by GPS sites closely located to the Mygdonian graben. Thus, extension in northwestern Greece is probably more distinctly associated with particular fault structures than indicated by FEM. The GPS network near the Mount Olympus

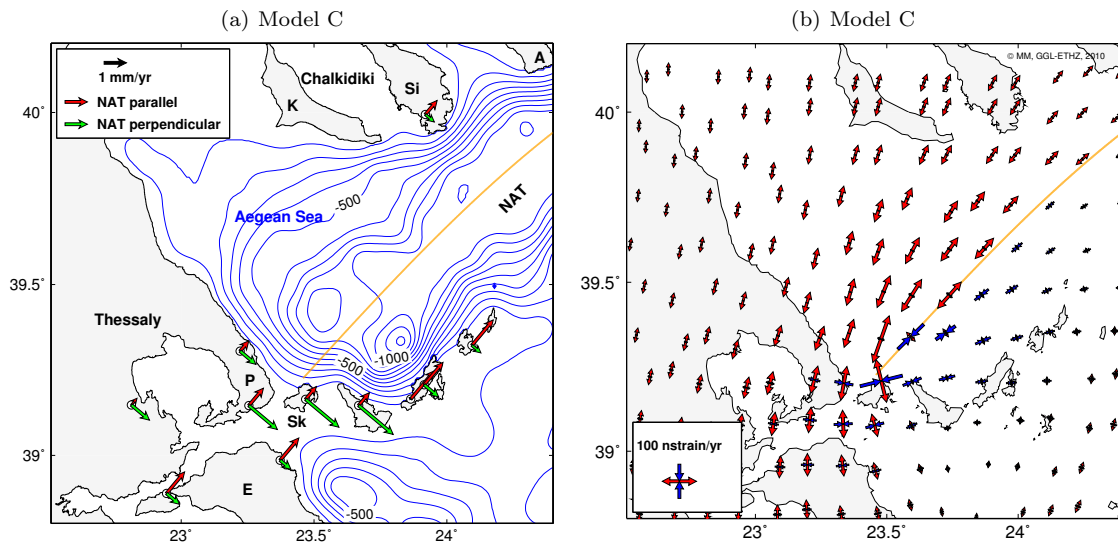


Figure 7.12: (a) Residuals (GPS rates minus annual averaged FEM displacement rates derived in version C) in the northwestern Aegean sea depicted by their fault-parallel (red arrows) and fault-perpendicular (green arrows) components, respectively (fault strike: 220°). The orange line depicts the modeled fault (NAT). The equidistance of the isobaths is 100 m. A: Athos peninsula, E: Evia, K: Cassandra peninsula, Si: Sithonia peninsula, NAT: North Aegean trough, P: Pelion, Sk: Skiathos. (b) Calculated strain rates in the northwestern Aegean sea (version C). Only selected strain rate axes are depicted following approximately a homogeneous grid spacing. No interpolation is applied. Red arrows denote extension, blue arrows compression.

is rather sparse. Additional observations are required for an interpretation of the deformation field in this area.

In summary, the analysis shows that the present-day velocity field of the North Aegean domain can be reconstructed to a large extent by applying the motion encountered at its margin as boundary conditions and by introducing the two major ENE-WSW to NE-SW trending dextral strike-slip faults (NAT, SEF). Maximum strike-slip on these faults amounts to 21 mm/yr and 10 mm/yr, respectively. In addition to dextral strike-slip, which is the prevailing deformation style in the North Aegean domain, NNE-SSW extension across the Mygdonian graben, between the Chalkidiki peninsula and Pelion and between Skyros and Agios Efstratios is revealed.

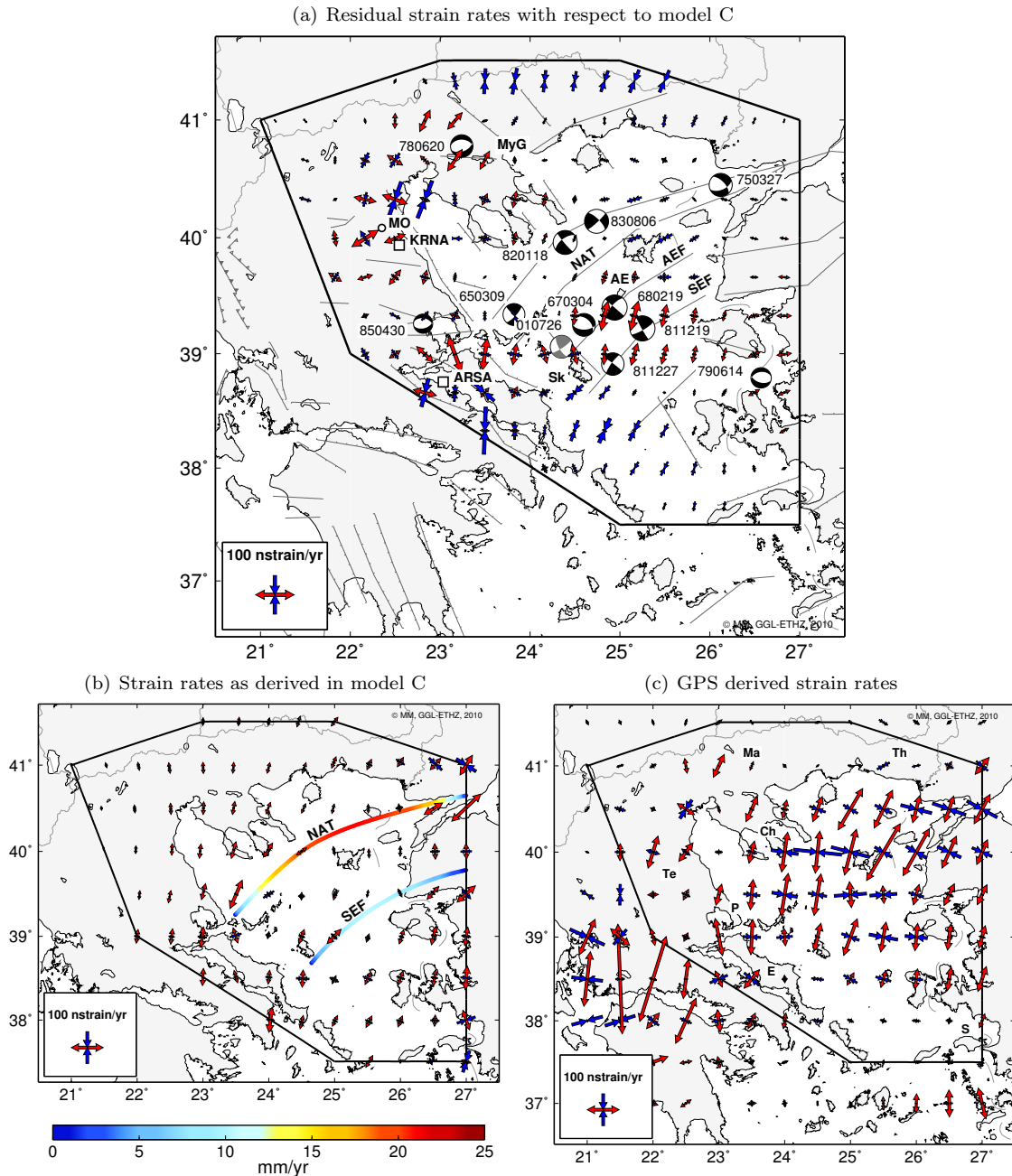


Figure 7.13: (a) Strain rates calculated with the method of collocation based on residuals (GPS rates minus annual averaged FEM displacement rates) of model C (Fig. 7.11 (a)). In addition to the residuals zero velocities were introduced along the border of the model (black polygon). A correlation length of 110 km and a σ_0 of 5 mm/yr were used. The black colored focal mechanisms were derived by *Taymaz et al.* [1991]. The gray colored focal mechanism represents the 2001 Mw 6.4 Skyros earthquake [*Melis et al.*, 2001]. (b) Strain rates and slip rates as derived in model C (Fig. 7.11 (b)). (c) Strain rates derived from collocated GPS rates as discussed in chapter 5.3. AE: Agios Efstratios, AEF: Agios Efstatios fault, Ch: Chalkidiki peninsula, E: Evia, Ma: Macedonia, MO: Mount Olympus, MyG: Mygdonian graben, NAT: North Aegean trough, P: Pelion, S: Samos, SEF: Skyros-Edremit fault, Sk: Skyros, Te: Thessaly, Th: Thrace.

7.5 Concluding remarks

Finite element models were developed and applied in order to investigate the strain rate fields associated with the dextral strike-slip faults in the North Aegean sea and the subduction along the central Hellenic trench. The results of the analyses were compared to present-day GPS rates. The most important findings are the following:

1. The modeling of deformation processes in the North Aegean domain reveals the concentration of strike-slip motion along ENE-WSW to NE-SW trending faults. The NAT acts as a distinct tectonic feature accommodating up to 21 mm/yr of strike-slip motion. The decreasing slip rates towards the Greek mainland agrees with GPS rates. Additional strike-slip motion of 14 mm/yr is distributed on several faults south of the NAT whereas 10 mm/yr is accommodated on the SEF and the AEF and 4 mm/yr on the PLF. Distinct NNE-SSW extension is calculated between Pelion and Chalkidiki and derived by the comparison with GPS rates between Skyros and Agios Efstratios.
2. An elementary FE model was set up to link the slowly deforming South Aegean sea with subduction processes along the central Hellenic trench. The conducted analysis shows that the GPS rates are in agreement with an uncoupled plate interface. Distinct stress build-up is calculated south of Crete as a consequence of slab geometry and temperature and pressure dependent rheology.

The models contain various simplifications to facilitate computation but are further extendable. The model describing the North Aegean domain could be improved by the inclusion of additional normal faults, by the specification of a not entirely elastic rheology and the onset of appropriate fault friction. Accordingly, a reasonable stress state has to be established at the beginning of the model run. The implementation of more accurate structural and physical information (e.g., variations of heat flow) and the modeling of complex fault structures would significantly increase the complexity of the model. This holds true also for the model describing the interaction of the South Aegean with the subducting slab. The extension of this model towards a three-dimensional, self-consistent model requires the inclusion of more sophisticated physical processes and a more detailed specification of geologic structures.

In conclusion, the application of the FE analysis provides valuable results in terms of testing model hypotheses. An important benefit of the method is that stress is an integral part of the analysis allowing more extensive conclusions. The definition of a reasonable scope and the location-dependent application are demanding aspects of the method.

8 Conclusions

The thesis covers three main topics. The research area comprises the Eastern Mediterranean with special focus on the Hellenic domain. The first of these topics deals with the evaluation of a long-term GPS data record (1993–2009), the analysis of GPS position time series and the calculation of accurate rates of crustal motion. The second topic focuses on the detailed analysis of the derived kinematic field and its discussion in terms of tectonic structures and seismicity. The objectives of the third topic are the formulation of geoscientific interpretations and the discussion of tectonic implications resulting from the conducted analyses. Following the main tasks outlined in the introduction, the most important results are presented, remaining problem areas are discussed, and a short outlook is given.

Computation of accurate GPS results

Accurate GPS rates were derived for sites of a continuous and campaign-type GPS network in Greece based on data from 1993 to 2009. Additional 72 IGS and EUREF sites located in Europe, North Africa and the Middle East were included to achieve this task. The GPS processing strategy applied in earlier studies was revisited. Enhancements were established in the fields of GPS data evaluation and of subsequent processing steps.

Recently developed or improved GPS evaluation models (e.g., related to tropospheric modeling, ocean tide loading modeling) were applied by using the Bernese GPS software 5.0. Moreover, products (orbits, EOPs) originating from recent reprocessing activities were used. The employment of reprocessed orbits/EOPs instead of IGS final orbits for the time period 1994–2003 reduces position artifacts most distinctly in the middle nineties. The resulting raw coordinate time series are characterized by repeatabilities of 1–3 mm/yr and 4–6 mm/yr in the horizontal and vertical components, respectively. Despite of the use of up-to-date processing models, pronounced seasonal signals are detected in some of the raw time series. The amplitudes of these signals amount to ~ 2 mm for sites in Greece.

Several routines were implemented for the postprocessing of GPS position estimates. These included handling of site specific information, robust outlier detection and mitigation of seasonal signals by spatial filtering. The efforts made in this field led to a reduction of seasonal signals by up to 30 percent (average for sites in Greece). The improved CGPS position time series allow the estimation of velocities with accuracies of a few tenths of a millimeter per year. Coseismic displacements can be detected at the millimeter level. In contrast, the precise determination of temporal characteristics of transient slip in the order of a few millimeters over a period of several months and the interpretation of small seasonal signals in terms of their origin (GPS related or tectonic) remain challenging. The reprocessing of data between 1995 and 2004 revealed displacements in the order of 3–4 mm at site DION associated with the 1999 Mw 5.9 Athens and the 2001 Mw 6.4 Skyros earthquakes, respectively. The temporal characteristics of these signals were not entirely resolved. Time dependent signals/artifacts not obviously related to seismic activity or another known physical process were observed in coordinate time series of several sites (e.g., APAX, PAXI, SKIN).

The derived factors for scaling the formal accuracies of CGPS rates only reflect temporal correlations. Additional error sources exist which depend on the evaluation strategy (e.g., applied

velocity model, employed orbits/EOPs). These can reach a few tenths of a millimeter and exceed the indicated accuracy of rates of CGPS sites but they are difficult to quantify exactly. Similar considerations apply to the scaling of formal accuracies of rates of campaign-type sites with one single factor. Although this is an efficient approach and appropriate for the majority of sites it does not take into account any heterogeneities of the data set.

A repeated reprocessing of the complete data set in the future will probably take advantage of enhanced GPS data evaluation techniques and improved products. However, for sites with poor tracking performance the gain of accuracy is most likely limited.

Analysis and modeling of the kinematic field

The evaluation of the extended continuous and campaign-type GPS network enhanced the knowledge of present-day crustal motion in Greece. Notably, this applies for the North Aegean sea and the Southeast Aegean sea. For instance, GPS rates indicate N-S to NNE-SSW extension from southern Bulgaria to central Greece in more detail and shed light on the kinematics at the western termination of the North Aegean trough.

The kinematic field was analyzed in terms of a kinematic block model in order to investigate the presence of slowly deforming regions. The Southwest Aegean sea and the eastern Peloponnesos are two regions associated with small deformations. Epirus, Western Macedonia, Thessaly and central Greece rotate uniformly clockwise. Residuals with respect to a single Euler pole for this region clearly show N-S extension in eastern Thessaly and across the Gulf of Evia. Furthermore, a slowly deforming and ccw rotating region was revealed comprising the islands of Limnos, Agios Efstratios and Alonissos. This block appears as a transition zone with respect to the cw rotating domain forming the western termination of the North Aegean trough. The derived block model shows that large parts of ongoing deformation are bound to distinct regions (e.g., NAT, Gulf of Corinth, Mygdonian graben, Gulf of Evia).

The calculation of strain rates using the method of collocation reveals valuable new findings. Important results are N-S to NNW-SSE extension (150 nstrain/yr) between Kalymnos and Tilos in the SE Aegean sea, diminishing shear strain rates along the NAT from the Saros (150 nstrain/yr) to the Sporades basin (75 nstrain/yr) and NNE-SSW extension in the order of 100 nstrain/yr between Pelion and the Sporades islands. The strain rates imply for the NAT that its ENE-WSW trending structures along the Saros basin accommodate significant extension in addition to dextral shear strain while its NE-SW trending structures along the Sporades basin are almost pure strike-slip faults.

The trade-off between block size and accepted residuals related to the block modeling and the dependency of the calculated strain rates on an isotropic covariance function are the main shortcomings of the respective methods. Nonetheless, they are valuable instruments for a first-order interpretation of the kinematic field.

A step towards a three-dimensional velocity field in Greece could be achieved. Vertical rates for 21 CGPS sites were derived. However, these rates are spatially isolated and in many cases characterized by accuracies which are in the range of the signal. Nevertheless, some trends were derived in this thesis such as uplift on Karpathos and Rhodes and in mainland Greece. Longer time series and refined evaluation models will most likely improve the accuracy of vertical rates. Revisiting the strategy of defining the geodetic datum (e.g., in combination with the analysis of a global GPS network) might enhance the robustness of the results in terms of possibly existing systematic errors.

The present-day GPS network covers wide areas of the Hellenic plate boundary zone whereas a trend to an increase in the number of CGPS sites operated by several agencies is noted. A further

densification of the GPS network focusing on active tectonic structures (e.g., North Aegean sea, Southeast Aegean sea) would provide additional constraints for geodynamic models with regional or local dimensions. In particular, this applies for the vertical velocity component. The prolongation of GPS time series will reveal new details about time-dependent geodynamic processes. Examples are volcanic processes on Nisyros, as well as stress build-up along the islands near the central Hellenic trench and along the North Aegean trough.

Tectonic implications

One major goal of the thesis was to elucidate the relation of crustal motion to geophysical parameters. In this context, GPS derived coseismic displacements were compared with an analytical dislocation model. Significant and clearly assignable displacements were derived for the 2006 Zakynthos earthquake series (Mw 5.0–5.7) and the 2008 Mw 6.4 NW Peloponnesos earthquake in addition to displacements related to earthquakes already discussed in former studies. The comparison of observed displacements with estimates calculated by an elastic dislocation model revealed a reasonable fit for the 2008 NW Peloponnesos earthquake. A less optimal fit was obtained for the 1997 Strofades, the 2001 Skyros and the 2003 Lefkada earthquakes. The geodetic data alone is not sufficient in all cases to improve the model parameters. GPS position estimates at significantly higher frequencies (>1 Hz) would improve the determination of co- and postseismic displacements and would enhance models relating displacements to earthquake rupture processes.

The two dominant dextral strike-slip faults, the North Aegean trough (NAT) and the Kefalonia fault zone (KFZ), were analyzed in terms of the model of a buried screw dislocation in an elastic half-space. This modeling approach reveals diminishing strike-slip rates along the NAT from the Ganos fault (22.5 mm/yr) and the Saros basin (21.2 mm/yr) towards the Chalkidiki peninsula (12.5 mm/yr) and the Sporades islands (4.9 mm/yr). The model points to locking depths between 5–10 km for the Ganos fault and along the Saros basins and 18 km between Pelion and the Sporades islands. The modeling shows that the NAT is a continuation of the North Anatolian fault zone (NAF) extending up to the Chalkidiki peninsula. Average annual seismic moment accumulation for strike-slip earthquakes diminishes from the Ganos fault towards the Sporades islands by about 80% if assuming that the fault is completely locked. Only a small amount of right-lateral strike-slip motion (<5 mm/yr) is transferred from the NAT towards Northern Evia which is rather diffuse in style. Strike-slip motion in the order of 19 mm/yr and a locking depth of ~ 11 km results for the KFZ. Moreover, GPS rates in NW Peloponnesos and southern Zakynthos do not rule out significant strain accumulation when being analyzed using a dislocation model describing strain accumulation at a subduction zone. Additional measurements and modeling efforts are required to investigate this topic in more detail. The two-dimensional dislocation models imply several simplifications of the real structures (e.g., fault geometry, rheology). However, the employed dislocation models provide a first-order characterization of the particular tectonic structures based on GPS rates. The results are useful for seismic hazard assessment.

Finite element analysis was employed as additional modeling approach. Two models were set up. The first one relates GPS rates in the South Aegean sea with subduction at the central Hellenic trench along a quasi two-dimensional cross-section. The model shows that the GPS rates are in agreement with a largely uncoupled subduction interface. Moreover, the rate of subsidence of the Nubian slab is narrowed down to 10–13 mm/yr. The value largely depends on the geometry of the slab. The second model was set up to derive the rates of strike-slip motion along the three major ENE-WSW to NE-SW trending dextral strike-slip faults in the North Aegean sea and to investigate the location, style and amount of complementary deformation zones. Most important results are dextral slip amounting to 21 mm/yr for the NAT, 10 mm/yr in total for the Agios Efstratios and the Skyros-Edremit faults and 4 mm/yr for the Psara-Lesvos trough. Moreover, NNE-SSW extension in the Sporades basin is calculated which extends towards Macedonia. Model residuals point to NNE-SSW extension between Skyros and Agios Efstratios in addition to the

dextral strike-slip faults.

The elementary finite element models developed provide important constraints on present-day tectonics. These can further be refined in order to expand the extent of derivable conclusions in future work. The establishment of proper initial conditions and the appropriate modeling of tectonic structures are challenging. GPS rates reasonably constrain models which are based on elastic rheology. Refined models with an extended parameter set (e.g., inelastic rheology, more detailed physical and structural information) are insufficiently constrained by GPS alone. Substantial knowledge from other disciplines is required. The advantage of finite element modeling is the explicit relation between displacements, rheology and stress formulated in the algorithms. Due to the inherent relationship between forces and deformation it offers the possibility of studying and also excluding mechanisms driving recent crustal movements in the Eastern Mediterranean. Especially in complex tectonic settings such as the Hellenic domain this approach is only marginally investigated so far. The FEM analysis will certainly be expanded in the future in integrating more detailed and sophisticated geophysical structures and by incorporating ongoing continuous and high-frequent GNSS observations.

The study of the three research topics conducted in this thesis has shed light on prominent seismotectonic features which are important for the understanding of ongoing crustal deformation in Greece. During the course of the thesis also numerous new questions arose which require additional in-depth investigations. One example is the phenomenon of silent earthquakes which have been found in other subduction zones and may also occur in the Hellenic subduction zone. Their detection could significantly help to better understand the potential of seismic hazard in Greece. The continuation and intensification of geodetic monitoring and its close cooperation with geophysical modeling will certainly offer a large spectrum of research opportunities for better understanding the strain and stress field occupying the complex Hellenic plate boundary zone.

Bibliography

- ABAQUS (2009), *Abaqus Analysis User's Manual, Version 6.9*, Dassault Systèmes.
- Aktug, B., J. M. Nocquet, A. Cingöz, B. Parsons, Y. Erkan, P. England, O. Lenk, M. Gürdal, A. Kilicoglu, H. Akdeniz, and A. Tekgül (2009), Deformation of western Turkey from a combination of permanent and campaign GPS data: Limits to block-like behavior, *J. Geophys. Res.*, *114*, doi:10.1029/2008JB006000.
- Altamimi, Z., X. Collilieux, J. Legrand, B. Garayt, and C. Boucher (2007), ITRF2005: A new release of the International Terrestrial Reference Frame based on time series of station positions and Earth Orientation Parameters, *J. Geophys. Res.*, *11*, doi:10.1029/2007JB004949.
- Ambraseys, N. N., and C. F. Finkel (1987), The Saros-Marmara earthquake of 9 August 1912, *Earthquake engineering and structural dynamics*, *15*, 189–211, doi:10.1002/eqe.4290150204.
- Ambraseys, N. N., and J. A. Jackson (1990), Seismicity and associated strain of central Greece between 1890 and 1988, *Geophys. J. Int.*, *101*, 663–708, doi:10.1111/j.1365-246X.1990.tb05577.x.
- Armijo, R., H. Lyon-Caen, and D. Papanastassiou (1991), A possible normal-fault rupture for the 464 BC Sparta earthquake, *Nature*, *351*(6322), 137–139, doi:10.1038/351137a0.
- Armijo, R., B. Meyer, G. C. P. King, A. Rigo, and D. Papanastassiou (1996), Quaternary evolution of the Corinth Rift and its implications for the Late Cenozoic evolution of the Aegean, *Geophys. J. Int.*, *126*, 11–53, doi:10.1111/j.1365-246X.1996.tb05264.x.
- Armijo, R., B. Meyer, A. Hubert, and A. Barka (1999), Westward propagation of the North Anatolian fault into the northern Aegean: Timing and kinematics, *Geology*, *27*, 267–270, doi:10.1130/0091-7613(1999)027<0267:WPOTNA>2.3.CO;2.
- Atzori, S., M. Manunta, G. Fornaro, A. Ganas, and S. Salvi (2008), Postseismic displacements of the 1999 Athens earthquake retrieved by the Differential Interferometry by Synthetic Aperture Radar time series, *J. Geophys. Res.*, *113*(B09309), doi:10.1029/2007JB005504.
- Avallone, A., P. Briole, A. M. Agatza-Balodimou, H. Billiris, O. Charade, C. Mitsakaki, A. Nercessian, K. Papazissi, D. Paradissis, and G. Veis (2004), Analysis of eleven years of deformation measured by GPS in the Corinth Rift Laboratory area, *Tectonics*, *336*, 301–311, doi:10.1016/j.crte.2003.12.007.
- Baumont, D., O. Scotti, F. Courboux, and N. Melis (2004), Complex kinematic rupture of the Mw 5.9, 1999 Athens earthquake as revealed by the joint inversion of regional seismological and SAR data, *Geophys. J. Int.*, *158*, 1078–1087, doi:10.1111/j.1365-246X.2004.02374.x.
- Benetatos, C., Z. Roumelioti, A. Kiratzi, and N. Melis (2002), Source parameters of the M 6.5 Skyros Island (North Aegean Sea) earthquake of July 26, 2001, *Annals of Geophysics*, *45*(3/4), 513–526.
- Benetatos, C., A. Kiratzi, C. Papazachos, and G. Karakaisis (2004), Focal mechanisms of shallow and intermediate depth earthquakes along the Hellenic Arc, *J. Geodynamics*, *37*, 253–296, doi:10.1016/j.jog.2004.02.002.

- Benetatos, C., A. Kiratzi, Z. Roumelioti, G. Stavrakakis, G. Drakatos, and I. Latoussakis (2005), The 14 August 2003 Lefkada Island (Greece) earthquake: Focal mechanisms of the mainshock and of the aftershock sequence, *Journal of Seismology*, *9*(2), 171–190, doi:10.1007/s10950-005-7092-1.
- Benetatos, C., D. Dreger, and A. Kiratzi (2007), Complex and Segmented Rupture Associated with the 14 August 2003 Mw 6.2 Lefkada, Ionian Islands, Earthquake, *Bulletin of the Seismological Society of America*, *97*, 35–51, doi:10.1785/0120060123.
- Beutler, G., H. Bock, R. Dach, P. Fridez, A. Gäde, U. Hugentobler, A. Jäggi, M. Meindl, L. Mervart, L. Prange, S. Schaer, T. Springer, C. Urschl, and P. Walser (2007), *Bernese GPS Software Version 5.0*, Astronomical Institute, University of Bern.
- Blewitt, G., and D. Lavallée (2002), Effect of annual signals on geodetic velocity, *J. Geophys. Res.*, *107*(B7), doi:10.1029/2001JB000570.
- Boehm, J., B. Werl, and H. Schuh (2006), Troposphere mapping functions for GPS and very long baseline interferometry from European Centre for Medium-Range Weather Forecasts operational analysis data, *J. Geophys. Res.*, *111*, doi:10.1029/2005JB003629.
- Bohnhoff, M., H.-P. Harjes, and T. Meier (2005), Deformation and stress regimes in the Hellenic subduction zone from focal Mechanisms, *Journal of Seismology*, *9*(3), 341–366, doi:10.1007/s10950-005-8720-5.
- Bohnhoff, M., M. Rische, T. Meier, D. Becker, G. Stavrakakis, and H.-P. Harjes (2006), Microseismic activity in the Hellenic Volcanic Arc, Greece, with emphasis on the seismotectonic setting of the Santorini-Amorgos zone, *Tectonophysics*, *423*, 17–33, doi:10.1016/j.tecto.2006.03.024.
- Briole, P., A. Rigo, H. Lyon-Caen, J. C. Ruegg, K. Papazissi, C. Mitsakaki, A. Balodimou, G. Veis, D. Hatzfeld, and A. Deschamps (2000), Active deformation of the Corinth rift, Greece: Results from repeated Global Positioning System surveys between 1990 and 1995, *J. Geophys. Res.*, *105*(B11), 25,605–25,625, doi:10.1029/2000JB900148.
- Brooks, M., J. E. Clews, N. S. Melis, and J. R. Underhill (1988), Structural development of Neogene basins in western Greece, *Basin Research*, *1*, 129–138, doi:10.1111/j.1365-2117.1988.tb00010.x.
- Bruyninx, C. (2004), The EUREF Permanent Network: a multi-disciplinary network serving surveyors as well as scientists, *Geoinformatics*, *7*, 32–35.
- Buiter, S. J. H., R. Govers, and M. J. R. Wortel (2002), Two-dimensional simulations of surface deformation caused by slab detachment, *Tectonophysics*, *354*, 195–210, doi:10.1016/S0040-1951(02)00336-0.
- Burchfiel, B. C., R. W. King, A. Todosov, V. Kotzev, N. Durmurdzanov, T. Serafimovski, and B. Nurce (2006), GPS results for Macedonia and its importance for the tectonics of the Southern Balkan extensional regime, *Tectonophysics*, *413*, 239–248, doi:10.1016/j.tecto.2005.10.046.
- Burchfiel, B. C., R. Nakov, N. Dumurdzanov, D. Papanikolaou, T. Tzankov, T. Serafimovski, R. W. King, V. Kotzev, A. Todosov, and B. Nurce (2008), Evolution and dynamics of the Cenozoic tectonics of the South Balkan extensional system, *Geosphere*, *4*(6), 916–938, doi:10.1130/GES00169.1.
- Burov, E. (2007), Plate rheology and mechanics, in *Treatise on Geophysics*, vol. 6: Crust and Lithosphere Dynamics, pp. 99–151, ISBN: 978-0-444-51928-3.
- Caputo, R., and S. Pavlides (1993), Late Cainozoic geodynamic evolution of Thessaly and surroundings (central-northern Greece), *Tectonophysics*, *223*(3-4), 339–362, doi:10.1016/0040-1951(93)90144-9.

- Caputo, R., S. Catalano, C. Monaco, G. Romagnoli, G. Tortorici, and L. Tortorici (2010), Active faulting on the island of Crete (Greece), *Geophys. J. Int.*, *183*(1), 111–126, doi:10.1111/j.1365-246X.2010.04749.x.
- Chatzipetros, A. A., S. B. Pavlides, and D. M. Mountrakis (1998), Understanding the 13 May 1995 western Macedonia earthquake: A paleoseismological approach, *Journal of Geodynamics*, *26*(2-4), 327–339, doi:10.1016/S0264-3707(97)00069-0.
- Cherchi, A., and L. Montadert (1982), Oligo-Miocene rift of Sardinia and the early history of the Western Mediterranean Basin, *Nature*, *298*, 736–739, doi:10.1038/298736a0.
- Clarke, P. J., R. R. Davies, P. C. England, B. Parsons, H. Billiris, D. Paradissis, G. Veis, P. A. Cross, P. H. Denys, V. Ashkenazi, R. Bingley, H.-G. Kahle, M.-V. Müller, and P. Briole (1998), Crustal strain in central Greece from repeated GPS measurements in the interval 1989-1997, *Geophys. J. Int.*, *135*, 195–214, doi:10.1046/j.1365-246X.1998.00633.x.
- CMT catalog (2011), Global Centroid-Moment-Tensor (CMT), www.globalcmt.org.
- Cocard, M., H.-G. Kahle, Y. Peter, A. Geiger, G. Veis, S. Felekis, D. Paradissis, and H. Billiris (1999), New constraints on the rapid crustal motion of the Aegean region: recent results inferred from GPS measurements (1993-1998) across the West Hellenic Arc, Greece, *Earth and Planetary Science Letters*, *172*, 39–47, doi:10.1016/S0012-821X(99)00185-5.
- D’Agostino, N., A. Avallone, D. Cheloni, E. D’Anastasio, S. Mantenuto, and G. Selvaggi (2008), Active tectonics of the Adriatic region from GPS and earthquake slip vectors, *J. Geophys. Res.*, *113*(B12413), doi:10.1029/2008JB005860.
- Damuser, G., A. Geiger, and M. V. Müller (1993), Modellierung von Verschiebungs- und Verzerrungsfeldern, *Tech. Rep. 218*, Institut für Geodäsie und Photogrammetrie, ETH Zürich, ISBN: 3-906513-34-3.
- Denys, P. H., P. A. Cross, G. Veis, H. Billiris, D. Paradissis, V. Ashkenazi, R. Bingley, P. Clarke, B. E. England, P. Parsons, H.-G. Kahle, and M. V. Müller (1995), GPS networks for determining the accumulation of current crustal strain in central Greece, in *Proceedings of 1st Turkish International Symposium on deformations*, vol. 2, pp. 748–758.
- Dong, D., P. Fang, Y. Bock, M. K. Cheng, and S. Miyazaki (2002), Anatomy of apparent seasonal variations from GPS-derived site position time series, *J. Geophys. Res.*, *107*, doi:10.1029/2001JB000573.
- Dow, J. M., R. E. Neilan, and C. Rizos (2009), The International GNSS Service in a changing landscape of Global Navigation Satellite Systems, *Journal of Geodesy*, *83*(3-4), 191–198, doi:10.1007/s00190-008-0300-3.
- Drucker, D., and W. Prager (1952), Soil Mechanics and Plastic Analysis or Limit Design, *Quarterly of Applied Mathematics*, *10*(2), 157–165.
- EMSC catalog (2009), European-Mediterranean Seismological Centre, <http://www.emsc-csem.org>.
- Ergintav, S., R. Bürgmann, S. McClusky, R. Çakmak, R. E. Reilinger, O. Lenk, A. Barka, and H. Özener (2002), Postseismic Deformation near the Izmit Earthquake (17 August 1999, M 7.5) Rupture Zone, *Bulletin of the Seismological Society of America*, *92*(1), 194–207, doi:10.1785/0120000836.
- Erickson, A., G. Simmons, and W. Ryan (1977), Review of Heatflow data from the Mediterranean and Aegean Seas, in *International Symposium of the Structural History of the Mediterranean Basins. Split (Yugoslavia)*, edited by B. Biju-Duval and L. Montadert, pp. 263–280.

- EUREFmail (2011), EUREF Permanent Network, http://www.epncb.oma.be/_newsmails/EUREFmail/.
- Faccenna, C., and T. W. Becker (2010), Shaping mobile belts by small-scale convection, *Nature*, *465*, 602–605, doi:10.1038/nature09064.
- Faccenna, C., T. W. Becker, F. P. Lucente, L. Jolivet, and F. Rossetti (2001), History of subduction and back-arc extension in the Central Mediterranean, *Geophys. J. Int.*, *145*, 809–820, doi:10.1046/j.0956-540x.2001.01435.x.
- Faccenna, C., C. Piromallo, A. Crespo-Blanc, L. Jolivet, and F. Rossetti (2004), Lateral slab deformation and the origin of the western Mediterranean arcs, *Tectonics*, *23*, doi:10.1029/2002TC001488.
- Feng, L., A. V. Newman, G. T. Farmer, P. Psimoulis, and S. C. Stiros (2010), Energetic rupture, coseismic and post-seismic response of the 2008 Mw 6.4 Achaia-Elia Earthquake in northwestern Peloponnese, Greece: an indicator of an immature transform fault zone, *Geophys. J. Int.*, *183*, 103–110, doi:10.1111/j.1365-246X.2010.04747.x.
- Floyd, M. A., H. Billiris, D. Paradissis, G. Veis, A. Avallone, P. Briole, S. McClusky, J.-M. Nocquet, K. Palamartchouk, B. Parsons, and P. England (2010), A new velocity field for Greece: Implications for the kinematics and dynamics of the Aegean, *J. Geophys. Res.*, *115*(B10403), doi:10.1029/2009JB007040.
- Fridtjov, I. (2008), *Continuum Mechanics*, Springer, ISBN: 978-3-540-74297-5.
- Fritsche, M., R. Dietrich, C. Knöfel, A. Rülke, S. Vey, M. Rothacher, and P. Steigenberger (2005), Impact of higher-order ionospheric terms on GPS estimates, *Geophys. Res. Letters*, *132*, doi:10.1029/2005GL024342.
- Fytikas, M. D., and N. Kolios (1979), Preliminary heat flow map of Greece, in *Terrestrial Heat Flow in Europe*, edited by V. Cermak and L. Rybach, pp. 197–205.
- Ganas, A. (2009), NOA GPS project, Website, <http://www.gein.noa.gr/gps.html>.
- Ganas, A., and T. Parsons (2009), Three-dimensional model of Hellenic Arc deformation and origin of Cretan uplift, *J. Geophys. Res.*, *114*(B06404), doi:10.1029/2008JB005599.
- Ganas, A., G. Drakatos, S. B. Pavlides, G. N. Stavrakakis, M. Ziazia, E. Sokos, and V. K. Karastathis (2005), The 2001 Mw = 6.4 Skyros earthquake, conjugate strike-slip faulting and spatial variation in stress within the central Aegean Sea, *J. Geodynamics*, *39*(1), 61–77, doi:10.1016/j.jog.2004.09.001.
- Ganas, A., E. Serpelloni, G. Drakatos, M. Kolligri, I. Adamis, C. Tsimi, and E. Batsi (2009), The Mw 6.4 SW-Achaia (Western Greece) Earthquake of 8 June 2008: Seismological, Field, GPS Observations, and Stress Modeling, *Journal of Earthquake Engineering*, *13*, 1101–1124, doi:10.1080/13632460902933899.
- Gautier, P., J.-P. Brun, R. Moriceau, D. Sokoutis, J. Martinod, and L. Jolivet (1999), Timing, kinematics and cause of Aegean extension: a scenario based on a comparison with simple analogue experiments, *Tectonophysics*, *315*(1-4), 31–72, doi:10.1016/S0040-1951(99)00281-4.
- Gilbert, L., K. Kastens, K. Hurst, D. Paradissis, H. Billiris, W. Höppe, and W. Schlüter (1994), Strain Results and Tectonics from the Aegean GPS Experiment, *EOS transactions AGU*, p. 116.
- Giunchi, C., A. Kiratzi, R. Sabadini, and E. Louvari (1996), A numerical model of the Hellenic Subduction Zone: Active stress field and sea-level changes, *Geophys. Res. Letters*, *23*(18), 2485–2488, doi:10.1029/96GL02166.

- Goldsworthy, M., J. Jackson, and J. Haines (2002), The continuity of active fault systems in Greece, *Geophys. J. Int.*, *148*(3), 596–618, doi:10.1046/j.1365-246X.2002.01609.x.
- Hampel, A., and A. Pfiffner (2006), Relative importance of trenchward upper plate motion and friction along the plate interface for the topographic evolution of subduction-related mountain belts, *Geological Society Special Publications*, *253*, 105–115, doi:10.1144/GSL.SP.2006.253.01.05.
- Haslinger, F., E. Kissling, J. Ansorge, D. Hatzfeld, E. Papadimitriou, V. Karakostas, K. Makropoulos, H.-G. Kahle, and Y. Peter (1999), 3D crustal structure from local earthquake tomography around the Gulf of Arta (Ionian region, NW Greece), *Tectonophysics*, *304*(3), 201–218, doi:10.1016/S0040-1951(98)00298-4.
- Hassani, R., D. Jongmans, and J. Chéry (1997), Study of plate deformation and stress in subduction processes using two-dimensional numerical models, *J. Geophys. Res.*, *102*(B8), 17,951–17,965, doi:10.1029/97JB01354.
- Hatzfeld, D., V. Karakostas, M. Ziazia, G. Selvaggi, S. Leborgne, C. Berge, R. Guiguet, A. Paul, P. Voidomatis, D. Diagourtas, I. Kassaras, I. Koutsikos, K. Makropoulos, R. Azzara, M. Di Bona, S. Baccheschi, P. Bernard, and C. Papaioannou (1997), The Kozani-Grevena (Greece) Earthquake of 13 May 1995 Revisited from a Detailed Seismological Study, *Bulletin of the Seismological Society of America*, *87*(2), 463–473.
- Hatzfeld, D., M. Ziazia, D. Kementzetidou, P. Hatzidimitriou, D. Panagiotopoulos, K. Makropoulos, P. Papadimitriou, and A. Deschamps (1999), Microseismicity and focal mechanisms at the western termination of the North Anatolian Fault and their implications for continental tectonics, *Geophys. J. Int.*, *137*(3), 891–908, doi:10.1046/j.1365-246x.1999.00851.x.
- Hollenstein, C. (2006), GPS deformation field and geodynamic implications for the Hellenic plate boundary region, Ph.D. thesis, ETH Zurich, No. 16593.
- Hollenstein, C., A. Geiger, H.-G. Kahle, and G. Veis (2006), CGPS time-series and trajectories of crustal motion along the West Hellenic Arc, *Geophys. J. Int.*, *164*, 182–191, doi:10.1111/j.1365-246X.2005.02804.x.
- Hollenstein, C., M. D. Müller, A. Geiger, and H.-G. Kahle (2008a), Crustal motion and deformation in Greece from a decade of GPS measurements, 1993-2003, *Tectonophysics*, *449*(1-4), 17–40, doi:10.1016/j.tecto.2007.12.006.
- Hollenstein, C., M. D. Müller, A. Geiger, and H.-G. Kahle (2008b), GPS-Derived Coseismic Displacements Associated with the 2001 Skyros and 2003 Lefkada Earthquakes in Greece, *Bulletin of the Seismological Society of America*, *98*(1), 149–161, doi:10.1785/0120060259.
- IGSmail (2011), International GNSS Service, <http://igs.cb.jpl.nasa.gov/mailman/listinfo/igsmail>.
- Jackson, J. (2002), Faulting, Flow, and the Strength of the Continental Lithosphere, *International Geology Review*, *44*(1), 39–61, doi:10.2747/0020-6814.44.1.39.
- Jackson, J., and D. McKenzie (1988), The relationship between plate motions and seismic moment tensors, and the rates of active deformation in the Mediterranean and Middle East, *Geophysical Journal*, *93*, 45–73, doi:10.1111/j.1365-246X.1988.tb01387.x.
- Janssen, C., M. Bohnhoff, Y. Vapnik, E. Görgün, F. Bulut, B. Plessen, D. Pohl, M. Aktar, A. I. Okay, and G. Dresen (2009), Tectonic evolution of the Ganos segment of the North Anatolian Fault (NW Turkey), *Journal of Structural Geology*, *31*, 11–28, doi:10.1016/j.jsg.2008.09.010.
- Jenny, S., S. Goes, D. Giardini, and H.-G. Kahle (2004), Earthquake recurrence parameters from seismic and geodetic strain rates in the eastern Mediterranean, *Geophys. J. Int.*, *157*, doi:10.1111/j.1365-246X.2004.02261.x.

- Jolivet, L., and C. Faccenna (2000), Mediterranean extension and the Africa-Eurasia collision, *Tectonics*, *19*(6), 1095–1106, doi:10.1029/2000TC900018.
- Jongsma, D. (1974), Heat Flow in the Aegean Sea, *Geophys. J. R. astr. Soc.*, *37*, 337–346, doi:10.1111/j.1365-246X.1974.tb04087.x.
- Kahle, H.-G., M. V. Müller, A. Geiger, G. Danuser, S. Mueller, G. Veis, H. Billiris, and D. Paradissis (1995), The strain field in northwestern Greece and the Ionian Islands: results inferred from GPS measurements, *Tectonophysics*, *249*, 41–52, doi:10.1016/0040-1951(95)00042-L.
- Kahle, H.-G., M. Cocard, Y. Peter, A. Geiger, R. Reilinger, A. Barka, and G. Veis (2000), GPS-derived strain rate field within the boundary zones of the Eurasian, African, and Arabian Plates, *J. Geophys. Res.*, *105*, 23,353 – 23,370, doi:10.1029/2000JB900238.
- Karabulut, H., Z. Roumelioti, C. Benetatos, A. K. Mutlu, S. Özalaybey, M. Aktar, and A. Kiratzi (2006), A source study of the 6 July 2003 (Mw 5.7) earthquake sequence in the Gulf of Saros (Northern Aegean Sea): Seismological evidence for the western continuation of the Ganos fault, *Tectonophysics*, *412*(3-4), 195–216, doi:10.1016/j.tecto.2005.09.009.
- Kellner, A. (2007), Different styles of deformation of the fore-arc wedge along the Chilean convergent margin: Insights from 3D numerical experiments, Ph.D. thesis, Mathematisch-Naturwissenschaftliche Fakultät der Universität Potsdam.
- King, M. A., and S. D. P. Williams (2009), Apparent stability of GPS monumentation from short-baseline time series, *J. Geophys. Res.*, *114*(B10403), doi:10.1029/2009JB006319.
- Kiratzi, A., and E. Louvari (2003), Focal mechanisms of shallow earthquakes in the Aegean Sea and the surrounding lands determined by waveform modelling: a new database, *J. Geodynamics*, *36*(1-2), 251–274, doi:10.1016/S0264-3707(03)00050-4.
- Kiratzi, A., E. Sokos, A. Ganas, A. Tselentis, C. Benetatos, Z. Roumelioti, A. Serpetsidaki, G. Andriopoulos, O. Galanis, and P. Petrou (2008), The April 2007 earthquake swarm near Lake Trichonis and implications for active tectonics in western Greece, *Tectonophysics*, *452*(1-4), 51–65, doi:10.1016/j.tecto.2008.02.009.
- Kiratzi, A. A. (2002), Stress tensor inversion along the westernmost North Anatolian Fault Zone and its continuation into the North Aegean Sea, *Geophys. J. Int.*, *151*(2), 360–376, doi:10.1046/j.1365-246X.2002.01753.x.
- Kissel, C., and C. Laj (1988), The Tertiary geodynamical evolution of the Aegean arc: a paleomagnetic reconstruction, *Tectonophysics*, *146*(1-4), 183–201, doi:10.1016/0040-1951(88)90090-X.
- Konstantinou, K. I., C. P. Evangelidis, and N. S. Melis (2011), The 8 June Mw 6.4 Earthquake in Northwest Peloponnese, Western Greece: A Case of Fault Reactivation in an Overpressured Lower Crust?, *Bulletin of the Seismological Society of America*, *101*(1), 438–445, doi:10.1785/0120100074.
- Kotzev, V., R. Nakov, T. Georgiev, B. C. Burchfiel, and R. W. King (2006), Crustal motion and strain accumulation in western Bulgaria, *Tectonophysics*, *413*(3-4), 127–145, doi:10.1016/j.tecto.2005.10.040.
- Kouba, J. (2002), The GPS Toolbox ITRF Transformations, *GPS Solutions*, *5*(3), 88–90, doi:10.1007/PL00012903.
- Koukouvelas, I. K., and A. Aydin (2002), Fault structure and related basins of the North Aegean Sea and its surroundings, *Tectonics*, *21*(5), doi:10.1029/2001TC901037.

- Kreemer, C., N. Chamot-Rooke, and X. Le Pichon (2004), Constraints on the evolution and vertical coherency of deformation in the Northern Aegean from a comparison of geodetic, geologic and seismologic data, *Earth and Planetary Science Letters*, *225*(3-4), 329–346, doi:10.1016/j.epsl.2004.06.018.
- Lagios, E., V. Sakkas, I. Parcharidis, and V. Dietrich (2005), Ground deformation of Nisyros Volcano (Greece) for the period 1995-2002: Results from DInSAR and DGPS observations, *Bulletin of Volcanology*, *68*(2), 201–214, doi:10.1007/s00445-005-0004-y.
- Laigle, M., A. Hirn, M. Sachpazi, and N. Roussos (2000), North Aegean crustal deformation: An active fault imaged to 10 km depth by reflection seismic data, *Geology*, *28*(1), 71–74, doi:10.1130/0091-7613(2000)28<71:NACDAA>2.0.CO;2.
- Laigle, M., A. Hirn, M. Sachpazi, and C. Clément (2002), Seismic coupling and structure of the Hellenic subduction zone in the Ionian Islands region, *Earth and Planetary Science Letters*, *200*, 243–253, doi:10.1016/S0012-821X(02)00654-4.
- Laigle, M., M. Sachpazi, and A. Hirn (2004), Variation of seismic coupling with slab detachment and upper plate structure along the western Hellenic subduction zone, *Tectonophysics*, *391*(1-4), 85–95, doi:10.1016/j.tecto.2004.07.009.
- Lambeck, K. (1995), Late Pleistocene and Holocene sea-level change in Greece and south-western Turkey: a separation of eustatic, isostatic and tectonic contributions, *Geophys. J. Int.*, *122*, 1022–1044, doi:10.1111/j.1365-246X.1995.tb06853.x.
- Langbein, J. (2008), Noise in GPS displacement measurements from Southern California and Southern Nevada, *J. Geophys. Res.*, *113*(B05405), doi:10.1029/2007JB005247.
- Le Pichon, X., and J. Angelier (1979), The hellenic arc and trench system: A key to the neotectonic evolution of the eastern mediterranean area, *Tectonophysics*, *60*(1-2), 1–42, doi:10.1016/0040-1951(79)90131-8.
- Legrand, J., N. Bergeot, C. Bruyninx, G. Wöppelmann, M.-N. Bouin, and Z. Altamimi (2010), Impact of regional reference frame definition on geodynamic interpretations, *Journal of Geodynamics*, *49*(3-4), 116–122, doi:10.1016/j.jog.2009.10.002.
- Letellier, T. (2004), Etude des ondes de marée sur les plateaux continentaux, Ph.D. thesis, Université de Toulouse III, Ecole Doctorale des Sciences de l'Univers, de l'Environnement et de l'Espace.
- Lister, G. S., G. Banga, and A. Feenstra (1984), Metamorphic core complexes of Cordilleran type in the Cyclades, Aegean Sea, Greece, *Geology*, *12*(4), 221–225, doi:10.1130/0091-7613(1984)12<221:MCCOCT>2.0.CO;2.
- Louvari, E., and A. Kiratzi (2001), Source parameters of the 7 September 1999 Athens (Greece) earthquake based on teleseismic data, *Journal of the Balkan Geophysical Society*, *4*(3), 51–60.
- Louvari, E., A. A. Kiratzi, and B. C. Papazachos (1999), The Cephalonia Transform Fault and its extension to western Lefkada Island (Greece), *Tectonophysics*, *308*(1-2), 223–236, doi:10.1016/S0040-1951(99)00078-5.
- Lyon-Caen, H., R. Armijo, J. Drakopoulos, J. Baskoutass, N. Delibassis, R. Gaulon, V. Kouskouna, J. Latoussakis, K. Makropoulos, P. Papadimitriou, D. Papanastassiou, and G. Pedotti (1988), The 1986 Kalamata (South Peloponnesus) Earthquake: Detailed Study of a Normal Fault, Evidences for East-West Extension in the Hellenic Arc, *J. Geophys. Res.*, *93*(B12), 14,967–15,000, doi:10.1029/JB093iB12p14967.

- Mahmoud, S., R. Reilinger, S. McClusky, P. Vernant, and A. Tealeb (2005), GPS evidence for northward motion of the Sinai Block: Implications for E. Mediterranean tectonics, *Earth and Planetary Science Letters*, *238*(1-2), 217–224, doi:10.1016/j.epsl.2005.06.063.
- Mai, M., and G. C. Beroza (2000), Source Scaling Properties from Finite-Fault-Rupture Models, *Bulletin of the Seismological Society of America*, *90*(3), 604–615, doi:10.1785/0119990126.
- Mao, A., C. G. A. Harrison, and T. H. Dixon (1999), Noise in GPS coordinate time series, *J. Geophys. Res.*, *104*(B2), 2797–2816, doi:10.1029/1998JB900033.
- Martinod, J., D. Hatzfeld, P. Savvaidis, and K. Katsambalos (1997), Rapid N-S extension in the Mygdonian Graben (Northern Greece) deduced from repeated geodetic surveys, *Geophys. Res. Letters*, *24*(24), 3293–3296, doi:10.1029/97GL03186.
- Masce, J., and E. Chaumillon (1998), An overview of Mediterranean Ridge collisional accretionary complex as deduced from multichannel seismic data, *Geo-Marine Letters*, *18*(2), 81–89, doi:10.1007/s003670050056.
- MATLAB (2009), Version 7.8.0.347 (R2009a), The MathWorks Inc.
- McClusky, S., S. Balassanian, A. Barka, C. Demir, S. Ergintav, I. Georgiev, O. Gurkan, M. Hamburger, K. Hurst, H.-G. Kahle, K. Kastens, G. Kekelidze, R. W. King, V. Kotzev, O. Lenk, S. Mahmoud, A. Mishin, M. Nadariya, A. Ouzounis, D. Paradissis, Y. Peter, M. Prilepin, R. Reilinger, I. Sanli, H. Seeger, A. Tealeb, M. N. Toksöz, and G. Veis (2000), Global Positioning System constraints on plate kinematics and dynamics in the eastern Mediterranean and Caucasus, *J. Geophys. Res.*, *105*(B3), 5695–5719, doi:10.1029/1996JB900351.
- McKenzie, D. (1972), Active Tectonics of the Mediterranean Region, *Geophys. J. R. astr. Soc.*, *30*(2), 109–185, doi:10.1111/j.1365-246X.1972.tb02351.x.
- McKenzie, D. (1978), Active tectonics of the Alpine-Himalayan belt: the Aegean Sea and surrounding regions, *Geophys. J. R. astr. Soc.*, *55*(1), 217–254, doi:10.1111/j.1365-246X.1978.tb04759.x.
- Meade, B. J., B. H. Hager, S. C. McClusky, R. E. Reilinger, S. Ergintav, O. Lenk, A. Barka, and H. Özener (2002), Estimates of Seismic Potential in the Marmara Sea Region from Block Models of Secular Deformation Constrained by Global Positioning System Measurements, *Bulletin of the Seismological Society of America*, *92*(1), 208–215, doi:10.1785/0120000837.
- Meier, T., M. Rische, B. Endrun, A. Vafidis, and H.-P. Harjes (2004), Seismicity of the Hellenic subduction zone in the area of western and central Crete observed by temporary local seismic networks, *Tectonophysics*, *383*(3-4), 149–169, doi:10.1016/j.tecto.2004.02.004.
- Melis, N. S., G. N. Stavrakakis, and J. Zahradnik (2001), Focal properties of the Mw=6.5 Skyros, Aegean Sea, earthquake, <http://www.orfeus-eu.org/Organization/Newsletter/vol13no2/skyros.html>.
- Metzger, S., S. Jónsson, and H. Geirsson (2011), Locking depth and slip-rate of the Húsavík Flatey fault, North Iceland, derived from continuous GPS data 2006-2010, *Geophys. J. Int.*, doi:10.1111/j.1365-246X.2011.05176.x.
- Meyer, B., R. Armijo, and D. Dimitrov (2002), Active faulting in SW Bulgaria: possible surface rupture of the 1904 Struma earthquakes, *Geophys. J. Int.*, *148*(2), 246–255, doi:10.1046/j.0956-540x.2001.01589.x.
- Moritz, H. (1973), *Least-Squares Collocation*, Reihe A, Theoretische Geodäsie, Heft Nr. 75, 91 pp., Deutsche Geodätische Kommission bei der Bayerischen Akademie der Wissenschaften.

- Motagh, M., J. Hoffmann, B. Kampes, M. Baes, and J. Zschau (2007), Strain accumulation across the Gazikoy-Saros segment of the North Anatolian Fault inferred from Persistent Scatterer Interferometry and GPS measurements, *Earth and Planetary Sciences Letters*, 255(3-4), 432–444, doi:10.1016/j.epsl.2007.01.003.
- Mueller, M. V. (1996), Satellite Geodesy and Geodynamics: Current deformation along the West Hellenic Arc, Ph.D. thesis, ETH Zurich, No. 11358.
- Mueller, S. (1984), Dynamic processes in the Alpine arc., *Annales Geophysicae*, 2, 161–164.
- Mueller, S., and H.-G. Kahle (1993), Crust-Mantle Evolution, Structure and Dynamics of the Mediterranean-Alpine Region, *Contributions of Space Geodesy to Geodynamics: Crustal Dynamics, volume 23 of AGU Geodynamic Series*, pp. 249–298.
- Nance, R. D. (2010), Neogene-Recent extension on the eastern flank of Mount Olympus, Greece, *Tectonophysics*, 488(1-4), 282–292, doi:10.1016/j.tecto.2009.05.011.
- NEIC catalog (2009), National Earthquake Information Center (NEIC), <http://earthquake.usgs.gov/earthquakes/eqarchives/epic/>.
- Neill, A. E. (1996), Global mapping functions for the atmosphere delay at radio wavelengths, *J. Geophys. Res.*, 101(B2), 3227–3246, doi:10.1029/95JB03048.
- Nyst, M., and W. Thatcher (2004), New constraints on the active tectonic deformation of the Aegean, *J. Geophys. Res.*, 109(B11406), doi:10.1029/2003JB002830.
- Okada, Y. (1985), Surface deformation due to shear and tensile faults in a half-space, *Bulletin of the Seismological Society of America*, 75(4), 1135–1154.
- Okal, E. A., C. E. Synolakis, B. Uslu, N. Kalligeris, and E. Voukouvalas (2009), The 1956 earthquake and tsunami in Amorgos, Greece, *Geophys. J. Int.*, 178(3), 1533–1554, doi:10.1111/j.1365-246X.2009.04237.x.
- Oral, M. B., R. E. Reilinger, M. N. Toksöz, R. W. King, A. A. Barka, I. Kinik, and O. Lenk (1995), Global Positioning System Offers Evidence of Plate Motions in Eastern Mediterranean, *Eos Trans. AGU*, 76(2), 9–11.
- Papadimitriou, E. E., and V. G. Karakostas (2008), Rupture model of the great AD 365 Crete earthquake in the southwestern part of the Hellenic Arc, *Acta Geophysica*, 56(2), 293–312, doi:10.2478/s11600-008-0001-6.
- Papadopoulos, G. A. (2002), The Athens, Greece, Earthquake (Ms 5.9) of 7 September 1999: An Event Triggered by the Izmit, Turkey, 17 August 1999 Earthquake?, *Bulletin of the Seismological Society of America*, 92(1), 312–321, doi:10.1785/0120000805.
- Papanastassiou, D., J. Latoussakis, and G. Stavrakakis (2001), A revised catalogue of earthquakes in the broader area of Greece for the period 1950-2000, in *Proceedings of the 9th International Congress of the Geological Society of Greece, Athens, September 2001*, *Bulletin of the Geological Society of Greece*, vol. XXXIV/4, pp. 1563–1566.
- Papanikolaou, D., M. Alexandri, and P. Nomikou (2006), Active faulting in the north Aegean basin, in *Postcollisional tectonics and magmatism in the Mediterranean region and Asia*, edited by Y. Dilek and S. Pavlides, pp. 189–209, Geological Society of America Special Paper 409, doi:10.1130/2006.2409(11).
- Papanikolaou, I. D., and D. I. Papanikolaou (2007), Seismic hazard scenarios from the longest geologically constrained active fault of the Aegean, *Quaternary International*, 171-172, 31–44, doi:10.1016/j.quaint.2007.03.020.

- Papazachos, B., D. Mountrakis, A. Psilovikos, and G. Leventakis (1979), Surface fault traces and fault plane solutions of the May-June 1978 major shocks in the Thessaloniki area, Greece, *Tectonophysics*, *53*(3-4), 171–183, doi:10.1016/0040-1951(79)90061-1.
- Papazachos, C. B., D. A. Vamvakaris, G. N. Vargemezis, and E. V. Aidona (2001), A study of the active tectonics and deformation in the Mygdonia basin (N. Greece) using seismological and neotectonic data, *Bulletin of the Geological Society of Greece*, *34*(1), 303–309.
- Penna, N. T., and M. P. Stewart (2003), Aliased tidal signatures in continuous GPS height time series, *Geophys. Res. Letters*, *30*(23), doi:10.1029/2003GL018828.
- Peter, Y. (2000), Present-day crustal dynamics in the Adratic-Aegean plate boundary zone inferred from continuous GPS-measurements., Ph.D. thesis, ETH Zurich, No. 13700.
- Peter, Y., H.-G. Kahle, M. Cocard, G. Veis, S. Felekis, and D. Paradissis (1998), Establishment of a continuous GPS network across the Kephallonia Fault Zone, Ionian islands, Greece, *Tectonophysics*, *294*(3-4), 253–260, doi:10.1016/S0040-1951(98)00103-6.
- Pirazzoli, P. A., J. Laborel, and S. C. Stiros (1996), Earthquake clustering in the Eastern Mediterranean during historical times, *J. Geophys. Res.*, *101*(B3), 6083–6097, doi:10.1029/95JB00914.
- Ranalli, G. (1987), *Rheology of the earth*, Allan & Unwin, Limited, ISBN: 0-04-551111-X.
- Ray, J. (2010), IGS Reprocessing Campaign, <http://acc.igs.org/reprocess.html>.
- Ray, J., Z. Altamimi, X. Collilieux, and T. van Dam (2008), Anomalous harmonics in the spectra of GPS position estimates, *GPS Solutions*, *12*(1), 55–64, doi:10.1007/s10291-007-0067-7.
- Reddy, J. N. (2002), *Energy principles and variational methods in applied mechanics*, John Wiley and Sons, ISBN: 0-471-17985-X.
- Reilinger, R., S. McClusky, P. Vernant, S. Lawrence, S. Ergintav, R. Cakmak, H. Ozener, F. Kadirov, I. Guliev, R. Stepanyan, M. Nadariya, G. Hahubia, S. Mahmoud, K. Sakr, A. ArRahaji, D. Paradissis, A. Al-Aydrus, M. Prilepin, T. Guseva, E. Evren, A. Dmitrotsa, S. V. Filikov, F. Gomez, R. Al-Ghazzi, and G. Karam (2006), GPS constraints on continental deformation in the Africa-Arabia-Eurasia continental collision zone and implications for the dynamics of plate interactions, *J. Geophys. Res.*, *111*(B05411), doi:10.1029/2005JB004051.
- Reilinger, R., S. McClusky, D. Paradissis, S. Ergintav, and P. Vernant (2010), Geodetic constraints on the tectonic evolution of the Aegean region and strain accumulation along the Hellenic subduction zone, *Tectonophysics*, *488*(1-4), 22–30, doi:10.1016/j.tecto.2009.05.027.
- Reilinger, R. E., S. C. McClusky, M. B. Oral, R. W. King, M. N. Toksoz, A. A. Barka, I. Kinik, O. Lenk, and I. Sanli (1997), Global Positioning System measurements of present-day crustal movements in the Arabia-Africa-Eurasia plate collision zone, *J. Geophys. Res.*, *102*(B5), 9983–9999, doi:10.1029/96JB03736.
- Roumelioti, Z., C. Benetatos, A. Kiratzi, G. Stavrakakis, and N. Melis (2004), A study of the 2 December 2002 (M5.5) Vartholomio (western Peloponnese, Greece) earthquake and of its largest aftershocks, *Tectonophysics*, *387*(1-4), 65–79, doi:10.1016/j.tecto.2004.06.008.
- Roumelioti, Z., A. Ganas, E. Sokos, P. Petrou, A. Serpetsidaki, and G. Drakatos (2007), Toward a joint catalogue of recent seismicity in western Greece: preliminary results, *Bulletin of the Geological Society of Greece*, *40*, 1257–1266.
- Sachpazi, M., C. Kontoes, N. Voulgaris, M. Laigle, G. Vougioukalakis, O. Sikioti, G. Stavrakakis, J. Baskoutas, J. Kalogeras, and J. C. Lepine (2002), Seismological and SAR signature of unrest at Nisyros caldera, Greece, *Journal of Volcanology and Geothermal Research*, *116*(1-2), 19–33, doi:10.1016/S0377-0273(01)00334-1.

-
- Savage, J. C. (1983), A Dislocation Model of Strain Accumulation and Release at a Subduction Zone, *J. Geophys. Res.*, *88*(B6), 4984–4996, doi:10.1029/JB088iB06p04984.
- Savage, J. C., and R. O. Burford (1973), Geodetic Determination of Relative Plate Motion in Central California, *J. Geophys. Res.*, *78*(5), 832–845, doi:10.1029/JB078i005p00832.
- Savage, J. C., J. L. Svarc, W. H. Prescott, and M. H. Murray (2000), Deformation across the forearc of the Cascadia subduction zone at Cape Blanco, Oregon, *J. Geophys. Res.*, *105*(B2), 3095–3102, doi:10.1029/1999JB900392.
- Sengör, A. M. C. (1979), The North Anatolian transform fault: its age, offset and tectonic significance, *Journal of the Geological Society*, *136*, 269–282, doi:10.1144/gsjgs.136.3.0269.
- Sengör, A. M. C., O. Tüysüz, C. Imren, M. Sakinç, H. Eyidogan, N. Görür, X. Le Pichon, and C. Rangin (2005), The North Anatolian Fault: A New Look, *Annu. Rev. Earth Planet. Sci.*, *33*, 37–112, doi:10.1146/annurev.earth.32.101802.120415.
- Serpetsidaki, A., E. Sokos, G.-A. Tselentis, and J. Zahradnik (2010), Seismic sequence near Zakynthos Island, Greece, April 2006: Identification of the activated fault plane, *Tectonophysics*, *480*(1-4), 23–32, doi:10.1016/j.tecto.2009.09.024.
- Shaw, B., N. N. Ambraseys, P. C. England, M. A. Floyd, G. J. Gorman, T. F. G. Higham, J. A. Jackson, J.-M. Nocquet, C. C. Pain, and M. D. Piggott (2008), Eastern Mediterranean tectonics and tsunami hazard inferred from the AD 365 earthquake, *Nature Geoscience*, *1*, 268–276, doi:10.1038/ngeo151.
- Snopek, K., T. Meier, B. Endrun, M. Bohnhoff, and U. Casten (2007), Comparison of gravimetric and seismic constraints on the structure of the Aegean lithosphere in the forearc of the Hellenic subduction zone in the area of Crete, *J. Geodynamics*, *44*(3-5), 173–185, doi:10.1016/j.jog.2007.03.005.
- Sobolev, S. V., and A. Y. Babeyko (2005), What drives orogeny in the Andean?, *Geology*, *33*(8), 617–620.
- Soudou, F., R. Kind, D. Hatzfeld, K. Priestley, W. Hanka, K. Wylegalla, G. Stavrakakis, A. Vafidis, H.-P. Harjes, and M. Bohnhoff (2006), Lithospheric structure of the Aegean obtained from P and S receiver functions, *J. Geophys. Res.*, *111*(B12307), doi:10.1029/2005JB003932.
- Soufleris, C., and G. S. Stewart (1981), A source study of the Thessaloniki (northern Greece) 1978 earthquake sequence, *Geophysical J. R. astr. Soc.*, *67*(2), 343–358, doi:10.1111/j.1365-246X.1981.tb02754.x.
- Spakman, W., M. J. R. Wortel, and N. J. Vlaar (1988), The Hellenic Subduction Zone: A tomographic image and its geodynamic implications, *Geophys. Res. Letters*, *15*(1), 60–63, doi:10.1029/GL015i001p00060.
- Steigenberger, P., M. Rothacher, R. Dietrich, M. Fritsche, A. Rülke, and S. Vey (2006), Reprocessing of a global GPS network, *J. Geophys. Res.*, *111*(B05402), doi:10.1029/2005JB003747.
- Stein, S., and M. Wysession (2003), *An Introduction to Seismology, Earthquakes and Earth Structure*, Blackwell Publishing Ltd., ISBN: 0-86542-078-5.
- Stiros, S. C. (1998), Historical seismicity, paleoseismicity and seismic risk in Western Macedonia, Northern Greece, *Journal of Geodynamics*, *26*(2-4), 271–287, doi:10.1016/S0264-3707(97)00080-X.
- Stiros, S. C. (2001), The AD 365 Crete earthquake and possible seismic clustering during the fourth to sixth centuries AD in the Eastern Mediterranean: a review of historical and archaeological data, *Journal of Structural Geology*, *23*(2-3), 545–562, doi:10.1016/S0191-8141(00)00118-8.

- Stiros, S. C. (2005), Geodetic evidence for mobilization of evaporites during the 1997 Strophades (W Hellenic Arc) Mw 6.5 earthquake, *Journal of Geophysics and Engineering*, 2(2), 111–117, doi:10.1088/1742-2132/2/2/005.
- Stiros, S. C. (2010), The 8.5+ magnitude, AD365 earthquake in Crete: Coastal uplift, topography changes, archeological and historical signature, *Quaternary International*, 216(1-2), 54–63, doi: 10.1016/j.quaint.2009.05.005.
- Stiros, S. C., P. Psimoulis, G. Vougioukalakis, and M. Fyticas (2010), Geodetic evidence and modeling of a slow, small-scale inflation episode in the Thera (Santorini) volcano caldera, Aegean Sea, *Tectonophysics*, 494(3-4), 180–190, doi:10.1016/j.tecto.2010.09.015.
- Straub, C. (1996), Recent Crustal Deformation and Strain Accumulation in the Marmara Sea Region, N.W. Anatolia, inferred from GPS Measurements, Ph.D. thesis, ETH Zurich, No. 11614.
- Straub, C., and H.-G. Kahle (1995), Active crustal deformation in the Marmara Sea region, NW Anatolia, inferred from GPS measurements, *Geophys. Res. Letters*, 22(18), 2533–2536, doi: 10.1029/95GL02219.
- Straub, C., H.-G. Kahle, and C. Schindler (1997), GPS and geologic estimates of the tectonic activity in the Marmara Sea region, NW Anatolia, *J. Geophys. Res.*, 102(B12), 27,587–27,601, doi:10.1029/97JB02563.
- Sykioti, O., C. C. Kontoes, P. Elias, P. Briole, M. Sachpazi, D. Paradissis, and I. Kotsis (2003), Ground deformation at Nisyros volcano (Greece) detected by ERS-2 SAR differential interferometry, *International Journal of Remote Sensing*, 24(1), 183–188, doi:10.1080/01431160305000.
- Taymaz, T., J. Jackson, and D. McKenzie (1991), Active tectonics of the north and central Aegean Sea, *Geophys. J. Int.*, 106(2), 433–490, doi:10.1111/j.1365-246X.1991.tb03906.x.
- Tibaldi, A., F. A. Pasquarè, D. Papanikolaou, and P. Nomikou (2008), Discovery of a huge sector collapse at the Nisyros volcano, Greece, by on-land and offshore geological-structural data, *Journal of Volcanology and Geothermal Research*, 177(2), 485–499, doi:10.1016/j.jvolgeores.2008.06.014.
- Tirel, C., F. Gueydan, C. Tiberi, and J.-P. Brun (2004), Aegean crustal thickness inferred from gravity inversion. Geodynamical implications, *Earth and Planetary Science Letters*, 228(3-4), 267–280, doi:10.1016/j.epsl.2004.10.023.
- Tregoning, P., and T. A. Herring (2006), Impact of a priori zenith hydrostatic delay errors on GPS estimates of station heights and zenith total delays, *Geophys. Res. Letters*, 33, doi:10.1029/2006GL027706.
- Tregoning, P., and C. Watson (2009), Atmospheric effects and spurious signals in GPS analyses, *J. Geophys. Res.*, 114, doi:10.1029/2009JB006344.
- Turcotte, D. L., and G. Schubert (2002), *Geodynamics*, Cambridge University Press, ISBN: 0-521-66624-4.
- Van Hinsbergen, D. J. J., C. G. Langereis, and J. E. Meulenkaamp (2005), Revision of the timing, magnitude and distribution of Neogene rotations in the western Aegean region, *Tectonophysics*, 396(1-2), 1–34, doi:10.1016/j.tecto.2004.10.001.
- Velasco, M. S., R. A. Bennett, R. A. Johnson, and S. Hreinsdóttir (2010), Subsurface fault geometries and crustal extension in the eastern Basin and Range Province, western U.S., *Tectonophysics*, 488(1-4), 131–142, doi:10.1016/j.tecto.2009.05.010.
- Vermeer, P., and R. de Borst (1984), Non-associated plasticity for soils, concrete and rock, *HERON*, 29.

- Walters, R. J., R. J. Holley, B. Parsons, and T. J. Wright (2011), Interseismic strain accumulation across the North Anatolian Fault from Envisat InSAR measurements, *Geophys. Res. Letters*, *38*, 5 pp., doi:10.1029/2010GL046443.
- Wdowinski, S., Y. Bock, G. Baer, L. Prawirodirdjo, N. Bechor, S. Naaman, R. Knafo, Y. Forrai, and Y. Melzer (2004), GPS measurements of current crustal movements along the Dead Sea Fault, *J. Geophys. Res.*, *109*(B05403), doi:10.1029/2003JB002640.
- Weertman, J., and J. R. Weertman (1964), *Elementary Dislocation Theory*, The MacMillan Company, New York.
- Wells, D. L., and K. J. Coppersmith (1994), New Empirical Relationships among Magnitude, Rupture Length, Rupture Width, Rupture Area, and Surface Displacement, *Bulletin of the Seismological Society of America*, *84*(4), 974–1002.
- Wilks, K. R., and N. L. Carter (1990), Rheology of some continental lower crustal rocks, *Tectonophysics*, *182*(1-2), 57–77, doi:10.1016/0040-1951(90)90342-6.
- Williams, S. D. P., Y. Bock, P. Fang, P. Jamason, R. M. Nikolaidis, L. Prawirodirdjo, M. Miller, and D. J. Johnson (2004), Error analysis of continuous GPS position time series, *J. Geophys. Res.*, *109*(B03412), doi:10.1029/2003JB002741.
- Wortel, M. J. R., and W. Spakman (1992), Structure and dynamics of subducted lithosphere in the Mediterranean region, *Proc. Kon. Ned. Akad. v. Wetensch.*, *95*(3), 325–347.
- Wright, T., B. Parsons, and E. Fielding (2001), Measurement of interseismic strain accumulation across the North Anatolian Fault by satellite radar interferometry, *Geophysical Research Letters*, *28*(10), 2117–2120, doi:10.1029/2000GL012850.
- Yaltirak, C., and B. Alpar (2002), Kinematics and evolution of the northern branch of the North Anatolian Fault (Ganos Fault) between the Sea of Marmara and the Gulf of Saros, *Marine Geology*, *190*(1-2), 351–366, doi:10.1016/S0025-3227(02)00354-7.
- Zahradnik, J., A. Serpetsidaki, E. Sokos, and G.-A. Tselentis (2005), Iterative Deconvolution of Regional Waveforms and a Double-Event Interpretation of the 2003 Lefkada Earthquake, Greece, *Bulletin of the Seismological Society of America*, *95*(1), 159–172, doi:10.1785/0120040035.
- Zahradnik, J., E. Sokos, and A. Tselentis (2008), Problems of quick identification of the fault plane for earthquake on Rhodes Island, Greece (July 15, 2008, Mw 6.4), http://www.emsc-csem.org/Doc/20080715_GREECE/Rhodes_15_07_08.pdf, Report to EMSC issued on July 31, 2008.
- Zhang, J., Y. Bock, H. Johnson, P. Fang, S. Williams, J. Genrich, S. Wdowinski, and J. Behr (1997), Southern California Permanent GPS Geodetic Array: Error analysis of daily position estimates and site velocities, *J. Geophys. Res.*, *102*(B8), 18,035–18,055, doi:10.1029/97JB01380.
- Zienkiewicz, O. C., and R. L. Taylor (2000), *The Finite Element Method. Vol. 1: The Basis*, Fifth ed., Butterworth-Heinemann Limited, ISBN: 0-7506-5049-4.

A Additional notes on GPS data processing

A.1 Positions and velocities used for aligning the GPS network to ITRF2005

LOCAL GEODETIC DATUM: IGS05
EPOCH: 2005-01-01 00:00:00

Type	Date ₁	Date ₂	Type	#	Site	X/VX [m]/[m/yr]	Y/VY [m]/[m/yr]	Z/VZ [m]/[m/yr]	CO
P	00:00:00.0000	99:152:0000	W	1	BOR1 12205M002	3738358.4574	1148173.7073	5021815.7734	R
V	00:00:00.0000	99:152:0000	W	1	BOR1 12205M002	-0.0167	0.0157	0.0097	R
P	99:152:0000	00:00:00.0000	W	2	BOR1 12205M002	3738358.4544	1148173.7102	5021815.7710	I
V	99:152:0000	00:00:00.0000	W	2	BOR1 12205M002	-0.0165	0.0157	0.0098	I
P	00:00:00.0000	00:118:44100	W	1	BRUS 13101M004	4027893.7448	307045.8278	4919475.1174	I
V	00:00:00.0000	00:118:44100	W	1	BRUS 13101M004	-0.0123	0.0173	0.0111	I
P	00:118:44100	00:00:00.0000	W	2	BRUS 13101M004	4027893.7475	307045.8242	4919475.1188	I
V	00:118:44100	00:00:00.0000	W	2	BRUS 13101M004	-0.0126	0.0166	0.0112	I
P	00:00:00.0000	00:331:00000	W	1	BUCU 11401M001	4093760.8821	2007793.8355	4445129.9955	I
V	00:00:00.0000	00:331:00000	W	1	BUCU 11401M001	-0.0141	0.0230	0.0146	I
P	00:331:00000	08:305:00000	W	2	BUCU 11401M001	4093760.8704	2007793.8106	4445129.9766	I
V	00:331:00000	08:305:00000	W	2	BUCU 11401M001	-0.0166	0.0170	0.0104	I
P	08:305:00000	00:00:00.00000	A	3	BUCU 11401M001	4093760.8877	2007793.8221	4445130.0293	I
V	08:305:00000	00:00:00.00000	A	3	BUCU 11401M001	-0.0210	0.0150	-0.0029	I
P	00:00:00.00000	99:085:00000	W	1	CAGL 12725M003	4893378.8198	772649.7879	4004182.1628	R
V	00:00:00.00000	99:085:00000	W	1	CAGL 12725M003	-0.0132	0.0197	0.0127	R
P	99:085:00000	01:192:00000	W	2	CAGL 12725M003	4893378.8173	772649.7840	4004182.1583	I
V	99:085:00000	01:192:00000	W	2	CAGL 12725M003	-0.0131	0.0197	0.0124	I
P	01:192:00000	00:00:00.00000	W	3	CAGL 12725M003	4893378.8195	772649.7885	4004182.1604	I
V	01:192:00000	00:00:00.00000	W	3	CAGL 12725M003	-0.0122	0.0199	0.0133	I
P	00:00:00.00000	97:105:36780	A	-	EBRE 13410M001	4833520.1548	41537.1102	4147461.5452	T
V	00:00:00.00000	97:105:36780	A	-	EBRE 13410M001	-0.0105	0.0196	0.0124	T
P	97:105:36780	00:00:00.00000	W	2	EBRE 13410M001	4833520.1548	41537.1102	4147461.5452	I
V	97:105:36780	00:00:00.00000	W	2	EBRE 13410M001	-0.0105	0.0196	0.0124	I
P	00:00:00.00000	00:00:00.00000	W	1	GENO 12712M002	4507892.3173	707621.4806	4441603.5093	I
V	00:00:00.00000	00:00:00.00000	W	1	GENO 12712M002	-0.0126	0.0194	0.0128	I
P	00:00:00.00000	07:317:00000	W	1	GLSV 12356M001	3512888.9546	2068979.8788	4888903.2051	I
V	00:00:00.00000	07:317:00000	W	1	GLSV 12356M001	-0.0191	0.0145	0.0093	I
P	07:317:00000	00:00:00.00000	A	2	GLSV 12356M001	3512888.9541	2068979.8901	4888903.2022	I
V	07:317:00000	00:00:00.00000	A	2	GLSV 12356M001	-0.0191	0.0123	0.0079	I
P	00:00:00.00000	03:113:00000	W	1	GRAS 10002M006	4581690.8964	556114.8321	4389360.7874	I
V	00:00:00.00000	03:113:00000	W	1	GRAS 10002M006	-0.0136	0.0189	0.0122	I
P	03:113:00000	04:295:43200	W	2	GRAS 10002M006	4581690.9028	556114.8348	4389360.7884	I
V	03:113:00000	04:295:43200	W	2	GRAS 10002M006	-0.0116	0.0188	0.0118	I
P	04:295:43200	00:00:00.00000	W	3	GRAS 10002M006	4581690.9007	556114.8375	4389360.7932	I
V	04:295:43200	00:00:00.00000	W	3	GRAS 10002M006	-0.0123	0.0183	0.0130	I
P	00:00:00.00000	95:001:00000	W	-	GRAZ 11001M002	4194423.8144	1162702.6946	4647245.4084	T
V	00:00:00.00000	95:001:00000	W	-	GRAZ 11001M002	-0.0169	0.0181	0.0110	T
P	95:001:00000	96:178:00000	A	-	GRAZ 11001M002	4194423.8144	1162702.6946	4647245.4084	T
V	95:001:00000	96:178:00000	A	-	GRAZ 11001M002	-0.0169	0.0181	0.0110	T
P	96:178:00000	01:152:00000	W	1	GRAZ 11001M002	4194423.8144	1162702.6946	4647245.4084	I
V	96:178:00000	01:152:00000	W	1	GRAZ 11001M002	-0.0169	0.0181	0.0110	I
P	01:152:00000	05:081:39000	W	2	GRAZ 11001M002	4194423.8190	1162702.6926	4647245.4096	I
V	01:152:00000	05:081:39000	W	2	GRAZ 11001M002	-0.0165	0.0184	0.0111	I
P	05:081:39000	05:310:00000	W	3	GRAZ 11001M002	4194423.8239	1162702.7009	4647245.4138	I
V	05:081:39000	05:310:00000	W	3	GRAZ 11001M002	-0.0214	0.0154	0.0055	I
P	05:310:39000	00:00:00.00000	W	4	GRAZ 11001M002	4194423.8165	1162702.6946	4647245.4106	I
V	05:310:39000	00:00:00.00000	W	4	GRAZ 11001M002	-0.0149	0.0183	0.0123	I
P	00:00:00.00000	04:341:00000	W	1	JOZE 12204M001	3664940.1651	1409153.8641	5009571.3906	I
V	00:00:00.00000	04:341:00000	W	1	JOZE 12204M001	-0.0167	0.0157	0.0110	I
P	04:341:00000	06:001:00000	W	2	JOZE 12204M001	3664940.1657	1409153.8622	5009571.3922	I
V	04:341:00000	06:001:00000	W	2	JOZE 12204M001	-0.0209	0.0113	0.0043	I
P	06:001:00000	00:00:00.00000	W	3	JOZE 12204M001	3664940.1651	1409153.8616	5009571.3902	I
V	06:001:00000	00:00:00.00000	W	3	JOZE 12204M001	-0.0169	0.0164	0.0099	I
P	00:00:00.00000	03:076:00000	W	1	KOSG 13504M003	3899225.1252	396731.9426	5015078.4315	I
V	00:00:00.00000	03:076:00000	W	1	KOSG 13504M003	-0.0136	0.0165	0.0114	I
P	03:076:00000	00:00:00.00000	W	2	KOSG 13504M003	3899225.1297	396731.9399	5015078.4244	I
V	03:076:00000	00:00:00.00000	W	2	KOSG 13504M003	-0.0137	0.0164	0.0105	I
P	00:00:00.00000	00:100:00000	W	1	LAMA 12209M001	3524522.9103	1329693.6290	5129846.3417	I
V	00:00:00.00000	00:100:00000	W	1	LAMA 12209M001	-0.0196	0.0136	0.0075	I
P	00:280:00000	06:001:00000	W	3	LAMA 12209M001	3524522.9192	1329693.6286	5129846.3403	I
V	00:280:00000	06:001:00000	W	3	LAMA 12209M001	-0.0174	0.0148	0.0096	I
P	06:001:00000	00:00:00.00000	A	4	LAMA 12209M001	3524522.9179	1329693.6283	5129846.3316	I
V	06:001:00000	00:00:00.00000	A	4	LAMA 12209M001	-0.0161	0.0149	0.0143	I
P	00:00:00.00000	00:00:00.00000	W	1	LAMP 12706M002	5073164.7552	1134512.5656	3683181.1455	I
V	00:00:00.00000	00:00:00.00000	W	1	LAMP 12706M002	-0.0138	0.0175	0.0161	I
P	00:00:00.00000	00:00:00.00000	W	1	MAR6 10405M002	2998189.4141	931451.7771	5533398.6808	I

continued on the next page

A Additional notes on GPS data processing

continued from the last page

Type	Date ₁	Date ₂	Type	#	Site	X/VX [m]/[m/yr]	Y/VY [m]/[m/yr]	Z/VZ [m]/[m/yr]	CO
V	00:00:000000	00:00:000000	W	1	MAR6 10405M002	-0.0126	0.0142	0.0143	I
P	00:00:000000	95:001:00000	A	-	MATE 12734M008	4641949.5576	1393045.4243	4133287.4651	T
V	00:00:000000	95:001:00000	A	-	MATE 12734M008	-0.0179	0.0188	0.0155	T
P	95:001:00000	96:108:00000	W	1	MATE 12734M008	4641949.5576	1393045.4243	4133287.4651	R
V	95:001:00000	96:108:00000	W	1	MATE 12734M008	-0.0179	0.0188	0.0155	R
P	96:108:00000	96:191:00000	W	2	MATE 12734M008	4641949.5554	1393045.4115	4133287.4683	R
V	96:108:00000	96:191:00000	W	2	MATE 12734M008	-0.0179	0.0188	0.0155	R
P	96:191:00000	99:169:00000	W	3	MATE 12734M008	4641949.5577	1393045.4227	4133287.4669	R
V	96:191:00000	99:169:00000	W	3	MATE 12734M008	-0.0179	0.0188	0.0155	R
P	99:169:00000	08:326:00000	W	4	MATE 12734M008	4641949.5574	1393045.4289	4133287.4632	I
V	99:169:00000	08:326:00000	W	4	MATE 12734M008	-0.0176	0.0191	0.0154	I
P	08:326:00000	00:00:00000	A	5	MATE 12734M008	4641949.6074	1393045.4793	4133287.5645	I
V	08:326:00000	00:00:00000	A	5	MATE 12734M008	-0.0306	0.0056	-0.0097	I
P	00:00:00000	00:00:00000	W	1	METS 10503S011	2892570.7877	1311843.4455	5512634.1335	I
V	00:00:00000	00:00:00000	W	1	METS 10503S011	-0.0155	0.0146	0.0116	I
P	00:00:00000	00:00:00000	W	1	NOT1 12717M004	4934546.2290	1321265.0130	3806456.1209	I
V	00:00:00000	00:00:00000	W	1	NOT1 12717M004	-0.0171	0.0173	0.0157	I
P	00:00:00000	98:211:00000	W	-	NOTO 12717M003	4934528.5101	1321262.3639	3806479.6429	T
V	00:00:00000	98:211:00000	W	-	NOTO 12717M003	-0.0173	0.0177	0.0164	T
P	98:211:00000	00:00:00000	W	2	NOTO 12717M003	4934528.5101	1321262.3639	3806479.6429	I
V	98:211:00000	00:00:00000	W	2	NOTO 12717M003	-0.0173	0.0177	0.0164	I
P	00:00:00000	00:00:00000	W	1	OBER 14208M001	4186558.4055	835027.1884	4723759.3436	I
V	00:00:00000	00:00:00000	W	1	OBER 14208M001	-0.0154	0.0173	0.0109	I
P	00:00:00000	97:313:00000	W	1	ONSA 10402M004	3370658.5479	711877.1413	5349786.9556	R
V	00:00:00000	97:313:00000	W	1	ONSA 10402M004	-0.0135	0.0144	0.0109	R
P	97:313:00000	99:033:00000	W	2	ONSA 10402M004	3370658.5467	711877.1392	5349786.9559	R
V	97:313:00000	99:033:00000	W	2	ONSA 10402M004	-0.0135	0.0144	0.0109	R
P	99:033:00000	00:00:00000	W	3	ONSA 10402M004	3370658.5413	711877.1383	5349786.9492	I
V	99:033:00000	00:00:00000	W	3	ONSA 10402M004	-0.0133	0.0146	0.0116	I
P	00:00:00000	00:00:00000	W	1	POTS 14106M003	3800689.6340	882077.3861	5028791.3145	I
V	00:00:00000	00:00:00000	W	1	POTS 14106M003	-0.0150	0.0160	0.0105	I
P	00:00:00000	99:071:57600	W	1	SJDV 10090M001	4433469.8639	362672.8398	4556211.7213	I
V	00:00:00000	99:071:57600	W	1	SJDV 10090M001	-0.0110	0.0218	0.0140	I
P	99:071:57600	00:00:00000	W	2	SJDV 10090M001	4433469.8584	362672.8207	4556211.7115	I
V	99:071:57600	00:00:00000	W	2	SJDV 10090M001	-0.0125	0.0186	0.0116	I
P	00:00:00000	00:00:00000	W	1	UZHL 12301M001	3907587.4544	1602428.6928	4763783.7553	I
V	00:00:00000	00:00:00000	W	1	UZHL 12301M001	-0.0163	0.0175	0.0116	I
P	95:001:00000	98:039:00000	A	2	VILL 13406M001	4849833.6945	-335049.0204	4116014.9324	R
V	95:001:00000	98:039:00000	A	2	VILL 13406M001	-0.0109	0.0204	0.0116	R
P	98:039:00000	01:113:00000	W	3	VILL 13406M001	4849833.6988	-335049.0224	4116014.9354	R
V	98:039:00000	01:113:00000	W	3	VILL 13406M001	-0.0109	0.0204	0.0116	R
P	01:113:00000	04:272:43200	W	4	VILL 13406M001	4849833.7029	-335049.0244	4116014.9382	R
V	01:113:00000	04:272:43200	W	4	VILL 13406M001	-0.0105	0.0201	0.0118	I
P	04:272:43200	00:00:00000	W	5	VILL 13406M001	4849833.7003	-335049.0259	4116014.9397	I
V	04:272:43200	00:00:00000	W	5	VILL 13406M001	-0.0106	0.0202	0.0117	I
P	00:00:00000	96:182:00000	W	1	WTZR 14201M010	4075580.5540	931853.7992	4801568.1357	R
V	00:00:00000	96:182:00000	W	1	WTZR 14201M010	-0.0151	0.0173	0.0114	R
P	96:182:00000	96:245:00000	W	2	WTZR 14201M010	4075580.5536	931853.7983	4801568.1352	R
V	96:182:00000	96:245:00000	W	2	WTZR 14201M010	-0.0151	0.0173	0.0114	R
P	96:245:00000	00:00:00000	W	3	WTZR 14201M010	4075580.5535	931853.7976	4801568.1332	I
V	96:245:00000	00:00:00000	W	3	WTZR 14201M010	-0.0151	0.0173	0.0111	I
P	00:00:00000	98:310:00000	W	1	ZIMM 14001M004	4331297.0714	567555.8797	4633133.9410	R
V	00:00:00000	98:310:00000	W	1	ZIMM 14001M004	-0.0126	0.0181	0.0127	R
P	98:310:00000	00:00:00000	W	2	ZIMM 14001M004	4331297.0621	567555.8813	4633133.9315	I
V	98:310:00000	00:00:00000	W	2	ZIMM 14001M004	-0.0125	0.0182	0.0130	I

Table A.1: Positions/velocities used to align the GPS network to ITRF05. Type denotes if the entry corresponds to a position (P) or a velocity (V). Date₁ and Date₂ denote the beginning and the end, respectively, of the particular section for which the coordinate/velocity pair is valid. The format of Date is year, day of year and seconds of a day (separated by a colon). A date consisting of zeros only means that the respective interval begins on the date where the earliest data of this site is available or ends on the date where the latest data of this site is available. Type indicates whether a site is used as a reference site (W) or not (A). "##" denotes the solution number as indicated in the files IGS09P06.ssc and IGS05_repro.snx, respectively. X, Y and Z denote the coordinates of the geocentric positions and VX, VY and VZ denote the components of the geocentric velocities. CO denotes the source of the position/velocity pairs: I: positions and velocities based on IGS09P06.ssc and ALL.snx (26.02.2009), R: positions and velocities based on IGS05_repro.snx, T: positions and velocities for time periods without a solution in the IGS combined solution. A position/velocity pair denoted by T is identical with the position/velocity pair of the subsequent interval.

A.2 Discontinuities and exclusion periods introduced in GPS time series

Dates of discontinuities which were modeled for the estimation of rates are listed in Table A.2. Discontinuities are classified according to the cause: 1: earthquake; 2: change of the antenna/dome configuration; 3: receiver change or firmware upgrade; 4: receiver and antenna changes; 5: other reasons (mostly unknown). The date refers to the first day of the new interval. The indicated date is not necessarily identical with the date of the event (e.g., antenna change). Differences may be caused, for instance, by missing data. Not modeled antenna changes are listed in Table A.3. Time periods in which data of particular GPS sites was processed but the resulting position estimates were not used for the calculation of their rates are listed in Table A.4.

Site	DOY	Year	MJD	Code	Remarks
AMFI	060	1999	51238	4	
AMFI	334	1999	51512	2	
AMFI	038	2000	51581	2	
AMFI	226	2001	52135	5	
AMFI	266	2003	52905	5	
APAX	263	1997	50711	4	
APAX	226	2003	52865	1	Lefkada earthquake on 14 August 2003
APAX	022	2008	54487	2	
ARHA	308	2000	51851	4	
ARHA	197	2008	54662	1	Rhodes earthquake on 15 July 2008
ARSA	290	1999	51468	4	
ARSA	322	2001	52231	4	
DION	297	1996	50379	4	
DION	250	1999	51428	1	Athens earthquake on 7 September 1999
DION	207	2001	52116	1	Skyros earthquake on 26 July 2001
DUKA	187	1996	50269	2	
DUKA	275	1996	50357	4	
DUKA	058	1997	50506	2	
DUKA	258	1997	50706	4	
DUKA	271	1998	51084	2	
DUKA	226	2003	52865	1	Lefkada earthquake on 14 August 2003
GERO	177	1995	49894	4	
GERO	270	2003	52909	4	
KAST	079	1998	50892	4	
KERI	321	1997	50769	1	Strofades earthquake on 18 November 1997
KERI	254	2003	52893	2	
KERI	094	2006	53829	1	Zakynthos earthquake series starting on 4 April 2006
KERI	160	2008	54625	1	NW Peloponnesos earthquake on 8 July 2008
KPTS	194	2005	53564	2	
NEAP	069	2004	53073	4	
NISI	100	2008	54565	5	
PAXI	326	1995	50043	2	
RLS	160	2008	54625	1	NW Peloponnesos earthquake on 8 July 2008
SKIN	272	1996	50354	4	
SKIN	342	1997	50790	4	
SKIN	160	2008	54625	1	NW Peloponnesos earthquake on 8 July 2008
TUC1	114	2000	51657	2	
ASSO	226	2003	52865	1	Lefkada earthquake on 14 August 2003
1KVL	226	2003	52865	1	Lefkada earthquake on 14 August 2003
FISK	226	2003	52865	1	Lefkada earthquake on 14 August 2003
TSAR	226	2003	52865	1	Lefkada earthquake on 14 August 2003
CG38	207	2001	52116	1	Skyros earthquake on 26 July 2001
KILL	160	2008	54625	1	NW Peloponnesos earthquake on 8 July 2008
KSSI	321	1997	50769	1	Strofades earthquake on 18 November 1997
KSSI	094	2006	53829	1	Zakynthos earthquake series starting on 4 April 2006
NSKR	207	2001	52116	1	Skyros earthquake on 26 July 2001
SNDO	160	2008	54625	1	NW Peloponnesos earthquake on 8 July 2008
STRO	321	1997	50769	1	Strofades earthquake on 18 November 1997
STRF	321	1997	50769	1	Strofades earthquake on 18 November 1997
VASI	226	2003	52865	1	Lefkada earthquake on 14 August 2003
VONW	226	2003	52865	1	Lefkada earthquake on 14 August 2003
AJAC	331	2008	54796	4	
ANKR	205	1996	50287	4	
ANKR	205	1997	50653	4	
ANKR	259	1998	51072	2	
ANKR	229	1999	51407	1	
ANKR	329	2000	51872	4	
ANKR	127	2008	54592	4	
BOR1	152	1999	51330	2	
BRST	207	2006	53942	2	
BRST	109	2007	54209	2	
BRST	164	2008	54629	4	
BRUS	118	2000	51661	2	
BUCU	331	2000	51874	5	
BUCU	305	2008	54770	4	
BZRG	334	2000	51877	4	
BZRG	182	2001	52091	5	
BZRG	199	2002	52473	2	
BZRG	346	2007	54446	4	
CAGL	192	2001	52101	4	
CAME	018	2001	51927	4	
CAME	349	2003	52988	4	
DUBR	190	2007	54290	4	
EBRE	105	1997	50553	4	
GLSV	317	2007	54417	4	
GRAS	113	2003	52752	4	

continued on the next page

continued from the last page

Site	DOY	Year	MJD	Code	Remarks
GRAS	295	2004	53299	4	
GRAZ	177	1996	50259	2	
GRAZ	127	2001	52036	4	
GRAZ	152	2001	52061	3	
GRAZ	081	2005	53451	2	
GRAZ	306	2005	53676	2	
GSR1	264	2008	54729	4	
HERS	049	1998	50862	4	
HERS	182	1998	50995	4	
HERS	220	2001	52129	2	
JOZE	341	2004	53345	5	
JOZE	001	2006	53736	5	
KARL	130	2001	52039	2	
KARL	184	2002	52458	2	
KOSG	076	2003	52715	5	
LAMA	280	2000	51823	2	
LAMA	001	2006	53736	5	
LAMA	322	2007	54422	4	
MATE	108	1996	50190	5	
MATE	191	1996	50273	4	
MATE	169	1999	51347	4	
MATE	326	2008	54791	4	
NICO	233	1999	51411	4	
NICO	162	2008	54627	4	
NOTO	211	1998	51024	4	
NSSP	037	2003	52676	4	
ONSA	033	1999	51211	4	
ORID	347	2002	52621	4	
ORID	021	2008	54486	3	
ORID	311	2008	54776	2	
OROS	227	2004	53231	5	
OROS	159	2007	54259	4	
PENC	142	2003	52781	4	
PENC	193	2007	54293	4	
POTS	276	1995	49993	2	
RAMO	199	2000	51742	2	
RAMO	077	2004	53081	5	
RIGA	013	2005	53383	4	
RIGA	142	2006	53877	2	
RIGA	350	2007	54450	4	
SFER	035	1998	50848	2	
SFER	153	1998	50966	4	
SFER	064	2002	52338	4	
SFER	159	2003	52798	5	
SJDV	071	1999	51249	2	
TELA	101	2000	51644	2	
TELA	186	2000	51729	2	
TORI	194	1998	51007	2	
UNPG	001	2000	51544	2	
UNPG	041	2000	51584	2	
UNPG	131	2000	51674	2	
UNPG	330	2000	51873	2	
UNPG	139	2002	52413	5	
UNPG	109	2006	53844	4	
UPAD	357	1997	50805	4	
VENE	274	1997	50722	4	
VENE	219	1999	51397	5	
VENE	032	2001	51941	4	
VENE	350	2001	52259	5	
VENE	301	2005	53671	4	
VILL	001	1995	49718	5	
VILL	039	1998	50852	5	
VILL	113	2001	52022	3	
VILL	272	2004	53276	2	
VILL	333	2006	54068	2	
WTZR	019	2009	54850	2	
ZECK	193	2001	52102	4	
ZECK	211	2006	53946	4	
ZIMM	310	1998	51123	2	
ZWEN	100	2000	51643	5	
ZWEN	251	2000	51794	2	
ZWEN	266	2004	53270	2	
ZWE2	166	2007	54266	2	

Table A.2: Offsets modeled for the estimation of rates. DOY: day of year, MJD: modified Julian date. Code: the numbers indicate the cause of an offset (1: earthquake, 2: change in the antenna/dome configuration, 3: receiver change or firmware upgrade, 4: receiver and antenna changes, 5: other causes (mostly unknown)).

Site	DOY	Year	MJD	Code	Remarks
DUKA	260	2003	52899	4	Campaign-type measurement using a different antenna type than for the preceding measurement. Centered monumentation. Note that the Lefkada earthquake on 14 August 2003 was modeled as a discontinuity.
DUKA	147	2006	53882	4	Campaign-type measurement using a different antenna type than for the preceding measurement. Centered monumentation.
DUKA	019	2008	54484	4	Campaign-type measurement using the same antenna type as for the preceding measurement. Centered monumentation.
DUKA	246	2008	54711	4	Campaign-type measurement using the same antenna type as for the preceding measurement. Centered monumentation.
GERO	041	2004	53045	4	Re-installation of the antenna which was used before 27 September 2003.
GERO	144	2006	53879	4	Campaign-type measurement using a different antenna type than for the preceding measurements. Centered monumentation.
GERO	184	2007	54284	4	Campaign-type measurement using the same antenna type as for the preceding measurement. Centered monumentation.
GERO	245	2008	54710	4	Campaign-type measurement using the same antenna type as for the preceding measurement. Centered monumentation.
KALY	061	2007	54161	2	Change of antenna.
SKIN	205	1998	51018	4	Campaign-type measurement using the same antenna type as for the preceding measurement. Centered monumentation.

Table A.3: Antenna changes not modeled for the estimation of rates. DOY: day of year, MJD: modified Julian date. Code: the numbers indicate the cause of an offset (2: change in the antenna/dome configuration, 4: receiver and antenna changes).

Site	DOY_1	$Year_1$	MJD_1	DOY_2	$Year_2$	MJD_2	Remarks
ANOK	042	2000	51585	172	2001	52081	Station start
APAX	250	2005	53620	111	2008	54576	Antenna malfunction
ARSA	023	2007	54123	180	2007	54280	Unknown (afterward, site ARSA was replaced by site ARS2)
KERI	094	2006	53829	110	2006	53845	Zakynthos earthquake series in April 2006
NEAP	066	2002	52340	357	2003	52996	Significantly lower quality of data than after the antenna change
NEOH	340	2005	53710	001	2020	58849	Unknown (likely due to a closely located radio transmitter)
NISI	100	2008	54565	123	2008	54588	Unstable monumentation
NISI	281	2008	54746	309	2008	54774	Unstable monumentation
ANKR	229	1999	51407	316	1999	51494	Kocaeli earthquake
BAHR	175	1996	50257	366	1996	50448	Unknown
BZRG	334	2000	51877	199	2002	52473	Antenna, receiver and firmware changes
CAME	119	2000	51662	018	2001	51927	Unknown (start of station)
GRAS	112	2007	54212	139	2007	54239	<i>EUREFmail</i> 3307, 3318 and 3348
HERS	110	1999	51288	219	2001	52128	
ISTA	316	2006	54051	265	2007	54365	<i>EUREFmail</i> 3177 and 3183 [according to <i>EU-REFmail</i> only till 006/2007]
ORID	283	2007	54383	311	2008	54776	Unknown
LAMA	100	2000	51643	279	2000	51822	<i>EUREFmail</i> 0636
SRJV	107	2000	51650	274	2000	51817	Unknown
UNPG	327	1998	51140	013	2000	51556	Unknown

Table A.4: Time periods in which data of the listed sites was processed but the resulting position estimates were not used for the calculation of rates. DOY: day of year, MJD: modified Julian date. The numbers 1,2 denote the beginning and the end of the periods, respectively.

A.3 Time series of parameters related to the GPS processing runs

Figure A.1: (on page 129) Parameters characterizing the quality of the GPS processing the final velocity results are based on. Reprocessed orbits and EOPs were used in the time period 1995–2003 [Steigenberger *et al.*, 2006]. Precise IGS orbits and EOPs were used after 2003. (a) σ a posteriori of the daily GPS solutions. (b) Percentage of resolved ambiguities. (c)-(f) RMS of Helmert transformation between IGS05 positions and positions obtained in the processing (only the set of reference sites is considered) ((c) north component, (d) east component, (e) up component and (f) total transformation, respectively). (g) Number of sites included in the processing (upper line) and effectively used reference sites (lower line).

Figure A.2: (on page 130) Parameters characterizing the quality of the GPS processing using IGS final orbits and EOPs. (a) σ a posteriori of the daily GPS solutions. (b) Percentage of resolved ambiguities. (c)-(f) RMS of Helmert transformation between IGS05 positions and positions obtained in the processing (only the set of reference sites is considered) ((c) north component, (d) east component, (e) up component and (f) total transformation, respectively). (g) Number of sites included in the processing (upper line) and effectively used reference sites (lower line).

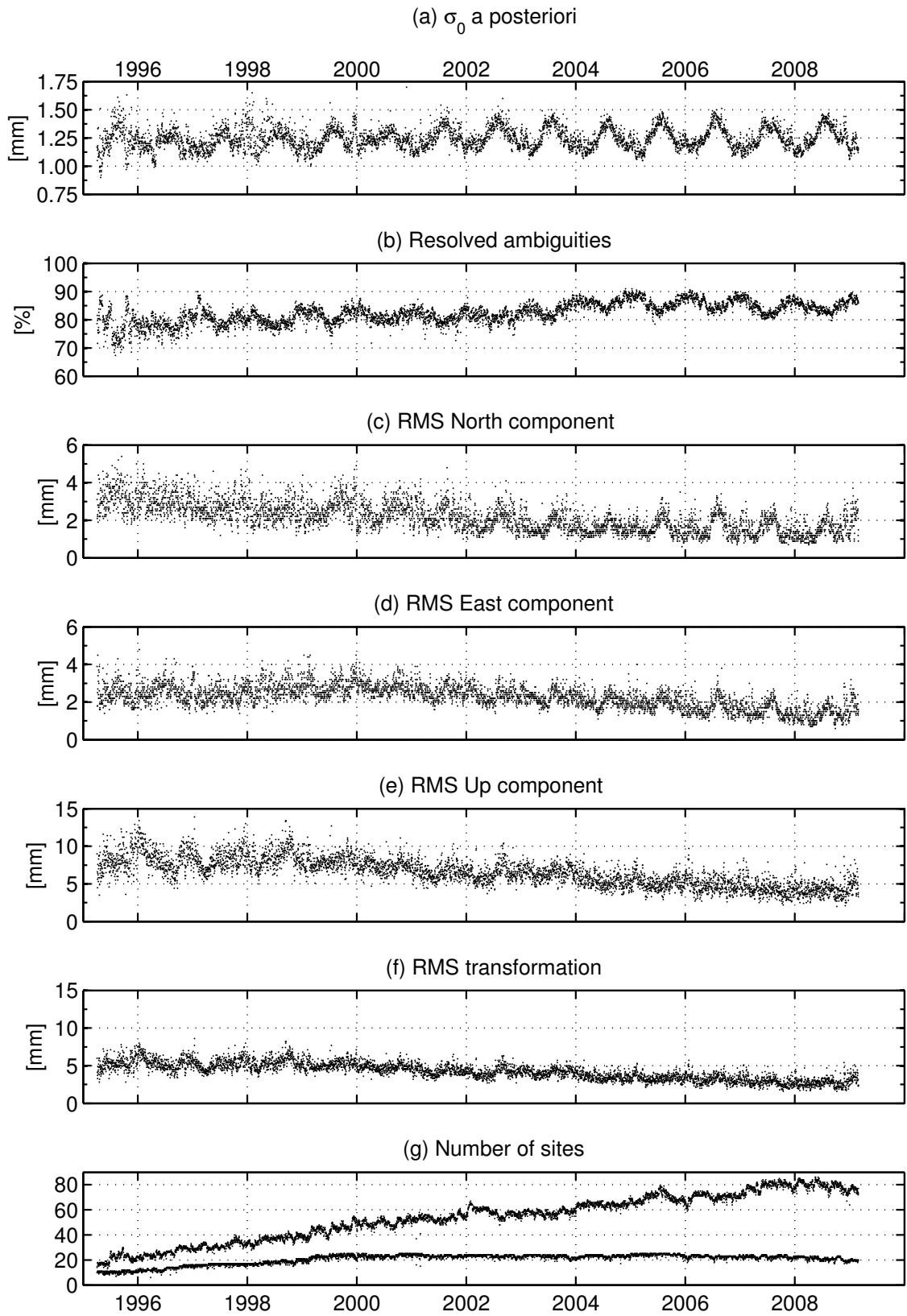


Figure A.1: Figure caption on page 128.

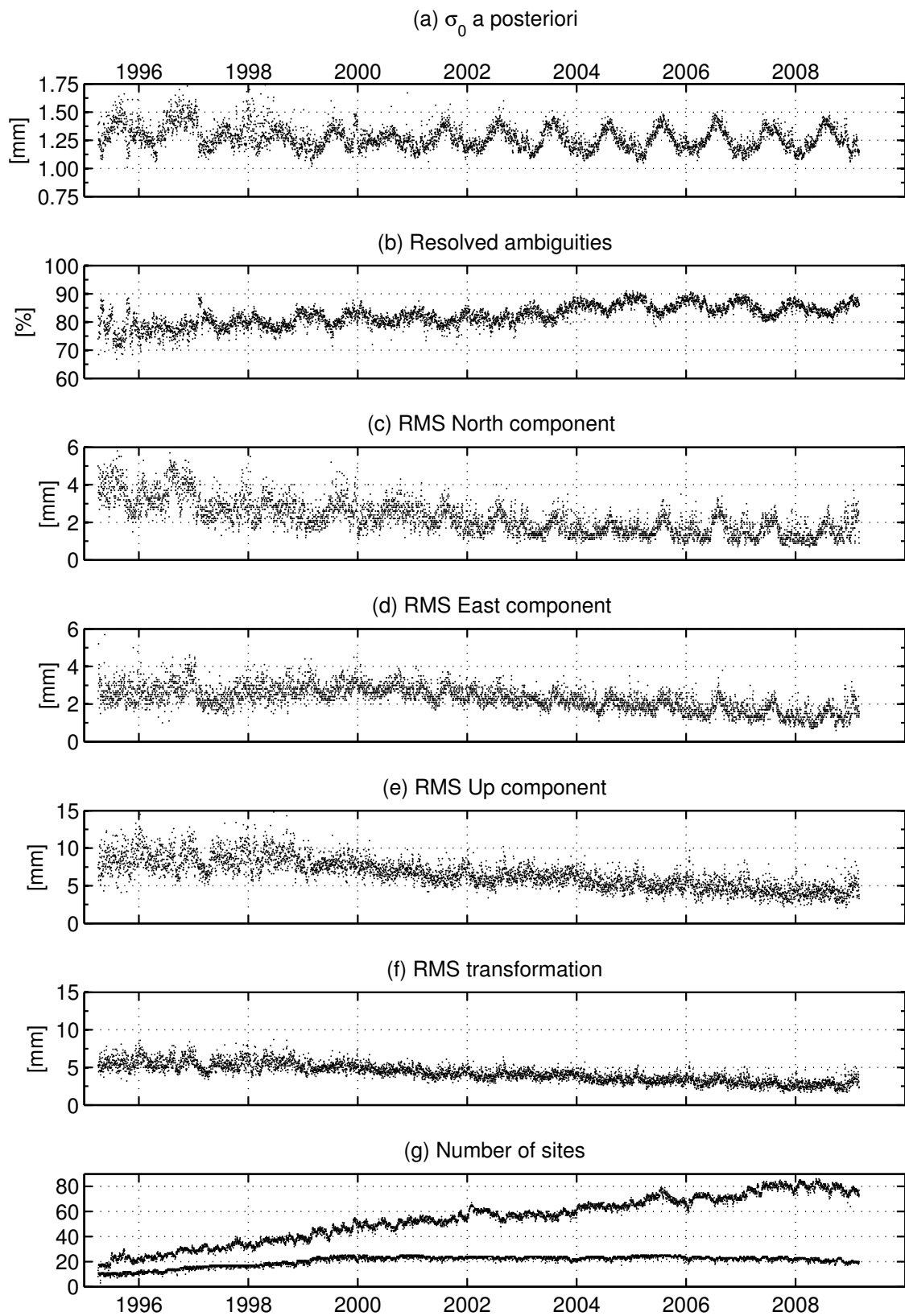


Figure A.2: Figure caption on page 128.

A.4 Sites selected for the algorithm reducing apparent scale changes

The sites selected for the algorithm which reduces apparent scale changes described in chapter 3.4.6 are listed in Table A.5. Figure A.4 shows the resulting improvement by means of the time series of two CGPS sites in Greece: KERI located in the Ionian sea and ARHA located in the SE Aegean sea.

Site	YY ₁	DOY ₁	YY ₂	DOY ₂	Site	YY ₁	DOY ₁	YY ₂	DOY ₂		
AJAC	10077M005	00	000	08	330	MATE	12734M008	99	169	08	325
BAHR	24901M002	97	001	00	000	METS	10503S011	00	000	00	000
BOR1	12205M002	00	000	98	365	MIKL	12335M001	04	001	00	000
BOR1	12205M002	99	152	00	000	NICO	14302M001	99	233	08	160
BRST	10004M004	00	000	06	206	NOT1	12717M004	00	000	00	000
BRUS	13101M004	00	000	00	117	NOTO	12717M003	00	000	00	000
BRUS	13101M004	00	118	00	000	NSSP	12312M001	00	000	03	036
BUCU	11401M001	00	331	00	000	NSSP	12312M001	03	037	00	000
CAGL	12725M003	00	000	01	191	OBER	14208M001	00	000	01	147
CAGL	12725M003	01	192	00	000	ONSA	10402M004	00	000	99	032
DRAG	20710S001	00	000	00	000	ONSA	10402M004	99	033	00	000
EBRE	13410M001	97	105	00	000	ORID	15601M001	02	347	08	020
ELAT	20706M001	00	000	02	040	PENC	11206M006	00	000	03	141
ELBA	12721M002	00	000	00	000	PENC	11206M006	03	142	07	192
GENO	12712M002	00	000	00	000	POTS	14106M003	95	276	00	000
GLSV	12356M001	00	000	07	316	RABT	35001M002	00	000	00	000
GRAS	10002M006	00	000	03	113	RAMO	20703S001	04	077	00	000
GRAS	10002M006	05	001	00	000	RIGA	12302M002	99	060	05	001
GRAZ	11001M002	96	177	01	126	SJDV	10090M001	99	071	00	000
GRAZ	11001M002	01	152	05	080	TEHN	20404M002	00	000	00	000
GRAZ	11001M002	05	310	00	000	TRAB	20808M001	00	000	00	000
GSR1	14501M001	00	000	08	263	UZHL	12301M001	00	000	00	000
HERS	13212M007	04	001	00	000	VILL	13406M001	00	000	98	038
JOZE	12204M001	00	000	04	340	VILL	13406M001	98	039	01	112
JOZE	12204M001	06	001	00	000	VILL	13406M001	01	113	04	271
KOSG	13504M003	00	000	03	075	WTZR	14201M010	96	014	09	018
KOSG	13504M003	03	076	00	000	ZECK	12351M001	00	000	01	192
LAMA	12209M001	00	000	00	100	ZECK	12351M001	01	193	06	210
LAMA	12209M001	00	280	05	365	ZECK	12351M001	06	211	00	000
LAMP	12706M002	00	000	00	000	ZIMM	14001M004	00	000	98	309
MAR6	10405M002	00	000	00	000	ZIMM	14001M004	98	310	00	000
MATE	12734M008	00	000	99	168						

Table A.5: Sites selected for the algorithm which reduces apparent scale changes in the network. YY₁/DOY₁ denotes the beginning and YY₂/DOY₂ denotes the end of the interval in which the site is selected. YY is the year and DOY is the day of year. A date consisting of zeros only means that the respective interval begins on the date where the earliest data of this site is available or ends on the date where the latest data of this site is available.

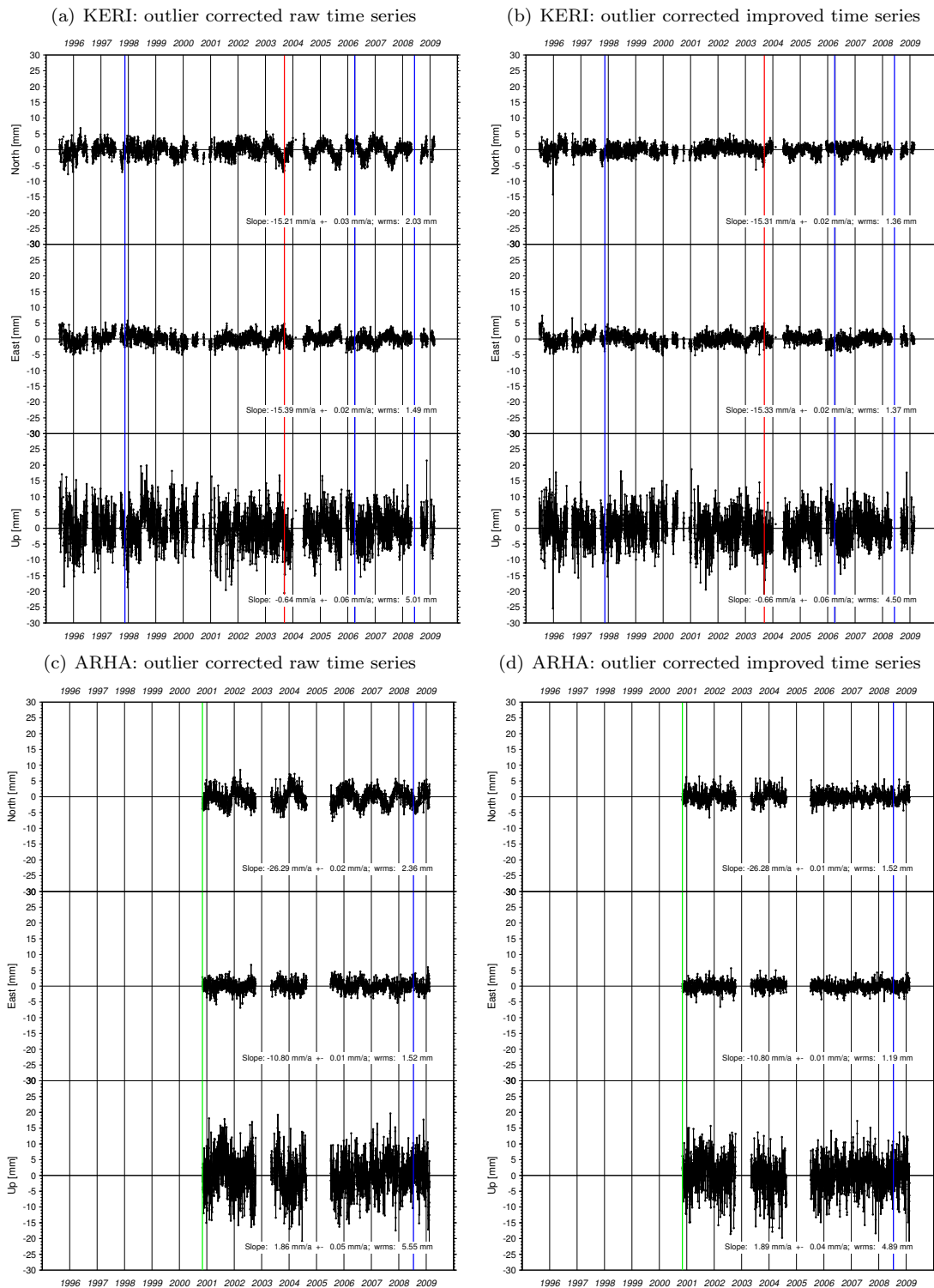


Figure A.3: The reduction of systematic, regional scale signals by the application of the method described in chapter 3.4.6 by means of two examples: site KERI located in the Ionian sea and site ARHA located in the SE Aegean sea. The time series are detrended. Vertical blue lines depict earthquakes having caused displacements at the particular site. The vertical red line depicts an antenna change. The vertical green line depicts an antenna and receiver change.

B Additional notes on the derived velocity field for the period 1993–2009

B.1 Pole of rotation for the Eurasian plate

ω	0.2661±0.0022	[°/Myr]	4.645e-09±3.814e-11	[rad/s]
λ_P	-96.12±1.09	[°]	-1.678e+00±1.904e-02	[rad]
ϕ_P	56.28±0.50	[°]	9.823e-01±8.805e-03	[rad]
ω_x	-0.0157±0.0029	[°/Myr]	-2.747e-10±5.015e-11	[rad/s]
ω_y	-0.1469±0.0006	[°/Myr]	-2.564e-09±9.978e-12	[rad/s]
ω_z	0.2214±0.0031	[°/Myr]	3.864e-09±5.406e-11	[rad/s]

Table B.1: Output parameters of the MATLAB program ROTPOL_CALC_V2.M after the final iteration. The resulting σ_0 a posteriori is 4.23235. The degree of freedom is 37. λ_P , ϕ_P are the longitude and latitude of the Euler pole, respectively and ω denotes the absolute value of the Euler vector Ω . ω_x , ω_y and ω_z denote the geocentric components of the Euler vector Ω .

Site	r_n [mm/yr]	r_e [mm/yr]	sr_n [-]	sr_e [-]	σ_{v_n} [mm/yr]	σ_{v_e} [mm/yr]
AJAC	-0.20	0.11	-1.16	0.64	0.04	0.04
BRST	-0.29	0.02	-0.83	0.05	0.08	0.08
BRUS	0.18	0.38	1.11	1.84	0.04	0.05
CAGL	-0.25	0.28	-1.07	0.94	0.06	0.07
EBRE	0.03	-0.11	0.20	-0.75	0.04	0.04
ELBA	-0.52	0.58	-1.31	1.49	0.09	0.09
GENO	0.07	-0.09	0.56	-0.83	0.03	0.03
GRAS	-0.14	0.31	-0.63	1.51	0.06	0.05
GRAZ	-0.42	-0.35	-1.54	-1.42	0.07	0.06
HERS	-0.19	0.13	-0.75	0.47	0.06	0.07
JOZE	0.21	0.27	1.29	1.82	0.04	0.04
KARL	0.16	-0.20	0.74	-0.91	0.05	0.05
KOSG	-0.24	-0.07	-1.34	-0.52	0.04	0.04
OBER	-0.33	0.29	-1.05	1.10	0.08	0.06
OROS	0.33	-0.01	0.61	-0.03	0.13	0.13
PENC	0.08	-0.29	0.30	-1.43	0.07	0.05
SJDV	0.18	-0.10	1.54	-1.00	0.03	0.03
TORI	0.02	-0.01	0.16	-0.09	0.03	0.03
VILL	-0.34	-0.24	-0.54	-0.37	0.15	0.15
WTZR	0.02	-0.01	0.25	-0.09	0.02	0.02

Table B.2: The derived pole of rotation for the Eurasian plate (Table B.1) is based on the rates of the sites listed in this table. r_n , r_e are the north and east components of the residuals (adjusted - observed), respectively, with respect to the derived Euler pole for Eurasia. sr_n , sr_e are the standardized residuals. σ_{v_n} , σ_{v_e} are the accuracies of the respective velocity components. The site locations and the residuals are depicted in Fig. B.1 (a) and Fig. B.2, respectively.

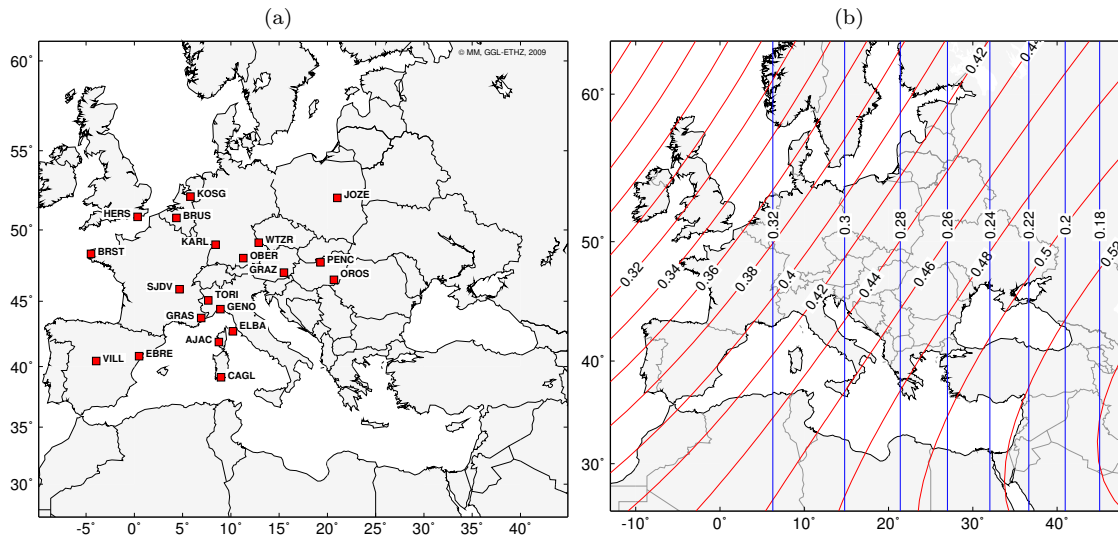


Figure B.1: (a) Sites used for the estimation of a pole of rotation for the Eurasian plate. The standardized residuals of the rates of these sites are all within a 95% confidence interval. (b) Velocity differences between the Eurasian pole of rotation derived in this thesis and the pole derived by *Altamimi et al.* [2007]. The difference in rates amounts to 0.56 mm/yr for sites in Greece. Blue contour lines depict the differences in the north component, red contour lines the differences in the east component. Units: [mm/yr].

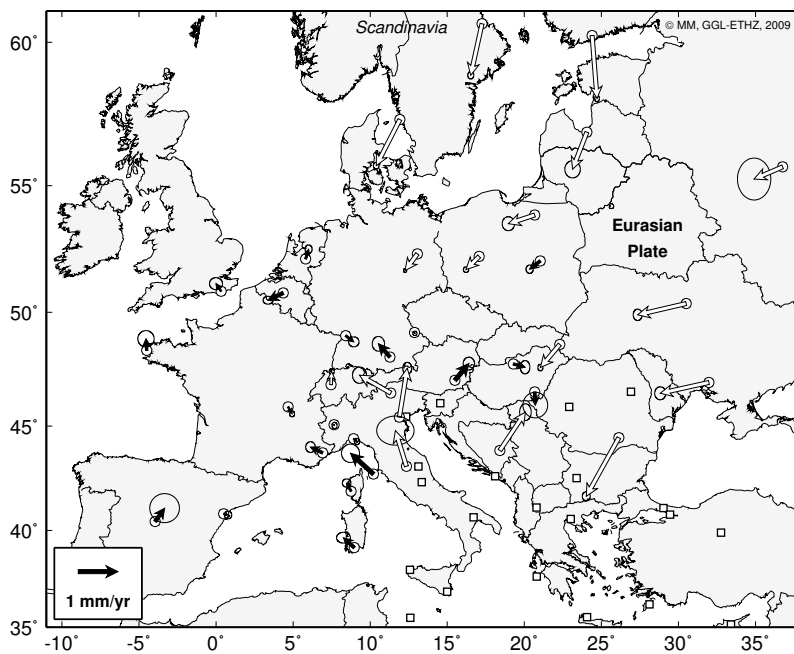


Figure B.2: Residual rates of CGPS sites located in Europe with respect to the block motion described by the estimated Euler pole for Eurasia. Black arrows depict sites used for the estimation of the Euler pole (Table B.2 and Fig. B.1 (a)). White arrows depict sites whose rates were not used for the pole estimation but show residuals below 2 mm/yr with respect to the motion of Eurasia. White squares depict sites whose rates differ by more than 2 mm/yr from the motion of Eurasia. The indicated error ellipses correspond to the 95% confidence region.

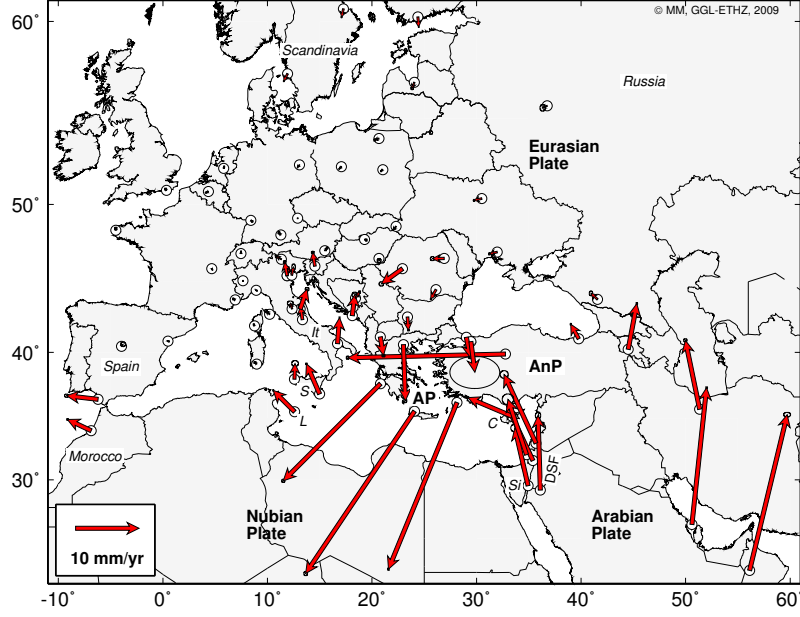


Figure B.3: Rates of CGPS sites in Europe, northern Africa and the middle East relative to Eurasia. AP: Aegean plate, AnP: Anatolian plate, C: Cyprus, DSF: Dead Sea fault, It: Italy, L: Lampedusa, S: Sicily, Si: Sinai peninsula. The error ellipses correspond to the 95% confidence region.

B.2 Nubian plate motion relative to Eurasia

The Euler vector $\Omega_{Nu,Eu}$ describing Nubian plate motion relative to Eurasia, $\mathbf{v}_{Nu,Eu}$, at an arbitrary point \mathbf{r} is derived by subtracting the Euler vector of Eurasia Ω_{Eu} from the Euler vector of Nubia Ω_{Nu} .

$$\mathbf{v}_{Nu,Eu} = \mathbf{r} \times \Omega_{Nu} - \mathbf{r} \times \Omega_{Eu} = \mathbf{r} \times (\Omega_{Nu} - \Omega_{Eu}) \quad (\text{B.1})$$

$$\Omega_{Nu,Eu} = \Omega_{Nu} - \Omega_{Eu} \quad (\text{B.2})$$

The Euler vector $\Omega_{Nu,Eu}$ describing Nubian plate motion relative to Eurasia is $\phi_P = -13.576^\circ\text{N}$, $\lambda_P = -36.314^\circ\text{E}$, $\omega_P = 0.0481^\circ/\text{Myr}$. The Euler vectors Ω_{Eu} and Ω_{Nu} were taken from *Altamimi et al.* [2007]. Ω_{Eu} indicated by *Altamimi et al.* [2007] is comparable with the Eurasian pole derived in this thesis (Table 4.1, Fig. B.1 (b)).

B.3 Comparison of rates of closely located continuous and campaign-type GPS sites

CGPS	EGPS	D	CGPS				EGPS				Statistics	
			v_e	v_n	s_{v_e}	s_{v_n}	v_e	v_n	s_{v_e}	s_{v_n}	$V_{\Delta v_e}$	$V_{\Delta v_n}$
ALON	CG12	6.3	-10.6	-19.5	0.2	0.2	-10.2	-20.4	0.3	0.4	-1.22	1.96
KARP	KRPN	1.6	-8.1	-9.0	0.1	0.1	-9.3	-9.3	0.3	0.3	4.31	0.71
KATC	KTTV	0.0	-9.0	-29.2	0.2	0.3	-9.6	-28.5	0.2	0.2	1.96	-1.94
KPTS	KRPT	8.2	-14.3	-31.2	0.4	0.3	-14.5	-29.8	0.2	0.2	0.50	-3.84
LIMS	LIMN	7.0	-16.0	-12.9	0.1	0.1	-15.9	-12.4	0.3	0.4	-0.45	-1.28
SMTZ	SMTK	3.5	-2.1	-3.2	0.2	0.3	-2.0	-3.8	0.4	0.5	-0.12	1.22

Table B.3: Differences between rates of closely located continuous and campaign-type (EGPS) GPS sites. The comparability is limited due to site spacing of up to 8.2 km and different measuring periods. Significant differences on the 95% confidence level are observed only for the east components of KARP and KRPN and the north components of KPTS and KRPT. D : Distance in [km]. v_e , v_n denote the east and north components, respectively, of the rates (in [mm/yr]). s_{v_e} , s_{v_n} denote the corresponding accuracies (in [mm/yr]). $V_{\Delta v_e}$ and $V_{\Delta v_n}$ denote normally distributed test values ($v_{CGPS} - v_{EGPS}$) of the particular velocity component.

B.4 Periodic motion of sites PAXI and APAX

The CGPS sites on the islands of Paxi (PAXI) and Andipaxi (APAX) exhibit significant periodic motion. The periodic motion is 3.5 to 6.5 times larger at site PAXI than at site APAX (Fig. B.4 and Fig. B.5 (a)). The phase lags of the annual sinusoidal terms in the north and east components agree within 10 days while agreement is worse in the up component (Tab. B.4). Baseline length changes in the range of -2.1–2.4 mm (-140–160 nstrain) are observed between APAX and PAXI (Fig. B.5 (b)). The cause of these seasonal signals is unknown. The signals might be related to hydrological effects in combination with karst formations as both the maximum in the up component of PAXI and the maximum precipitation in Greece is observed during the winter. Ocean tide loading effects not properly corrected might also contribute to the observed signal. Noteworthy, amplitudes of seasonal terms in the range of 1–2 mm are also observed at other sites in Greece.

Site	North				East				Up			
	$A_{2\pi}$	$\phi_{2\pi}$	$A_{4\pi}$	$\phi_{4\pi}$	$A_{2\pi}$	$\phi_{2\pi}$	$A_{4\pi}$	$\phi_{4\pi}$	$A_{2\pi}$	$\phi_{2\pi}$	$A_{4\pi}$	$\phi_{4\pi}$
APAX	1.8	52.2	0.3	-73.0	0.5	91.1	0.2	-112.8	1.1	-20.0	1.0	63.5
PAXI	6.3	61.3	0.8	-98.0	3.3	84.9	0.8	-12.0	6.5	82.5	2.7	-1.7

Table B.4: Amplitudes A and phase lags ϕ of the annual and semiannual sinusoidal terms (denoted as 2π and 4π , respectively) of the particular coordinate components of sites APAX and PAXI. The annual and semiannual terms were estimated according to Eq. (3.7) based on improved time series. A and ϕ were derived based on Eq. (3.8). A is indicated in [mm] and ϕ is indicated in [days].

B.5 Conspicuous signals in the time series of site SKIN

The time series of site SKIN in the northern part of Zakynthos exhibits signals which are not clearly assignable to a known technical or tectonic origin. The following characteristics visible in the detrended time series of SKIN influence the estimation of interseismic velocities in the order of up to 2 mm/yr (Fig. B.6 (a)):

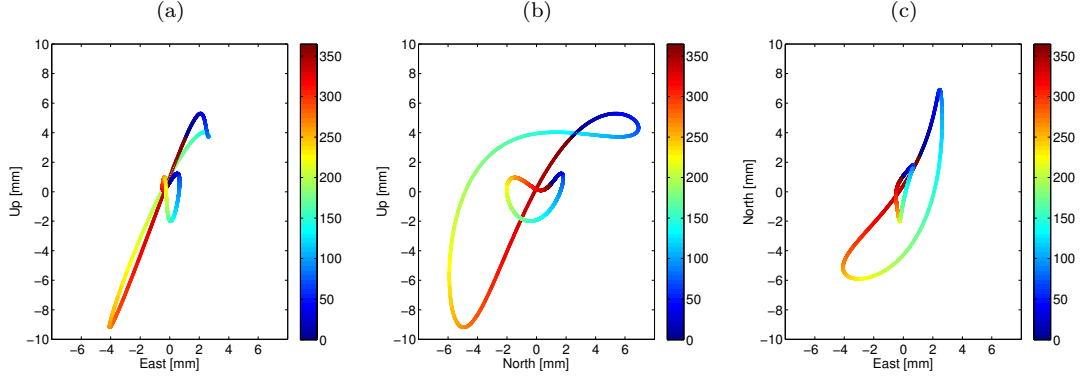


Figure B.4: Periodic motion of sites APAX (small loop) and PAXI (large loop) as derived by Eq. (3.7) (see Table B.4). The color scheme indicates the day of year. (a) East and up components (b) North and up components (c) East and north components.

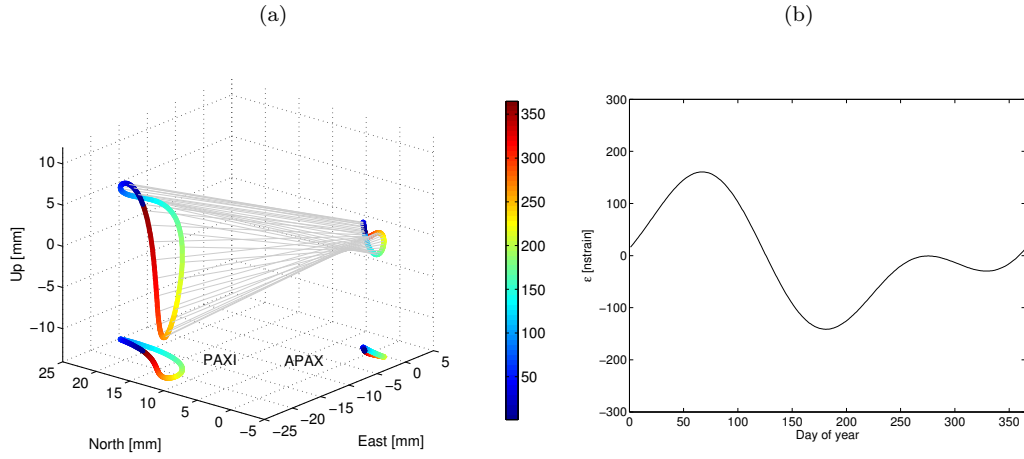


Figure B.5: (a) Periodic motion of sites APAX and PAXI as derived by Eq. (3.7) (see Table B.4). The color scheme indicates the day of year. (b) Deformation along the baseline between sites APAX and PAXI in case that both signals can be related to a physical process causing island-wide deformation.

- Northward shift in mid 2001 (~ 5 mm/yr) and southward shift in mid 2003 (~ 4.5 mm/yr).
- Larger westward velocity component (~ 1 mm/yr) before mid 2002 than afterward.

In addition, the magnitudes of displacements related to the antenna changes in 1996 and 1997 are not precisely known. A true non-linear motion of the antenna is likely because no antenna and receiver changes occurred between July 1998 and September 2003. *Hollenstein* [2006] already observed a slight deviation from the linear trend to the southeast at the end of 2003. These signals became more pronounced after processing additional data for the period 2004–2009. The spatial extent of the process causing these signals can be confined to northern Zakynthos since the time series of KERI in the south of the island does not show similar signals (Fig. B.6 (b)).

A small coseismic displacement (2 ± 1 mm) directed south related to the 2003 Lefkada earthquake can be deduced from the time series (Fig. 6.5). The derived displacement is only a fraction of the southward shift in mid 2003. The directions of both the coseismic and the transient motion agree with those of calculated coseismic displacements (chapter 6.5.2). A relation between the southward motion prior to the Lefkada earthquake and the earthquake itself remains speculative.

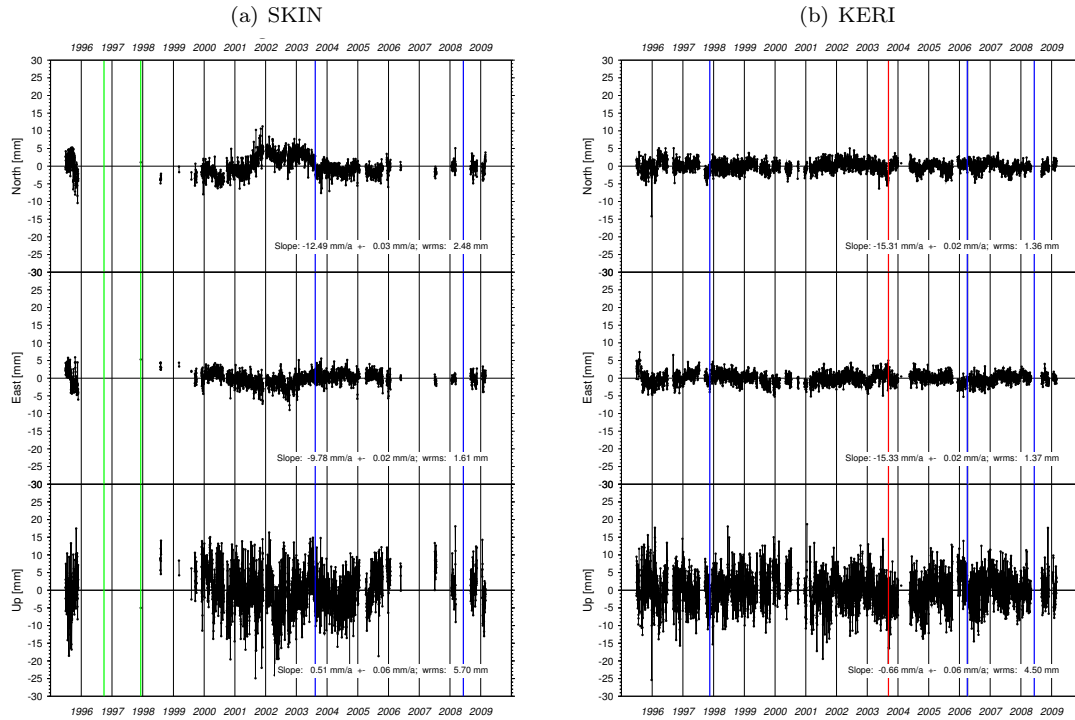


Figure B.6: Improved time series with a linear trend removed. The slope and the formal accuracy of the removed trend and the coordinate precision are listed. (a) Site SKIN. The blue lines depict the 2003 Mw 6.2 Lefkada and the 2008 Mw 6.4 NW Peloponnesos earthquakes, respectively. The green lines denote receiver and antenna changes. (b) Site KERI. Blue lines depict the 1997 Mw 6.6 Strofades, the 2006 Zakynthos earthquakes (Mw 5.0–5.7) and the 2008 Mw 6.4 NW Peloponnesos earthquakes, respectively. The red line indicates an antenna change.

Obviously, a linear site motion is not adequate for site SKIN. Rates vary by up to 2 mm/yr depending on the interpretation of the signals. No discontinuities were introduced in the time series for the estimation of interseismic rates between 242/1997–160/2008. It is noted that an interseismic velocity of SKIN directed more westward would mean less cw rotation and higher shear strain rates on Zakynthos (Fig. B.7).

B.6 Notes on the use of the data from Straub et al. [1997] and McClusky et al. [2000]

Data from *Straub et al.* [1997] and *McClusky et al.* [2000] are used in this thesis. The velocities of the former data set are listed in ITRF94 relative to Istanbul. The reference frame of the latter data set was derived by minimizing the horizontal velocities of 16 IGS stations in Europe and Asia. The data is listed in an Eurasian-fixed frame. Transformation of data of *McClusky et al.* [2000] into ITRF2005 was realized by a 7 parameter Helmert transformation

$$\dot{\mathbf{X}}_{new} = \mathbf{R} \cdot \dot{\mathbf{X}} + \dot{\mathbf{T}} + \dot{\mathbf{X}} \quad (\text{B.3})$$

The term $\dot{\mathbf{R}} \cdot \mathbf{X}$ was omitted as temporal derivatives of the transformation parameters are very small. Transformation parameters were estimated by a set of corresponding site velocities, in particular campaign-type sites in the Aegean domain. Velocities originating from *Straub et al.* [1997] had to be transformed into ITRF2005 via the system of *McClusky et al.* [2000] because

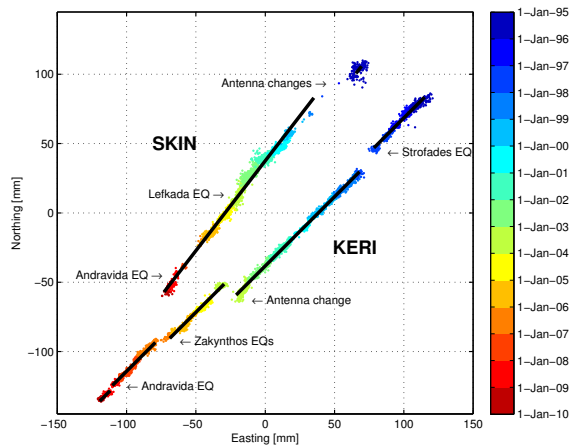


Figure B.7: Horizontal positions of SKIN and KERI. The color scheme indicates the date of the position estimates, the black lines depict the interseismic trend for the position. Note that earthquake displacements cannot directly be derived from the black lines. The interseismic motion of SKIN fits less optimal to a linear model than the site motion of KERI. The origin of the signals observed in the time series of SKIN is unknown.

there were no sites which were included both in the processing of *Straub et al. [1997]* and the processing of this thesis.

The RMS of the misfit between the transformed velocities of *McClusky et al. [2000]* and the velocities processed in ITRF2005 are 0.9 mm/yr for the east and north components, respectively. The RMS of the misfit between the transformed rates of *Straub et al. [1997]* and the rates of *McClusky et al. [2000]* are 1.5 and 0.9 mm/yr for the east and north components, respectively. The residuals are shown in Fig. B.8. The three data sets correspond on the 1-2 mm/yr level. The accuracies of the rates of the two data sets were scaled to account for inconsistencies related to the reference frame when the rates were used in combination with velocities derived in this thesis.

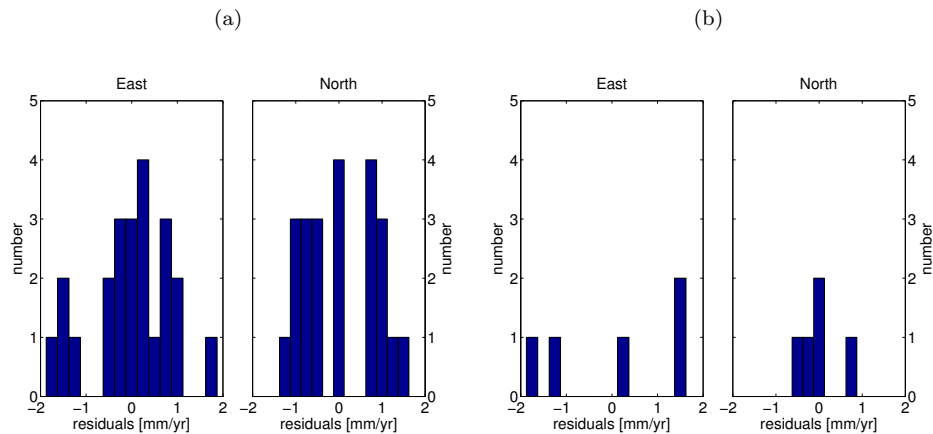


Figure B.8: (a) Residuals after transforming velocities from *McClusky et al. [2000]* into the Eurasian-fixed frame which was derived in this thesis. (b) Residuals after transforming velocities from *Straub et al. [1997]* into the frame of *McClusky et al. [2000]*.

C GPS velocity results

C.1 Introduction

The derived rates of CGPS sites are listed in appendix C.2, those of campaign-type GPS sites are listed in appendix C.3. Vertical rates are listed for all CGPS sites irrespective of the time series length. No vertical rates are indicated for campaign-type sites. Offsets introduced in the time series and time periods in which particular data was excluded from the velocity estimation are listed in appendix A.2. The indicated accuracies were scaled as described in chapter 3.4.7. The coordinate precision listed for CGPS sites is calculated component-by-component by

$$s_c^2 = \frac{\sum_{i=1}^n p_i r_i r_i}{\sum_{i=1}^n p_i} \cdot \frac{n}{(n-u)} \quad (C.1)$$

where p denotes the weight of a daily position estimate which is based on the formal error derived by the Bernese GPS software, r denotes the residual with respect to the applied velocity model, n denotes the number of daily position estimates and u denotes the number of unknown model parameters. The time series of CGPS sites in Greece are depicted in appendix D. The residual time series of campaign-type GPS sites in Greece are depicted in appendix E.

C.2 Rates of continuous GPS sites

IGS and EUREF sites

Site	λ	φ	Time	v_e	v_n	v_{up}	s_{v_e}	s_{v_n}	$s_{v_{up}}$	s_{c_e}	s_{c_n}	$s_{c_{up}}$	R
AJAC	8.763	41.927	021/00-059/09	-0.1	0.2	1.3	0.1	0.1	0.2	1.0	0.9	3.8	(a)
ANKR	32.758	39.887	174/95-059/09	-24.9	-0.6	-0.3	0.1	0.1	0.3	1.5	1.6	4.9	(a)
AQUI	13.350	42.368	001/04-059/09	-0.3	2.1	1.9	0.2	0.1	0.3	2.0	1.7	4.2	(a)
BACA	26.912	46.562	019/06-059/09	-1.9	-0.0	2.0	0.1	0.1	0.6	0.9	0.9	4.1	(a)
BAHR	50.608	26.209	175/96-059/09	2.3	21.6	-0.1	0.1	0.1	0.2	1.7	1.7	7.5	(a)
BOR1	17.073	52.277	094/95-059/09	-0.3	-0.3	0.7	0.1	0.1	0.1	0.8	0.9	2.9	(a)
BRST	-4.497	48.380	120/99-059/09	-0.0	0.3	1.8	0.1	0.1	0.3	1.1	1.1	4.5	(a)
BRUS	4.359	50.798	094/95-059/09	-0.4	-0.2	1.8	0.1	0.1	0.1	1.4	1.1	3.2	(a)
BUCU	26.126	44.464	048/99-059/09	-0.8	-1.5	3.4	0.1	0.1	0.2	0.9	1.1	4.5	(b)
BZRG	11.337	46.499	078/98-059/09	-0.8	0.5	2.5	0.1	0.1	0.3	0.9	1.1	3.7	(b)
CAGL	8.973	39.136	064/96-059/09	-0.3	0.2	1.2	0.1	0.1	0.2	1.7	1.3	4.3	(a)
CAME	13.124	43.112	119/00-359/08	1.1	3.1	1.7	0.1	0.1	0.4	1.5	1.4	5.2	(a)
DEVA	22.914	45.878	019/06-059/09	-3.3	-2.4	1.9	0.1	0.1	0.6	1.0	0.9	3.9	(a)
DRAG	35.392	31.593	038/00-059/09	-4.0	8.5	3.7	0.1	0.1	0.2	1.3	1.1	4.5	(a)
DUBR	18.110	42.650	266/00-039/09	0.4	3.3	-0.0	0.2	0.2	0.4	1.9	1.8	3.7	(b)
EBRE	0.492	40.821	033/96-059/09	0.1	-0.0	1.3	0.1	0.1	0.1	1.5	1.5	4.8	(b)
ELAT	34.921	29.509	219/97-040/02	-2.1	9.1	0.1	0.3	0.2	0.9	1.9	1.7	6.4	(a)
ELBA	10.211	42.753	001/04-059/09	-0.6	0.5	1.4	0.1	0.1	0.3	1.1	1.2	4.0	(a)
GENO	8.921	44.419	204/98-059/09	0.1	-0.1	1.0	0.1	0.1	0.1	0.8	1.0	3.9	(a)
GLSV	30.497	50.364	080/98-059/09	-1.2	-0.3	0.6	0.1	0.1	0.2	1.3	1.7	5.1	(a)
GRAS	6.921	43.755	094/95-059/09	-0.3	0.1	1.2	0.1	0.1	0.2	1.0	1.1	3.0	(a)
GRAZ	15.493	47.067	094/95-059/09	0.4	0.4	1.2	0.1	0.1	0.3	0.8	0.8	3.4	(a)
GSR1	14.544	46.048	001/04-059/09	-0.3	2.2	1.7	0.1	0.1	0.3	1.1	0.9	3.1	(a)
HALY	36.100	29.139	155/04-273/07	-0.4	11.8	0.3	0.2	0.2	0.7	0.8	1.0	3.3	(b)
HERS	0.336	50.867	094/95-059/09	-0.1	0.2	1.2	0.1	0.1	0.2	1.3	1.2	3.6	(a)

continued on the next page

continued from the last page

Site	λ	φ	Time	v_e	v_n	v_{up}	s_{v_e}	s_{v_n}	$s_{v_{up}}$	s_{c_e}	s_{c_n}	$s_{c_{up}}$	R
ISTA	29.019	41.104	345/99-059/09	0.6	-3.2	1.5	0.1	0.1	0.2	2.5	2.2	4.7	(a), (1)
JOZE	21.032	52.097	095/95-059/09	-0.3	-0.2	2.1	0.1	0.1	0.2	1.0	1.1	4.3	(a)
KARL	8.411	49.011	120/99-059/09	0.2	-0.2	1.6	0.1	0.1	0.2	0.9	0.9	3.4	(b)
KATZ	35.688	32.995	219/97-040/02	-5.0	10.8	-0.0	0.3	0.2	0.9	1.7	1.5	5.8	(b)
KOSG	5.810	52.178	094/95-059/09	0.1	0.2	0.5	0.1	0.1	0.1	0.9	1.1	3.3	(a)
LAMA	20.670	53.892	096/95-059/09	-0.7	-0.2	0.1	0.1	0.1	0.3	0.9	1.0	3.7	(a)
LAMP	12.606	35.500	085/99-017/09	-3.4	3.4	1.2	0.1	0.1	0.1	0.9	1.2	4.3	(a)
MAR6	17.259	60.595	060/99-059/09	-0.3	-1.3	8.2	0.1	0.1	0.1	1.0	1.2	3.5	(a)
MATE	16.704	40.649	094/95-059/09	0.3	4.1	1.8	0.1	0.1	0.1	1.0	1.1	3.4	(a)
METS	24.395	60.217	094/95-059/09	0.1	-1.6	5.1	0.1	0.1	0.1	1.1	1.4	4.1	(a)
MIKL	31.973	46.973	001/04-059/09	-1.2	-0.3	1.4	0.1	0.1	0.3	0.8	0.9	3.9	(a)
MILO	12.584	38.008	068/05-059/09	0.1	2.5	<i>0.2</i>	0.2	0.2	0.5	2.0	1.7	4.9	(a)
NICO	33.396	35.141	233/97-059/09	-6.9	2.9	0.8	0.1	0.1	0.2	1.1	1.5	4.4	(a)
NOT1	14.990	36.876	252/00-059/09	-2.1	4.7	0.5	0.1	0.1	0.2	1.3	1.2	4.0	(a)
NOTO	14.990	36.876	256/95-249/00	-2.1	4.8	0.2	0.2	0.2	0.8	1.2	1.4	4.7	(a)
NSSP	44.503	40.226	029/98-059/09	1.4	7.2	0.9	0.1	0.1	0.3	0.8	1.1	4.3	(a)
OBER	11.280	48.086	302/96-147/01	-0.3	0.3	0.3	0.1	0.1	0.3	0.7	0.9	2.9	(a)
ONSA	11.926	57.395	094/95-059/09	-0.6	-1.2	3.7	0.1	0.1	0.1	0.9	1.1	3.6	(a)
ORID	20.794	41.127	203/00-059/09	0.5	-2.9	1.5	0.1	0.1	0.4	1.0	0.9	4.1	(a)
OROS	20.671	46.555	001/04-059/09	0.0	-0.3	1.5	0.1	0.1	0.6	0.7	0.8	3.7	(a)
PADO	11.896	45.411	331/01-059/09	0.2	1.2	1.1	0.1	0.1	0.1	0.9	1.2	2.9	(b)
PENC	19.282	47.790	121/96-059/09	0.3	-0.1	0.4	0.1	0.1	0.2	0.9	1.2	4.0	(a)
POTS	13.066	52.379	096/95-059/09	-0.3	-0.4	0.8	0.1	0.1	0.1	0.7	0.8	3.9	(a)
RABT	-6.854	33.998	138/00-059/09	-3.7	1.8	1.0	0.1	0.1	0.3	1.3	1.6	6.2	(a)
RAMO	34.763	30.598	077/04-059/09	-3.4	7.4	2.0	0.1	0.1	0.3	0.8	0.8	3.5	(b)
RIGA	24.059	56.949	060/99-059/09	-0.4	-0.9	2.6	0.1	0.1	0.3	1.1	1.3	3.9	(a)
SFER	-6.206	36.464	087/96-054/09	-5.0	0.6	2.4	0.1	0.1	0.4	1.9	1.6	5.6	(a)
SJDV	4.677	45.879	200/98-059/09	0.1	-0.2	1.2	0.1	0.1	0.1	0.7	0.8	3.0	(a)
SOFI	23.395	42.556	167/97-059/09	0.1	-2.1	0.9	0.1	0.1	0.1	2.0	1.5	5.4	(a)
SRJV	18.414	43.868	325/99-059/09	0.6	1.0	1.2	0.1	0.1	0.3	1.2	1.7	5.3	(a)
TEHN	51.334	35.697	275/04-059/09	-2.2	10.9	1.7	0.1	0.1	0.4	1.0	1.0	4.0	(b)
TELA	34.781	32.068	219/97-040/02	-2.9	8.7	0.3	0.4	0.4	1.3	1.7	1.6	6.0	(a)
TORI	7.661	45.063	074/98-059/09	0.0	-0.0	2.1	0.1	0.1	0.1	0.9	1.0	4.1	(b)
TRAB	39.776	40.995	346/99-331/07	-1.3	2.3	0.5	0.1	0.1	0.2	0.8	1.2	4.5	(a)
TUBI	29.451	40.787	184/99-059/09	0.6	-4.8	-1.0	1.6	1.0	0.3	46.8	30.9	8.9	(a), (1)
UNPG	12.356	43.119	001/98-059/09	-0.3	0.9	1.7	0.2	0.1	0.5	1.4	1.1	3.7	(a)
UPAD	11.878	45.407	094/95-324/01	-0.4	2.1	-0.7	0.1	0.1	0.4	0.8	1.0	3.8	(b)
UZHL	22.298	48.632	185/99-059/09	-0.5	-0.6	1.2	0.1	0.1	0.1	0.8	1.0	4.2	(a)
VE NE	12.332	45.437	350/01-205/07	0.3	1.3	-0.1	0.1	0.2	0.3	1.0	1.6	2.7	(b)
VILL	-3.952	40.444	094/95-059/09	0.2	0.3	-0.6	0.2	0.1	0.5	1.4	1.4	5.0	(a)
WTZR	12.879	49.144	014/96-059/09	0.0	-0.0	1.0	0.1	0.1	0.1	0.9	1.0	3.4	(a)
YIBL	56.112	22.186	003/04-059/09	5.9	24.6	0.2	0.2	0.2	0.7	2.4	1.7	7.5	(a)
ZECK	41.565	43.788	262/97-059/09	-1.0	0.9	1.3	0.1	0.1	0.5	1.2	1.6	5.4	(a)
ZIM2	7.465	46.877	326/07-059/09	-0.5	-0.6	-0.2	0.5	0.5	2.1	0.8	0.9	3.7	(b)
ZIMM	7.465	46.877	094/95-059/09	0.0	0.3	2.5	0.1	0.1	0.1	0.8	1.0	3.4	(a)
ZWE2	36.758	55.699	301/04-342/08	-0.8	-0.3	0.8	0.3	0.3	1.3	1.8	1.6	6.9	(a)
ZWEN	36.759	55.699	096/95-075/03	-0.7	-0.3	-0.0	0.2	0.2	0.7	1.8	2.3	7.7	(a)

Table C.1: Rates of IGS and EUREF sites included in the GPS processing. The GPS velocity solution was aligned to ITRF2005. The horizontal rates are indicated relative to Eurasia (Euler pole: $\phi = 56.28^\circ\text{N}$, $\lambda = -96.12^\circ\text{E}$, $\omega = 0.266^\circ/\text{Myr}$). λ and φ denote the longitude and the latitude of the GPS sites. Time indicates the period the velocity estimation is based on (format: day of year/year). v_e , v_n and v_{up} denote the rates in the east, north and up components, respectively. s_{v_e} , s_{v_n} and $s_{v_{up}}$ denote the corresponding scaled accuracies. s_{c_e} , s_{c_n} and $s_{c_{up}}$ denote the coordinate precision. The positions are indicated in $[\circ]$, the rates and their accuracies in $[\text{mm}/\text{yr}]$ and the coordinate precision in $[\text{mm}]$. Remarks (R): (a) Velocity estimation based on Eq. (3.5). (b) Velocity estimation based on Eq. (3.7). (1) Rates are influenced by postseismic effects related to the 1999 Mw 7.5 Izmit earthquake. Vertical rates written in italics indicate that the velocity estimation is actually based on data spanning less than 4 years.

CGPS sites in Greece

Site	λ	φ	Time	v_e	v_n	v_{up}	s_{v_e}	s_{v_n}	$s_{v_{up}}$	s_{c_e}	s_{c_n}	$s_{c_{up}}$	R
ALON	23.864	39.165	261/04-199/08	-10.6	-19.5	<i>0.6</i>	0.2	0.2	0.9	0.9	1.0	4.2	(a)
AMFI	21.165	38.864	183/95-059/09	-8.0	-3.5	-0.2	0.1	0.1	0.4	1.5	1.3	4.5	(a)
ANOK	19.797	39.712	042/00-162/08	-4.0	0.8	0.3	0.2	0.2	0.9	2.8	3.3	13.3	(a)
APAX	20.249	39.141	096/95-164/08	-0.4	2.9	0.3	0.1	0.1	0.4	1.0	1.2	4.2	(b)
ARHA	28.121	36.214	308/97-045/09	-10.8	-26.3	1.9	0.1	0.1	0.2	1.2	1.5	4.9	(a)
ARSA	23.034	38.755	273/97-059/09	-10.6	-19.7	1.5	0.1	0.1	0.3	1.2	1.5	4.0	(a), (1)
AUT1	23.004	40.567	090/05-059/09	0.3	-8.8	<i>-1.1</i>	0.1	0.1	0.4	0.8	1.1	3.4	(b)
DION	23.933	38.079	108/95-059/09	-16.5	-25.4	1.6	0.1	0.1	0.3	2.0	1.9	5.7	(a)
DUKA	20.543	38.564	095/95-247/08	-4.8	-4.4	0.1	0.2	0.2	0.8	1.2	1.3	4.4	(a)
EFSS	24.989	39.540	102/05-222/08	-13.6	-16.1	<i>0.3</i>	0.2	0.2	0.6	0.9	1.1	3.5	(b)
GERO	20.342	38.180	149/95-246/08	-5.9	-3.3	-0.9	0.1	0.1	0.3	1.5	1.6	4.8	(b)
KALY	26.985	36.950	195/05-276/08	-18.6	-24.1	<i>-2.3</i>	0.3	0.4	1.3	1.6	2.2	6.7	(a)
KARP	21.810	38.917	042/00-059/09	-8.1	-9.0	1.5	0.1	0.1	0.4	2.1	3.2	8.2	(a)
KAST	21.269	40.519	039/96-020/09	0.2	-3.6	1.5	0.1	0.1	0.5	2.1	1.9	7.5	(a), (2)
KATC	27.781	35.951	278/05-169/08	-9.0	-29.2	<i>0.1</i>	0.2	0.3	1.0	1.3	1.5	5.2	(b)
KERI	20.808	37.655	179/95-059/09	-15.3	-15.3	-0.7	0.1	0.1	0.3	1.4	1.4	4.5	(a)
KPTS	27.161	35.547	051/01-274/08	-14.3	-31.2	1.4	0.4	0.3	1.1	2.6	1.8	7.4	(a), (3)
LIMS	25.181	39.897	258/02-178/08	-16.0	-12.9	0.2	0.1	0.1	0.4	0.9	0.8	4.0	(a)
NEAP	25.610	35.261	066/02-059/09	-18.1	-28.1	0.3	0.1	0.1	0.5	1.6	1.8	5.9	(a)
NEOH	23.222	39.306	013/02-059/09	-5.9	-14.1	<i>0.3</i>	0.1	0.2	0.5	1.3	1.4	4.4	(a)
NISI	27.131	36.611	271/02-280/08	-11.0	-26.8	-7.4	0.2	0.1	0.5	1.7	1.6	5.1	(a)
NOA1	23.864	38.047	084/06-059/09	-17.3	-25.8	<i>1.6</i>	0.3	0.5	1.3	1.9	3.1	7.8	(a)
PAXI	20.128	39.236	199/95-345/00	-0.3	2.8	0.0	0.1	0.1	0.4	1.4	1.6	5.0	(b)
RLS	21.465	38.056	210/06-059/09	-13.6	-23.1	<i>0.7</i>	0.3	0.3	1.4	0.9	0.9	3.9	(b)
SKIN	20.702	37.931	178/95-059/09	-9.6	-12.5	0.5	0.1	0.1	0.3	1.6	2.5	5.7	(a), (4)
SMTZ	25.473	40.476	331/03-273/08	-2.1	-3.2	0.6	0.2	0.3	1.0	1.1	1.5	5.5	(a), (5)
TILO	27.394	36.380	182/05-175/08	-12.6	-30.2	<i>0.2</i>	0.2	0.2	0.7	1.1	1.2	4.3	(a)
TUC2	24.071	35.533	233/97-059/09	-17.2	-25.6	0.7	0.1	0.1	0.4	1.2	1.4	4.2	(a), (6)
VLSM	20.589	38.177	045/06-059/09	-6.4	-11.0	<i>0.1</i>	0.3	0.3	0.8	1.7	1.8	5.2	(a)

Table C.2: Rates of CGPS sites in Greece. The GPS velocity solution was aligned to ITRF2005. The horizontal rates are indicated relative to Eurasia (Euler pole: $\phi = 56.28^\circ\text{N}$, $\lambda = -96.12^\circ\text{E}$, $\omega = 0.266^\circ/\text{Myr}$). λ and φ denote the longitude and the latitude of the GPS sites. Time indicates the period the velocity estimation is based on (format: day of year/year). v_e , v_n and v_{up} denote the rates in the east, north and up components, respectively. s_{v_e} , s_{v_n} and $s_{v_{up}}$ denote the corresponding scaled accuracies. s_{c_e} , s_{c_n} and $s_{c_{up}}$ denote the coordinate precision. The positions are indicated in [$^\circ$], the rates and their accuracies in [mm/yr] and the coordinate precision in [mm]. Remarks (R): (a) Velocity estimation based on Eq. (3.5). (b) Velocity estimation based on Eq. (3.7). (1) Data of sites ARSA and ARS2 combined. (2) Data of sites KAST and KAS2 combined. (3) Data of sites KPTH and KPTS combined. (4) See appendix B.5. (5) Data of sites SMTP and SMTZ combined. (6) Data of sites TUC1 and TUC2 combined. Vertical rates written in italics indicate that the velocity estimation is actually based on data spanning less than 4 years.

C.3 Rates of campaign-type GPS sites

Site	λ	φ	v_e	v_n	s_{v_e}	s_{v_n}	Remarks
1KVL	20.656	38.791	-3.9	-10.2	0.4	0.4	(1)
AETO	21.835	37.244	-23.7	-26.2	0.5	0.7	
AKIT	23.296	35.873	-17.7	-26.9	0.3	0.3	
AMAT	19.854	39.524	-2.4	1.8	0.3	0.4	
ARTA	20.988	39.166	-7.3	-4.3	0.2	0.2	
ASKT	25.566	40.928	-0.6	-1.5	0.2	0.2	
ASSO	20.548	38.371	-6.6	-6.9	0.5	0.6	(2)
ASTP	26.406	36.586	-16.5	-29.5	0.2	0.2	
ATKO	21.120	38.494	-8.4	-16.0	0.7	0.9	
CG01	22.620	39.490	-4.3	-10.3	0.3	0.3	
CG02	22.241	39.608	-3.3	-10.1	0.3	0.3	
CG03	22.332	39.433	-3.6	-8.3	0.3	0.3	
CG05	23.186	39.361	-7.4	-15.8	1.0	1.1	
CG06	21.958	39.237	-6.0	-8.6	0.3	0.3	
CG08	22.242	39.089	-7.5	-11.3	0.4	0.4	
CG09	22.812	39.148	-7.2	-13.5	0.4	0.4	
CG10	23.254	39.146	-7.4	-15.8	0.3	0.3	
CG11	23.668	39.147	-9.2	-20.7	0.7	0.7	(3)
CG12	23.915	39.207	-10.1	-20.4	0.3	0.4	(3)
CG17	23.372	38.986	-10.2	-17.2	0.7	0.7	(4)
CG20	22.623	38.651	-9.0	-12.9	0.9	1.0	
CG31	22.285	38.348	-13.8	-16.7	0.6	0.7	(5)
CG33	22.869	38.428	-14.4	-17.8	0.8	0.9	
CG35	23.540	38.445	-14.6	-22.6	0.6	0.6	
CG38	24.109	38.661	-13.9	-24.0	0.5	0.5	(6)
CG43	22.192	38.130	-15.3	-25.4	0.6	0.7	(5)
CG50	23.355	38.209	-18.3	-25.7	1.0	1.2	
CG53	23.854	38.230	-17.8	-24.6	1.2	1.6	
CG57	23.445	38.066	-17.6	-26.6	0.9	1.0	
CG58	23.615	38.018	-20.6	-27.8	0.9	1.0	
CG66	23.944	37.822	-18.3	-26.9	1.5	1.6	
CHLE	21.142	37.890	-18.2	-26.1	1.0	1.2	(7)
DAMN	24.419	35.171	-18.7	-24.8	0.4	0.4	
DOBR	23.569	41.823	0.8	-2.9	0.4	0.5	
DOXA	21.925	37.702	-20.3	-24.9	0.6	0.7	
FISK	20.577	38.460	-5.2	-6.8	0.2	0.3	(1)
GERM	22.413	36.475	-22.8	-24.8	0.7	0.8	
GVDO	24.074	34.837	-23.3	-27.0	0.8	0.9	
HIOS	26.085	38.443	-20.6	-22.8	0.6	0.7	
K2AM	20.372	38.221	-6.6	-2.8	2.5	2.6	
KARI	20.665	39.734	-3.1	-1.9	0.3	0.3	
KILL	21.136	37.941	-14.2	-19.4	0.7	0.9	(8)
KITH	22.984	36.307	-18.1	-26.5	0.4	0.4	
KLLI	22.142	38.397	-13.0	-13.7	0.5	0.6	(5)
KONS	23.954	41.078	0.4	-3.1	0.4	0.5	
KOSI	26.929	36.752	-17.4	-27.2	0.2	0.2	
KRNA	22.544	39.937	0.4	-6.8	0.2	0.2	
KRPN	21.798	38.905	-9.3	-9.3	0.3	0.3	
KRPT	27.224	35.493	-14.5	-29.8	0.2	0.2	
KSSI	20.989	37.723	-14.1	-18.3	1.1	1.3	(9)
KSZO	29.586	36.150	-11.2	-12.8	0.8	1.0	
KTTV	27.781	35.952	-9.6	-28.5	0.2	0.2	
KYNS	24.410	37.363	-17.6	-26.9	0.7	0.9	
L2PE	21.291	38.697	-11.9	-6.1	0.6	0.8	
LAKA	21.973	38.228	-15.6	-26.3	0.3	0.3	
LEON	22.823	37.184	-19.2	-26.6	0.2	0.3	
LESV	26.451	39.234	-22.3	-14.7	0.5	0.6	
LIMN	25.126	39.851	-15.9	-12.4	0.3	0.4	
LKTR	20.509	38.132	-8.7	-8.8	0.3	0.4	
MESS	21.122	38.370	-12.2	-16.0	0.7	0.8	
MILS	24.521	36.747	-18.2	-25.8	0.9	0.9	
MKN2	25.379	37.449	-18.6	-26.1	0.2	0.2	
MOMC	25.402	41.545	0.6	-2.3	0.4	0.5	
MONE	23.042	36.735	-20.3	-26.5	0.7	0.8	
NEVA	22.945	38.888	-9.7	-15.0	0.2	0.2	
NEVR	23.846	41.355	0.2	-2.8	0.4	0.5	
NSKR	24.543	38.887	-14.2	-24.8	0.4	0.5	(6)
OMAL	23.932	35.325	-18.1	-25.2	0.8	0.9	
OTHF	19.429	39.865	-2.6	1.7	0.1	0.2	
OTHO	19.379	39.856	-4.5	3.7	0.3	0.3	
PARG	20.473	39.292	-3.0	0.3	0.3	0.3	
PELA	24.094	39.322	-10.8	-20.0	0.7	0.7	
PETR	23.125	41.459	0.2	-3.6	0.4	0.4	

continued on the next page

continued from the last page							
Site	λ	φ	v_e	v_n	s_{v_e}	s_{v_n}	Remarks
PNTN	19.861	39.749	-4.5	0.3	0.4	0.4	
POLZ	23.444	40.373	0.6	-7.5	0.2	0.3	(10)
PRSL	21.486	38.655	-9.5	-5.7	0.6	0.6	
ROUM	24.694	35.404	-18.1	-25.3	0.3	0.4	
SAMO	26.989	37.780	-21.2	-23.1	0.2	0.2	
SARA	20.732	38.364	-9.4	-9.5	0.9	1.0	
SAT1	23.916	41.597	0.1	-3.9	0.8	1.0	
SERV	22.043	40.188	-1.4	-4.8	0.4	0.5	
SEVA	24.392	38.086	-17.0	-26.3	0.2	0.2	
SFIN	23.566	35.422	-18.2	-23.1	0.7	0.7	
SKAL	24.244	41.375	0.2	-3.0	0.2	0.2	
SKIA	23.468	39.165	-8.4	-18.2	0.9	0.8	
SMTK	25.513	40.466	-2.0	-3.8	0.4	0.5	
SNDO	21.580	38.014	-15.9	-23.2	0.6	0.7	(8)
SOXO	23.428	40.789	0.4	-4.2	0.2	0.2	
SPE1	18.458	40.063	1.2	3.7	0.5	0.6	
SRTA	22.388	37.034	-21.2	-26.1	0.6	0.7	
STHN	23.919	39.994	-1.7	-9.1	0.2	0.2	
STRF	21.014	37.250	-19.5	-16.7	0.3	0.4	(11)
STRO	21.016	37.250	-17.3	-18.5	1.0	1.3	(12)
STRV	22.409	37.098	-19.4	-25.0	0.5	0.6	
TERO	20.880	39.463	-4.4	-2.9	0.3	0.4	
THAS	24.627	40.593	-0.4	-3.6	0.3	0.3	
THIR	25.439	36.346	-18.2	-30.2	0.2	0.2	
TSAR	20.678	38.167	-6.9	-10.0	0.8	0.9	(1)
VASI	20.573	38.607	-5.0	-8.1	0.6	0.6	(2)
VONW	20.846	38.910	-4.9	-11.3	0.5	0.6	(2)
VRES	23.136	40.798	-0.0	-5.8	0.3	0.4	
XRIS	21.878	36.791	-21.1	-24.7	0.2	0.2	
ZAHA	21.644	37.490	-23.5	-26.5	0.6	0.7	
ZAKR	26.206	35.129	-17.3	-27.9	0.2	0.3	

Table C.3: Horizontal rates of campaign-type sites in Greece and southern Bulgaria. The GPS velocity solution was aligned to ITRF2005. The rates are relative to Eurasia (Euler pole: $\phi = 56.28^\circ\text{N}$, $\lambda = -96.12^\circ\text{E}$, $\omega = 0.266^\circ/\text{Myr}$). λ and φ denote the longitude and the latitude of the GPS sites. v_e and v_n denote the rates in the east and north components, respectively. s_{v_e} and s_{v_n} denote the corresponding scaled accuracies. The positions are indicated in $[\circ]$ and the rates and their accuracies in $[\text{mm}/\text{yr}]$. Remarks: (1) Offset after the 2003 Mw 6.2 Lefkada earthquake. (2) Data after the 2003 Mw 6.2 Lefkada earthquake omitted. (3) Data prior to the 2001 Mw 6.4 Skyros earthquake omitted. (4) Data prior to the year 2001 omitted (erroneous information related to excentric marker). (5) Data prior to the 1995 Ms 6.2 Aigion earthquake omitted. (6) Offset after the 2001 Mw 6.4 Skyros earthquake. (7) Rates of CHLE were not used for any analyses due to supposed monument instabilities. (8) Offset after the 2008 Mw 6.4 NW Peloponnesos earthquake. (9) Data prior to the 1997 Mw 6.6 Strofades and after the 2006 Zakynthos earthquake series omitted. (10) Site POLZ was operated as continuous site between 2005 and 2006. Additional data of the year 2010 was processed to derive a more accurate velocity. (11) Data after the 1997 Mw 6.6 Strofades earthquake omitted. (12) Data prior to the 1997 Mw 6.6 Strofades earthquake omitted.

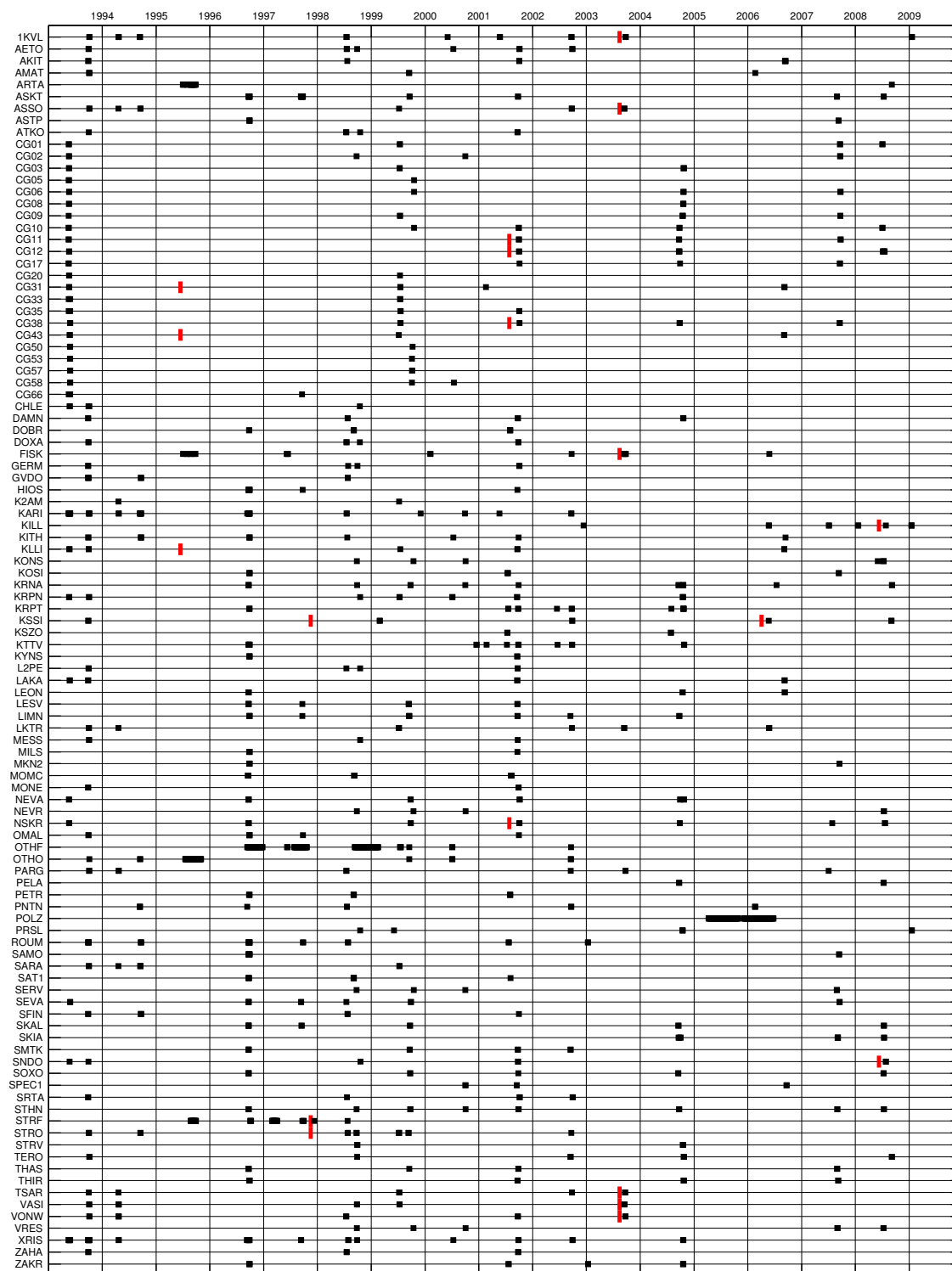


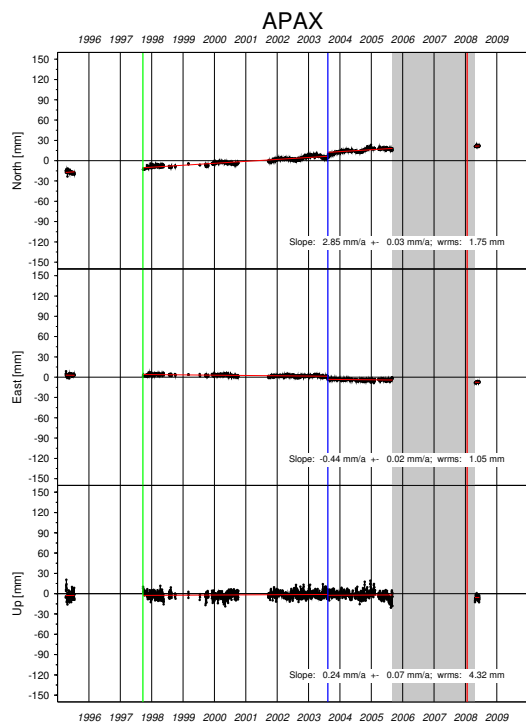
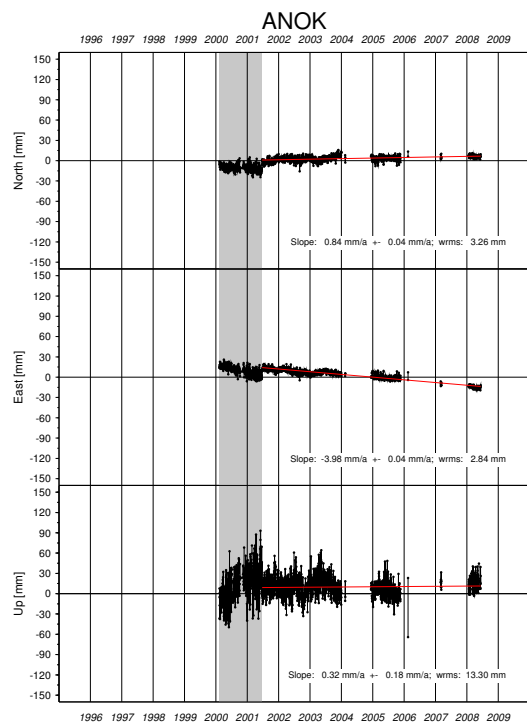
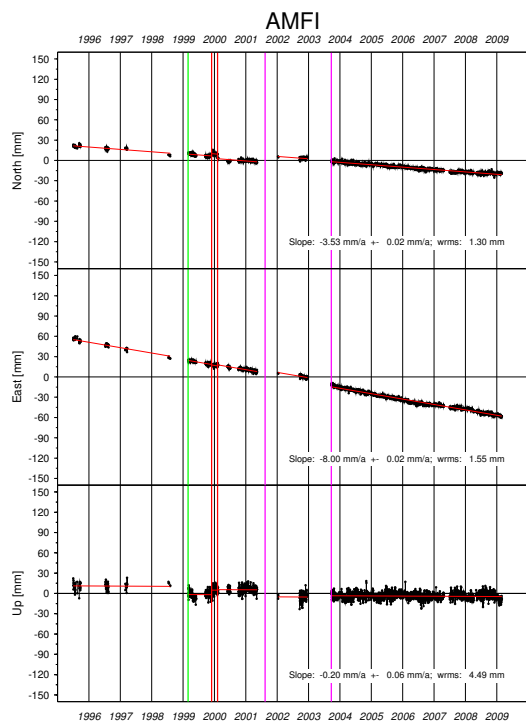
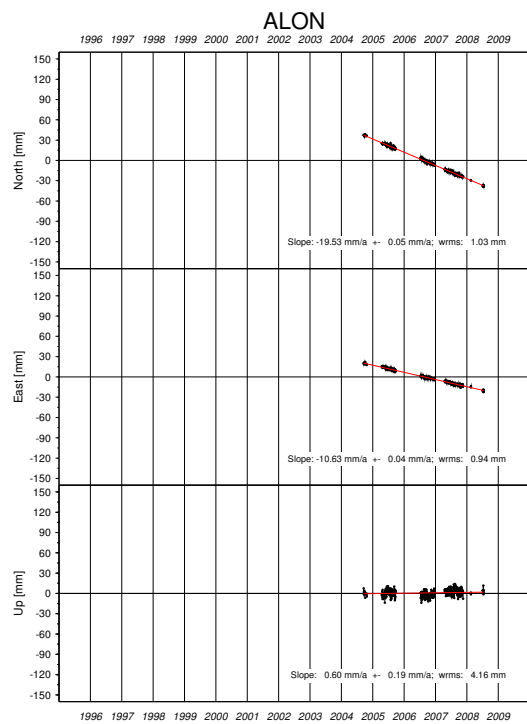
Figure C.1: Occupation history of campaign-type GPS sites. Black squares depict site occupations lasting one day or longer. Red lines denote earthquakes in close distance to the respective site (1995 Ms 6.2 Aigion, 1997 Mw 6.6 Strofades, 2001 Mw 6.4 Skyros, 2003 Mw 6.2 Lefkada, 2006 Zakynthos (Mw 5.0–5.7), 2008 Mw 6.4 NW Peloponnesos).

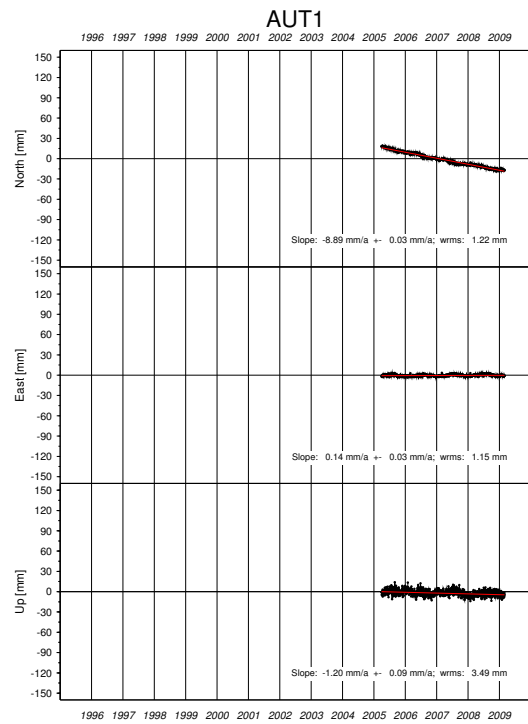
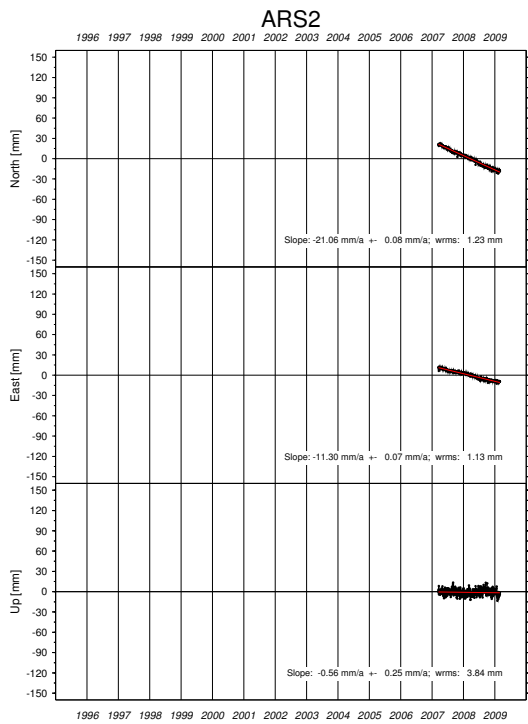
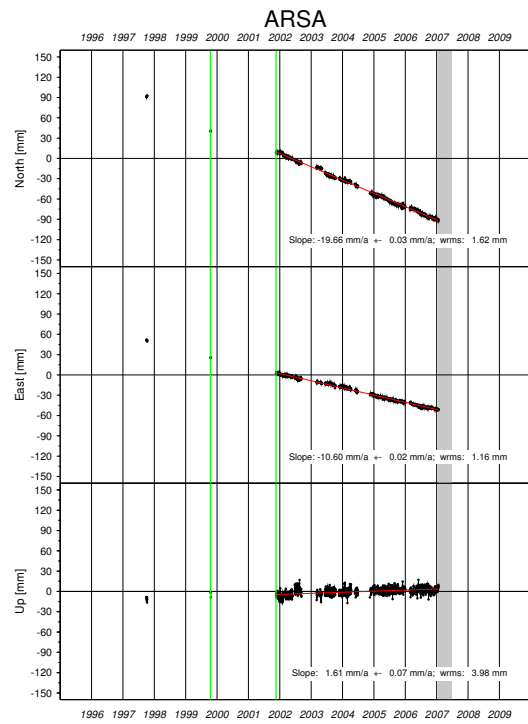
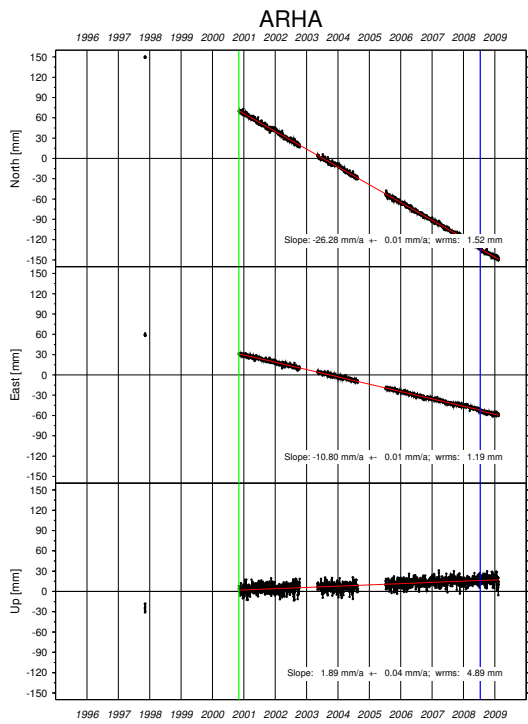
D Time series of continuous GPS sites in Greece

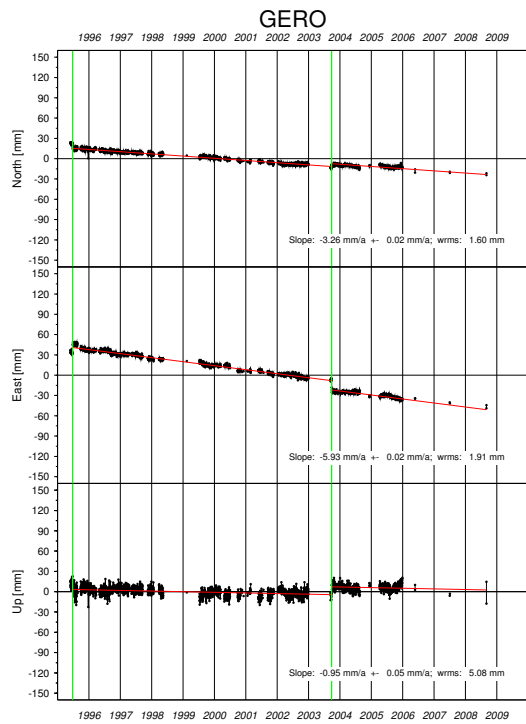
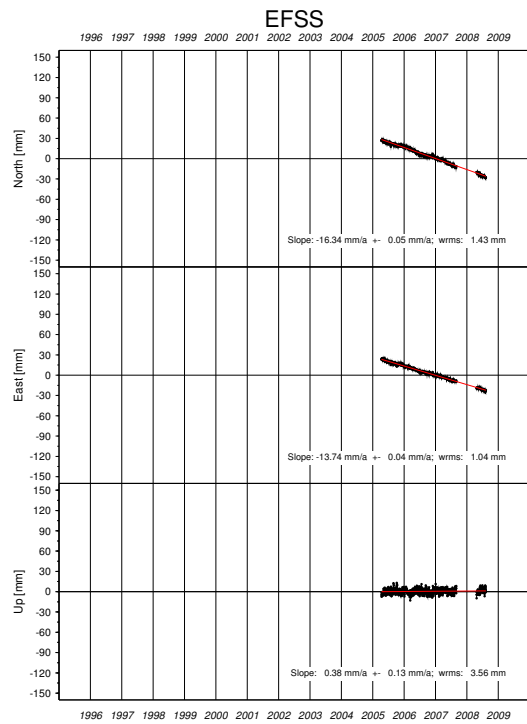
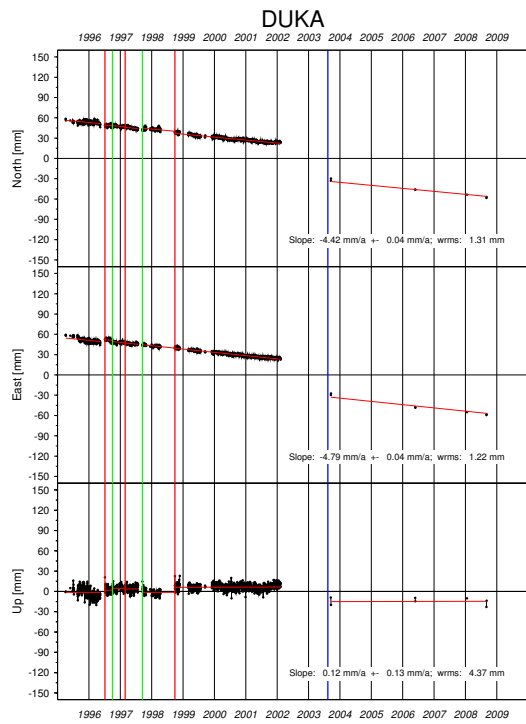
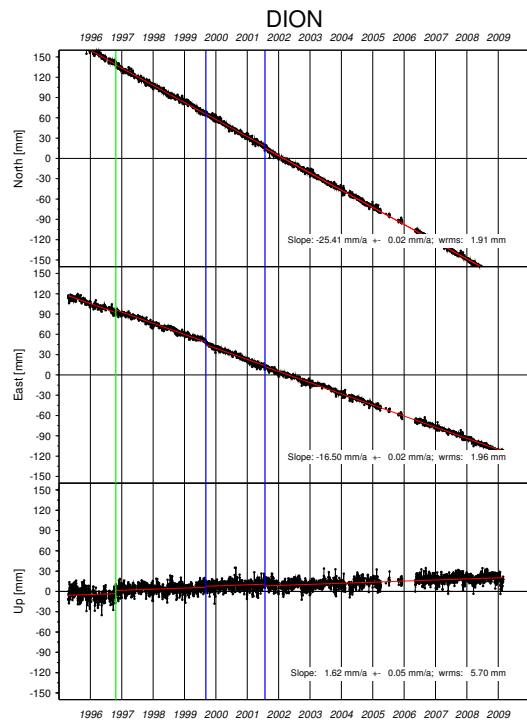
In this chapter improved position time series of CGPS sites located in Greece are shown. Position outliers were removed from the time series (chapters 3.4.3) and systematic signals affecting GPS position estimates on a regional scale were reduced (chapter 3.4.6). Motion indicated by the time series is relative to Eurasia (details concerning the pole of rotation are found in appendix B.1). Offsets modeled for the estimation of rates are depicted by vertical lines. The applied color scheme indicating the cause of the offset is explained in Table D.1. Time intervals in which derived position estimates were not used for the calculation of rates are shaded in gray. The dates of modeled offsets and exclusion periods are listed in appendix A.2. The rates relative to Eurasia, the corresponding unscaled formal errors and the coordinate precision derived by Eq. (C.1) are indicated for each time series.

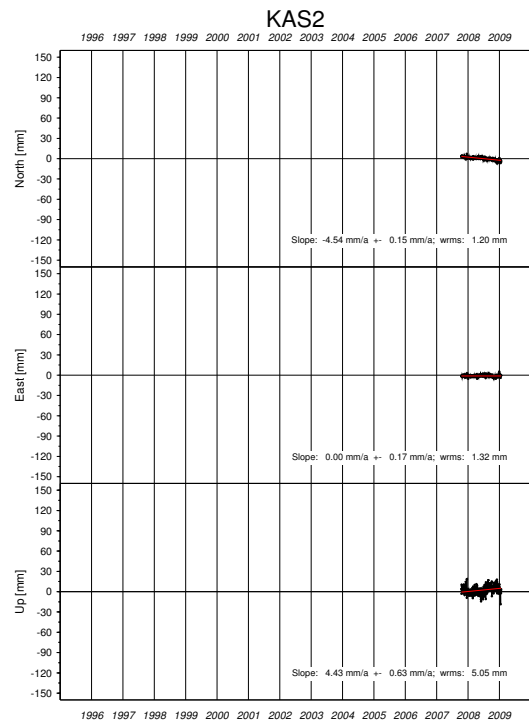
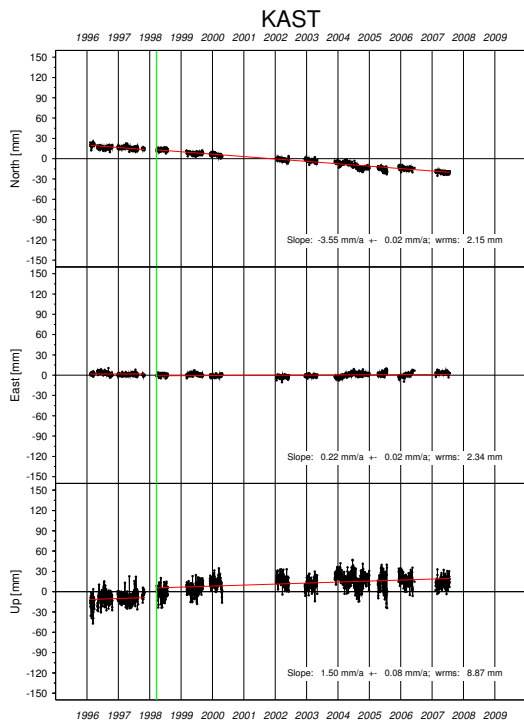
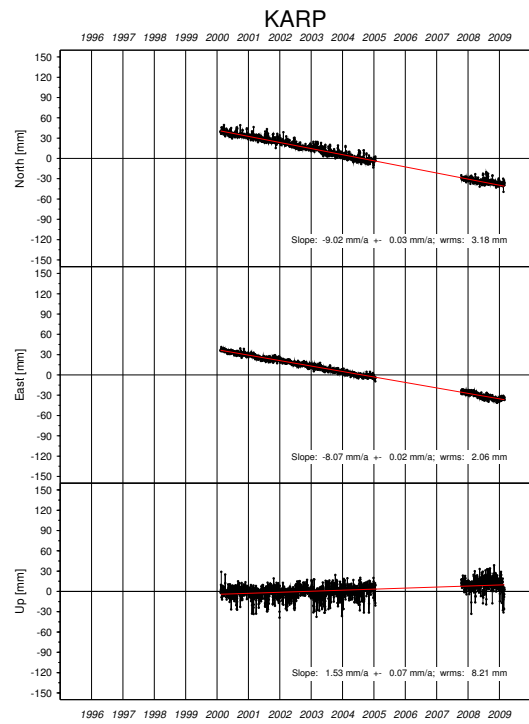
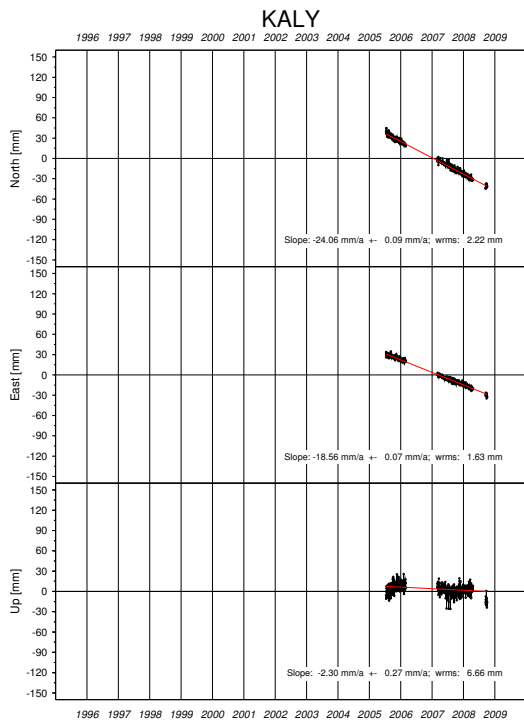
Event	Code	Color
Earthquake	1	blue
Antenna change	2	red
Receiver change or firmware upgrade	3	orange
Receiver and antenna change	4	green
Offset with unknown cause	5	violet

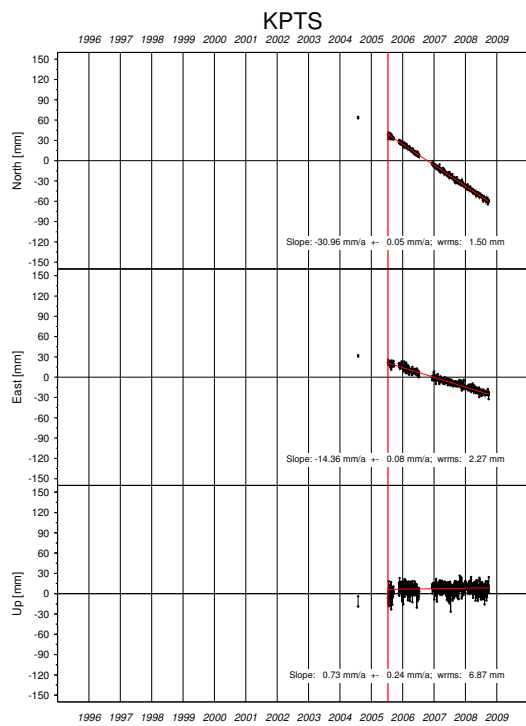
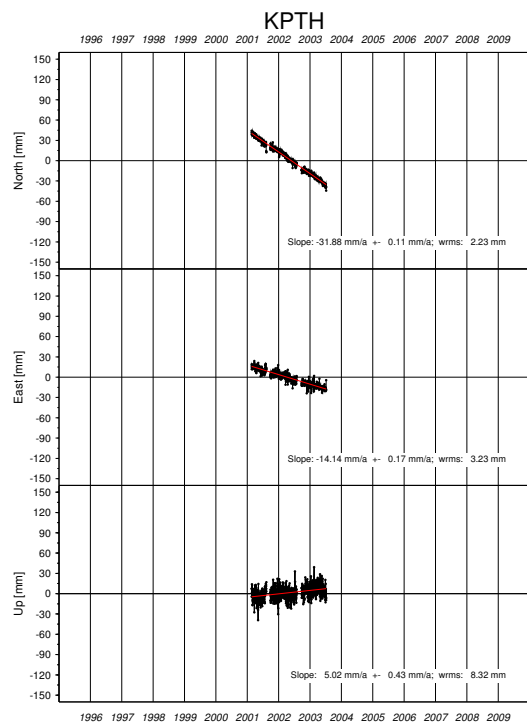
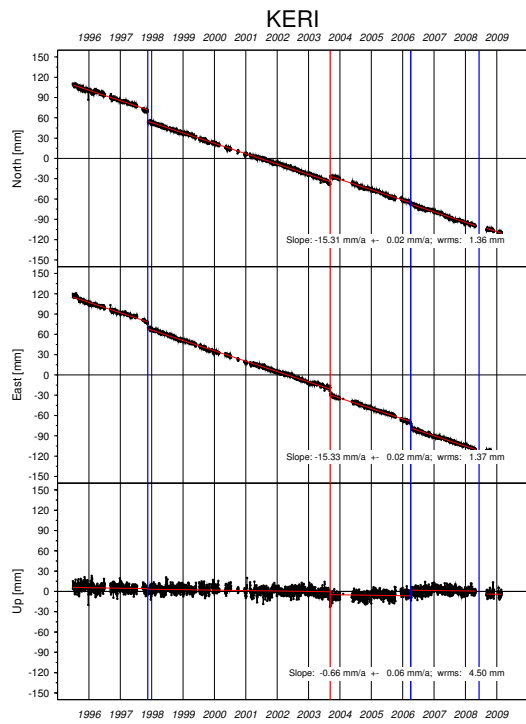
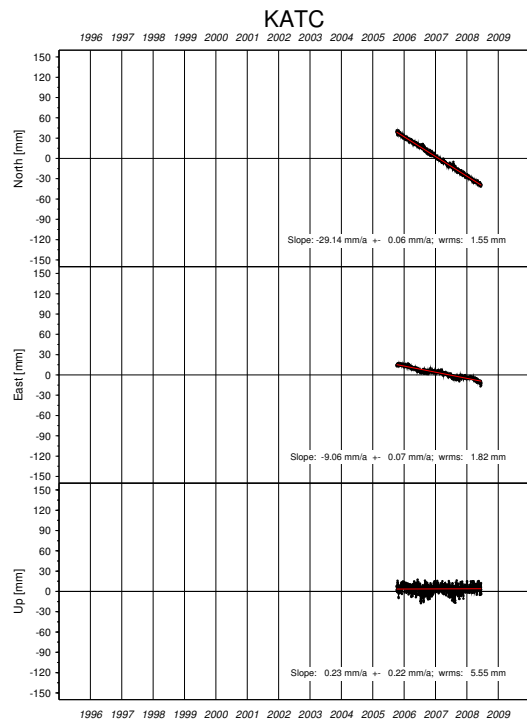
Table D.1: Applied color scheme indicating the cause of the offsets which were introduced in the time series.

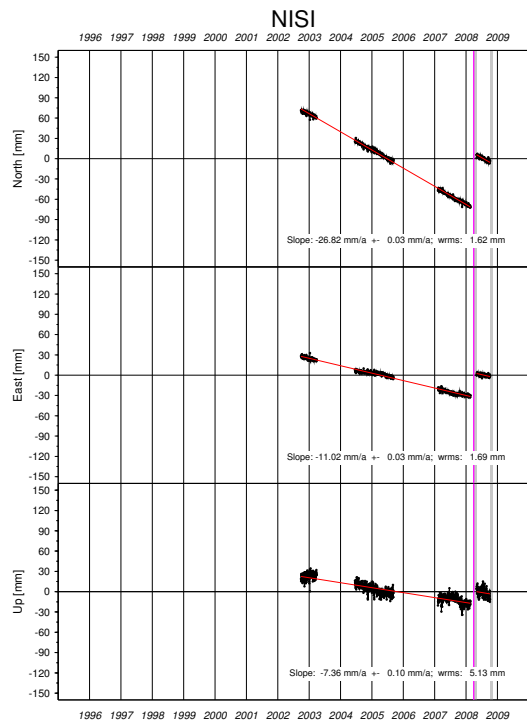
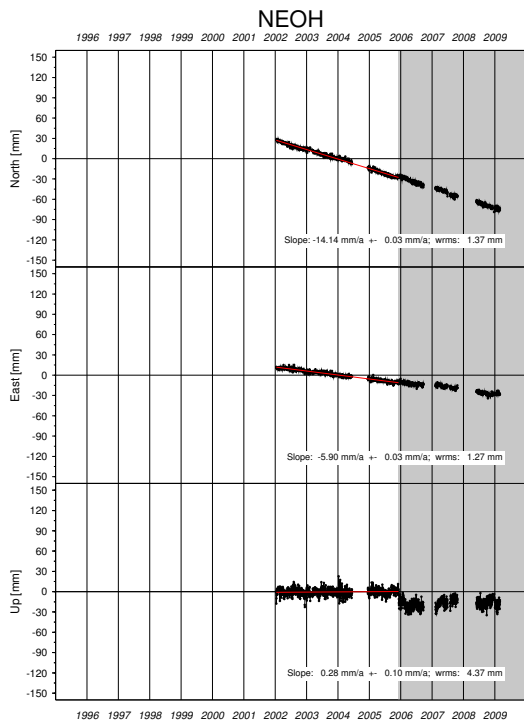
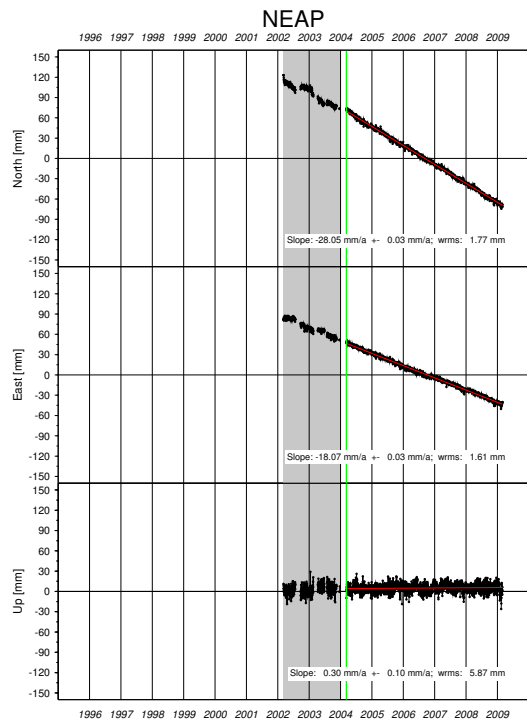
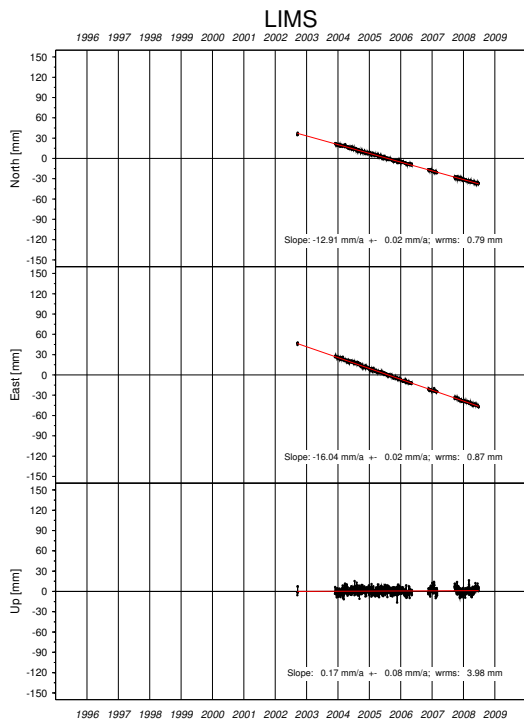


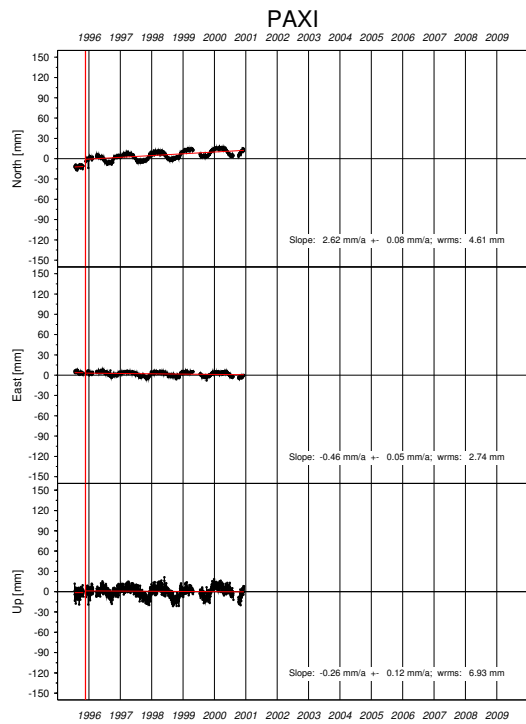
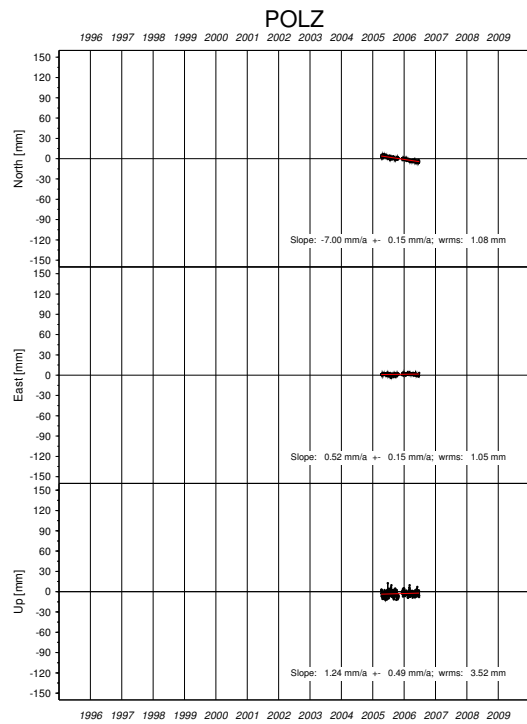
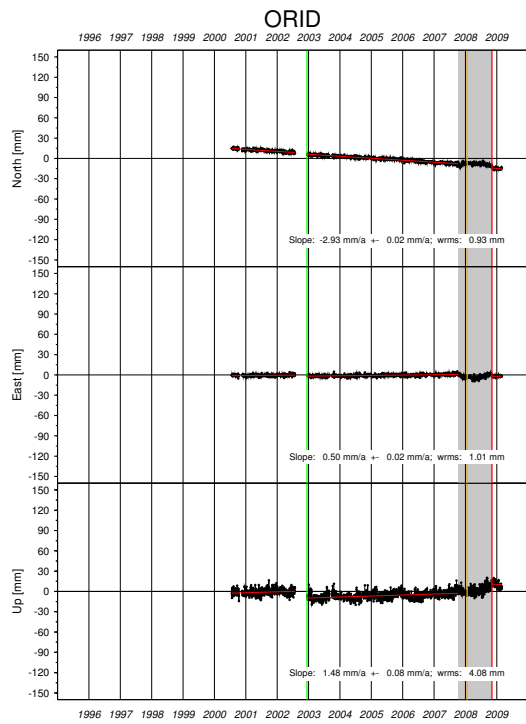
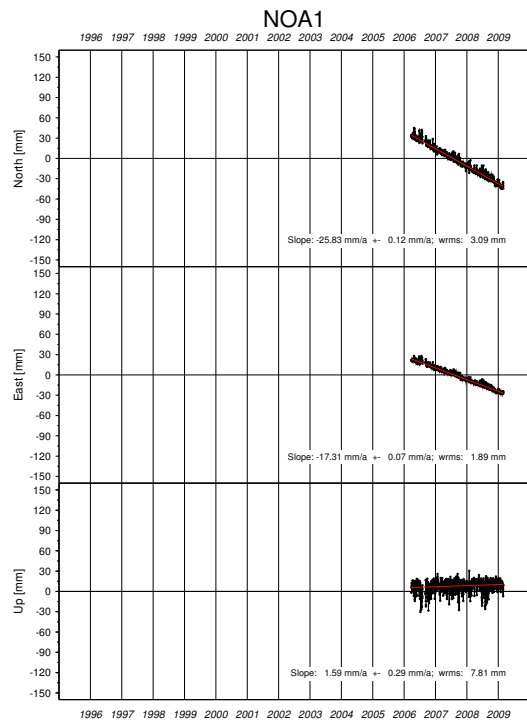


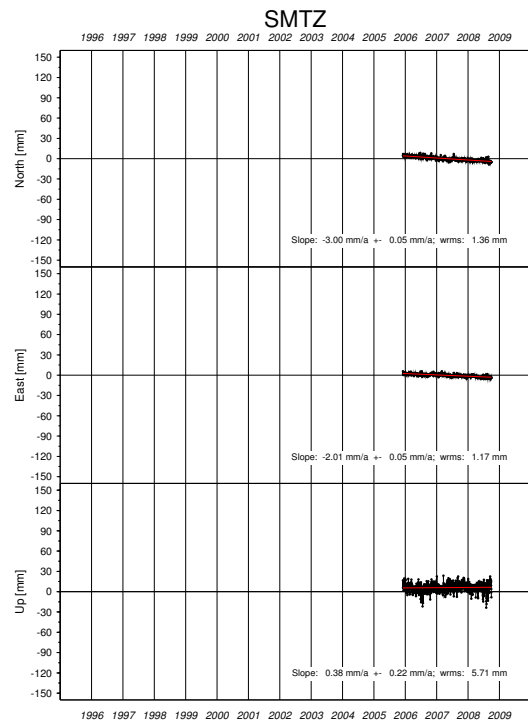
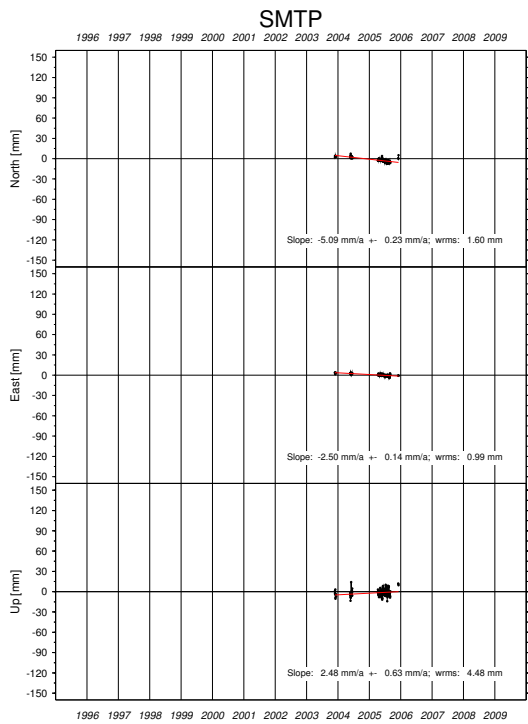
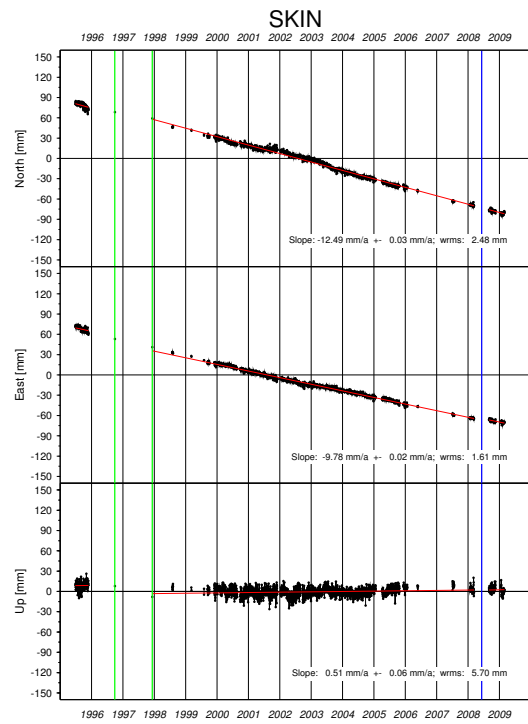
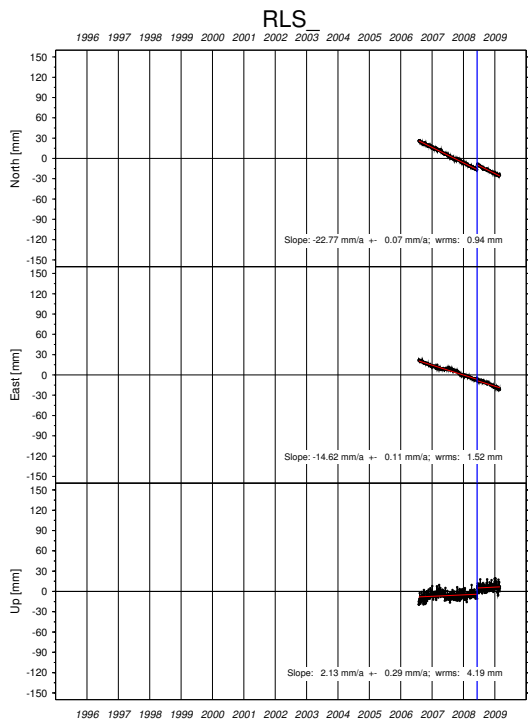


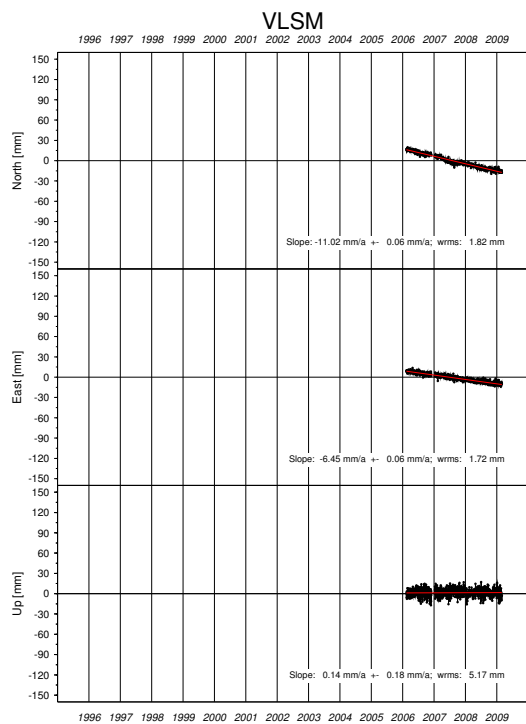
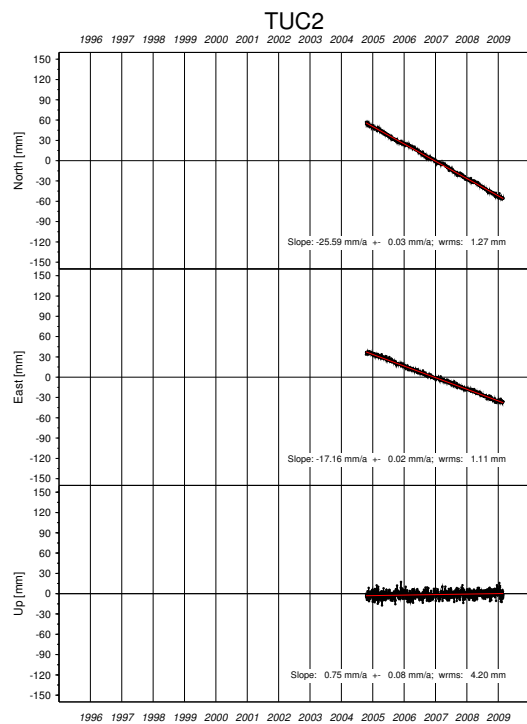
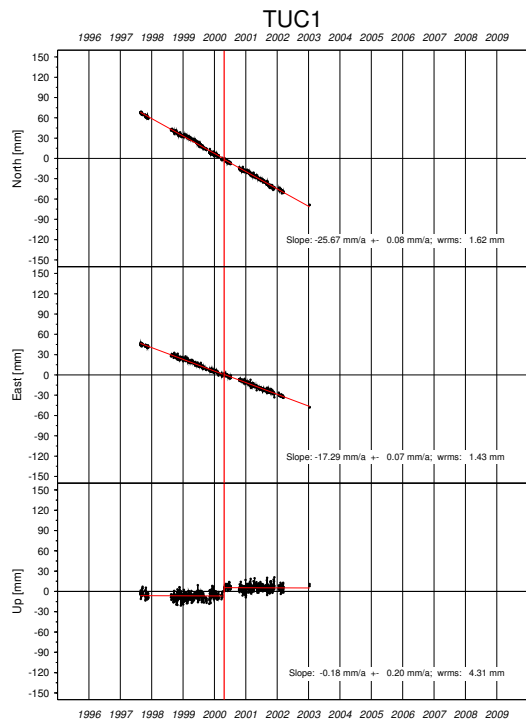
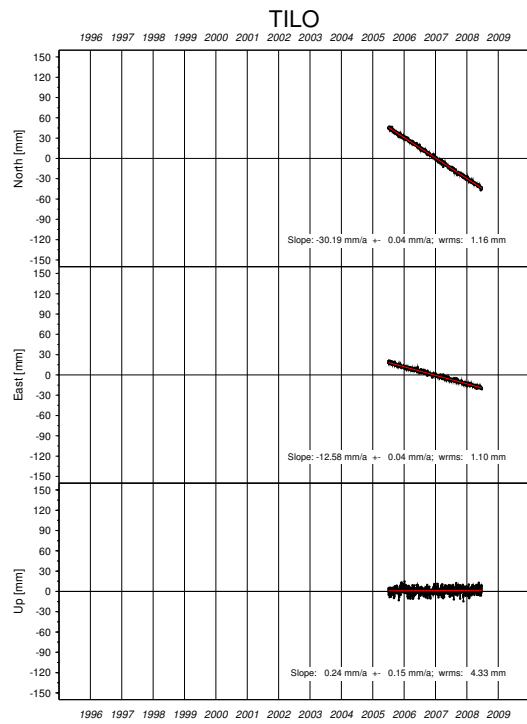












E Residual time series of campaign-type GPS sites in Greece

In this chapter coordinate residuals with respect to the derived velocity are shown for each campaign-type site (Figures E.2 to E.5). Rates are estimated by using the Bernese GPS software subprogram ADDNEQ2. The number of residuals is larger than the number of site occupations (Fig. C.1) since the GPS data was processed in daily sessions. Modeled offsets are listed in Table A.2 and depicted in the corresponding figures. Site velocities and additional comments on particular campaign-type sites are listed in Table C.3. Histograms of the coordinate residuals in the north, east and up components, respectively, are depicted in Figure E.1.

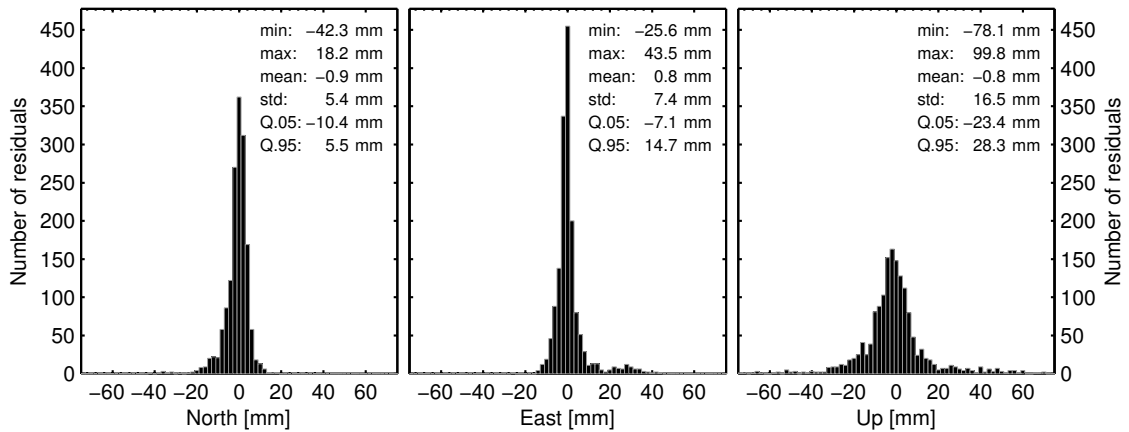


Figure E.1: Daily coordinate residuals of campaign-type sites with respect to the velocity derived by using the Bernese GPS software subprogram ADDNEQ2. The statistic is based on 1573 residuals in each coordinate component. $Q.05$ and $Q.95$ denote the 5th and 95th percentiles, respectively.

Figure E.2: (Figures on the next pages) Coordinate residuals of campaign-type GPS sites with respect to a linear motion estimated by using the Bernese GPS software subprogram ADDNEQ2. Black vertical lines depict earthquakes which occurred close to the respective site. Observations at site CG17 prior to the date depicted by dashed black lines refer to an excentric marker. They were omitted.

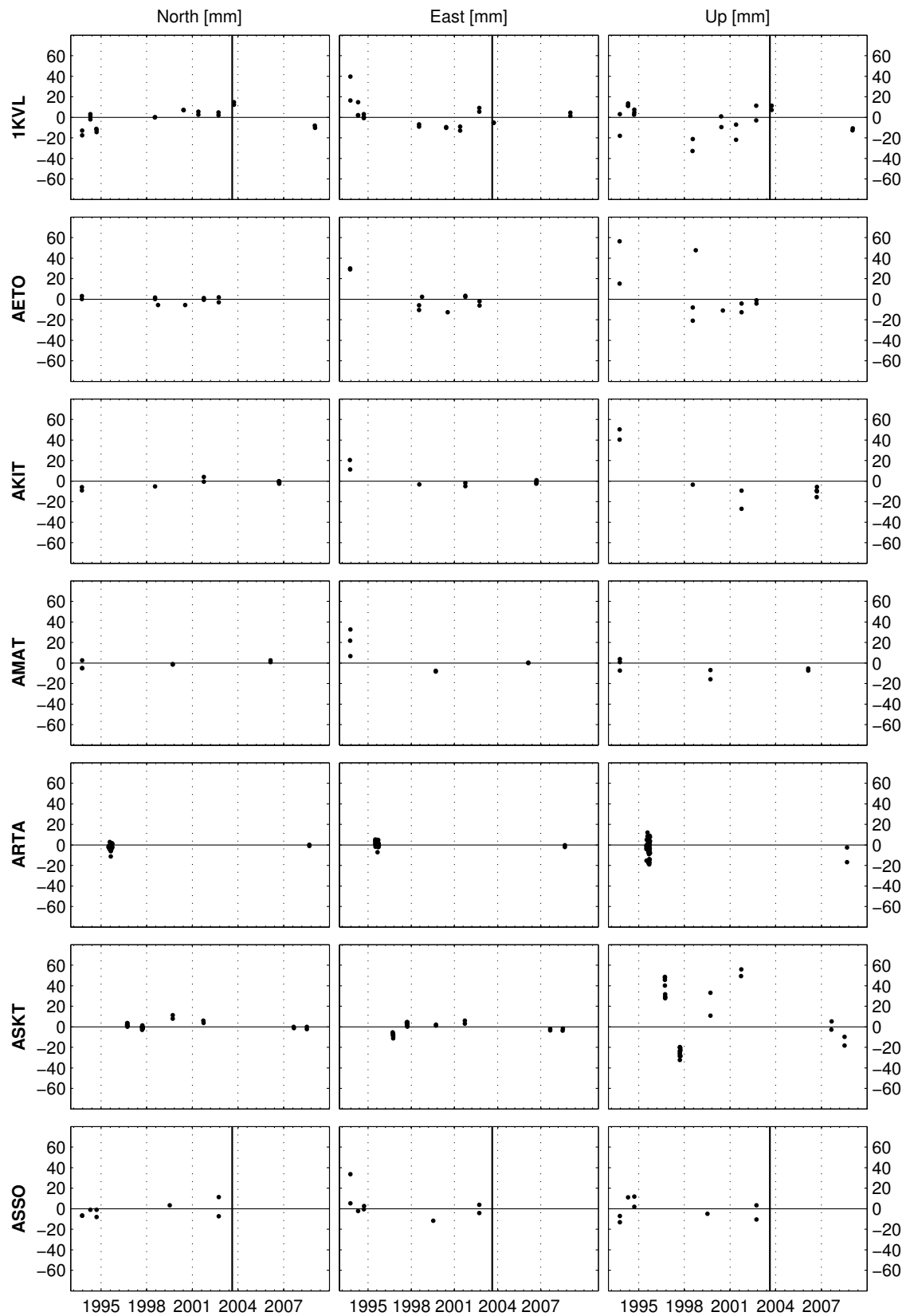


Figure E.2: (Continued)

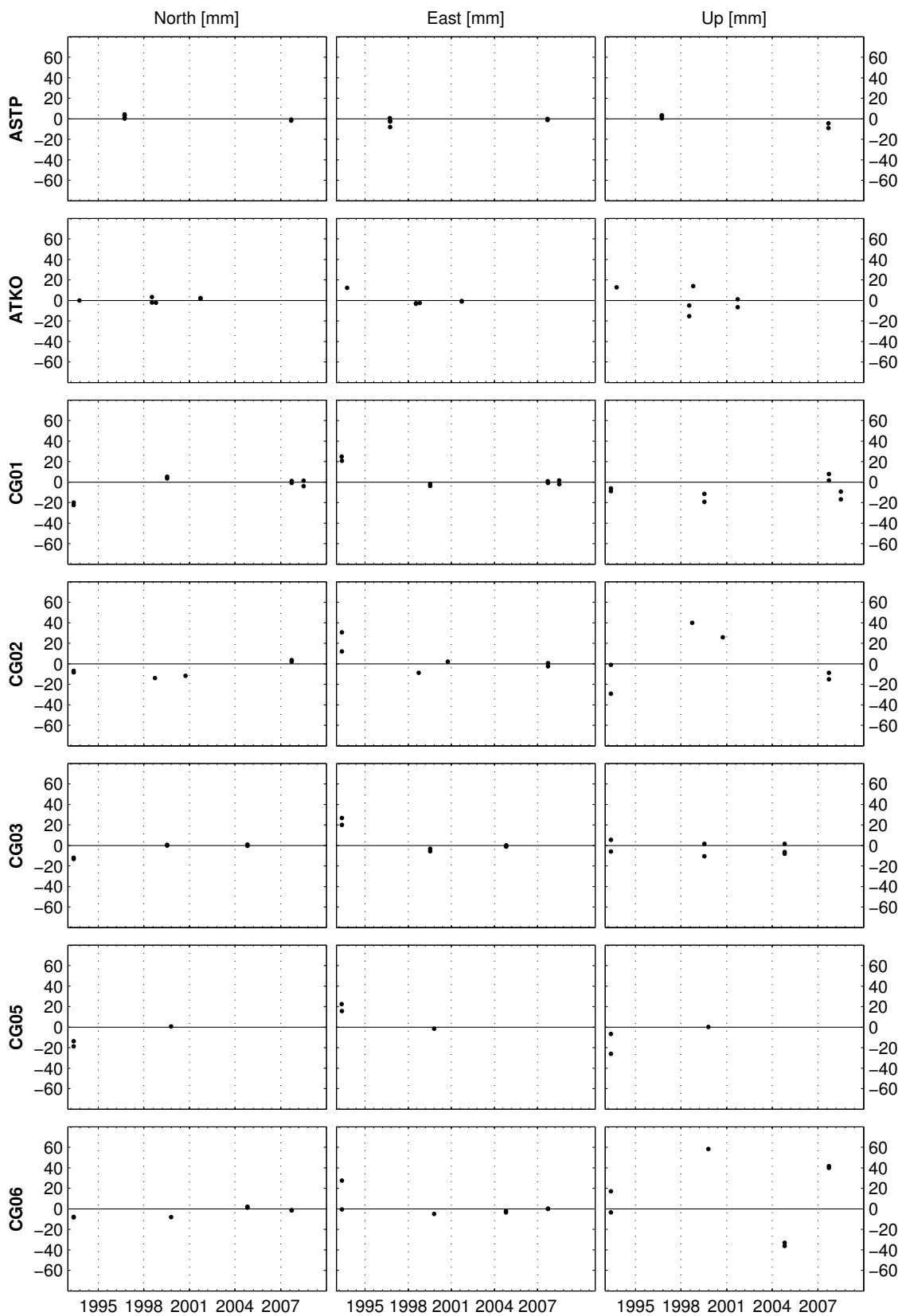


Figure E.2: (Continued)

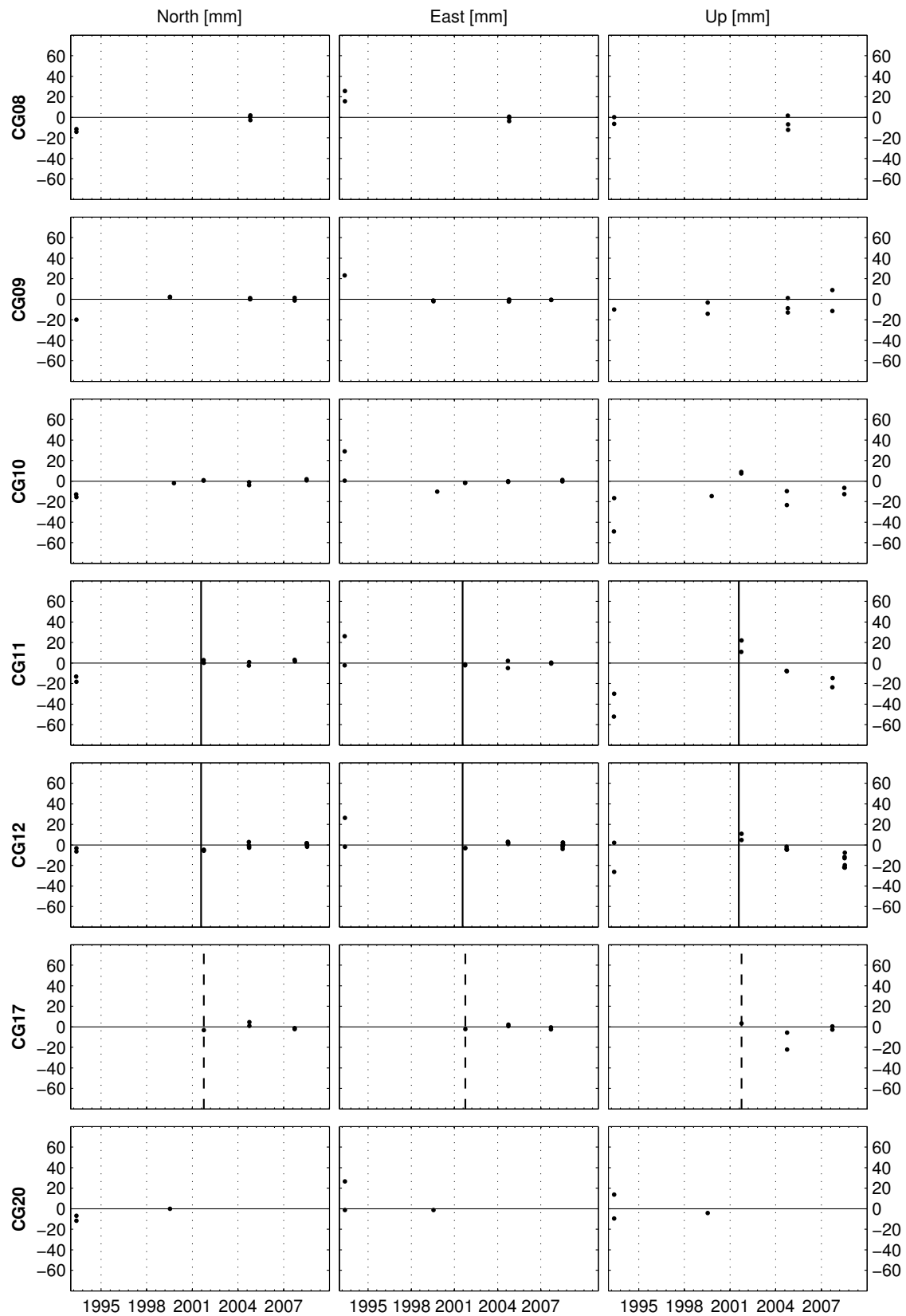


Figure E.2: (Continued)

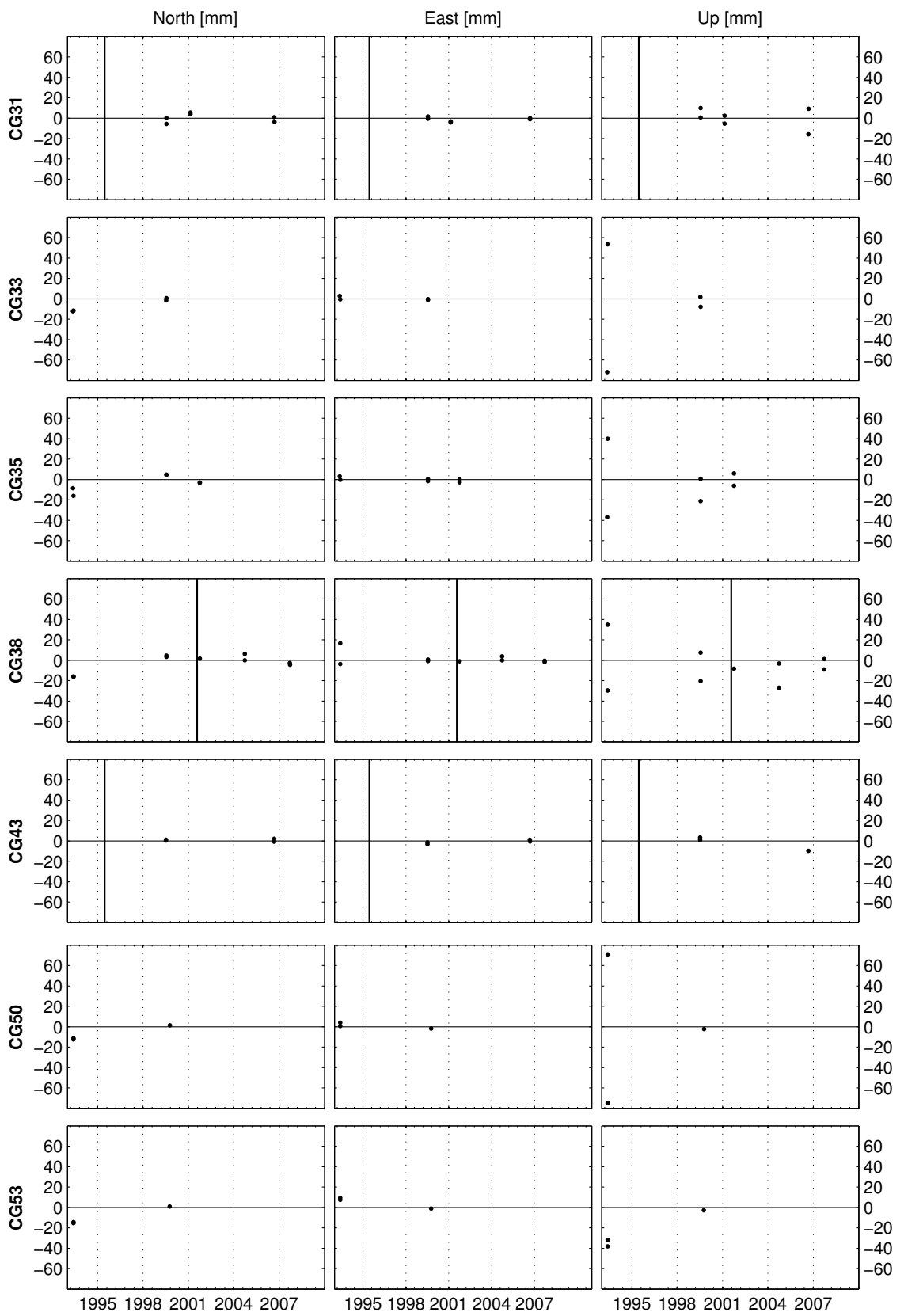


Figure E.2: (Continued)

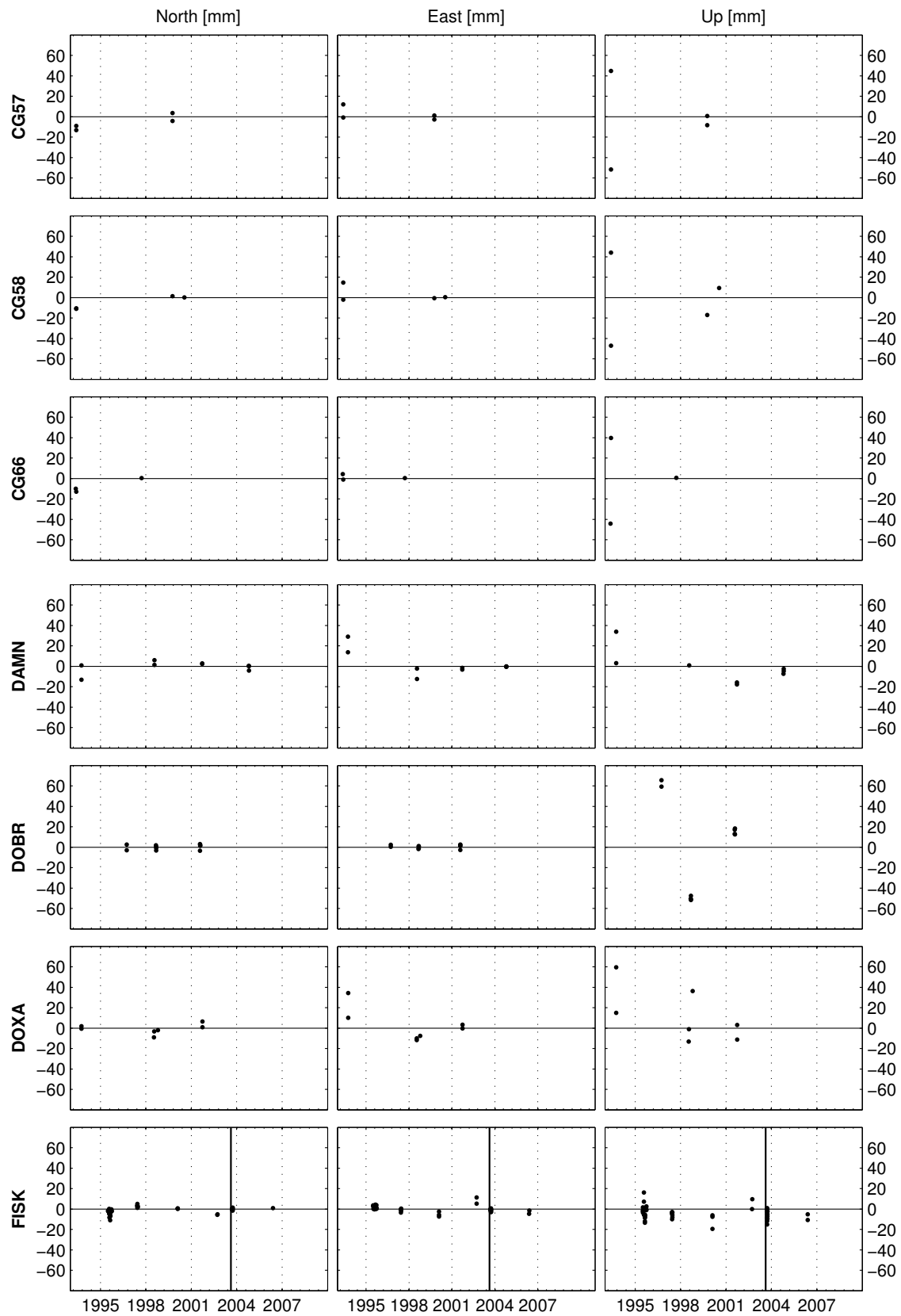


Figure E.2: (Continued)

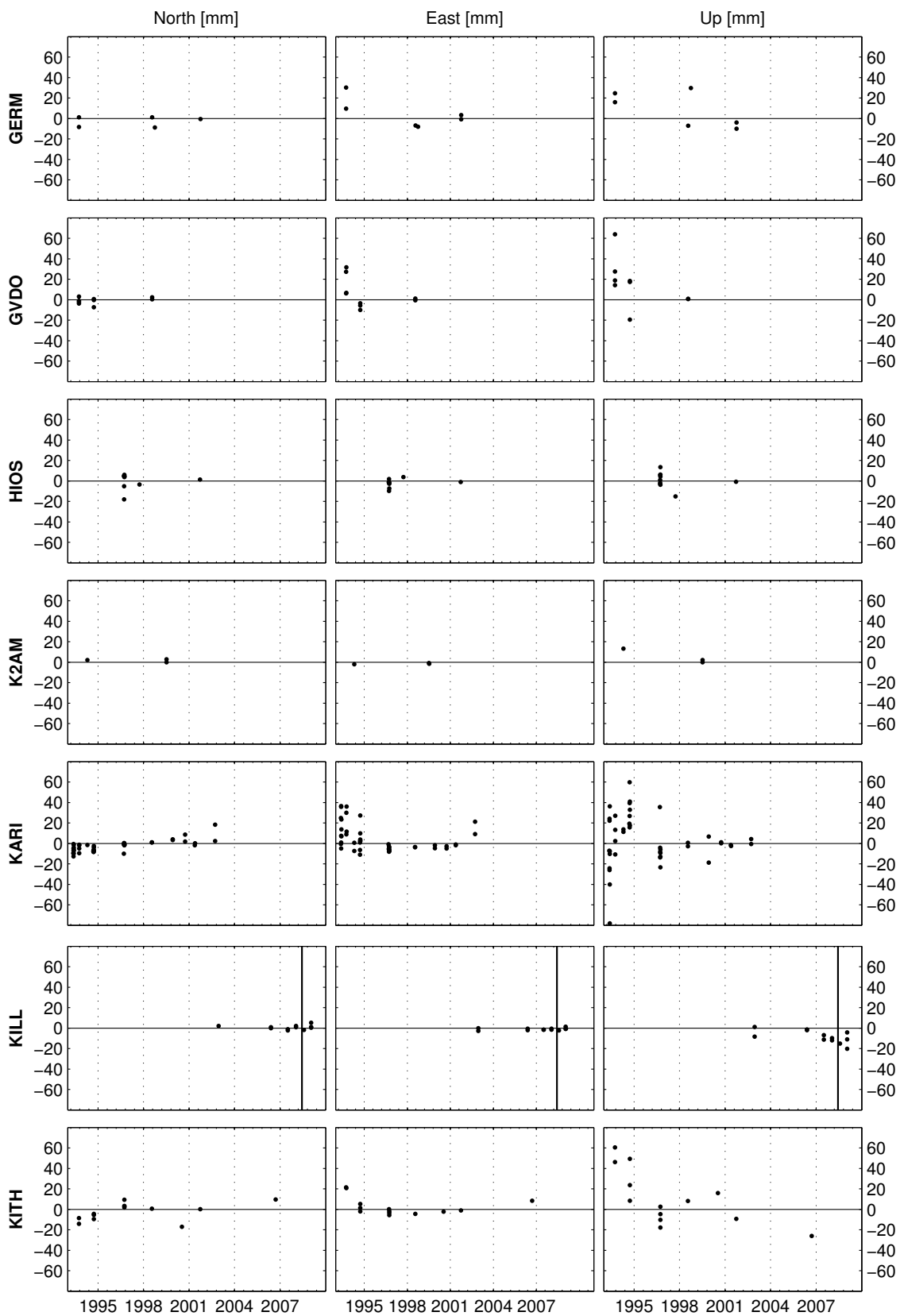


Figure E.2: (Continued)

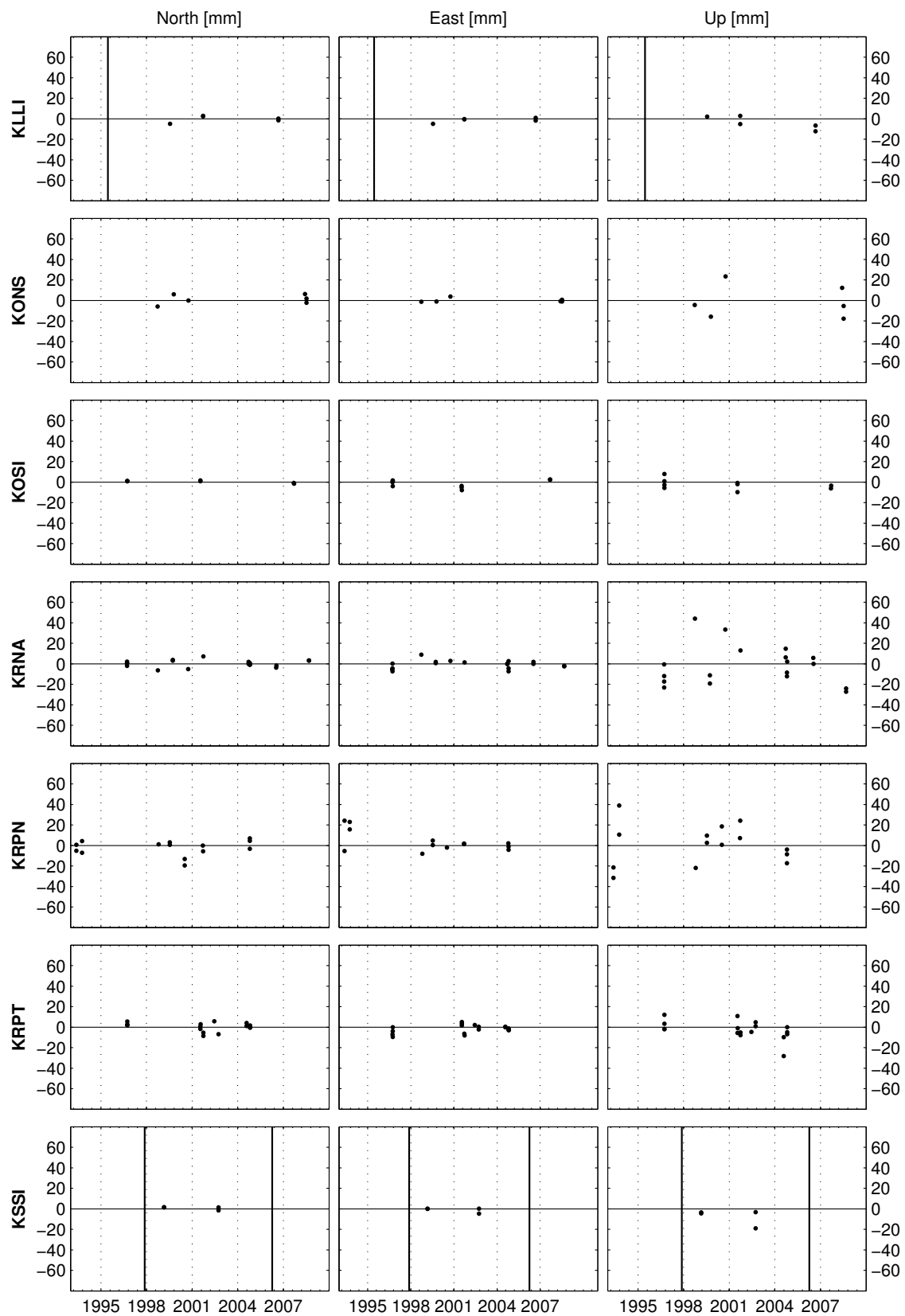


Figure E.2: (Continued)

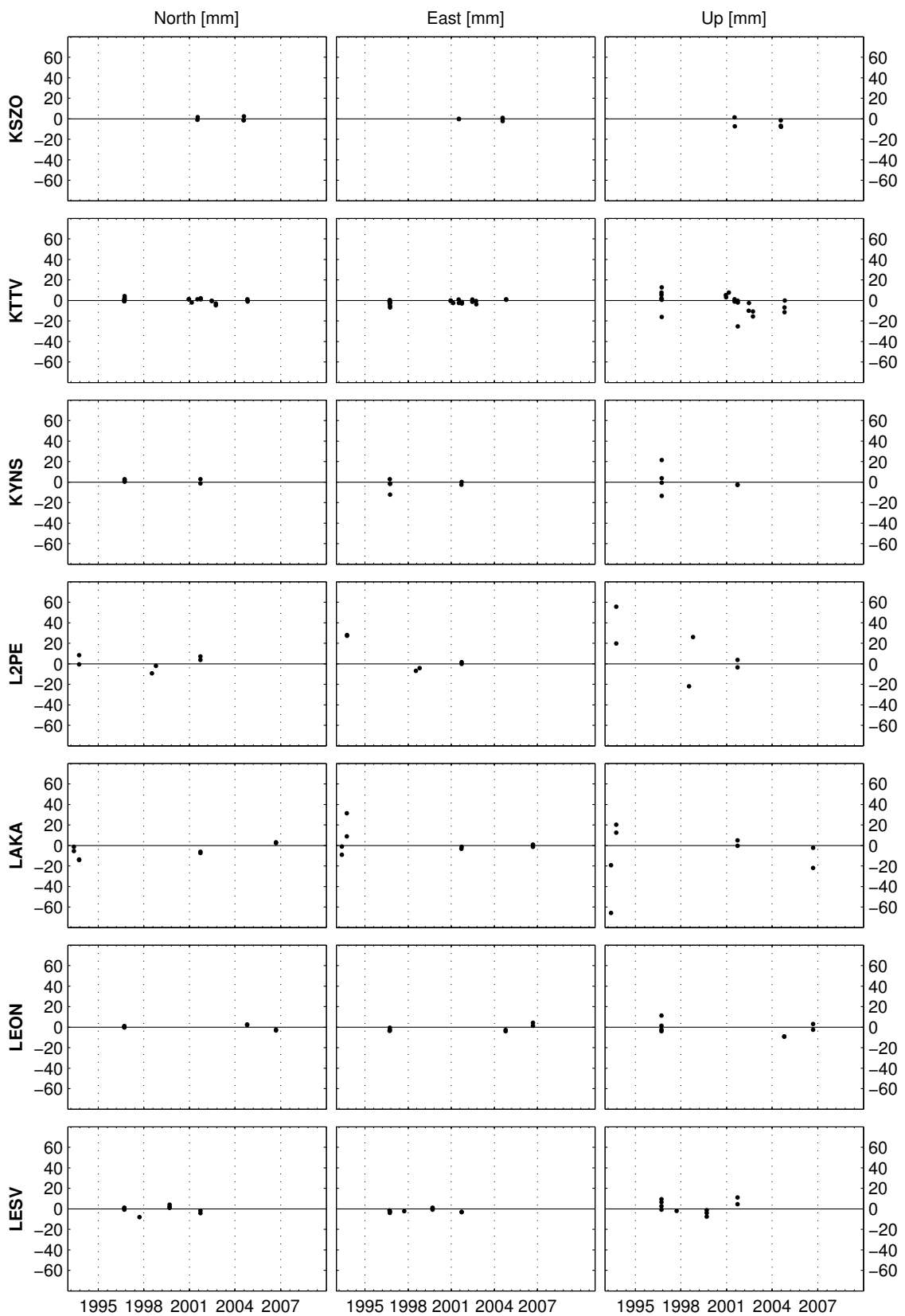


Figure E.2: (Continued)

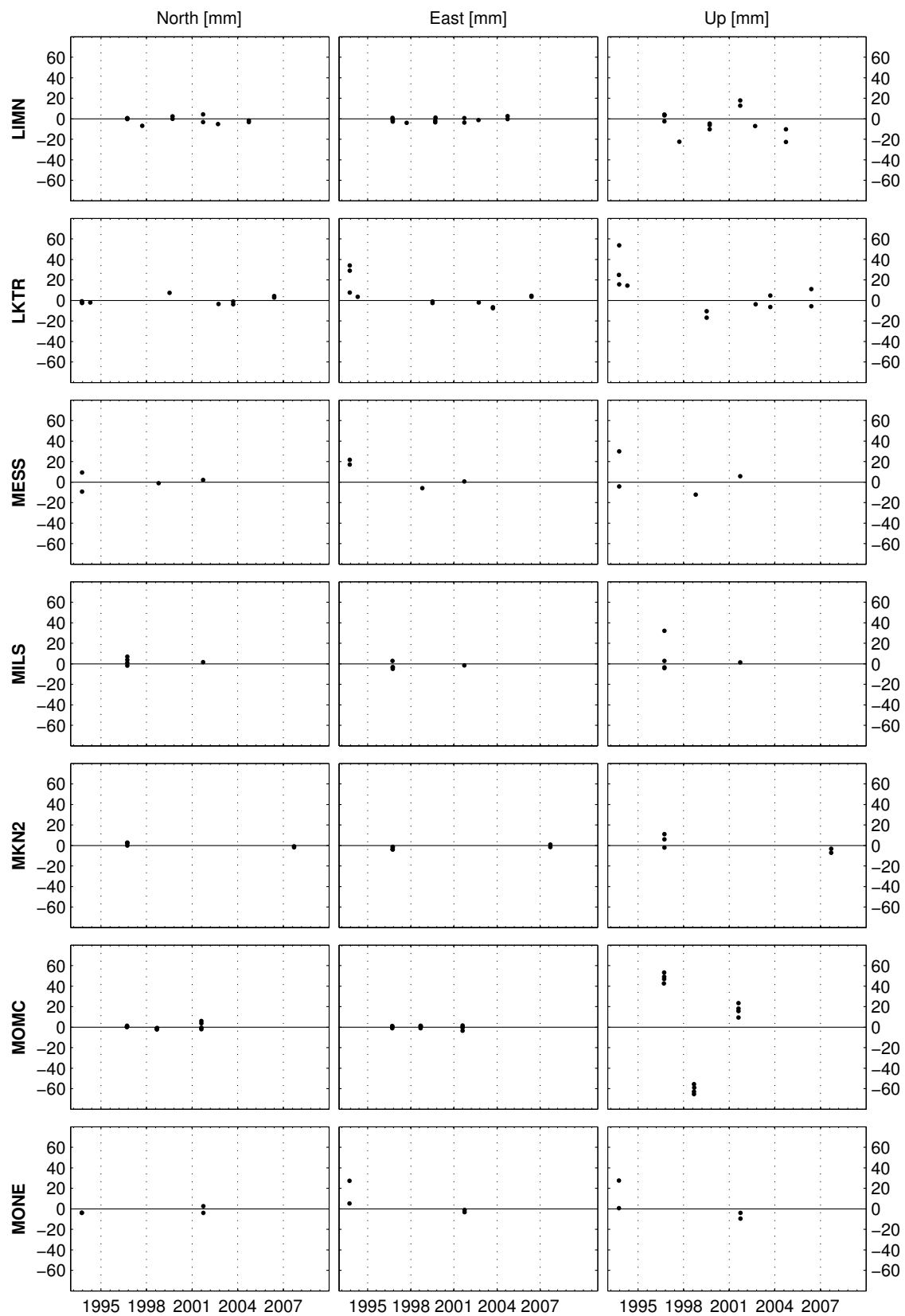


Figure E.2: (Continued)

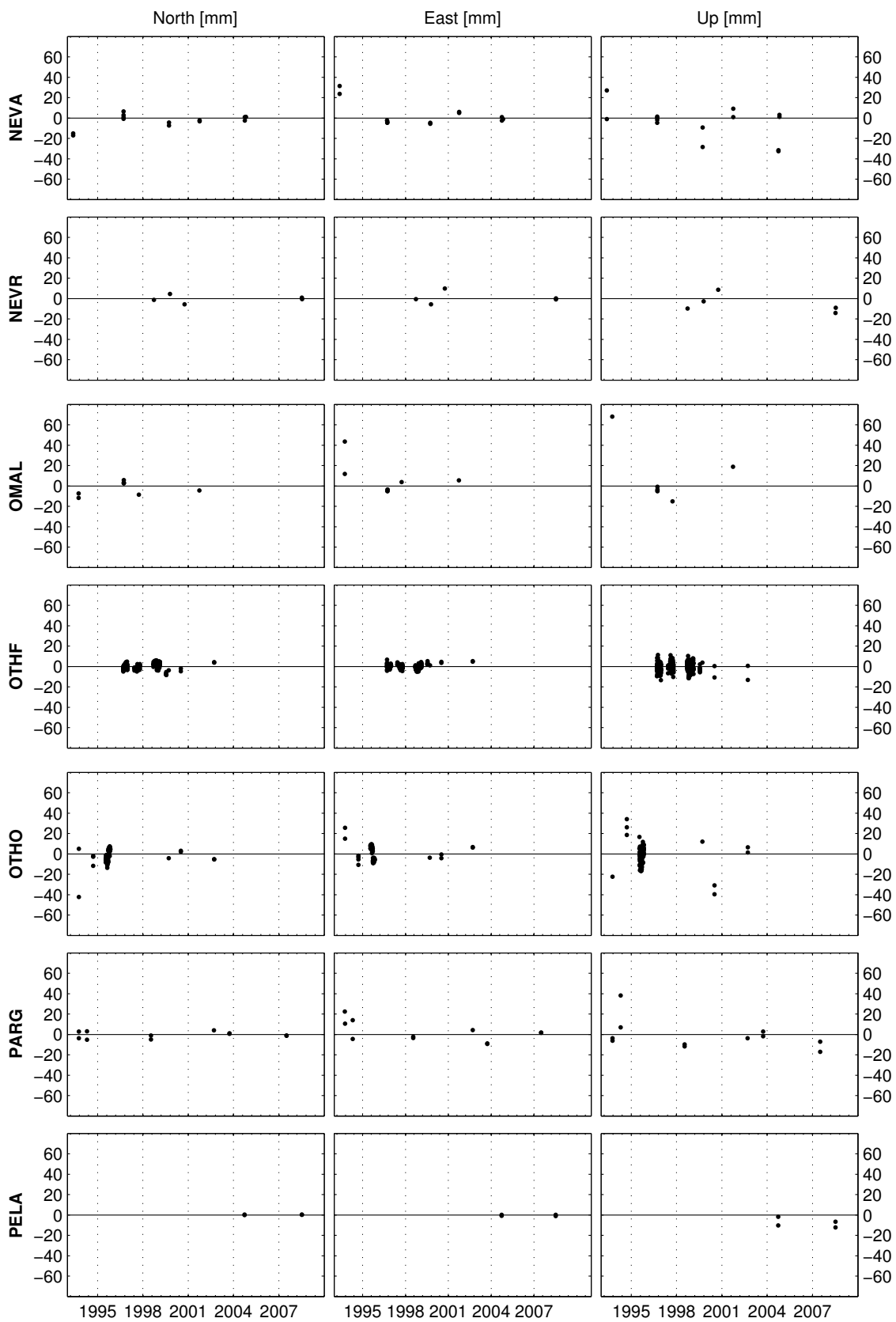


Figure E.2: (Continued)

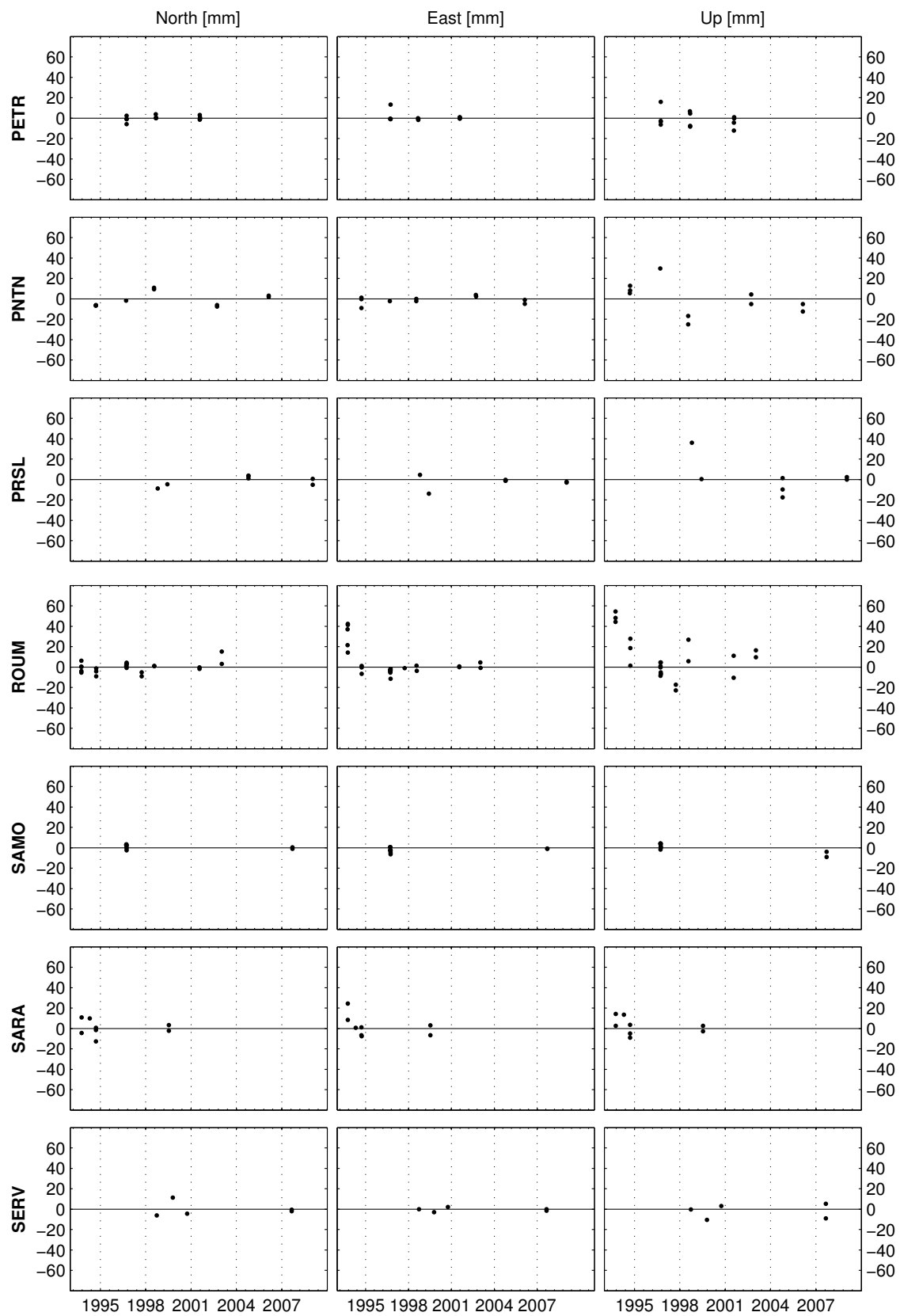


Figure E.2: (Continued)

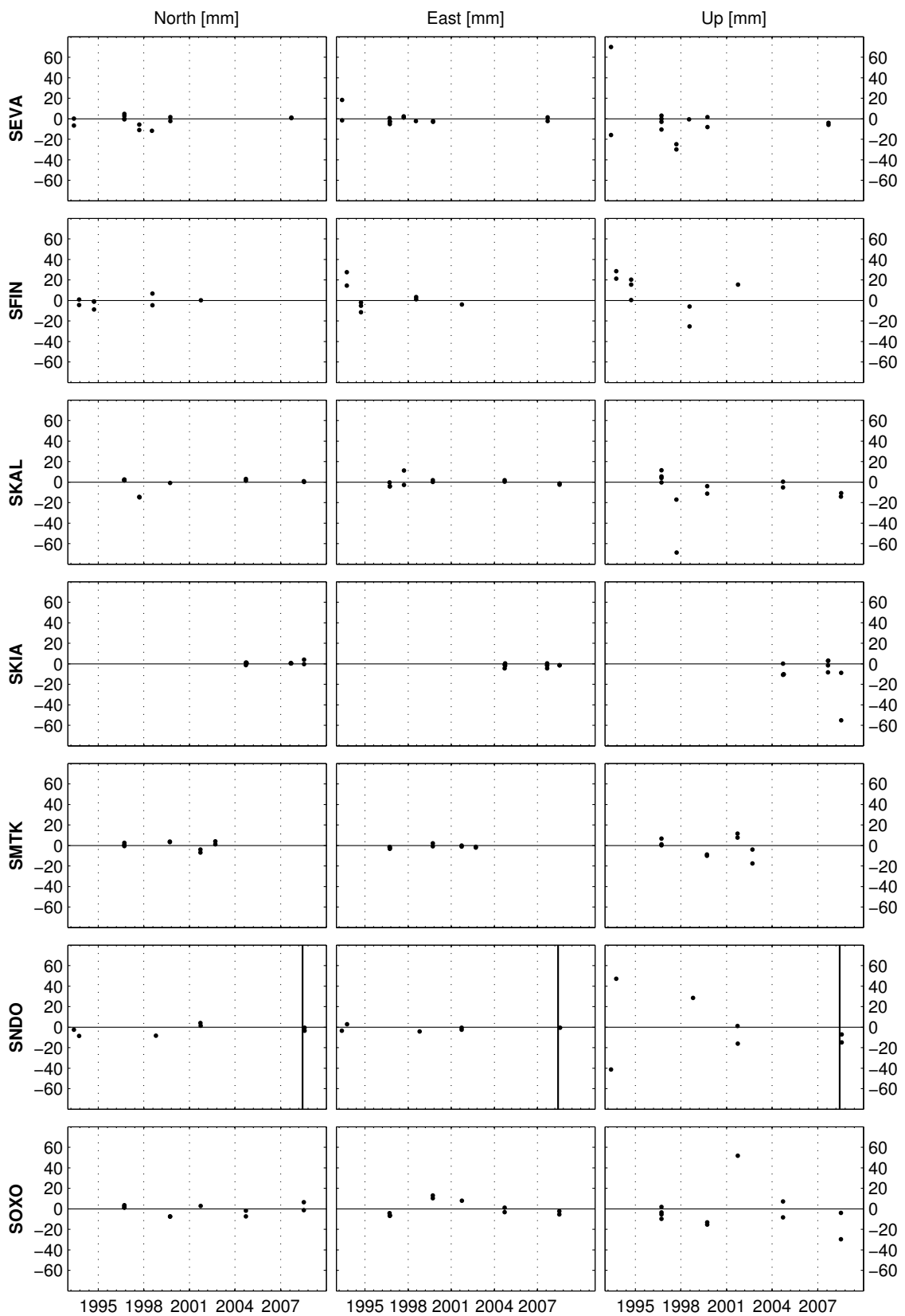


Figure E.2: (Continued)

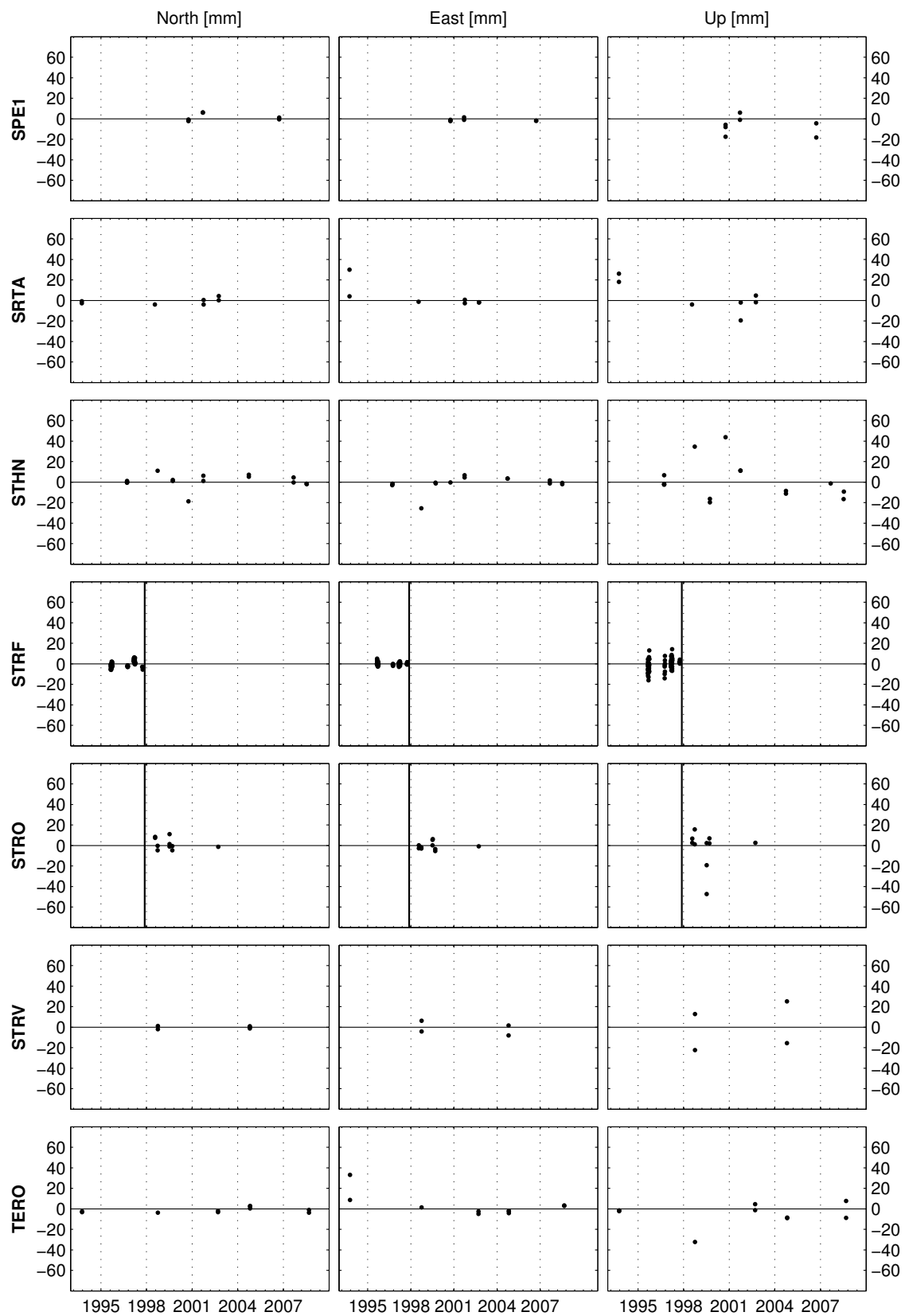


Figure E.2: (Continued)

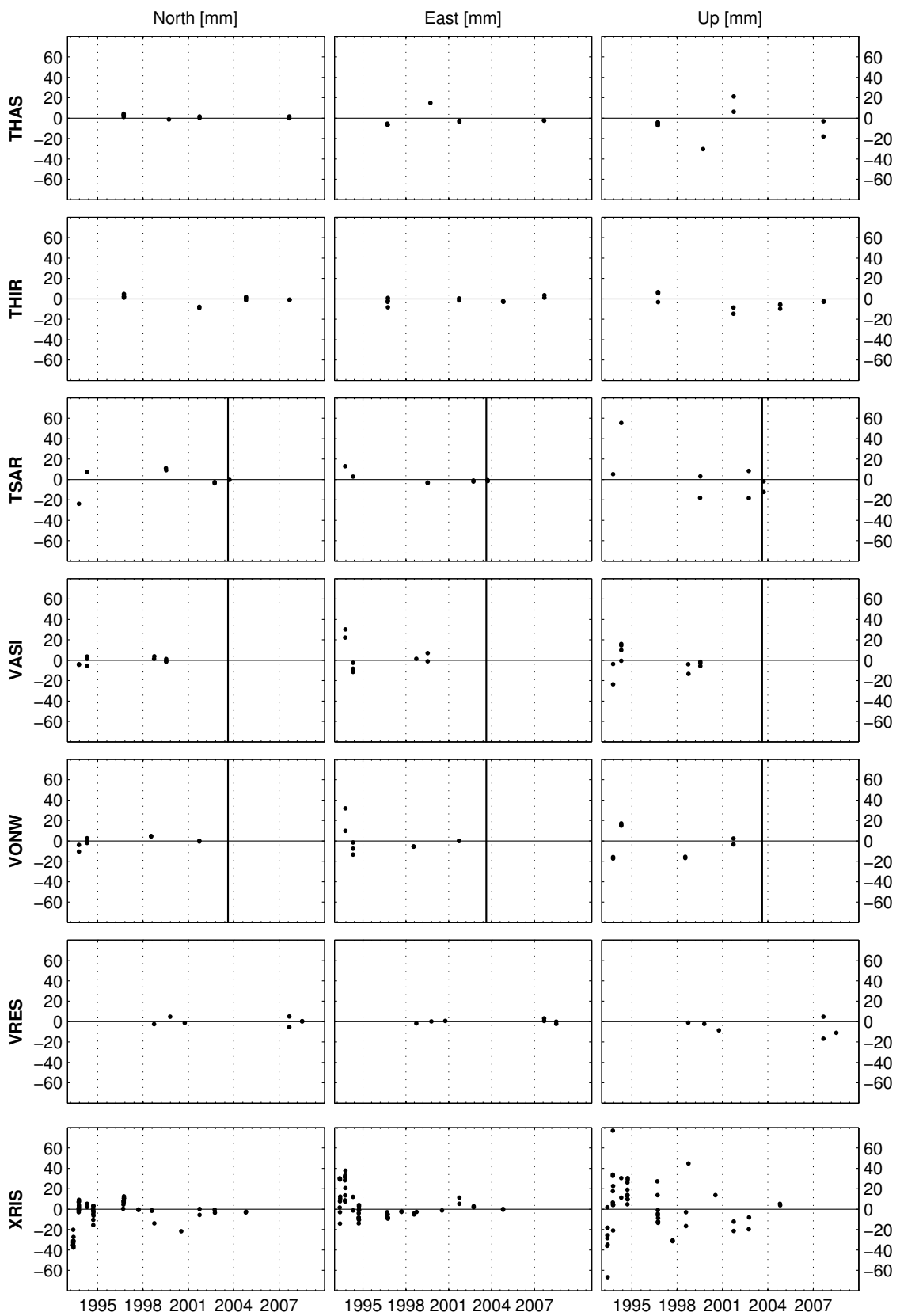


Figure E.2: (Continued)

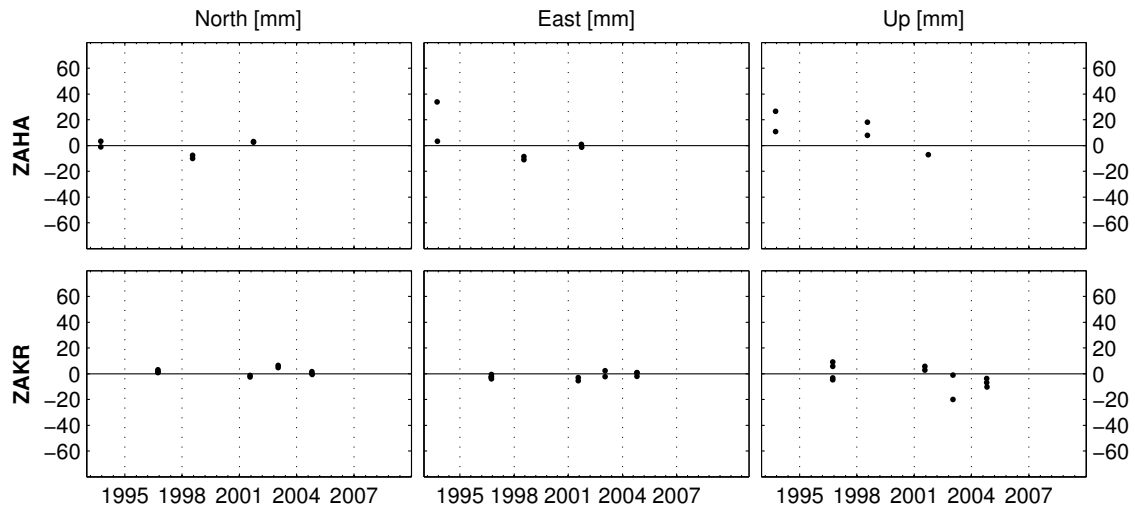


Figure E.2: (Continued)

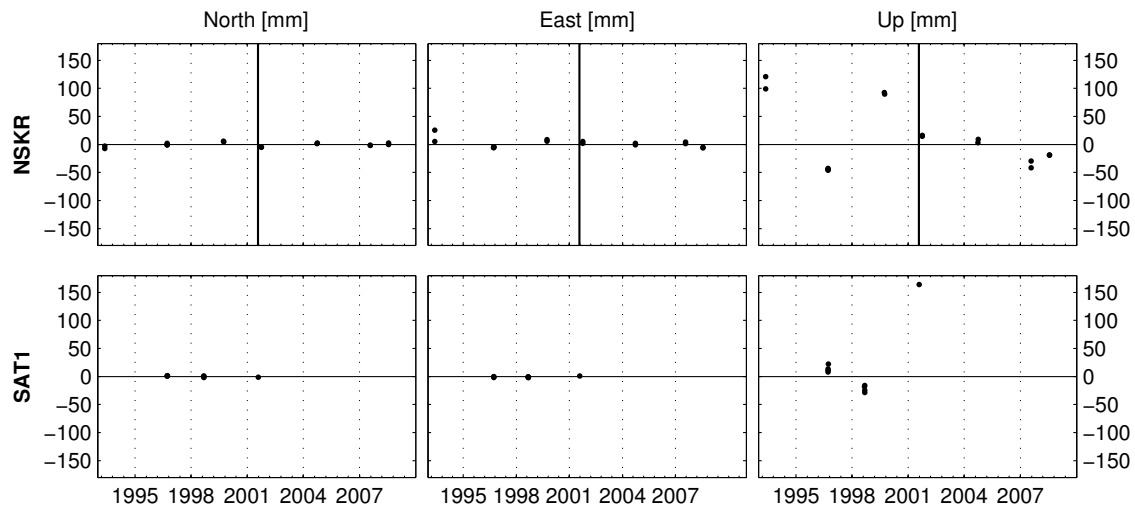


Figure E.3: Coordinate residuals of campaign-type sites NSKR and SAT1 with respect to a linear motion estimated by using the Bernese GPS software subprogram ADDNEQ2. Continuation of Fig. E.2. Note the different scale. The vertical black lines depict the 2001 Mw 6.4 Skyros earthquake.

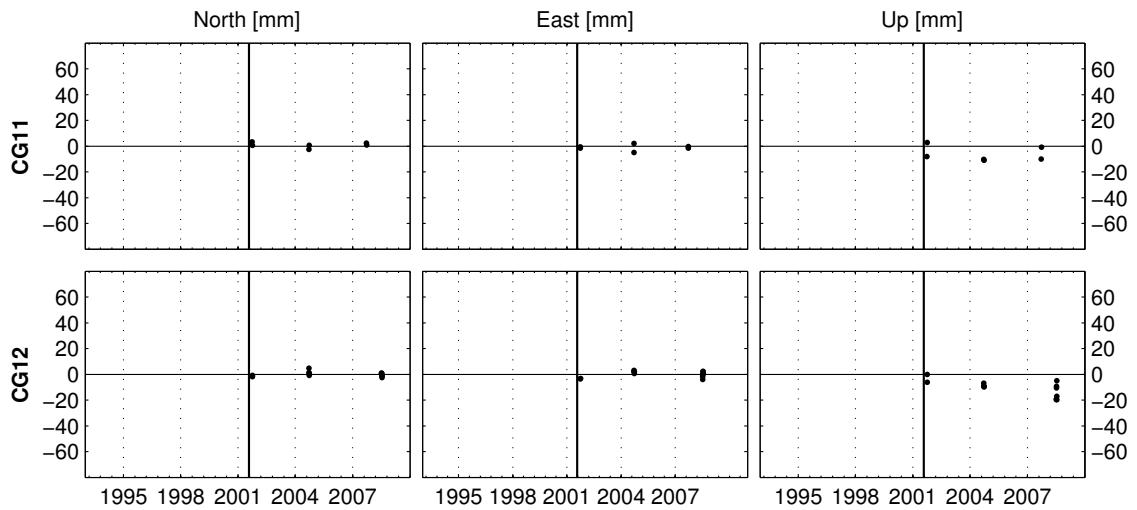


Figure E.4: Coordinate residuals of campaign-type sites CG11 and CG12 with respect to a linear motion estimated by using the Bernese GPS software subprogram ADDNEQ2. The rates of these sites were estimated in an additional ADDNEQ2 run where data of the years 1993 and 1994 was omitted (chapter 3.6.3). The vertical black lines depict the 2001 Mw 6.4 Skyros earthquake.

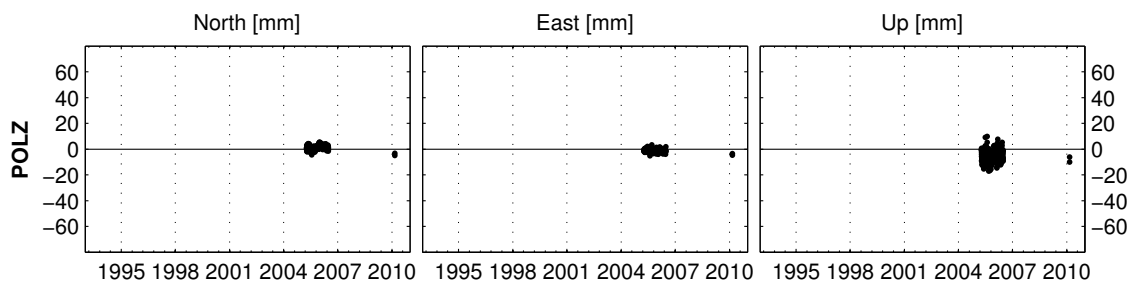


Figure E.5: Coordinate residuals of campaign-type GPS site POLZ with respect to a linear motion estimated by using the Bernese GPS software subprogram ADDNEQ2. The velocity of site POLZ was estimated in an additional ADDNEQ2 run where also data of the year 2010 was included.

F Additional notes on the applied dislocation models

F.1 Statistics of the locking depth models

The model of a buried screw dislocation in an elastic half-space was applied for the NAT and the KFZ in chapters 4.4.2 and 4.5.1, respectively. The optimal parameters of the model were derived by solving the global optimization problem by the application of a simulated annealing algorithm in combination with a pattern search algorithm after the last iteration. Both algorithms are implemented in the software package MATLAB [MATLAB, 2009]. Standard deviations of the estimated parameters were derived by a sensitivity analysis. 1000 sets were generated by randomly varying the normally distributed observations. The search space was limited to speed up the optimization algorithm. This procedure is similar to procedures outlined in *Velasco et al.* [2010] and *Metzger et al.* [2011]. The model parameters are strongly correlated (Figures F.1, F.2 and F.3).

Ganos fault: profile P1

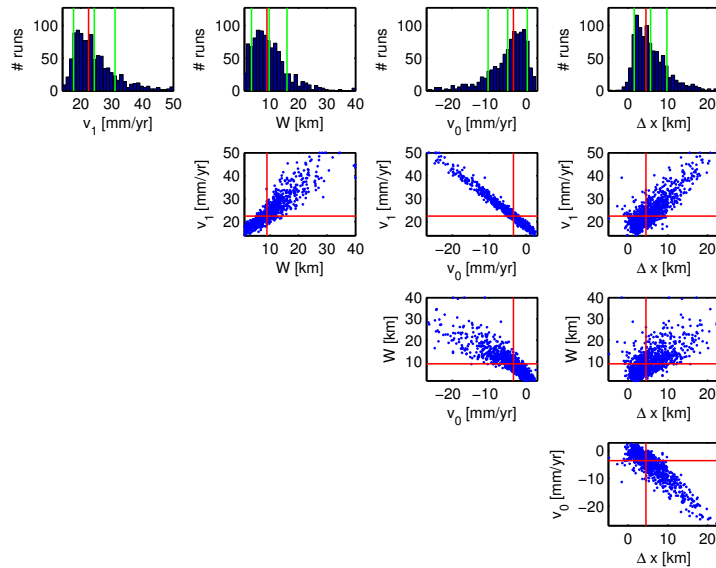


Figure F.1: Sensitivity analysis based on 1000 samples aiming at the derivation of standard deviations of the estimated parameters of the model of a buried screw dislocation in an elastic half-space. Model parameters: v_0 : constant fault-parallel velocity, v_1 : difference of fault-parallel velocity across the fault, W : locking depth, Δx : estimated fault-location along the cross-section. The red lines depict the parameters providing the best fit to the observations. The middle green lines depict the average of the parameters obtained based on randomly varied observations. 68% of the obtained parameters are located between the outer green lines.

North Aegean trough: profiles P2 and P4

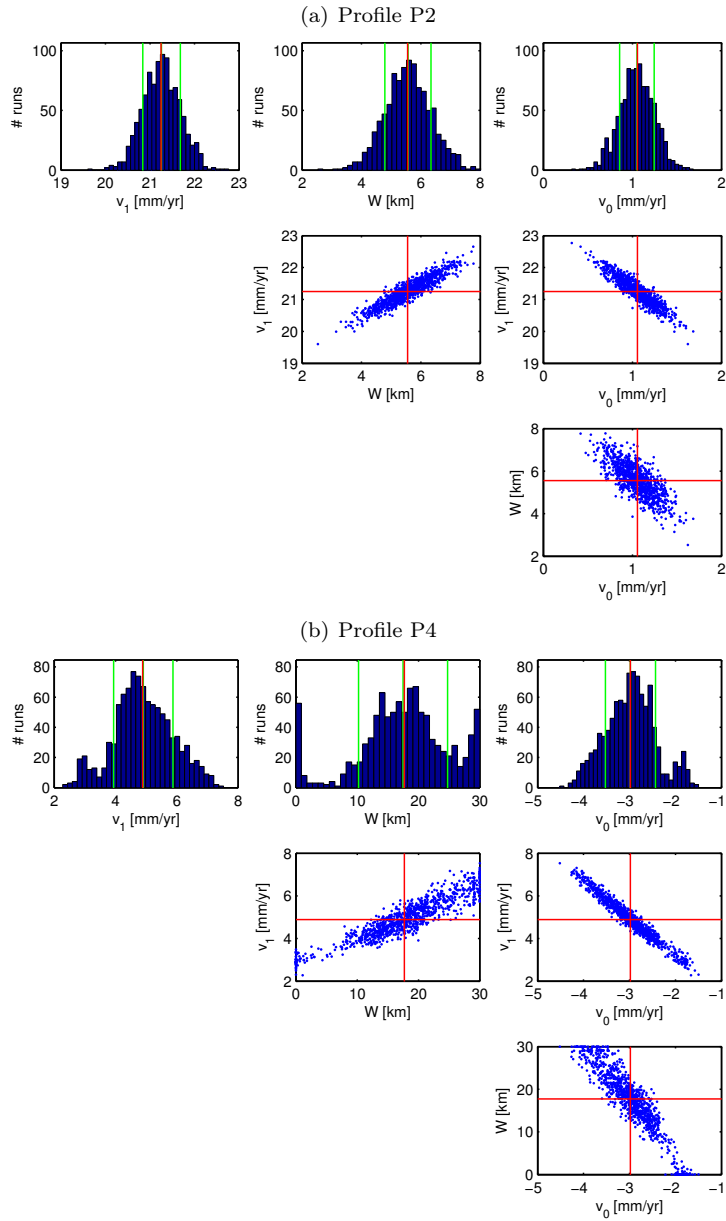


Figure F.2: Sensitivity analysis based on 1000 samples aiming at the derivation of standard deviations of the estimated parameters of the model of a buried screw dislocation in an elastic half-space. Model parameters: v_0 : constant fault-parallel velocity, v_1 : difference of fault-parallel velocity across the fault, W : locking depth. The red lines depict the parameter values providing the best fit to the observations. The middle green lines depict the average of the parameters obtained based on randomly varied observations. 68% of the obtained parameters are located between the outer green lines. (a) Profile P2. (b) Profile P4.

Kefalonia fault zone

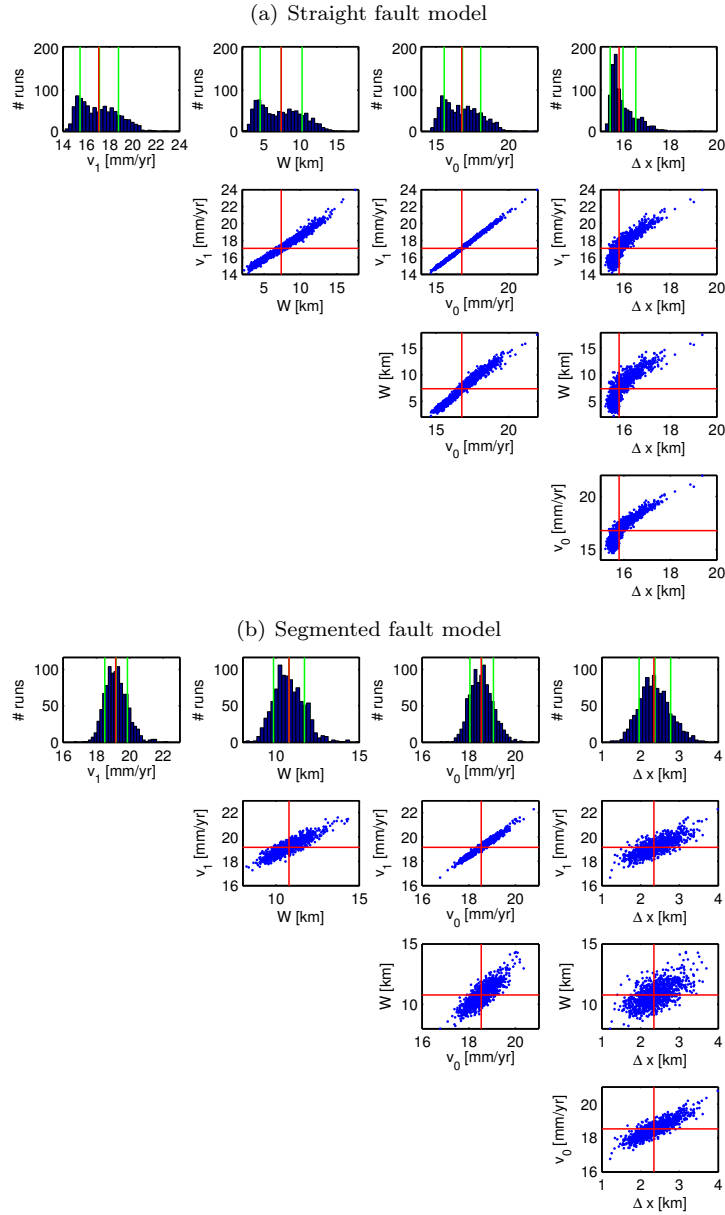


Figure F.3: Sensitivity analysis based on 1000 samples aiming at the derivation of standard deviations of the estimated parameters of the model of a buried screw dislocation in an elastic half-space. Model parameters: v_0 : constant fault-parallel velocity, v_1 : difference of fault-parallel velocity across the fault, W : locking depth, Δx : estimated fault-location along the cross-section. The red lines depict the parameters providing the best fit to the observations. The middle green lines depict the average of the parameters obtained based on randomly varied observations. 68% of the obtained parameters are located between the outer green lines. (a) Straight fault model. (b) Segmented fault model.

F.2 Description of the dislocation model for the calculation of strain accumulation at a subduction zone

Savage [1983] proposed a two-dimensional dislocation model describing strain accumulation at a subduction zone based on an edge dislocation in an elastic half-space (Figure F.4). The strain along the x-axis ε_{xx} and the expected uplift w are calculated by

$$\varepsilon_{xx}(x) = \left(\frac{2b_x}{\pi} \right) s \sin \alpha (s - x \cos \alpha) \left(x - \frac{s \cos \alpha}{D^2} \right) \quad (\text{F.1})$$

$$w(x) = \left(\frac{b_x \sin \alpha}{\pi} \right) \left\{ \frac{x s \sin \alpha}{D^2} + \arctan \left(\frac{x - s \cos \alpha}{s \sin \alpha} \right) - \frac{\pi}{2} \right\} \quad (\text{F.2})$$

$$\text{where} \quad D^2 = x^2 + s^2 - 2xs \cos \alpha$$

The parameter s is the downdip width of the main thrust zone, α is the dip and b_x is the dip slip component of the Burgers vector (positive for normal slip).

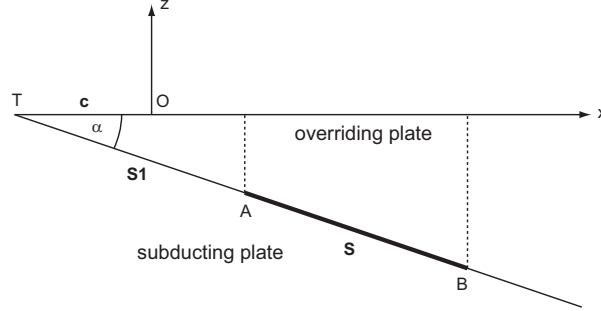


Figure F.4: Sketch of the dislocation models proposed by *Savage* [1983] and *Savage et al.* [2000]. The thick line indicates the locked portion of the plate interface. The x-axis is directed towards the back arc. $s = \overline{TB}$, $s1 = \overline{TA}$ and $c = \overline{TO}$. $c = 0$ in Eqs. (F.1) and (F.2).

The solution of a locked segment of the fault can be generated by superposing two dislocation solutions, one representing reverse slip from the surface to the top of the buried fault segment and the other representing normal slip from the surface to the bottom of the buried fault (Figure F.4). Thus, the velocity $u(x)$ of the forearc in the direction of plate convergence is

$$u(x) = f(x, s) - f(x, s1) + u_0 \quad (\text{F.3})$$

with

$$f(x, s) = -\frac{b}{\pi} \left\{ \{s - (x + c) \cos \alpha\} \frac{s \sin \alpha}{(x + c)^2 + s^2 - 2(x + c)s \cos \alpha} + \cos \alpha \arctan \frac{x + c - s \cos \alpha}{s \sin \alpha} \right\} \quad (\text{F.4})$$

where $f(x, s1)$ is analog to $f(x, s)$, u_0 is the velocity of the back arc and b is the rate of plate convergence [*Savage et al.*, 2000]. The parameter c adjusts the location of the trench in x-direction.

G Additional notes on finite element modeling

G.1 Strain tensors used in this thesis

Strain and strain rate calculations were performed in chapters 5 and 7. In brief, the used strain measures shall be described. The corresponding theory is based on *Fridtjov* [2008] except noted otherwise.

Assuming a body which was deformed from the unstrained reference configuration K_0 at time t_0 to the present configuration K at time t . The motion is given by the displacement vector $\mathbf{u}(\mathbf{r}_0, t)$:

$$\mathbf{u}(\mathbf{r}_0, t) = \mathbf{r}(\mathbf{r}_0, t) - \mathbf{r}_0 \quad (\text{G.1})$$

where \mathbf{r}_0 represents an arbitrarily chosen particle. The location of a particle is described by the coordinates X_i in configuration K_0 and by the coordinates x_i in configuration K . The displacement gradients H_{ik} represent the displacement gradient tensor \mathbf{H} . The tensor is defined by

$$\mathbf{H} = \frac{\partial \mathbf{u}}{\partial \mathbf{r}_0} \Leftrightarrow H_{ik} = \frac{\partial u_i}{\partial X_k} \quad (\text{G.2})$$

From Eq. (G.1) it follows

$$\frac{\partial x_i}{\partial X_k} = \frac{\partial X_i}{\partial X_k} + \frac{\partial u_i}{\partial X_k} \Leftrightarrow F_{ik} = \delta_{ik} + H_{ik} \Leftrightarrow \mathbf{F} = \mathbf{I} + \mathbf{H} \quad (\text{G.3})$$

where

$$\mathbf{F} = \frac{\partial \mathbf{r}}{\partial \mathbf{r}_0} \Leftrightarrow F_{il} = \frac{\partial x_i}{\partial X_l} \quad (\text{G.4})$$

The Green strain tensor is defined by

$$\boldsymbol{\varepsilon} = \frac{1}{2}(\mathbf{F}^T \mathbf{F} - \mathbf{I}) = \frac{1}{2}(\mathbf{H} + \mathbf{H}^T + \mathbf{H}^T \mathbf{H}) \Leftrightarrow \varepsilon_{kl} = \frac{1}{2} \left(\frac{\partial u_k}{\partial X_l} + \frac{\partial u_l}{\partial X_k} + \frac{\partial u_i}{\partial X_k} \frac{\partial u_i}{\partial X_l} \right) \quad (\text{G.5})$$

Deformation is small in case that

$$|H_{ij}| \equiv \left| \frac{\partial u_i}{\partial X_j} \right| \ll 1 \Leftrightarrow \text{norm} \mathbf{H} \ll 1 \quad (\text{G.6})$$

Small deformations imply small strains and small rotations. Under the assumption of small deformations we get for an arbitrary field $f(\mathbf{r}, t) = f(\mathbf{r}(\mathbf{r}_0, t), t)$

$$\frac{\partial f}{\partial X_i} = \frac{\partial f}{\partial x_k} \frac{\partial x_k}{\partial X_i} = \frac{\partial f}{\partial x_k} \left(\delta_{ki} + \frac{\partial u_k}{\partial X_i} \right) \approx \frac{\partial f}{\partial x_i} \equiv f_{,i} \quad (\text{G.7})$$

Small deformations usually imply small displacements. Therefore, the particle reference \mathbf{r}_0 can be replaced with the place vector \mathbf{r} and as the particle coordinates the place coordinates x_i can be

used instead of the coordinates X_i . If the displacement gradients are small quantities compared with 1 the products of H_{ij} components can be neglected compared to the H_{ij} components. Thus, the Green strain tensor is reduced to

$$\boldsymbol{\varepsilon} = \frac{1}{2} (\mathbf{H} + \mathbf{H}^T) \Leftrightarrow \varepsilon_{ij} = \frac{1}{2} (H_{ij} + H_{ji}) = \frac{1}{2} (u_{i,j} + u_{i,j}) \quad (\text{G.8})$$

This strain tensor is sometimes called the *small strain tensor* or the *infinitesimal strain tensor*. The strain rate analysis in chapter 5 is based on infinitesimal strain. The simplification is reasonable since the displacements only amount to a few centimeters per year and the corresponding strain rates do not significantly exceed $10^{-6}/yr$.

The default strain measure for geometrically nonlinear analyses in the finite element software Abaqus is *logarithmic* or *natural* strain [ABAQUS, 2009]. Logarithmic strain is defined by

$$\boldsymbol{\varepsilon}_{LE} = \frac{1}{2} \ln (\mathbf{F}^T \mathbf{F}) \quad (\text{G.9})$$

Strains derived by using the finite element method are logarithmic strains in this thesis.

G.2 Supplementary notes on the FE model of the central Hellenic trench (chapter 7.3)

G.2.1 Geometry of the FE model

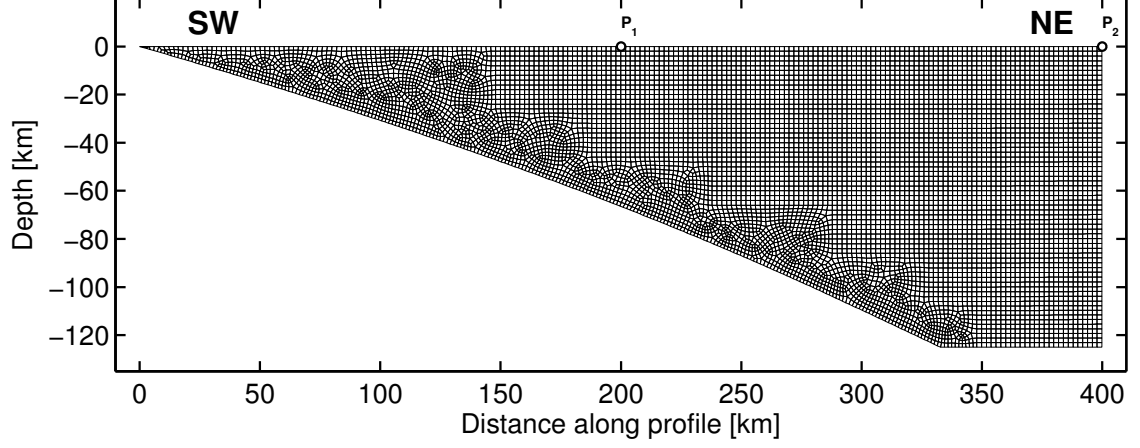


Figure G.1: Mesh of the Aegean plate as adopted in the finite element model. Only a part of the mesh is shown since it is uniform along the profile between kilometers 350 and 600. The average element size amounts to 2 km. The element size is smaller along the contact to the Nubian slab. The location of the profile in the Aegean sea is depicted in Fig. 7.3. The variations over time of the horizontal and vertical rates of points P_1 and P_2 are depicted in Figure G.2.

G.2.2 Energy fractions in the FE model

The total energy E_T of the FE model is the sum of the internal energy E_I , the kinetic energy E_K and the frictional energy dissipation E_{FD} minus the external work E_W

$$E_T = E_I + E_K + E_{FD} - E_W \quad (\text{G.10})$$

The internal energy E_I is the sum of the strain energy E_{SE} , the plastic energy dissipation E_{PD} , the creep energy dissipation E_{CD} and the artificial strain energy E_{AE} .

$$E_I = E_{SE} + E_{PD} + E_{CD} + E_{AE} \quad (\text{G.11})$$

The term E_K equals zero for a quasi-static analysis. The artificial strain energy E_{AE} amounts to a few percents of the creep dissipation energy E_{CD} .

Figure G.2 depicts the energy fractions in the model as well as the average annual displacement of two element nodes of selected models during the simulation runs. The locations of the two points (P_1 located at $x = 200$ km, $y = 0$ km, P_2 located at $x = 400$ km, $y = 0$ km) are depicted in Figure G.1.

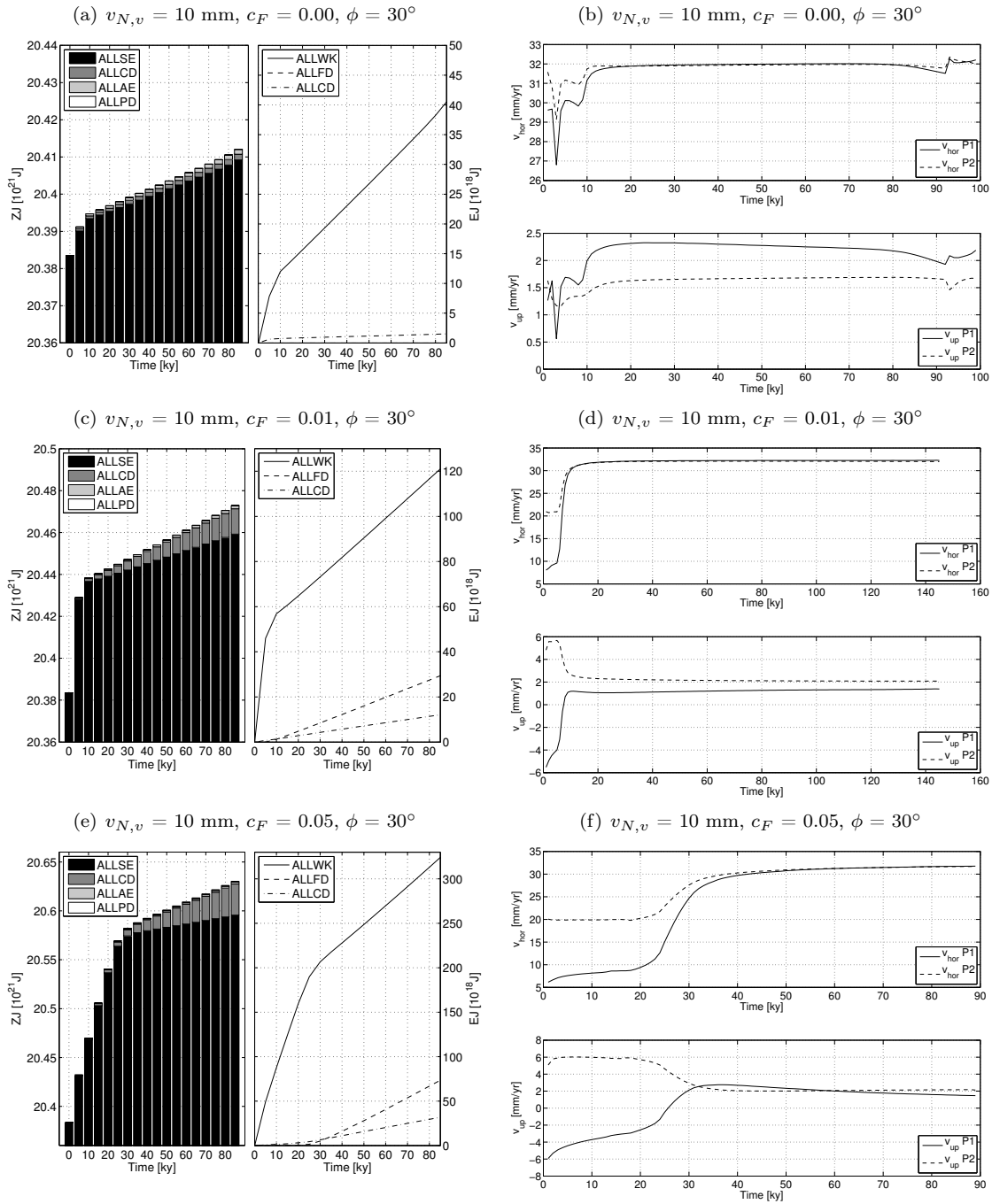


Figure G.2: Figures on the left side: Energy fractions contained in the FE model. ALLSE: strain energy, ALLCD: creep dissipation energy, ALLAE: artificial energy, ALLPD: plastic dissipation energy, ALLFD: frictional dissipation energy, ALLWK: external work. Figures on the right side: Average annual displacements of two points during the calculation period. Both points are located at the surface of the model, at $x = 200$ km and $x = 400$ km, respectively (Fig. G.1). $v_{N,v}$: vertical rate of Nubian slab, c_F : coefficient of friction, ϕ : angle of internal friction.

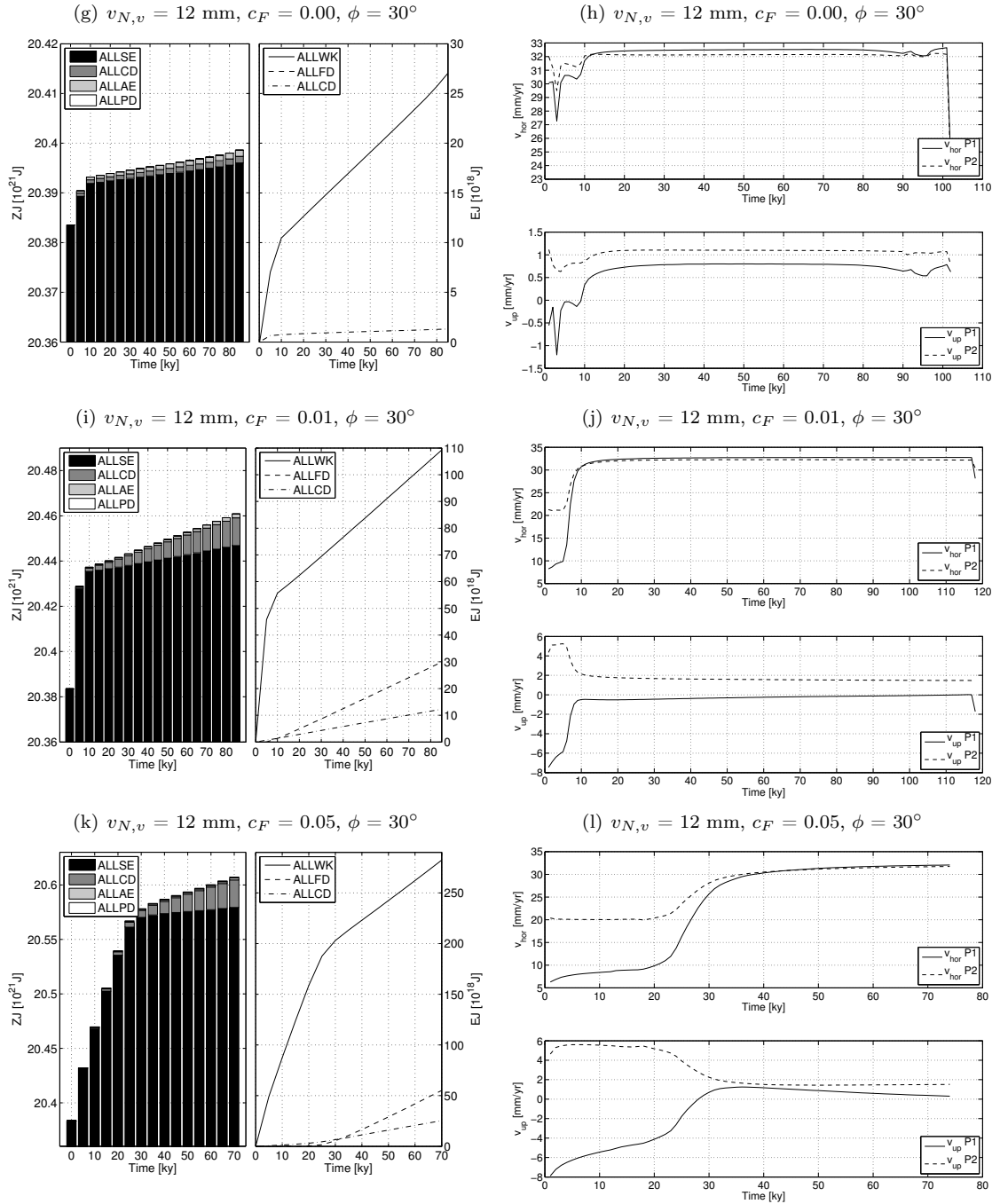


Figure G.2: (continued)

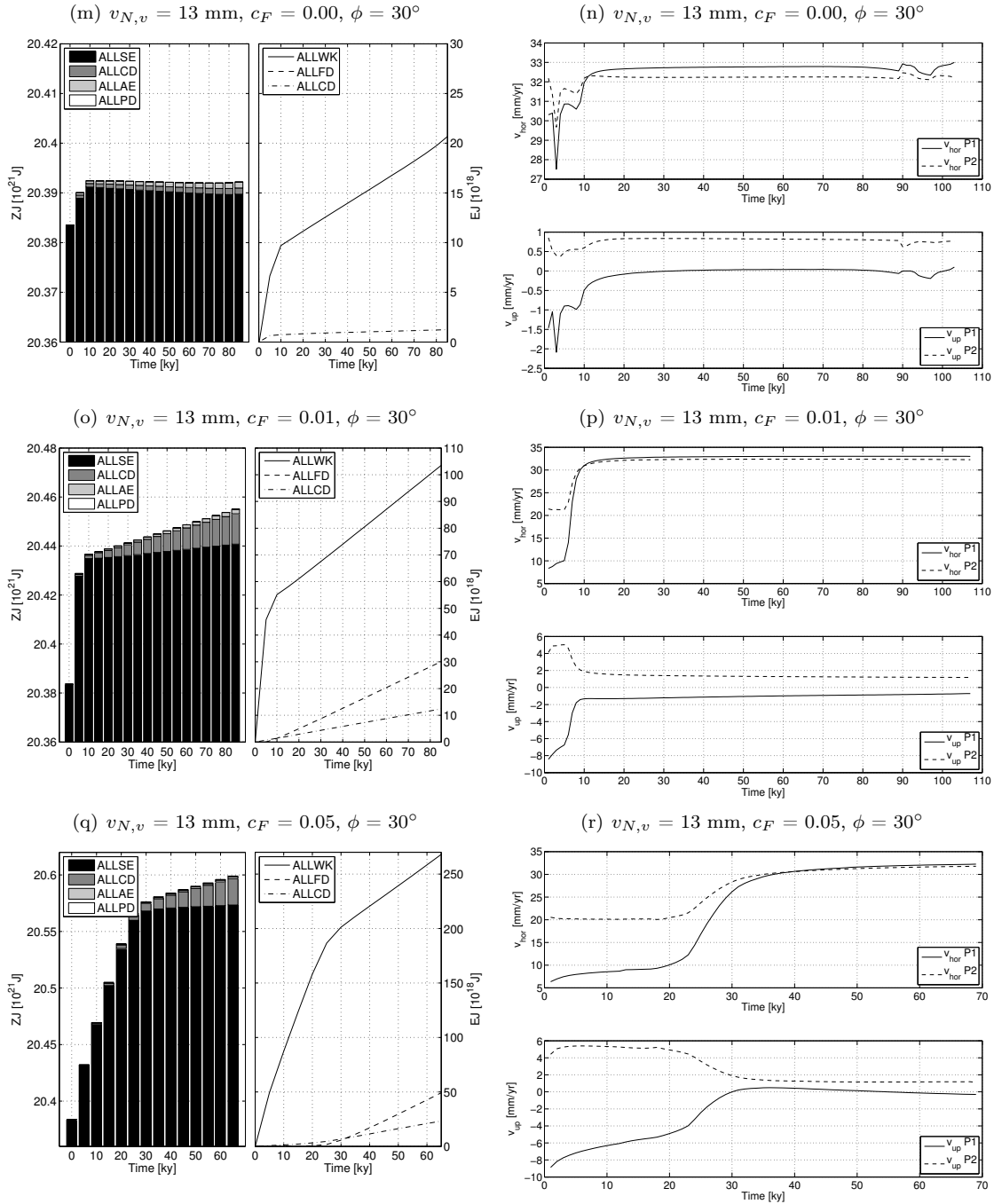


Figure G.2: (continued)

G.3 Supplementary notes on the FE model of the North Aegean domain (chapter 7.4)

G.3.1 Statistics of the model residuals

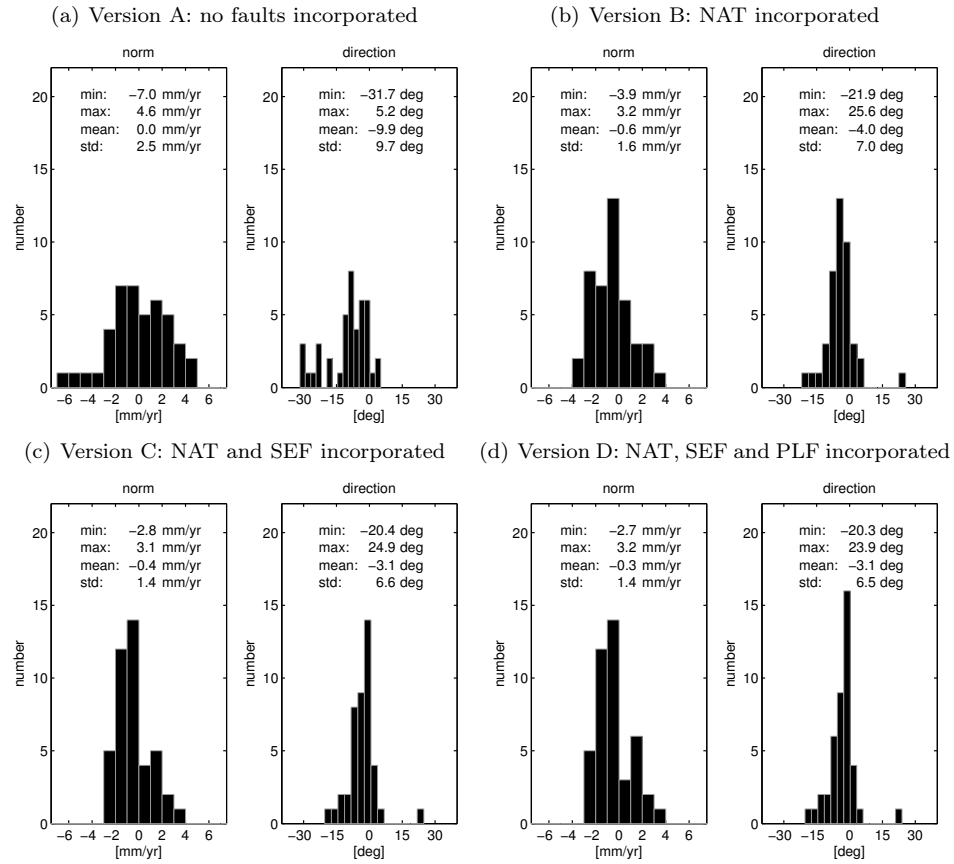


Figure G.3: Histograms of the magnitude and the direction of the residual vectors (GPS rates minus FEM displacement rates) for model versions A–D. The statistic is based on 43 residual vectors. NAT: North Aegean trough, SEF: Skyros-Edremit fault, PLF: Psara-Lesvos fault.

G.3.2 Errors in calculated strain rates due to the used projection method

The North Aegean domain was mapped to the model geometry of the finite element model by a stereographic projection. Points on the Earth's surface were projected on a plane which is tangential to the sphere in point P ($\phi=39.0^\circ\text{N}$, $\lambda=24.0^\circ\text{E}$) and is located by a distance $k = 1000$ m below this point. The projection center is the counterpole of point P . The distance between point P and an arbitrary point A is different on a sphere and in the model (Fig. G.4). The maximum influence of projection errors on the calculated strain can be approximated by

$$\varepsilon = \frac{\Delta L}{L} \quad (\text{G.12})$$

$$\frac{\Delta L}{L'} = \frac{\Delta L}{\alpha L} = \frac{1}{\alpha} \varepsilon \quad (\text{G.13})$$

$$\alpha = \frac{L'}{L} \quad (\text{G.14})$$

where L denotes the length of an arbitrary line segment in reality, L' denotes the length of the same line segment in the model and ΔL denotes the change in length of the line segment L . The factor α is minimum ~ 0.9994 in the model domain as derivable from Fig. G.4. Therefore, the error on calculated strain does not exceed a thousandth part.

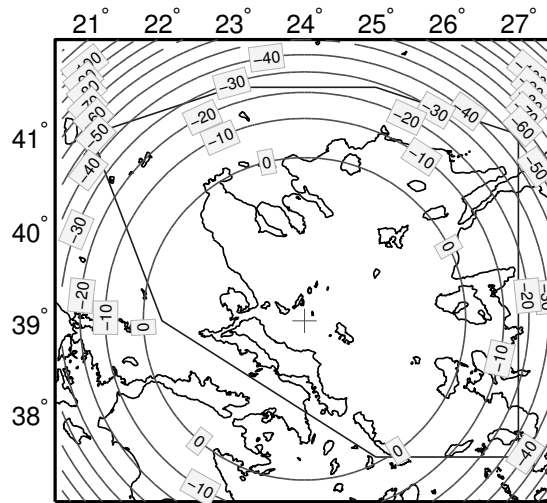


Figure G.4: Difference between the spherical distance and the projected distance between the center (depicted by a plus sign) and arbitrary points in the model domain. Unit: [m].